UNIVERSITY OF SOUTHAMPTON

FACULTY OF ENGINEERING, SCIENCE AND MATHEMATICS

School of Physics & Astronomy

Growth, Spectroscopy and Utilisation of Novel Low Dimensional Nanostructures: Carbon Nanotubes and Quantum Dots

by

Konstantinos Nikolaos Bourdakos

Thesis for the degree of Doctor of Philosophy

March 2008

UNIVERSITY OF SOUTHAMPTON

ABSTRACT

FACULTY OF ENGINEERING, SCIENCE AND MATHEMATICS
SCHOOL OF PHYSICS & ASTRONOMY
For the degree of Doctor of Philosophy
GROWTH, SPECTROSCOPY AND UTILISATION OF NOVEL LOW DIMENSIONAL NANOSTRUCTURES: CARBON NANOTUBES AND QUANTUM DOTS
By Konstantinos Nikolaos Bourdakos

The work presented in this thesis deals with two important low dimensional nanostructures: carbon nanotubes (CNTs) and quantum dots (QDs). In the part of the work related to CNTs a novel method for growing CNTs without the need of metal catalyst is presented. The as produced CNTs were grown by means of chemical vapour deposition on Si-Ge islands and on Ge dots grown with the Stransky – Krastanow method on top of silicon substrates. Through rigorous characterisation products of the method were identified as single wall carbon nanotubes (SWCNTs) with diameters of 1.6 and 2.1 nm. Acquired Raman spectra showed very low intensity or none D – band while the G' band was of high intensity indicating that the as produced CNTs may be of high quality. A by-product of this method is amorphous fibres which can be easily eliminated when exposed to HF vapour. As this method does not employ metal particles it is fully compatible with the front end silicon processing and therefore opens up the prospect of merging carbon nanotubes with silicon technology.

Furthermore CNTs were utilised as probes for atomic force microscopy (AFM). For the fabrication of the CNT probes two methods were applied successfully: the surface growth method and the pick up method. The latter was found to be substantially more efficient than the former and although not proper for mass production it is ideal for laboratory use as it can potentially generate thousands of CNT probes. The as fabricated CNT probes, had diameters in the range of 4 to 7 nm. Using CNT probes the surface of a mesoporous material with pore diameter of 7 to 12 nm and repeated distance of 15 to 18 nm was imaged, proving the high resolution that can be achieved with such probes and that AFM can be applied successfully to mesoporous materials. The latter has the potential to considerably expand the knowledge and the control of such materials to the nanoscale.

In the part of the work related to QDs a time resolved two colour pump photoluminescence (PL) technique was applied, with the aim to probe the coherent properties of the excitonic ground state of a single Stransky-Krastanow InGaAs QD. The method comprises of two pulses of different energy; a delayed blue pulse that pumps the GaAs barrier and an infrared (IR) pulse that pumps the excitonic ground state of the QD. The PL of the 1^{st} excitonic excited state of the QD is used in order to probe the occupancy of the ground state. The detection is carried out at zero laser background and thus having a considerably higher signal to noise ratio than other pump and probe methods. A PL intensity variation and a red shift in the energy of the 1^{st} excitonic excited state were observed, with both effects being dependant upon the intensity of the IR pulse but independent of the time delay and its energy. Further investigations showed that the IR excitation causes all PL and absorption lines of the QD to red shift, induces broadening of the absorption lines and increases the background absorption. Comparison with temperature dependent PL measurements showed that although heating might contribute to the above effects it cannot be the sole reason for their occurrence. Because of the above effects the time resolved two colour pump method cannot be applied as such for probing the coherence of QD ground excitonic state and needs to be modified further.

Dedicated to the memory of my father Ioannis Bourdakos
and my uncle Athanasios Alevizakos.

Αφιερώνεται στη μνήμη του πατέρα μου Ιωάννη Μπουρδάκου
και του θείου μου Αθανασίου Αλεβιζάκου.

Table of contents

List of Figures

DECLARATION OF AUTHORSHIP

I, ……Konstantinos Nikolaos Bourdakos……., [please print name]

declare that the thesis entitled [enter title]

…… Growth, Spectroscopy and Utilisation of Novel Low Dimensional Nanostructures: Carbon Nanotubes and Quantum Dots……..

and the work presented in the thesis are both my own, and have been generated by me as the result of my own original research. I confirm that:

- this work was done wholly or mainly while in candidature for a research degree at this University;
- where any part of this thesis has previously been submitted for a degree or any other qualification at this University or any other institution, this has been clearly stated;
- where I have consulted the published work of others, this is always clearly attributed;
- where I have quoted from the work of others, the source is always given. With the exception of such quotations, this thesis is entirely my own work;
- I have acknowledged all main sources of help;
- where the thesis is based on work done by myself jointly with others, I have made clear exactly what was done by others and what I have contributed myself;
- parts of this work have been published as: [please list references]

1. T. Ushino, K. N. Bourdakos, C. H. de Groot, P. A. Ashburn, S. Wang, M. E. Kiziroglou, G. Dilliway, D. C. Smith, ' Metal catalyst free low temperature carbon nanotube growth on SiGe islands' Applied Physics Letters 86, 23, (2005).
2. T. Ushino, K. N. Bourdakos, C. H. de Groot, P. A. Ashburn, M. E. Kiziroglou, G. Dilliway, D. C. Smith, 'Catalyst free low temperature direct growth of carbon nanotubes', IEEE Proceedings on Nanotechnology, 2005.
3. T. Ushino, K. N. Bourdakos, C. H. de Groot, P. A. Ashburn, D. C. Smith, 'Method of manufacturing carbon nanotubes', UK Patent Application 0426863.7.

4. T. Uchino, K.N. Bourdakos, C.H. de Groot, P. Ashburn, D.C. Smith, “Ge-catalyzed Vapour-Liquid-Solid growth of Carbon Nanotubes”, 36th ESSDERC Proceeding, 214, 2006.
5. H. B. Yin, K. N. Bourdakos, T. Melvin, D. C. Smith, ‘Purification of Nanostructures’, UK Patent Application 0508200.3.

Signed: ……..

Date:…….

Acknowledgements

There are a number of people and organisations whose influence and support were very important for the realisation of this thesis. I would first like to acknowledge EPSRC and the School of Physics and Astronomy of the University of Southampton which were my main sources of funding, without whose support this work would have not have been possible.

The guidance, support, and help of my supervisor Dr D. C. Smith was invaluable especially during the writing of the thesis and I would also like to thank him for teaching and helping me to develop my physical background around many aspects of the low dimensional systems and nanostructures and also learning how to implement rigorous research methods .

I would also like to acknowledge Dr. T. Ushino who conceived the idea of metal-catalyst-free growth of single walled carbon nanotubes and also for his support and help during the corresponding experimental work and the writing of the corresponding chapter, Prof. P. Ashburn and Dr. K. DeGroot, for their active support and contribution on the metal-catalyst-free growth of single walled carbon nanotubes, Dr. I. Nandhakumar, Dr. N. Gale, and Dr. X. Li, for their help and contribution in the project of carbon nanotube probes, Prof. J. J. Baumberg for his support on the work related to quantum dots, Dr. L. Besombes for teaching me the fundamental aspects of single quantum dot spectroscopy, Dr. T Melvin and Dr. HB Yin, for their help and contribution in the work related to the purification and selection of carbon nanotubes (although the latter was not finally included in this thesis, the acquired knowledge related to carbon nanotubes was very important), Prof. P. Savvidis, Prof. P. Lagoudakis and Dr. S. Mailis for their support and stimulating discussions.

As most of the writing of this thesis was carried out while working at the University of Surrey I would like to thank Prof. J. Allam and Dr. R. J. Curry for their support and also Prof. A. Monkman from the University of Durham.

There are also a number of people whose inspiration, encouragement, and support were very valuable for starting, developing and completing this work. Thus I would like to acknowledge Prof. T. Alexopoulos and Prof. A. McLeod for their encouragement to carry

on with a Ph. D., my sister Kalliopi Bourdakou for her support and help, D. Strogiloudi for invaluable moral support. Furthermore I would like to acknowledge my father Ioannis Bourdakos and my mother Dimitra Bourdakou for supporting me in my decision to work in physics, my uncle Athanasios Alevizakos for his support and for stimulating my curiosity and interest towards the physical sciences, and also for the inspiration that they gave to me with their struggle against the Nazi occupation of Greece and their uncompromised, consistent and proud stand against any kind of tyranny during the dark political ages in Greece that followed after the end of WWII. Finally I would like to thank Ms Emma J. Cockwell for her love and invaluable support and help for almost all of the period of this work.

« *Υπάρχει τέλος ένας αριθμός ανθρώπων των οποίων η έμπνευση, ενθάρυνση, και υποστήριξη στάθηκαν πολύτιμα στο ξεκίνημα, την πρόοδο και την ολοκλήρωση αυτής της εργασίας. Έτσι θα ήθελα να ευχαριστήσω τους κ.κ. καθηγητές Θ. Αλεξόπουλο και A. McLeod, για την ενθάρυνση τους να ξεκινήσω την διδακτορική εργασία, την αδερφή μου Καλλιόπη Μπουρδάκου για την βοήθεια και υποστήριξή της, την Δ. Στρογγυλούδη για την ανεκτίμητη ηθική της συμπράσταση. Επιπλέον θα ήθελα να εκφράσω την ευγνομωσύνη μου προς τον πατέρα μου Ιωάννη Μπουρδάκο, και την μητέρα μου Δήμητρα Μπουρδάκου για την υποστήριξη που μου παρείχαν στην απόφασή μου να ασχοληθώ με τη φυσική, τον θείο μου Αθανάσιο Αλεβιζάκο για την υποστήριξή του και την ενθάρυνση της περιέργειας και του ενδιαφέροντος μου προς τις φυσικές επιστήμες, καθώς επίσης και για την έμπνευση που μου παρείχαν οι αγώνες τους εναντίον της ναζιστικής κατοχής της Ελλάδας καθώς και η ασυμβίβαστη, συνεπής και υπερήφανη στάση τους εναντίον κάθε μορφής τυραννίας κατά την ζοφερή πολιτική περίοδο στην Ελλάδα που ακολούθησε μετά το τέλος του β' παγκοσμίου πολέμου* ».


YATTAAAAAAAAAAAAA!!!!

Chapter 1 Introduction

A new exciting and rapidly developing forefront field[1] in physical and life sciences as well as in engineering has emerged in recent years, the field of Nanotechnology. It promises[2] to revolutionise existing domains of technology such as electronics and also to introduce new, for instance nanofluidics and nanomechanics. Nanotechnology is the field of study and fabrication of physical, chemical and biological systems with dimensions that range from that of an individual atom or molecule, up to submicron scales. Its impact on science and technology but also on economy and society is considered by some authors to potentially be as profound[2] as that of semiconductor and information technology in the second half of the twentieth century.

The above consideration is not just a speculation but is based on the current economic trends and predictions. In the year 2000 the microsystems market[2] was approximately $15 billion, which with a projected annual rate of 15-20% is expected to rise at $100 billion by the end of the decade. The nanosystems market was about $100 million and is expected[2] to have an astonishing two hundred and fifty fold increase until the end of the decade, reaching $25 billion. Furthermore the importance of Nanotechnology is supported by the investments of some governments in the corresponding research domains, as for instance in the U.S.A. which in the year 2001 invested[2] almost half billion dollars in the National Nanotechnology Initiative (NNI). Also developments in nanotechnology related to electronics industry are included in the International Roadmap for Semiconductors under the sections Emerging Research Devices and Emerging Research Materials[3]. The degree of the importance of nanotechnology is also reflected in the fact that major publishing companies and institutions have issued a number of journals focusing exclusively on nanotechnology, for instance “Nature Nanotechnology” by McMillan Publications, “Nanotechnology” by the Institute of Physics (IOP), “Nanoletters” by the American Chemical Society (ACS), “Physica E – Low Dimensional Systems and Nanostructures” by Willey Interscience, “Journal of Nanoparticle Research” by Springer, “Nanotoday” by Elsevier.

The promises of nanotechnology, for revolutionising old but also inventing new applications in the whole spectrum of modern life, lie in its core definition; nanoparticles with sizes smaller than 100 nm have different properties than that of the bulk material[1] and so do the nanostructures assembled from them. This is a consequence of the fact that the particles whose dimensions are smaller than the characteristic lengths associated with particular effects are likely to exhibit different physical and chemical properties than the ones of the bulk material, leading to a behaviour that depends upon size[1]. Thus a number of physical and chemical properties such as the electronic structure, the melting point, the reactivity and the mechanical properties, have been observed to change when one or more dimensions of a particle become smaller than a critical size[1]. The exploitation of those properties as well as the possibility to control them by varying the size, have an enormous field of potential applications, ranging from the fabrication of ultra-strong materials, drug delivery, medical imaging and new therapies up to optoelectronic applications and quantum computing[1,2,4].

It is this wide range of properties and applications associated with the nanoparticles that makes their study a highly interdisciplinary field. For this reason nanotechnology incorporates a big spectrum of subjects that starts from topics in chemistry such as the catalysis of nanoparticles[1] and goes up to topics in physics and engineering such as the quantum dot lasers[5].

1.1 A Brief History of Nanotechnology

Although nanotechnology has only recently emerged as a new scientific and technological field, there is evidence that the exploitation of the unique properties of nanoparticles has a much longer history. An artefact from the fourth century A.D., the Lycurgus cup (which resides in the British museum[6]) is made from dichroic glass that changes its colour when held up to the light. This kind of glass owes its properties to the inclusion of silver and gold nanoparticles[6]. In a similar manner the colourful windows of medieval cathedrals are made from glass (stained glass) containing metal nanoparticles[1,7].

Nanoparticles have also been exploited in other aspects of ancient technology, such as metallurgy and the preparation of dyes. It was found recently through the means

of transmission electron microscopy studies that the unique properties of the legendary Damascus swords, which were manufactured in the seventh century A.D. are due to steel containing carbon nanotubes and cementite nanowires[8]. Furthermore the study of a recipe for a hair dye found in a text from the Greco – Roman times, used by ancient Egyptians about 4000 years ago, showed that its properties are due to the formation of PbS nanocrystals inside the hair[9].

In relatively more recent years the development of photography started in the 18th century and was based on silver nanoparticles[1] which were sensitive to light. The photographic film is an emulsion[1,10] consisting of a thin layer of gelatine containing silver halides which lie on a layer of transparent cellulose acetate. The silver halides are decomposed by the light yielding silver nanoparticles which are the pixels of the image[1]. Already in 1802 Thomas Wedgwood together with Sir Humphrey Davy presented a paper[11,12] with the title "An account of a method of copying paintings upon glass and of making profiles by the agency of light upon nitrate of silver", in which they described a method for producing photographic images using silver nitrate. Although the images were not permanent their method was considered as a breakthrough. Later[1] in the 19th century the technology of photography was developed further with milestones the production of the first colour photograph in 1861 by J. C. Maxwell and the development of a flexible film that could be rolled by Eastman in1883.

In 1908 G. Mie[1] published a paper in Annalen der Physic in which he provided an explanation of the dependence of the colour of the glass upon metal particle size and kind. In 1930's work published by I. Langmuir and K. Blodgett led later on in the 1960's to the fabrication of Langmuir-Blodgett films which exhibit extremely high periodicity at the nanometer scale[4]. In 1932 in work published by Rooksby[5,13,45] and was based on X – ray analysis, the colour of some silicate glasses was related to small inclusions of semiconductor materials such as CdSe and CdS. Such glasses (i. e. glasses dopped with semiconductors) have been used[5,45] since the 1960s as optical filters with sharp cut – off. It was not until the 1980s that it was understood[16,17,18,19,45] that those semiconductor inclusions were owing their properties to the effect of quantum confinement.

[1] The term nanoparticle here, although close, does not completely comply with the definition given above, as the size[10] of the silver – halide grains are usually between 1μm and 500 nm.

At the end of 1950s R. Feynman presented[1,2,4] a prophetic lecture at an annual meeting of the American Physical Society (29 December 1959) with the title "There is Plenty of Room at the Bottom"[14,15]. He described a technological vision of assembling nano-objects atom by atom or molecule by molecule having different properties than the bulk. A couple of years before, in 1957, Ralph Landauer[1] who was working for IBM, considered the possibility of nano-sized electronics and realized the impact of the quantum effects at this scale of dimensions.

The research and the discoveries in the domain of nanoscience followed an exponential trend in the decades of 1960's up to today. A number of the milestones will be briefly mentioned below: discovery of porous silicon[1] (nanometer size pores) in 1956 by Uhlir , discovery of magnetic fluids[1] in 1960s, study of conduction electrons in metal nanoparticles[1] in 1960s, fabrication of the first quantum well[1] in 1970s at Bell labs and IBM, Mann, Kuhn, Aviram and Ratner introduced the ideas of molecular electronics[4] in 1970s, development of molecular beam epitaxy (MBE)[4] in 1980s, Ekimov and Onushchenko reported the first observation of three dimensional quantum confinement[16,17,18,19] in 1981, synthesis of fullerene[20] in 1985, invention of scanning tunneling microscopy (STM)[21,22] and atomic force microscopy (AFM)[23,24] in the 1980s, development of the colloidal[25] quantum dots at Bell labs in the mid – 1980s, B. J. v Wees, H. v Houten, D. Wharam, M. Peper, observed the quantization of conductance[1] in 1987, T. A. Foulton, G. J. Dolan observed the Coulomb blockade[1] in the late 1980s, electron beam lithography[1] was introduced in the late 1980s, the fabrication[1] of layered (with nanometer thick layers) alternating metal magnetic and nonmagnetic materials exhibiting giant magnetoresistance with applications in magnetic storage was first achieved in the late 1980s, discovery of carbon nanotubes[26] by Iijima in 1990, growth of self assembled[27] quantum dots by means of MBE in 1993, utilization[28] of carbon nanotubes in scanning probe microscopy in the middle 1990s, fabrication[29,30] of the first single walled carbon nanotube field effect transistor in 1998, first demonstration of quantum dots as fluorescent biological labels in 1998[31,32], fabrication[33] of a single graphene sheet and demonstration of a high mobility FET device by Novoselov, and Geim in 2004.

1.2 The necessity of Nanotechnology

Nanotechnology is not only a domain with exciting potential applications but also a necessity for future economic development. This can be easily demonstrated in the domain of electronics. According to the Moors' law the computing power is doubled every one and a half years[4]. This means that the circuits on the silicon chips need to shrink at the same rate.

However there are physical limitations to this ever shrinking scheme which consequently puts a barrier to the computing speed that can be achieved by the silicon technology in the future. The most important of these limitations are going to be discussed briefly here. First the scaling down of the silicon devices requires the corresponding decrease of the thickness of the insulating layers[4]. Thinner insulating layers would result in higher electric fields which can lead to electron tunnelling or even avalanche breakdown, rendering the devices unreliable or even destroying them[4].

Second the fabrication of ever shrinking devices will at some point need to deal with the dispersion of the bulk properties of materials[4,34]. A doped semiconductor material, to a good approximation, can be considered a homogeneous medium. This approximation though breaks down at very small (nanoscale) dimensions. For example a typical p-type (boron doped) semiconductor has an impurity concentration of $N_A = 10^{23}/m^3$ which corresponds to a surface doping concentration of $N_{AS} = (N_A)^{2/3} \approx 5 \cdot 10^{14}/m^2$. This means that for a MOS-FET with channel of $1\mu m \times 1\mu m$ there is an average of 500 impurity atoms under the gate. As these impurities follow a statistical distribution in the semiconductor, the deviation of their average number $< N >$ per surface area is proportional to $1/\sqrt{< N >}$. So in this case the statistical deviation from average is going to be approximately 4%. However if this device shrinks by a factor of 100 ($0.1\mu m \times 0.1\mu m$ channel) the corresponding average number of impurity atoms under the gate would be 5 and the consequent standard deviation about 44%. This implies a big deviation to the threshold voltage of such kind of devices resulting in a non reliable operation of the integration circuit. The increase of the doping concentration has been considered as temporary solution, as the same problem will reoccur at a smaller scale. Furthermore high doping levels will result in smaller widths of the depletion zone at p-n

junctions and thus increasing the probability of carrier tunnelling and avalanche breakdown[4].

Third, the occurrence of the effects of quantum confinement when one or more of the dimensions of the fabricated devices becomes comparable or smaller than a critical size, as it was mentioned above. In this case, as it will be discussed below (Chapter 2 and Chapter 5), the electronic structure of the material will defer dramatically from the bulk resulting in a different function of the device. However the exploitation of structures and devices manifesting the effect of quantum confinement might lead to a new generation of quantum nanoscale devices which may play a key role in future nanoelectronics[4], as will be discussed below.

Finally, the heat dissipation of the integration circuits creates one more problem in the scaling down of the electronic devices. Even though the power consumption on a logic gate of a modern very large scale integration circuit (VLSI) can be as small as 10^{-5}W, the total amount of power that must be dissipated can be as high as 100 W due to the large number of devices[4]. Further scaling down is expected to increase the need for heat dissipation as operation power scaling cannot be achieved precisely in CMOS devices[35]. However the heat dissipation is limited due to the limited thermal conductivity of the materials[34] and therefore sets one more obstacle in the scaling down of the electronic devices.

The above limitations impose a barrier in the scaling down of the electronic devices of the integrated circuits. The difficulty of continuing the ever shrinking scheme of the electronic devices is characteristically expressed in the Executive Summary of the 2007 edition of the International Roadmap for Semiconductors (ITRS): "…*since 2001, we have reached the point where the horizon of the Roadmap challenges the most optimistic projections for continued scaling of CMOS*[2] *(for example, MOSFET channel lengths below 9 nm). It is also difficult for most people in the semiconductor industry to imagine how we could continue to afford the historic trends of increase in process equipment and factory costs for another 15 years! Thus, the ITRS must address post-CMOS devices*"[3]. As is underlined elsewhere in the same text, it is very likely that the conventional path of scaling will not be able to meet the future application requirements

[2] Complementary Metal-Oxide-Silicon (CMOS).

which are set by performance and power consumption[3]. Therefore there is a need for the introduction of new materials and device architecture in order to overcome the scaling barriers in the future[3].

There are several proposals in order to go beyond the scaling barriers and many of them exploit devices (such as resonant tunnel device single electron device, quantum dots)[3,4] and materials (such as graphene nanoribbons, carbon nanotubes, quantum dots)[3,4] coming from the field of nanotechnology. Some of these ideas propose modifications to the current CMOS architecture in order to extend the CMOS scaling such as carbon nanotube[3] FETs while others propose a whole new paradigm of computing such as quantum computing exploiting nanostructures such as quantum dots[4]. These two later nanostructures i.e. carbon nanotubes and quantum dots are the systems studied in this thesis.

1.3 Two important nanostructures: Carbon Nanotubes and Quantum Dots

Two of the most intense studied systems of the nanotechnology field are carbon nanotubes and quantum dots. Their importance becomes obvious if it is pointed out that they are considered as the building blocks of nannoscience[25]. A short description of these nanostructures will be given below (for more details see Chapter 2 and Chapter 5) and their importance in the field of nanotechnology and technology in general, as well as the contribution of the work reported in this thesis towards their development and study, will be discussed briefly.

Carbon nanotubes[36] can be thought of as a seamless cylinder made up by rolling a graphene sheet. Their length[36,37] can vary from a few nanometers to several micrometers while their diameter (in the case of single walled carbon nanotubes) is in the range of subnanometer to approximately three nanometers. Their electronic properties[36,37] depend very strongly on their diameter and chirality (the way the grapheme sheet has been rolled off) and they can exhibit metallic or semiconducting behaviour. They are one dimensional systems as the charge carriers can move freely only along the direction of their axis while their movement along their circumference is restricted, from the imposed quantum confinement due to their small diameter. It is this one dimensional character that

a lot of their astonishing properties arise from such as ballistic transport, extremely high current density. Because of their unique electronic properties and nanoscale size they are considered as very strong candidates as channels[3] in silicon FETs in the case of semiconducting carbon nanotubes or interconnects[3] in VLSIs in the case of metallic carbon nanotubes. However in order to exploit carbon nanotubes in nanoelectronics a number of issues must be resolved. Techniques that allow the selection of carbon nanotubes according to their electronic properties and enable selective positioning of them on a substrate must be developed further. Also in order to be able to use carbon nanotubes in the front end silicon processing facilities one has to get rid of the heavy metal catalyst, which are mixed with carbon nanotubes during their growth. This latter issue is addressed in this thesis where a method for growing carbon nanotubes without the need for metal catalyst is presented.

The fabrication of nanoelectronic devices though is only one fraction of the potential application of carbon nanotubes. Because of their optical properties, carbon nanotubes behave as excellent saturable absorbers with potential applications in laser fabrication[38,39,40]. Related to their optical properties and more specifically their ability to absorb infrared light as well as their size it is also their potential medical applications[41] in cancer treatment.

Due to their unique mechanical properties[36] (they are tens of times stronger than steel) they have been considered as possible reinforcement for structural materials. These mechanical properties associated with their small size and cylindrical geometry render carbon nanotubes as ideal probes in scanning probe microscopy for ultra high resolution. In this thesis different methods for fabricating probes for scanning probe microscopy by utilising carbon nanotubes are explored. Additionally by using carbon nanotube probes ultra high resolution images of surfaces of mesoporous materials were acquired by means of AFM, showing that knowledge and control of such materials can be extended down to the nanoscale.

As it was mentioned above another important entity of the nanotechnology field is quantum dots. This term refers to structures in which the charge carriers are confined in all three directions resulting in the formation of discrete energy levels similar to those of an atom. There is a variety of methods[5,42,43] and systems that can be fabricated bearing

the properties of quantum dots, such as lithographically fabricated quantum dots, modulated electric field quantum dots, nanocrystals[45], and self assembled quantum dots. Their dimensions range from a hundred of nanometers down to a few nanometers and can have a variety of shapes such as pyramidal, spherical, or other patterned shapes. Their properties[5,42,43,45,44] strongly depend on their size, shape and also on the material they are made of. Most commonly used materials are various alloys of InGaAs, InAs, Si, Ge, CdS, CdSe, CdTe, PbS.

Due to the similarities of some aspects of the electronic properties of quantum dots with those of an atom[5], they are considered as potential candidates for the realisation of quantum computing and in general of quantum information processing[5] as for instance in quantum cryptography as single photon emitters. Therefore it is necessary to acquire knowledge upon their optical and more significantly their coherent properties. A method for studying the coherent properties of the excitonic ground state of quantum dots is explored in this thesis as well as some aspects of their optical properties.

Quantum information processing though is only one aspect of the possible applications of quantum dots. Due to their optical properties[5,45] such high quantum efficiency, the possibility of tailoring them by controlling their size, shape and material and also the possibility of being solution processible for some of them they have a vast range of applications. This range extends in optoelectronics with applications such as quantum dot lasers, infrared emitters and sensors, hybrid organic-inorganic photovoltaics and light emitting diodes (LEDs), in life sciences[46] as fluorescent labels in high-resolution cellular imaging, for studying intracellular processes at the single-molecule level, for in vivo long-term observation of cell trafficking, diagnostics, and tumour targeting, in nanoelectronics as single electron transistors[5], or components in resonant tunnelling devices[3].

1.4 Structure of the thesis

In this thesis two distinct experimental topics have been studied, therefore it has been divided into two parts. The first part consists of three chapters (chapters 2 – 4) and presents the experimental results on growth and utilisation of carbon nanotubes. The second part (chapters 5 – 6) presents the experimental results on the coherent and optical

properties of self assembled InGaAs quantum dots. Below is a short summary of the contents of each chapter.

The second chapter can be considered as consisting of two parts. The first part is concerned mainly with aspects of the physical properties of carbon nanotubes. It starts with a general discussion about carbon science and the various carbon allotropes. It proceeds with a description of the geometrical features of carbon nanotubes. Then the derivation of their electronic properties is presented in brief. A section on resonant Raman spectroscopy gives the basic physics behind this followed by a section about aspects of the phonon properties and Raman spectroscopy of carbon nanotubes, as this is going to be one of the main characterisation tools of the experimental part of this thesis. The second part is concerned with the growth of carbon nanotubes. It contains brief descriptions of the main methods of growth and it focuses on the method of chemical vapour deposition which is the one that was used during the experiments. It follows a section on the mechanism of growth with which the chapter closes.

The third chapter presents the major experimental results of the thesis related to a novel growth method of carbon nanotubes without the need of metal catalyst. It starts with an introduction in which major achievements and challenges in carbon nanotube nanoelectronics are presented along with a brief discussion about the need for carbon nanotubes free of metal particles for their incorporation into the front end silicon technology and an outline of the experimental section of the chapter. Then follows an overview describing the efforts by other workers for a metal – catalyst – free method of growth carbon nanotubes. Finally the experimental part of the chapter follows. It is divided in two sections in which the two variants of the novel method for growing carbon nanotubes without the need of metal catalyst are described in detail. In the same sections the respective characterisation data of the as grown carbon nanotubes are presented along with discussion and conclusions for each of the variants.

The fourth chapter presents the experimental results of the utilisation of carbon nanotubes as probes for scanning probe microscopy. It starts with a short introduction discussing the advantages of AFM, its limitations and the advantages of carbon nanotubes AFM probes in comparison with the conventional probes. The chapter continues with a discussion on the issue of the tip convolution error which limits the

lateral resolution of the AFM imaging. A literature review of the field of fabrication of carbon nanotube probes and the corresponding achievements in terms of AFM resolution follows. In the next section different fabrication methods of carbon nanotube AFM probes are discussed. Then follows the experimental section of the chapter in which the methodology and the results of two different methods of fabricating carbon nanotube AFM probes are presented. The need of further engineering the carbon nanotube probes arising from their mechanical properties is explained and the corresponding experimental results are presented in the next section. The last section of the chapter presents the results of AFM imaging surfaces of mesoporous materials by using carbon nanotube AFM probes along with conclusions.

In the fifth chapter some background knowledge on quantum dots and on theory of coherence in matter is presented. The chapter starts with a short introduction in quantum dots followed by a section describing the various fabrication techniques and the corresponding types of quantum dots. The next section deals with the electronic structure of quantum dots starting with the single particle picture, continuing with the description of excitons in quantum dots and finishing with a discussion on various excitonic complexes. The final section contains some theory of coherence in matter, starting with a discussion of the coherence of a two level system and finishing with the description of the optical Bloch equations and the rotating wave approximation.

Finally, in the sixth chapter the experimental results on single quantum dot spectroscopy are reported. The chapter starts with a description of the sample and the initial pump and probe experiments. It then continues with a description of the time resolved two colour pump method and discusses its advantages in comparison with the conventional pump and probe when applied to the study of the coherent properties of the excitonic ground state of a quantum dot. The next section presents the collected data from the spectroscopic characterisation of the quantum dot by means of non –resonant, resonant photoluminescence measurements and photoluminescence excitation spectroscopy (PLE). It is followed by a presentation and discussion of the data acquired through the time resolved two colour pump method. The effort to interpret these data is presented in the remaining sections starting with those that contain the data of the temperature dependence of the quantum dot photoluminescence, the data of extensive

resonant excitation measurements and finally the PLE data for various values of the laser power. The chapter finishes with conclusions.

References

[1] C. P. Poole Jr., F. J. Owens, “Introduction to Nanotechnology”, p. xi, John Wiley & Sons, Hoboken, New Jersey, U.S.A., (2003).

[2] B. Bhushan, "Introduction to Nanotechnology",p.1, in "Springer Handbook of Nanotechnology", B. Bhushan, (ed.),Springer-Verlag, Berlin, Heidelberg, (2004).

[3] INTERNATIONAL TECHNOLOGY ROADMAP FOR SEMICONDUCTORS, 2007 EDITION, EXECUTIVE SUMMARY, (http://www.itrs.net/).

[4] A. Nabok, "Organic and Inorganic Nanostructures",ARTECH HOUSE, INC, (2005).

[5] D. Bimberg, M. Grundmann, N. N. Ledentsov, "Quantum Dot Heterostructures", John Wiley & Sons, Chichester, New York, (1999).

[6] http://www.britishmuseum.org/explore/highlights/highlight_objects/pe_mla/t/the_lycurgus_cup.aspx

[7] “A Brief History of Stained Glass”, The Stained Glass Museum, Ely Cathedral, Ely, Cambridgeshire http://www.stainedglassmuseum.com/briefhis.shtml

[8] M. Reibold, P. Paufler, A. A. Levin,W. Kochmann, N. Pätzke, D. C. Meyer,"Carbon nanotubes in an ancient Damascus sabre",Nature, 444, 286, (2006).

[9] P. Walter,E. Welcomme, P. Halle´got, N. J. Zaluzec, C. Deeb, J. Castaing, P. Veyssie`re, R. Bre´niaux, J.-L. Le´veˆque, G. Tsoucaris, "Early Use of PbS Nanotechnology for an Ancient Hair Dyeing Formula",Nano Lett., 6, 2215, (2006).

[10] F. G. Smith, T. A. King, D. Wilkins, "Optics and Photonics: An Introduction", Second Edition, John Wiley & Sons Ltd, Chichester, (2007).

[11] H. Gernsheim, “A concise history of photography”, Thames and Hudson, London, (1965)

[12] R. Leggat, "A History of Photography from its beginnings till the 1920s" http://www.rleggat.com/photohistory/index.html

[13] H. P. Rooksby, "The Colour of Selenium Ruby Glasses", J. Soc. Glass Tech., 16, 171, (1932).

[14] R. P. Feynman, “There’s Plenty of Room at the Bottom: An Invitation to Enter a New Field of Physics” in “Handbook of Nanoscience, Engineering, and Technology” ed. W. A. Goddard, D. W. Brenner, S. E. Lyshevski, G. J Iafrate, CRC Press, London, New York, (2003).

[15] http://www.zyvex.com/nanotech/feynman.html

[16] A.I. Ekimov, A. A. Onushchenko "Quantum size effect in 3-dimensional microscopic semiconductor crystals",JETP Letters, 34, 345, (1981).

[17] A.I. Ekimov, A. A. Onushchenko "Quantum size effect in the optical-spectra of semiconductor micro-crystals", Soviet Physics Semiconductors-USSR, 16, 775, (1982).

[18] A.I. Ekimov, A. A. Onushchenko "Size quantization of the electron-energy spectrum in a microscopic semiconductor crystal", JETP Letters, 40, 1136, (1984).

[19] A.I. Ekimov, A. L. Efros, A. A. Onushchenko "Quantum size effect in semiconductor microcrystals", Solid State Communications, 56, 921, (1985).

[20] H.W. Kroto, J.R. Heath, S.C. O'Brien, R.F. Curl, R.E. Smalley, "C60: Buckminsterfullerene", Nature 318, 162 (1985).

[21] G. Binnig, H. Rohrer, C. Gerber, and E. Weibel, ‘‘Surfacestudies by scanning tunneling microscopy,’’ Phys. Rev. Lett. 49, 57, (1982).

[22] G.Binnig, H. Rohrer, ‘‘Nobel Lecture: Scanning tunneling microscopy—from birth to adolescence,’’ Rev.Mod. Phys. 59, 615, (1987).

[23] G. Binnig, C. F. Quate, Ch. Gerber, “Atomic Force Microscope”, Phys. Rev. Lett. 56, 930, (1986).

[24] Binnig, G., 1986, ‘‘Atomic Force Microscope and Method forImaging Surfaces with Atomic Resolution,’’ US Patent No.4,724,318.

[25] A. P. Alivisatos, "Birth of a Nanoscience Building Block", ACS Nano, 2, 1514, (2008).

[26] S. Iijima, " Helical microtubules of graphitic carbon", Nature, 354, 56, (1991).

[27] D. Leonard, M. Krishnamurthy, C. M. Reaves, S. P. Denbaars, P. M. Petroff, "Direct formation of quantum-sized dots from uniform coherent islands of InGaAs on GaAs surfaces", Appl. Phys. Lett. 63, 3203 (1993)

[28] H. J. Dai , J. H. Hafner, A. G. Rinzler, D. T. Colbert, R. E. Smalley, “Nanotubes as nanoprobes in scanning probe microscopy”, Nature, 384, 147, (1996).

[29] S. J. Tans, A.R.M. Verschueren, C. Dekker, "Room-temperature transistor based on a single carbon nanotube", Nature, 393, 49, (1998)

[30] R. Martel, T. Schmidt, H. R. Shea, T. Hertel, Ph. Avouris, "Single- and multi-wall carbon nanotube field-effect transistors", Appl. Phys. Lett., 73, 2447, (1998).

[31] M. Bruchez, M. Moronne, P. Gin, S. Weiss, A. P. Alivisatos, "Semiconductor nanocrystals as fluorescent biological labels Science" 281, 2013, (1998).

[32] W. C. W. Chan, S. M. Nie, Quantum dot bioconjugates for ultrasensitive nonisotopic detection Science 281, 2016, (1998).

[33] K. S. Novoselov, A. K. Geim, S. V. Morozov, D.Jiang, Y. Zhang, S. V. Dubonos, I. V. Grigorieva, A. A. Firsov, "Electric field effect in atomically thin carbon films", SCIENCE, 306, 666, (2004).

[34] J.M. Martínez-Duart, R.J. Martín-Palma, F. Agulló-Rueda, "Nanotechnology for Microelectronics and Optoelectronics", Elsevier,London, (2006)

[35] G. N. Parsons, “Engineering Challenges in Molecular Electronics” in “Handbook of Nanoscience, Engineering, and Technology” ed. W. A. Goddard, D. W. Brenner, S. E. Lyshevski, G. J Iafrate, CRC Press, London, New York, (2003).

[36] R. Saito, G. Dresselhaus, M. S. Dresselhaus, "Physical Properties of Carbon Nanotubes", Imperial College Press, (1998).

[37] M.S. Dresselhaus, G. Dresselhaus, P.C. Eklund, "Science of Fullerenes and Carbon Nanotubes", Academic Press (1996).

[38] T. R. Schibli, K. Minoshima, H. Kataura, E. Itoga, N. Minami, S. Kazaoui, K. Miyashita,M. Tokumoto, Y. Sakakibara, "Ultrashort pulse-generation by saturable absorber mirrors based on polymer-embedded carbon nanotubes", Optics Express, 13, 80253, (2005).

[39] A. G. Rozhin, Y. Sakakibara,S. Namiki,M. Tokumoto, H. Kataura, Y. Achiba, "Sub-200-fs pulsed erbium-doped fiber laser using a carbon nanotube-polyvinylalcohol mode locker", Appl. Phys. Lett. 88, 051118, (2006).

[40] F. Wang, A. G. Rozhin, V. Scardaci, Z. Sun, F. Hennrich, I. H. White, W. I. Milne, A. C. Ferrari, "Wideband-tuneable, nanotube mode-locked, fibre laser", Nature Nanotechnology 3, 738, (2008).

[41] N. W. S. Kam, M. O'Connell, J. A. Wisdom, H. Dai, "Carbon nanotubes as multifunctional biological transporters and near-infrared agents for selective cancer cell destruction", PNAS, 102, 11600, (2005).

[42] P. Michler (editor), "Single Quantum Dots: Fundamentals, Applications and New Concepts", Springer Verlag, Berlin, Heidelberg, (2003).

[43] L. Jacak, P. Hawrylak, A. Wójs, "Quantum Dots", Springer Verlag, Berlin, Heidelberg, (1998).

[44] F. Rossi (editor), "Semiconductor Macroatoms: Basic Physics and Quantum – device Applications", Imperial College Press, London, (2005).

[45] U. Woggon, "Optical Properties of Semiconductor Quantum Dots", Springer Verlag, Berlin, Heidelberg, New York, (1997).

[46] X. Michalet,F. F. Pinaud, L. A. Bentolila, J. M. Tsay, S. Doose, J. J. Li, G. Sundaresan, A. M. Wu, S. S. Gambhir, S. Weiss, "Quantum Dots for Live Cells, in Vivo Imaging, and Diagnostics", Science,307,538,(2005).

PART I

Carbon Nanotubes

Chapter 2 Physical Properties of Carbon Nanotubes

2.1 Introduction

Carbon is one of the most studied materials due to its importance in numerous applications and effects as for instance the phenomenon of life itself. Until the middle of the '80s it was thought that the knowledge on carbon was complete or almost complete. Then the discovery of fullerenes and later of carbon nanotubes and recently of graphene (as an isolated sheet) produced an avalanche of scientific discoveries reviving the carbon science.

In the following some general information and an outline of the properties of carbon is going to be given. Then the focus will be placed on carbon nanotubes and their electronic properties as those has been derived from the electronic structure of graphene and on other aspects of carbon nanotube science such as Raman spectroscopy and synthesis that play an important role in the experimental part of this thesis. A brief section on the Raman effect has also been included.

2.2 Hybridization of Carbon

Carbon exhibits an enormous diversity of compounds and forms, much bigger than any other known element. One of the reasons is the many possible configurations of the electronic states of the carbon atom which is known as the hybridization of atomic orbitals[1]. Carbon is the sixth element of the periodic table and is at the top of column IV. The ground electronic state configuration of the carbon atom is $1s^2 2s^2 2p^2$. The $2s$ and $2p$ states are close in energy (while their energy difference from the $1s$ state is very big) and therefore can be mixed under a small perturbation. The absence of nearby inner atomic orbitals in carbon facilitates hybridizations in which only the valence s and p orbitals participate and allows three possible hybridizations sp, sp^2, sp^3 (Figure 2-1). This is one of the main differences between carbon and other elements of group IV such as Ge and Si which exhibit primarily sp^3 hybridization.

The sp hybrid orbital is formed by the mixing of the $2s$ and one of the $2p$ orbital. Overlapping of two sp hybrid orbitals belonging to neighbouring carbon atoms give rise to a σ bond as for example in molecule of acetylene $(HC \equiv CH)$. The remaining unhybridized p orbitals overlap and form two π bonds.

In the case of the sp^2 hybridisation the mixing of the $2s$ and two of the $2p$ orbitals forms three equivalent hybrid orbitals. They all lay on the same plane forming angles of 120° between each other. Overlap with sp^2 orbitals of neighbouring atoms give rise to σ bonds. The remaining p orbital is normal to the plane of the hybrid ones and form a π bond with the corresponding p of a neighbouring atom. A very well known example of sp^2 hybridisation is poly – acetylene $(-HC=CH-)_n$.

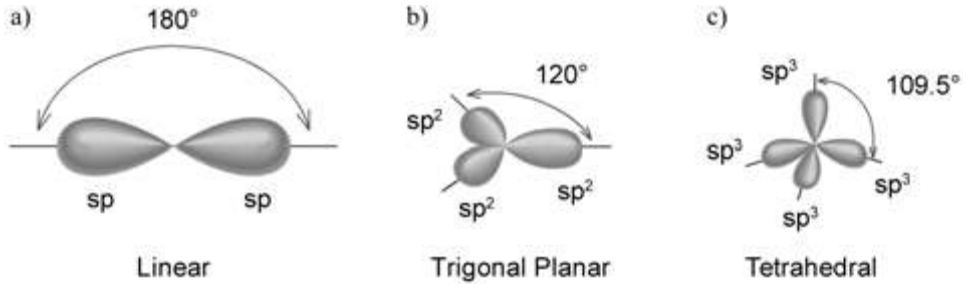

Figure 2-1 Different hybridizations of the carbon atom.

Finally four equivalent sp^3 hybrid orbitals are formed by the mixing of the $2s$ with all of the $2p$ orbitals. They are tetrahedrally oriented and their overlap with ones from neighbouring atoms give rise to σ bonds as in the molecule of methane (CH_4).

2.3 Allotropes of Carbon

Due to its rich hybridization carbon occurs in different structural modifications which are known as the allotropes of carbon. The allotropes although they have the same chemical composition (in this case carbon) and exist in the same state of matter (solid state) they exhibit different physical properties as a result of their different structure.

Some of the most known carbon allotropes are: Diamond, Graphite, Fullerenes (Buckmisterfullerene, or Buckyball), Single Walled Carbon Nanotubes (SWCNT). Bellow is presented some brief information about them.

2.3.1 Diamond

The diamond lattice structure can be cubic or hexagonal (Figure 2-2). The latter is known as Lonsdaleite, it has a wurtzite structure and C – C bond length equal to 1.52 Å . The most common form is the cubic one in which each carbon atom is linked to four other carbon atoms via sp^3 σ bonds in a tetrahedral array[2]. The bond length is 1.5444 Å which is 10% larger the corresponding length for graphite. Its atomic density though is $1.77 \cdot 10^{23}$ cm^{-3} which is 56% bigger than the one of graphite and the highest known one. Diamond has an FCC lattice structure with a diatomic basis (the second atom is at $\left(1/4, 1/4, 1/4\right)$ position) and a lattice constant of 3.567 Å.

Diamond is a wide gap semiconductor with a band-gap of 5.47 eV (226.7 nm). It is known as the hardest material that can be found in nature with Mohs hardness 10. It has along with graphite the highest thermal conductivity (25 W cm^{-1} K^{-1}) and the highest melting point (4500 K). The mass density of both forms of diamond is 3.52 g cm^{-3}.

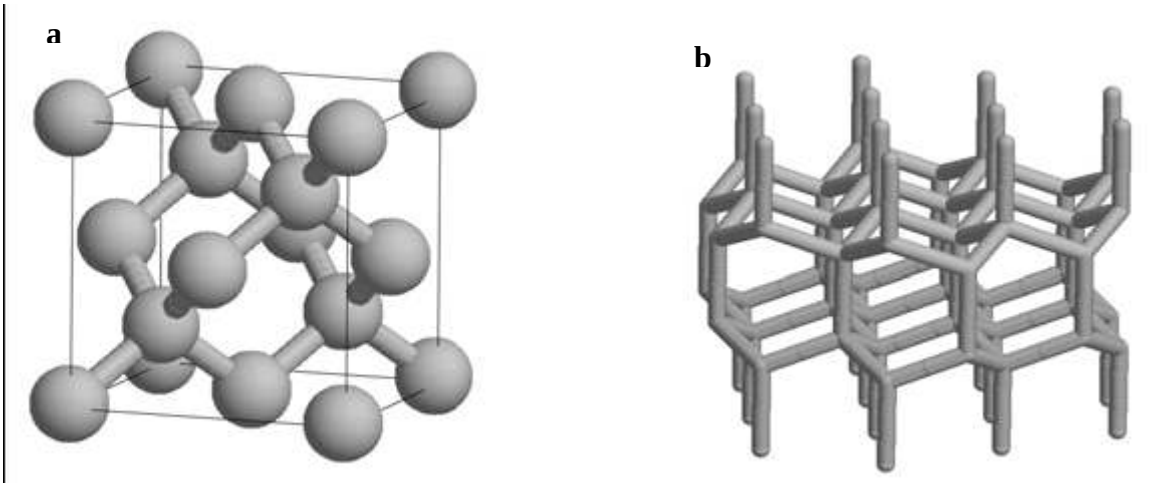

Figure 2-2 Lattice structure of diamond **a**) cubic form, **b**) hexagonal form (Lonsdaleite)

2.3.2 Graphite

Graphite is one of the most common forms of carbon. It consists of layers of hexagonal honeycomb networks (graphene). In graphene each carbon atom is connected with three other carbon atoms via sp^2 σ bonds and a delocalised π bond. The band-gap of graphene as it will be shown below is zero therefore graphite is considered as a zero gap semiconductor or semimetal. The in plane conductivity is very high while the conduction between the graphene planes is difficult.

The graphene sheets are stacked in an ABAB… sequence (Bernal stacking). In Bernal stacking as it can be seen in Figure 2-3 the A and B atoms in consecutive layers

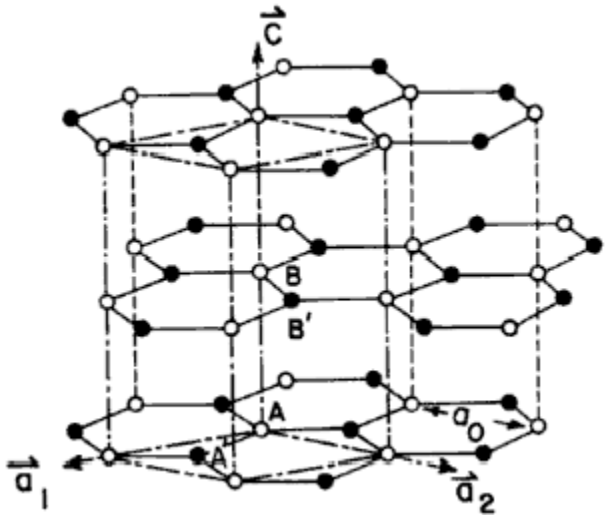

Figure 2-3 Lattice structure of hexagonal single crystal graphite. Open circles denote **A** and **B** carbon sites and black circles denote **A'** and **B'**. a_0 is the in plane lattice constant. The unit cell vectors $\boldsymbol{a_1, a_2, c}$ are also shown. After ref. 2

are on the top of each other while the A' and B' are above the centre of the hexagons of the previous layer. The nearest neighbour distance a_{c-c} is 1.421 Å and the in plane lattice constant a_o 2.456 Å. The c- axis lattice constant c_o is 6.708 Å and the inter-planar distance 3.354 Å.

Another ordered graphite phase is the rhombohedral graphite. It has a_o equal to 2.456 Å, c_o equal to 10.044 Å and inter-plane distance of 3.438 Å. The Bernal stacking

graphite is more stable than the rhombohedral one. Both of them have a density[3] of 2.26 g/cm^3.

2.3.3 Fullerenes

Molecules composed solely of carbon atoms are called carbon clusters. When consisted of up to ten atoms, carbon clusters are mostly stable in the form of linear chains[4]. For numbers of carbon atoms between 10 and 30 the most stable form is the ring[5,6]. However the stability of the formed ring depend upon its size, with certain rings being much more stable (11, 15, 19, 23 carbon atoms) than others. This effect has been explained in terms of the Hückel model[7]. Formation of carbon clusters with number of atoms between 30 and 40 is unlikely[7].

Carbon clusters with more than 40 atoms form cages[7]. From those structures the most stable one is for 60 atoms. C_{60} or fullerene was discovered by Kroto et al. in 1985[8].

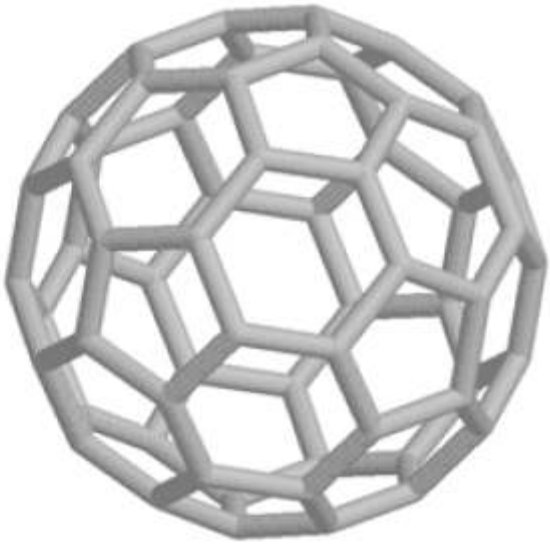

Figure 2-4 C60 Buckminsterfullerene

2.3.4 Carbon Nanotubes

Carbon Nanotubes were discovered by Iijima in 1991[9]. It was very soon realised that they had amazing properties, a fact that ignited a vast scientific research on almost every aspect of their properties and potential applications. Sixteen years later although carbon nanotubes have not managed to become the silicon of the 21st century (at least not yet) they are by far one of the most representative and versatile laboratories of nanoscale physics and their study has produced a huge and valuable amount of knowledge.

2.3.5 Lattice structure of carbon nanotubes

Single Walled Carbon Nanotubes (SWCNT) can be thought as a graphene sheet that has been rolled up to form a seamless cylinder. The cylinders ends are usually closed with half fullerene caps. Two quantities characterise the shape of SWCNTs as well as their physical properties as it will be shown below; their diameter d_t and their chiral angle θ ($0 \le |\theta| \le 30^0$). In Figure 2-5 $\mathbf{C}_h$ is the chiral vector which is defined by two integers (n, m) and the basis vectors $\mathbf{a}_1, \mathbf{a}_2$ of the graphene sheet[10]:

$$\mathbf{C}_h = n\mathbf{a}_1 + m\mathbf{a}_2 \equiv (n, m) \qquad (1)$$

The chiral angle θ is defined as the angle between the chiral vector $\mathbf{C}_h$ and the so-called "zigzag" direction (n, 0). The integers (n, m) determine d_t and θ:

$$d_t = \frac{1}{\pi}\sqrt{n^2 + m^2 + nm}\ \text{a}, \qquad \sin\theta = \frac{\sqrt{3}\,m}{2\sqrt{n^2 + m^2 + nm}} \qquad (2)$$

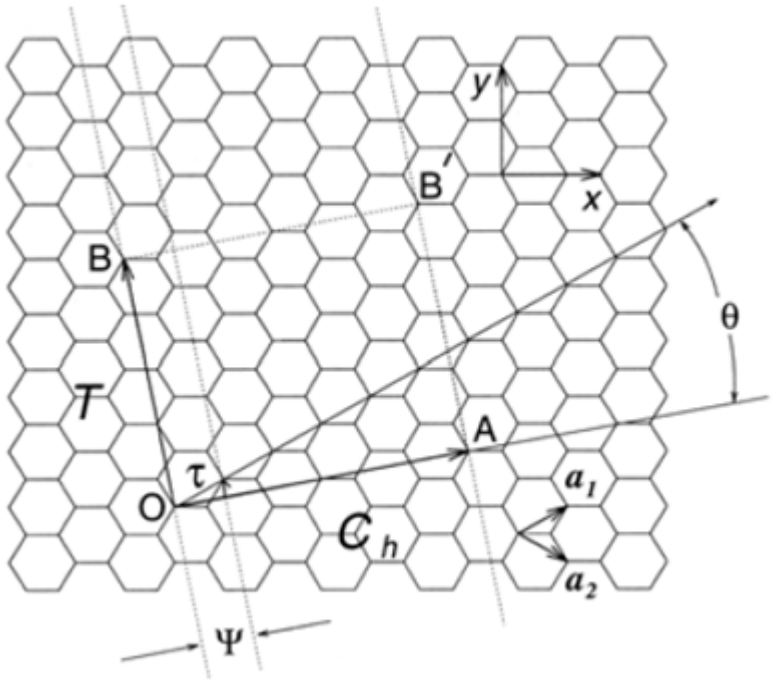

Figure 2-5 Unit cell of a single walled carbon nanotube. (After 7)

A single walled carbon nanotube whose chiral vector has n,m coordinates is consequently called an (n,m) nanotube. According to their n,m numbers nanotubes can be classified as armchair nanotubes when $n=m$, zigzag nanotubes with $(n,0)$ and chiral nanotubes for all the other n,m numbers $(n\neq m, m\neq 0)$. A nanotube of each of the above classes is depicted in Figure 2-6.

Vector $\mathbf{T}$ in Figure 2-5 is called translation vector and is defined as a vector which is perpendicular to the chiral vector, and runs from point $O(0,0)$ to the first to the first equivalent lattice site B. Equivalently $\mathbf{T}$ can be defined by the following equations:

$$\mathbf{T}=t_1\mathbf{a}_1+t_2\mathbf{a}_2,\qquad t_1=\frac{2m+n}{d_R},\qquad t_2=-\frac{2n+m}{d_R} \tag{3}$$

with d_R being the biggest common divider of $(2n+m, 2m+n)$. The rectangle which is defined by vectors $\mathbf{C}_h$ and $\mathbf{T}$ is the unit cell of the a SWCNT. The number N of hexagons in the SWCNT unit cell is given by the relation:

$$N = \frac{\left|\mathbf{C}_h \times \mathbf{T}\right|}{\left|\mathbf{a}_1 \times \mathbf{a}_2\right|} \quad (4)$$

The diameter of the thinnest SWCNT that can be closed with half of a C_{60} was reported to be 6.78 Å. Nanotubes with diameters as small as 4 Å which are encapsulated in a matrix have also been found[11,12,13].

The metallicity of a SWCNT can be determined from its diameter and chirality as it will be shown below. As it can be seen from equations (2) the metallicity of a SWCNT can be equivalently determined by the (n,m) numbers. When ratio $\frac{n-m}{3}$ is an integer then the corresponding nanotube is metallic; otherwise a semiconducting one. A list with some of the geometrical features of SWCNTs and their values is given in Table 2-1.

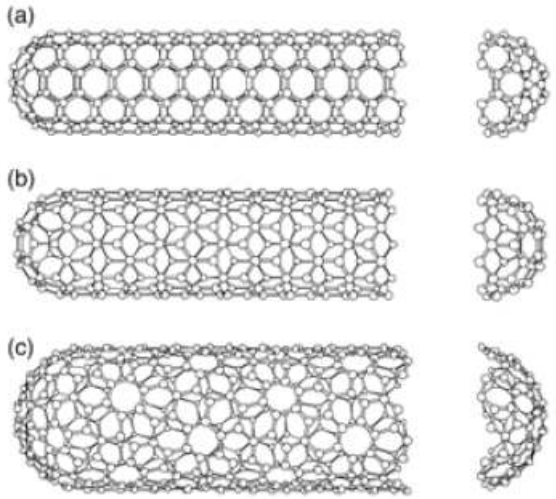

Figure 2-6 a) (5, 5) armchair, b) (9, 0) zig-zag and c) (10, 5) chiral nanotube. After 7.

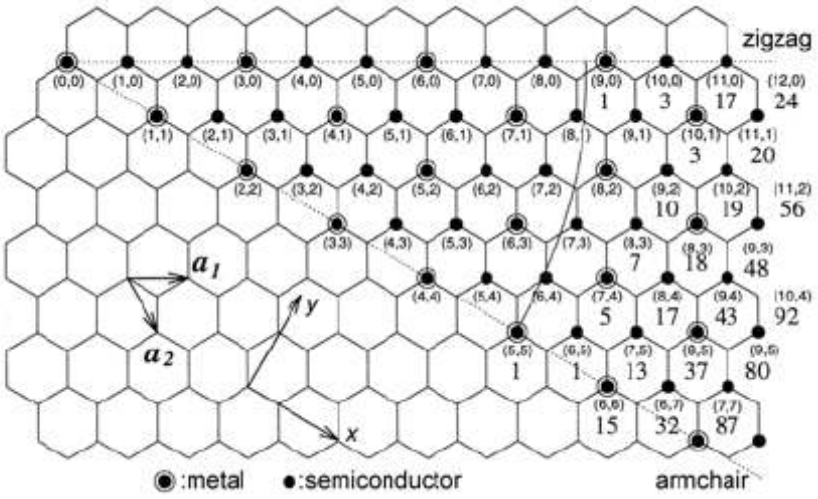

Figure 2-7 The metalicty of SWCNTs for various (n,m) numbers. After 7.

One of the most often forms in which SWCNTs are found is bundles. The nanotubes have triangular arrangement in the bundles and they are hold together by Van der Waals forces. The cohesion of the nanotubes in the bundles is relatively strong and so far relatively complicated and low efficiency methods based on surfactant solutions or

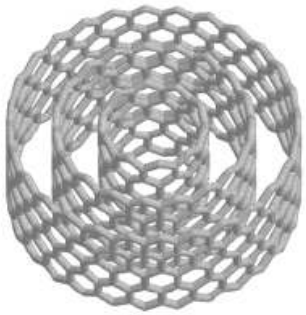

Figure 2-8 A multiwalled carbon nanotube.

DNA solutions need to be applied in order to separate them[14,15].

In the case now of multi walled nanotubes (MWCNT) two or more SWCNTs have been nested the one inside the other (Figure 2-8). In the special case that only two nanotubes have been nested the MWCNT is called Double Walled Carbon Nanotube (DWCNT). The corresponding graphene stacking inside the MWCNTs cannot be AB or ABC due to the radius of curvature and from this point of view MWCNTs can be

considered as turbostratic[iii]. However there is some correlation between the different layers thus MWCNTs cannot be considered completely turbostratic. The distance between the different cells has been calculated to be 3.39 Å and has been measured (through TEM lattice fringes images[16]) as 3.4 Å which is close with the interlayer distance of the turbostratic graphite (3.44 Å).

Table 2-1

Symbol	Name	Formula	Value
$a_{C\text{-}C}$	carbon-carbon distance		1.421 Å (graphite)
a	length of unit vector	$\sqrt{3}\, a_{C\text{-}C}$	2.46 Å
$\boldsymbol{a1}, \boldsymbol{a_2}$	unit vectors	$\left(\frac{\sqrt{3}}{2}, \frac{1}{2}\right)a, \left(\frac{\sqrt{3}}{2}, -\frac{1}{2}\right)a$	in (x,y) coordinates
$\boldsymbol{b1}, \boldsymbol{b_2}$	Reciprocal lattice vectors	$\left(\frac{1}{\sqrt{3}}, 1\right)\frac{2\pi}{a}, \left(\frac{1}{\sqrt{3}}, -1\right)\frac{2\pi}{a}$	in (x,y) coordinates
$\mathbf{C}_h$	Chiral vector	$\mathbf{C}_h = n\mathbf{a}_1 + m\mathbf{a}_2 \equiv (n, m)$	n, m integers
L	Circumference of nanotube	$L = \lvert\mathbf{C}_h\rvert = a\sqrt{n^2 + m^2 + nm}$	$0 \le \lvert m\rvert \le n$
d_t	Diameter of nanotube	$d_t = \frac{L}{\pi} = \frac{1}{\pi}\sqrt{n^2 + m^2 + nm}$ $\boldsymbol{a}$	
θ	Chiral angle	$\sin\theta = \frac{\sqrt{3}\, m}{2\sqrt{n^2 + m^2 + nm}}, \cos\theta = \frac{2n + m}{2\sqrt{n^2 + m^2 + nm}}$ $\tan\theta = \frac{\sqrt{3}m}{2n + m}$	$0 \le \theta \le 30^o$

[iii] This term comes from the field of carbon fibres. In turbostratic carbon fiber, the sheets of carbon atoms are haphazardly folded, or crumpled, together.

2.4 Band structure of SWCNTs

The band structure of SWCNTs can be derived from the one of graphene by imposing the appropriate boundary conditions, which are the result of the sheet folding. The basis of

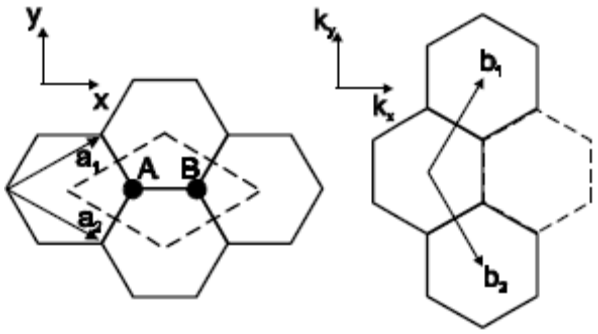

Figure 2-9 A piece of the graphene sheet in real space (left) and the corresponding piece of the reciprocal lattice (right). **A** and **B** consist the basis of the lattice and the dashed lines (on the left) depict the primitive cell (Wigner – Seitz cell) for the graphene sheet. After [17]

the graphene sheet consists of two atoms as it can been seen in Figure 2-9. The band structure of the graphene sheet can be derived from the energy dispersion of the π electrons of the primitive cell. This energy dispersion in a tight binding approximation (for the formed bonding $(-)$ and antibonding $(+)$ π - orbitals) is given by the following equation[18]:

$$E(k_x, k_y) = \pm\gamma_0 \left[1 + 4\cos\left(\frac{\sqrt{3}k_x a}{2}\right)\cos\left(\frac{k_y a}{2}\right) + 4\cos^2\left(\frac{k_y a}{2}\right) \right]^{\frac{1}{2}} \quad (5)$$

where γ_0 is the energy overlap integral between the nearest neighbours. A representation in three dimensions of the above equation is given in Figure 2-10. It can be seen that the conduction and the valence bands have six contact points at the Fermi level. At these points the energy gap between them becomes zero and for this reason graphene (and consequently graphite) is considered as a semi-metal or zero - gap semiconductor. These points are also depicted by black dots in the energy contour plot of the bonding (valence) band in Figure 2-10 b). Two of those points $(\mathrm{K}, \mathrm{K}')$ form the basis of the reciprocal lattice of graphene.

In the vicinity of the K points the energy dispersion has approximately radial symmetry in the (k_x, k_y) plane. Therefore in those regions equation (4) can be simplified as[19,20]:

$$E - E_F = \frac{\sqrt{3}a}{2}\gamma_0 |\mathbf{k} - \mathbf{k_F}| \quad (6)$$

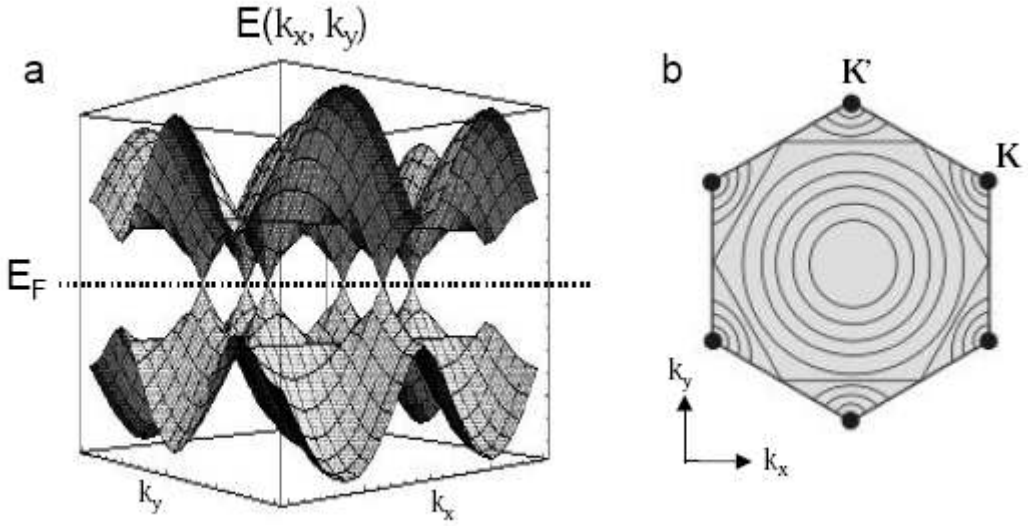

Figure 2-10 a) Representation of the energy dispersion of the π - electrons in the first Brillouin zone of grapphene. **b)** Contour plot of energy in the first Brillouin zone for the boning band.

In order to form carbon nanotubes the graphene sheet must be fold as seamless cylinder. This imposes circular boundary conditions in the circumferential direction. The latter is due to the fact that any wave function of an electron or a phonon must have a phase shift of an integer multiple of 2π around the circumference. Therefore the component of the $\mathbf{k}$ vector around the circumference $(\mathbf{k_c})$ is now quantized according to the condition:

$$\mathbf{k_c} \cdot C_h = 2\pi q \quad (q = 0,1,2,...n) \quad (7)$$

Now there are only discrete modes that the $\mathbf{k}$ vector can be and they are represented as a set of discrete parallel lines in the first Brilluine zone of graphene (Figure 2-11). These lines run parallel to the nanotube's axis and there are N of them

(equal to the number of hexagons in the nanotube unit cell) (Figure 2-12). Lines whose number differ by N are equivalent (or identical). The segment of those lines between $-\frac{\pi}{|\mathbf{T}|}$ to $\frac{\pi}{|\mathbf{T}|}$ consists the one dimensional first Brillouin zone of the nanotube. The spacing Δk between the discrete lines depends only upon the diameter of the SWCNT :

$$\Delta k = \frac{2\pi}{|\mathbf{C_h}|} = \frac{2}{d} \qquad (8)$$

According now to the zone folding or confinement approximation[1,7,21] the electronic band structure of SWCNTs is given by the electronic energies of graphene along the allowed modes of the $\mathbf{k}$ vector. These modes can be thought as one dimensional conduction channels. More specifically in Figure 2-12 the $\frac{\pi}{|\mathbf{T}|}, -\frac{\pi}{|\mathbf{T}|}$ segments of the k -lines have been drawn on the graphene reciprocal lattice from the first segment that is a centred on a Γ point up to the next segment that is a centred on a Γ point. Each of these segments cut a different part of the graphene brillouin zone. When all of those segments get folded on to one (the first one) they will form the nanotube band-structure in the one dimensional first Brillouin zone.

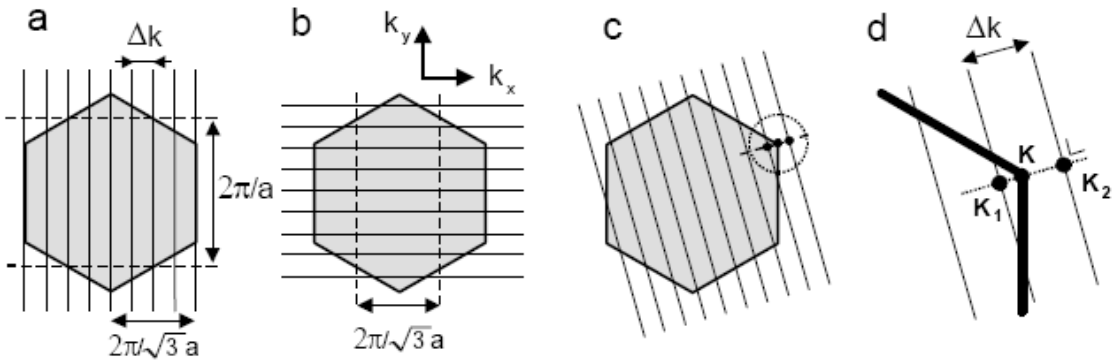

Figure 2-11 Discrete modes of the $\mathbf{k}$ vector of SWCNTs superimposed on the first Brilluin zone of graphene.

In Figure 2-11 the one dimensional conduction channels(k - lines) are shown for an armchair, a zigzag and a chiral SWCNT. For the armchair SWNT the imposed

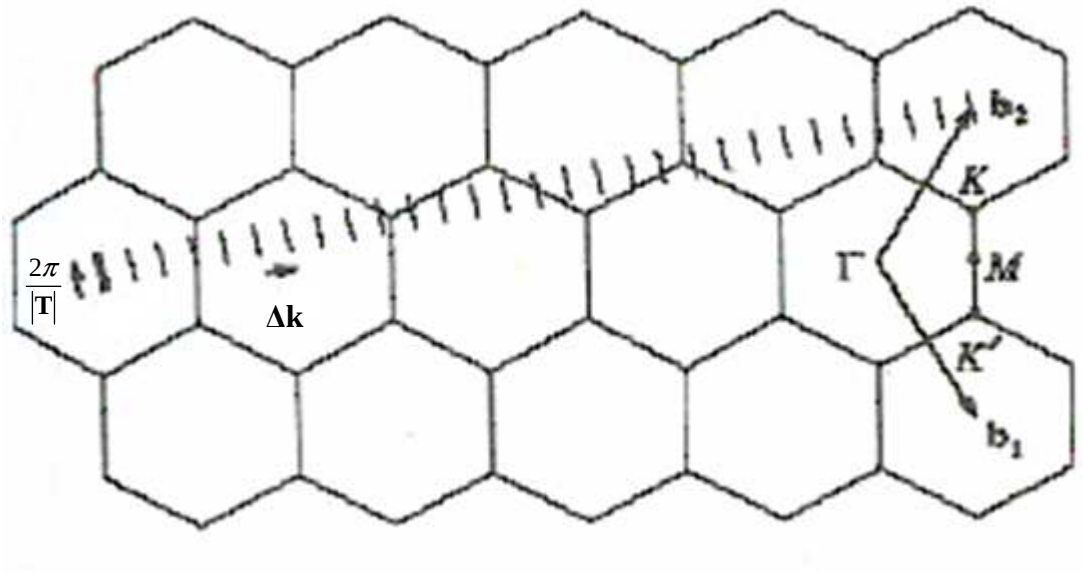

Figure 2-12 Extended zone scheme of a (4,2) SWCNT superimposed on the reciprocal lattice of graphene. There are 28 discrete bands which correspond to the 28 hexagons of the (4,2) nanotube unit cell. The length of each band is $\frac{2\pi}{|\mathbf{T}|}$ and the spacing between them is $\frac{2\pi}{|\mathbf{C_h}|}$. The 1st and the 29th bands are identical. After 1.

quantization condition is $n\sqrt{3}k_x a = 2\pi q \ (q = 0,1,2,3,...,n)$ and the channels that are allowed are parallel to the k_y direction. In the case of the zizag SWCNT the quantization condition is $nk_y a = 2\pi q \ (q = 0,1,2,3,...,n)$ and the lines are parallel to the k_x direction. By substituting the above quantization conditions in equation (5) the dispersion relations for the armchair and the zizag SWCNTs can be obtained:

$$E_{armchair}(k_y) = \pm\gamma_0\left[1 + 4\cos\left(\frac{\pi q}{n}\right)\cos\left(\frac{k_y a}{2}\right) + 4\cos^2\left(\frac{k_y a}{2}\right)\right]^{\frac{1}{2}} \quad (9)$$

$$E_{zigzag}(k_x) = \pm\gamma_0 \left[1 + 4\cos\left(\frac{\sqrt{3}k_x a}{2} \right) \cos\left(\frac{\pi q}{n} \right) + 4\cos^2\left(\frac{\pi q}{n} \right) \right]^{\frac{1}{2}} \quad (10)$$

The above dispersion relations have been plotted for an armchair $(5,5)$ (upper left) and a zigzag $(10,0)$ (lower left) nanotubes in Figure 2-13 for the positive part of the 1st Brillouin zone in each case.

2.5 Electronic Density of States

The density of states (DOS) of a solid depends upon the inverse gradient of the dispersion of the energy[22]. In the case of SWCNTs the dependence is upon the inverse slop of the one dimensional dispersion curves[21] as it can be seen from the following equation[23]:

$$D(E) = \frac{|\mathbf{T}|}{2\pi N} \sum_{\pm} \sum_{\mu=1}^{N} \int \frac{1}{\frac{dE_\mu^{\pm}(k)}{dk}} \delta\left(E_\mu^{\pm}(k) - E\right) dE \qquad (11)$$

where $D(E)$ is the DOS in units of states / C – atom /eV, and the summation is taken for the N conduction $(+)$ and valence $(-)$1- dimensional sub- bands. From Figure 2-13 (left) it can be seen that the slope of the dispersion curves at some points vanishes which has as a consequence the appearance of singularities (Van Hove singularities). Those singularities appear as horizontal spikes in the right hand side of Figure 2-13 where the corresponding density of states has been plotted.

More specifically for the armchair nanotube (Figure 2-13, upper plots) there is a clear crossing of sub-bands at the Fermi level. This yield a finite DOS at the Fermi level and therefore this nanotube is considered as metallic. On the contrary there is no crossing of sub-bands at the Fermi level for the zigzag nanotube (Figure 2-13, lower plots). This leads to a zero DOS around the Fermi and consequently to a formation of an energy band gap. Therefore this nanotube is considered as semiconducting.

Going further from the Fermi energy to the next two sub-bands, in the case of the armchair nanotube, the vanishing slop of those curves can be observed. This results to a pair of Van Hove singularities around the Fermi level. The energy difference between them is denoted as ΔE_{sub} (Figure 2-13). Similarly for the zigzag nanotube a pair of Van

Hove singularities has been formed around the Fermi level and their energy difference is denoted as ΔE_{gap} (Figure 2-13) and corresponds to the energy band-gap.

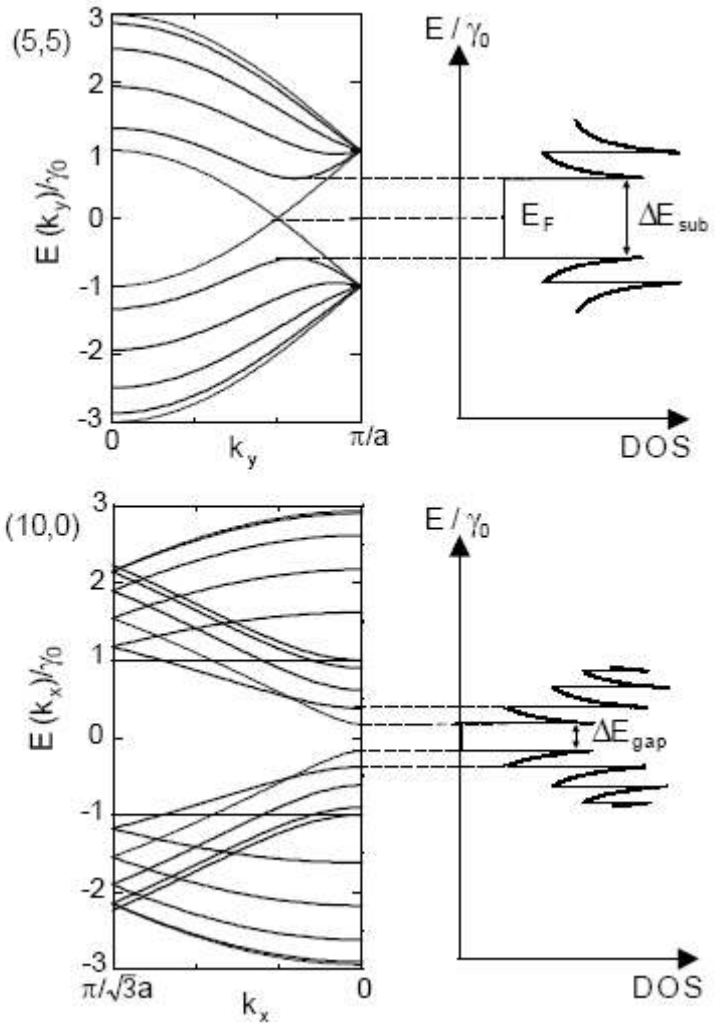

Figure 2-13 Dispersion and Dos for an armcahair $(5,5)$ and a zigzag $(10,0)$ nanotubes.

In the case of chiral nanotubes it was initial expected that the number of Van Hove singularities would be much higher than the one of armchair or zigzag nanotubes due to the fact that their unit cell is often about one order of magnitude bigger[24] (Figure 2-14). It was found though that near the Fermi level there is a universal DOS which depends only upon the diameter and the metallicity of the nanotube[20,25,26,27].

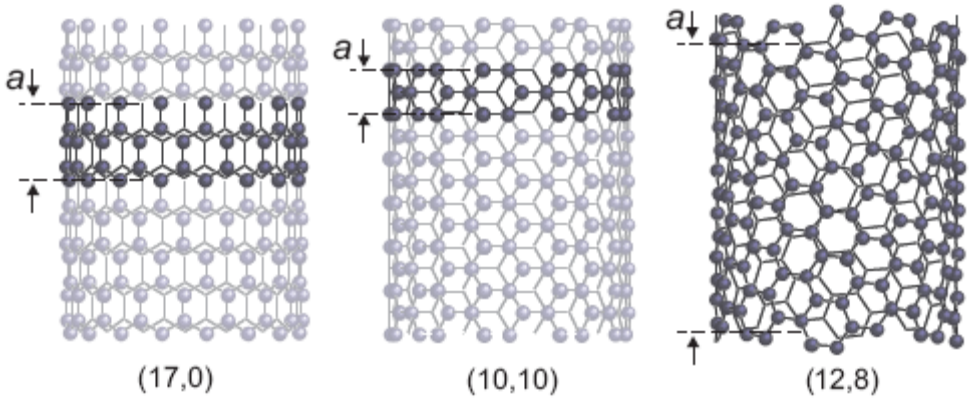

Figure 2-14 Unit cells of a zigzag, armchair and chiral nantoubes. After Maultzsch.

Near the **K** point of the first Brillouin zone of graphene, the energy dispersion has approximately a radial behaviour in the k_x, k_y plane (equation (6), Figure 2-10b). In the case of semiconducting nanotubes the projection of the **K** point on the closest permitted k - line corresponds to the first Van-Hove singularity (point $\mathbf{K}_1$ in Figure 2-11d). Similarly the projection of the **K** point on the second closest permitted k - line corresponds to the second Van-Hove singularity (point $\mathbf{K}_2$ in Figure 2-11d). In the same manner the third and the fourth Van-Hove singularities correspond to the projections of the **K** point on the third and the fourth closest k - lines respectively. Semiconducting nanotubes with different chirality will only have their k - lines differently oriented around the **K** point. The distances between the **K** point and its nearest projections will always be $\frac{1}{3}\Delta k$, $\frac{2}{3}\Delta k$, $\frac{4}{3}\Delta k$, and $\frac{5}{3}\Delta k$ for the first, second, third and fourth nearest k - lines respectively independently of chirality and diameter[20,25,26]. The corresponding energies can be calculated from equation (6) and in the case of the first Van-Hove singularity is $E_1 = \pm\frac{\alpha\gamma_0}{\sqrt{3}d}$ (with (+) and (-) for the conduction and the valence band respectively). This is a very important results as it predicts that the energy band-gap of a semiconducting nanotube is:

$$\Delta E_{gap} = \frac{2\alpha\gamma_0}{\sqrt{3}d} \qquad (12)$$

Equation (12) and depends only upon its diameter. This result has been confirmed experimentally by scanning tunnelling microscopy (STM) measurements[27,28]. In a similar fashion on can calculate the energies for the second, third and so on Van – Hove singularities. All of them are independent of chirality depend only upon the diameter of the nanotube. However this rule applies only for energies in the vicinity of the Fermi energy where the energy can be well approximated by a radial function around the **K** point.

For metallic nanotubes now there is always a k - line going through the **K** point. Therefore the first two neighbouring k - lines around the **K** point are at distance of Δk at either side of it. Similarly the two second closest k - lines are at distance $2\Delta k$ and so on. It is obvious that the singularities for each pair of k - lines overlap with each other as they appear at the same energy. The first, second and third Van-Hove singularities appear at $E_1 = \pm\frac{3\alpha\gamma_0}{\sqrt{3}d}$, $E_2 = \pm\frac{6\alpha\gamma_0}{\sqrt{3}d}$, and $E_3 = \pm\frac{9\alpha\gamma_0}{\sqrt{3}d}$ respectively calculated using equation (6). In the same fashion the energies fourth and so on Van-hove singularities can be calculated again though for the range of energy that equation (6) is valid. For this range of energies as for the semiconducting nanotubes the DOS depends only upon the diameter and not on the chirality.

Finally although they are not going to be analysed the limitations of the zone folding approximation have to be noted. In this approximation as it was described above the curvature of the nanotube and its effect on the relative positions of the carbon atoms was not taken into account in the derivation of the nanotube band-structure and density of states. However due to the curvature of the nanotube the π lobes make an angle with each other and they are not parallel as in graphene. As a consequence the Fermi points do not coincide exactly with the **K** points in the reciprocal lattice. This induces a small energy band-gap (in the order of 10 meV) in chiral metallic nanotubes[29,30,31].

2.6 Raman Spectroscopy

Raman spectroscopy is a powerful tool for nanotube characterisation (ref Jorio new journal). Here it will be given a brief description of the Raman effect and both its classical and semi-classical interpretations (the latter is often called as (quantum mechanical interpretation" in the related literature although in the light – matter interaction that take place during this effect only the ewlectronic excitations are quantized). The text that follows is a small summary of much more extensive and comprehensive treatments that can be found in text books such as references [32], [33], [34], [35].

2.6.1 The Raman effect

When monochromatic radiation of frequency ω_1 is incident on a material system some of it will be scattered. Most of the scattered light will have the same frequency as the incident light (Rayleigh scattering) but there will be some that its frequency is shifted (Raman scattering). When the shift is negative it is called a Stokes shift and when it is positive it is called an anti-Stokes shift. Because there is a change in the frequency and therefore energy of the scattered light Raman scattering is an inelastic scattering process.

The difference in energy is due to exchange of energy with relatively low energy excitations. This is why raman is powerful because it tells us about the excitations of the system.

Finally the intensities of the scattered light in both Raman and Rayleigh scattering have linear dependence upon the irradiance of the incident light and therefore are considered as linear processes.

2.6.2 Classical theory of Raman scattering.

In the classical theory of the Raman effect monochromatic light of angular frequency ω_1 impinges on molecule. The time dependent electric field $\mathbf{E}$ of the radiation induces a time dependent electric dipole moment which can be written as a sum of time dependent induced electric dipole moments:

$$\mathbf{p} = \mathbf{p}^{(1)} + \mathbf{p}^{(2)} + \mathbf{p}^{(3)} + \ldots \qquad (13)$$

Because $\mathbf{p}^{(1)} >> \mathbf{p}^{(2)} >> \mathbf{p}^{(3)}$ (13) is a rapidly converging series. The relationship between $\mathbf{p}^{(1)}$, $\mathbf{p}^{(2)}$, $\mathbf{p}^{(3)}$, and $\mathbf{E}$ are given by the following equations:

$$\mathbf{p}^{(1)} = \boldsymbol{\alpha} \cdot \mathbf{E} \qquad (14)$$

$$\mathbf{p}^{(2)} = \frac{1}{2}\boldsymbol{\beta} : \mathbf{EE} \qquad (15)$$

$$\mathbf{p}^{(3)} = \frac{1}{6}\boldsymbol{\gamma} \vdots \mathbf{EEE} \qquad (16)$$

In equation (14) $\boldsymbol{\alpha}$ is the polarizability which is a second rank tensor. In equation (15) $\boldsymbol{\beta}$ is the hyperpolarizability which is a third rank tensor and $\mathbf{EE}$ is a vector dyad or the direct product of vector $\mathbf{E}$ with itself. In equation (16) $\boldsymbol{\gamma}$ is the second hyperpolarizability and it is a third rank tensor while $\mathbf{EEE}$ is a direct product of three vectors. Equations (15) and (16) are associated with nonlinear scattering processes such as hyper and second hyper Raman scattering. Equation (14) is associated with Raman scattering as it will be analysed below.

Equation (14) can be written in component form as follows:

$$p_\rho = \alpha_{\rho\sigma} E_\sigma \qquad (17)$$

where ρ, σ can be x, y, z and summation is implied over repeated subscripts (p_ρ and E_σ are the components of electric dipole moment and the electric field respectively). The variation of polarizability due to molecular vibrations can be approximated by a Taylor expansion over the normal coordinates of the vibration:

$$\alpha_{\rho\sigma} = \left(\alpha_{\rho\sigma}\right)_0 + \sum_k \left(\frac{\partial \alpha_{\rho\sigma}}{\partial Q_k}\right)_0 Q_k + \frac{1}{2}\sum_{k,l}\left(\frac{\partial^2 \alpha_{\rho\sigma}}{\partial Q_k \partial Q_l}\right)_0 Q_k Q_l \ldots \qquad (18)$$

where $\left(\alpha_{\rho\sigma}\right)_0$ is the value of $\alpha_{\rho\sigma}$ at the equilibrium configuration and Q_k, $Q_l \ldots$ are the normal coordinates of vibration associated with vibrational frequencies $\omega_k, \omega_l \ldots$ and the summations are over all normal coordinates. All derivatives are taken at the equilibrium position (this is what the subscript 0 stands for). For relatively small vibrations and therefore small values of Q_k, $Q_l \ldots$ one can keep only the first order terms. Focusing now on only one normal mode of the vibration equation (18) and neglecting higher order

terms (responsible for two and three..phonon effects) in the modes expansion can be written as:

$$(\alpha_{\rho\sigma})_k = (\alpha_{\rho\sigma})_0 + (\alpha'_{\rho\sigma})_k Q_k \qquad (19)$$

where

$$(\alpha'_{\rho\sigma})_k = \left(\frac{\partial \alpha_{\rho\sigma}}{\partial Q_k}\right)_0 \qquad (20)$$

Equation (20) gives the components of a new tensor $\boldsymbol{\alpha}'_k$ which is called the derived polarizability tensor. All of the components of this tensor are derivatives of polarizability over the normal coordinate Q_k. Equation (19) is valid for all tensor components therefore it can be rewritten in a tensor form as:

$$\boldsymbol{\alpha}_k = \boldsymbol{\alpha}_0 + \boldsymbol{\alpha}'_k Q_k \qquad (21)$$

where $\boldsymbol{\alpha}_k$ is a tensor whose components $(\alpha_{\rho\sigma})_k$ are given from equation (19) and Q_k is a scalar quantity that multiplies all of the components of $\boldsymbol{\alpha}'_k$. For small vibrations around the equilibrium position the motion can be considered as harmonic therefore the dependence of Q_k upon time will be:

$$Q_k = Q_{k_0} \cos(\omega_k t + \delta_k) \qquad (22)$$

where Q_{k_0} is the amplitude of the normal coordinate and δ_k a phase factor.

The electric field as a function of time will be:

$$\mathbf{E} = \mathbf{E}_0 \cos(\omega_1 t) \qquad (23)$$

where $\mathbf{E}_0, \omega_1$ are the amplitude and the frequency of the electric field respectively, of the incident monochromatic radiation. Combining equations (14), (21), (22), (23) an expression for electric dipole moment (with respect to the k normal mode) as a function of time can be written:

$$\mathbf{p}^{(1)} = \boldsymbol{\alpha}_0 \mathbf{E}_0 \cos(\omega_1 t) + \boldsymbol{\alpha}'_k \mathbf{E}_0 Q_{k_0} \cos(\omega_k t + \delta_k)\cos(\omega_1 t) \qquad (24)$$

By using the identity:

$$\cos \mathrm{A} \cos \mathrm{B} = \frac{1}{2}[\cos(\mathrm{A}+\mathrm{B}) + \cos(\mathrm{A}-\mathrm{B})] \qquad (25)$$

equation (24) can be written as:

$$\mathbf{p}^{(1)} = \boldsymbol{\alpha}_0 \mathbf{E}_0 \cos(\omega_1 t) + \frac{1}{2}\boldsymbol{\alpha}'_k \mathbf{E}_0 Q_{k_0} \cos[(\omega_1 - \omega_k)t + \delta_k] + \frac{1}{2}\boldsymbol{\alpha}'_k \mathbf{E}_0 Q_{k_0} \cos[(\omega_1 + \omega_k)t + \delta_k] \qquad (26)$$

Equation (26) consists of three harmonic terms and describes the oscillation of the induced electric dipole as a function of time. According to the theory of the Hertzian dipole, an oscillating electric dipole emits electromagnetic radiation with frequency equal to the frequency of the oscillation. Therefore according to equation (26) the induced electric dipole will emit at three distinct frequencies: ω_1 which corresponds to Rayleigh scattering, $\omega_1 - \omega_k$ which corresponds to the Stokes line – Raman scattering, $\omega_1 + \omega_k$ which corresponds to the anti-Stokes line – Raman scattering. Figure 2-15 gives a schematic representation of the classical theory of the Raman effect.

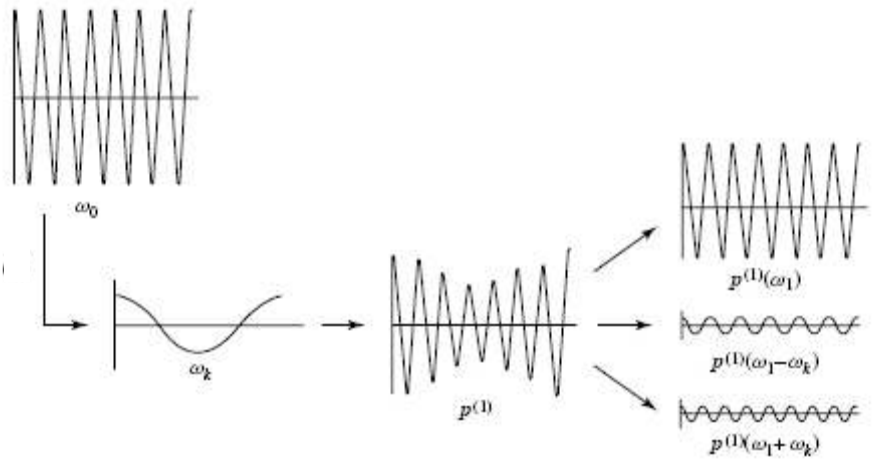

Figure 2-15 Schematic representation of the classical theory of the Raman effect. Incident radiation $\omega_0 = \omega_1$ is modulated by the oscillating electric dipole which was vibrating with frequency ω_k. The modulated radiation now contains three frequencies $\omega_1, \omega_1 - \omega_k, \omega_1 + \omega_k$, which correspond to Rayleigh scattering, Raman scattering – Stokes line and Raman scattering – anti-Stokes line respectively. After 32.

2.6.3 Evaluation of the classical theory of Raman scattering.

The classical theory of Raman scattering predicts correctly the frequency of the Stokes and anti-Stokes lines. The classical theory turns out to be quiet adequate for qualitative characterisation purposes such as identification of molecular species from their Raman spectra.

However there are some serious limitations of the classical theory of the Raman effect. One that can be easily seen from equation (26) is the prediction that the Stokes and anti-Stokes lines are of the same intensity which contradicts the experimental data in

most of the cases as the anti-Stokes lines are usually one order of magnitude weaker than the Stokes lines. Also it cannot provide any information of how derived polarizability $\boldsymbol{\alpha}'_k$ is related to the properties of the scattering system such as its transition frequencies.

2.6.4 Quantum mechanical theory of Raman scattering.

Below the main points of the quantum mechanical treatment of the Raman effect will be summarised (all presented information here can be found in references 32, 33, 34, 35, 36, 37. The treatment in reality is semi-classical i.e. in the light – mater interaction only the matter is quantised, whereas the light is entered as a classical field.

Raman scattering can be described as a three steps process: 1) The incident light excites a real or a virtual electronic excitation of the system, which in many cases, particularly in semiconductors, is an electron hole pair. 2) A scattering event involving the electronic excitation takes place with the consequent emission (Stokes) or absorption (anti – Stokes) of a low excitation of the system e.g. a phonon, and resulting in a change of the state of the electronic excitation. 3) The electronic excitation de-excites emitting light.

The scattering rate Γ of the above process for c. w. excitation can be calculated from the light – semiconductor dipole Hamiltonian for the incoming and scattered light $\hat{\mathbf{H}}_{dipole}^{in,scat}$ and the carrier – phonon Hamiltonian $\hat{\mathbf{H}}_{phonon}$ as follows:

$$\Gamma \propto |M|^2 \begin{cases} \delta(\omega_{scat} - \omega_{in} + \omega_{phonon})(N_{phonon} + 1) - Stokes \\ \delta(\omega_{scat} - \omega_{in} - \omega_{phonon})(N_{phonon}) - Anti - Stokes \end{cases} \qquad (27)$$

where $\omega_{scat}, \omega_{in}$ are the frequencies of the scattered and incoming light respectively, ω_{phonon} is the frequency of the emitted or absorbed phonon. N_{phonon} is the phonon occupancy which is given from the Bose – Einstein distribution function:

$$N_{phonon}(\hbar\omega_{phonon}) = \frac{1}{e^{\frac{\hbar\omega_{phonon}}{k_B T}} - 1} \qquad (28)$$

In relation (27) $|M|^2$ is given by:

$$|M|^2 = \sum_{k,l} \left| \frac{\langle 0|\hat{\mathbf{H}}_{dipole}^{scat}|k\rangle\langle k|\hat{\mathbf{H}}_{phonon}|l\rangle\langle l|\hat{\mathbf{H}}_{dipole}^{in}|0\rangle}{(E_k + i\Gamma_k - \hbar\omega_{scat})(E_l + i\Gamma_l - \hbar\omega_{in})} \right|^2 \qquad (29)$$

where $|0\rangle$ is ground state, $|k\rangle, |l\rangle$ are intermediate states of the electronic excitation, of energies E_k, E_l respectively, Γ_k, Γ_l are damping constants associated with the finite lifetime of each state in the form $\Gamma = \frac{\hbar}{\tau}$. The delta functions in relation (27) indicate energy conservation. In the case of phonons with finite lifetime these delta functions should be replaced by Lorentzians (it must be noted that equation (29) is an approximation, as the accurate expression for $|M|^2$ must include all terms that can be derived from the six Feynman diagrams that contribute to the one phonon Raman scattering process[37,38]).

Equation (29) can be further simplified to give two very important approximations, which are valid in different limits of the light frequency. The first approximation can be derived when the energies of the incoming ($\hbar\omega_{in}$) and scattered ($\hbar\omega_{scat}$) light are far from resonance with any of the intermediate states $|k\rangle, |l\rangle$. In this case the weights of all of the terms of the sum in equation (29) can be considered as similar and thus $|M|^2$ can be approximated as:

$$|M|^2 \propto \left|\langle 0|\hat{\mathbf{H}}^{scat}_{dipole}\hat{\mathbf{H}}_{phonon}\hat{\mathbf{H}}^{\text{int}}_{dipole}|0\rangle\right|^2 \qquad (30)$$

The second approximation is the in the case that either the energy of the incoming or of the scattered light is in resonance with one of the intermediate states. Under this condition the term of the sum in equation (29) to whom the resonant state corresponds will have significantly bigger contribution than the other terms and therefore $|M|^2$ can be approximated as[37]:

$$|M|^2 \propto \left|\frac{\langle 0|\hat{\mathbf{H}}^{scat}_{dipole}|k\rangle\langle k|\hat{\mathbf{H}}_{phonon}|k\rangle\langle k|\hat{\mathbf{H}}^{in}_{dipole}|0\rangle}{(E_k + i\Gamma_k - \hbar\omega_{scat})(E_k + i\Gamma_k - \hbar\omega_{in})}\right|^2 \qquad (31)$$

where $|k\rangle$ is the resonant state. Clearly in the continuum of states more than one state can be near resonance and all these states have to be taken into account in the matrix element. However it will still be the case that the nature of the resonance state or states will affect the Raman spectra more than any other states. Therefore the selection rules standardly obtained within the non resonant approximation may not apply.

2.7 Raman Spectroscopy of Carbon Nanotubes

In the following section the main features of the SWCNT Raman spectra will be discussed. As in this thesis Raman spectroscopy of carbon nanotubes is a characterisation tool this section is not going to be a deep analysis of Raman scattering on carbon nanotubes. Instead the focus will be on the aspects of Raman spectroscopy of carbon nanotubes that were used for characterisation purposes. Further information can be found in references 1, 7, 21, 39, 46 and references therein.

Raman spectroscopy is a very powerful tool for characterising carbon nanotubes. From the raman signals of carbon nanotubes information such as diameter, metalicity, defects can be deduced. There is a vast number of phonon modes associated with carbon nanotubes but only a few of them are Raman active. The main features that can be observed in a nanotube raman spectrum (Figure 2-17) are the radial breathing modes (RBM), the D band, the G band, and the G' band.

The fact that raman signals can be relatively easy observed on a single carbon nanotube is quite surprising. The relatively high strength of the Raman signal in carbon nanotubes is however connected with their electronic structure. The fact that the density of states of SWCNT contain large van Hove singularities (Figure 2-13), allows the performance of resonance Raman spectroscopy even on a single SWCNT. Selection rules allow only optical transitions between mirrored singularities across the Fermi level. Therefore when the energy of the incoming or scattered light equals the energy E_{ii} of an optical transition (i.e. the energy between two mirrored singularities) resonance takes place and the intensity of the Raman signal is very high as it can be seen from equation (31). In fact to a reasonable approximation Raman scattering will be obtained for that exhibit resonance for a given excitation wavelength.

Therefore to interpret Raman spectra requires the knowledge of the energies E_{ii} of all (n,m) SWCNT and their corresponding diameters. For this purpose there are maps that relate the E_{ii} energies with the diameter and the type (metallic or semiconducting) of SWCNTs, called Kataura plots. Such a map is presented in Figure 2-16 (after 23) for SWCNT diameters up to 3 nm calculated by using a first neighbour tight binding model.

Deviations from this model are expected for the E_{11}^{s} (E_{11} optical transition for semiconducting nanotubes) and for SWCNTs with diameter smaller than 1 nm. (why). The width[40,41] of the resonances (here is considered as equal with the width of the singularity) is between 40 and 60 meV.

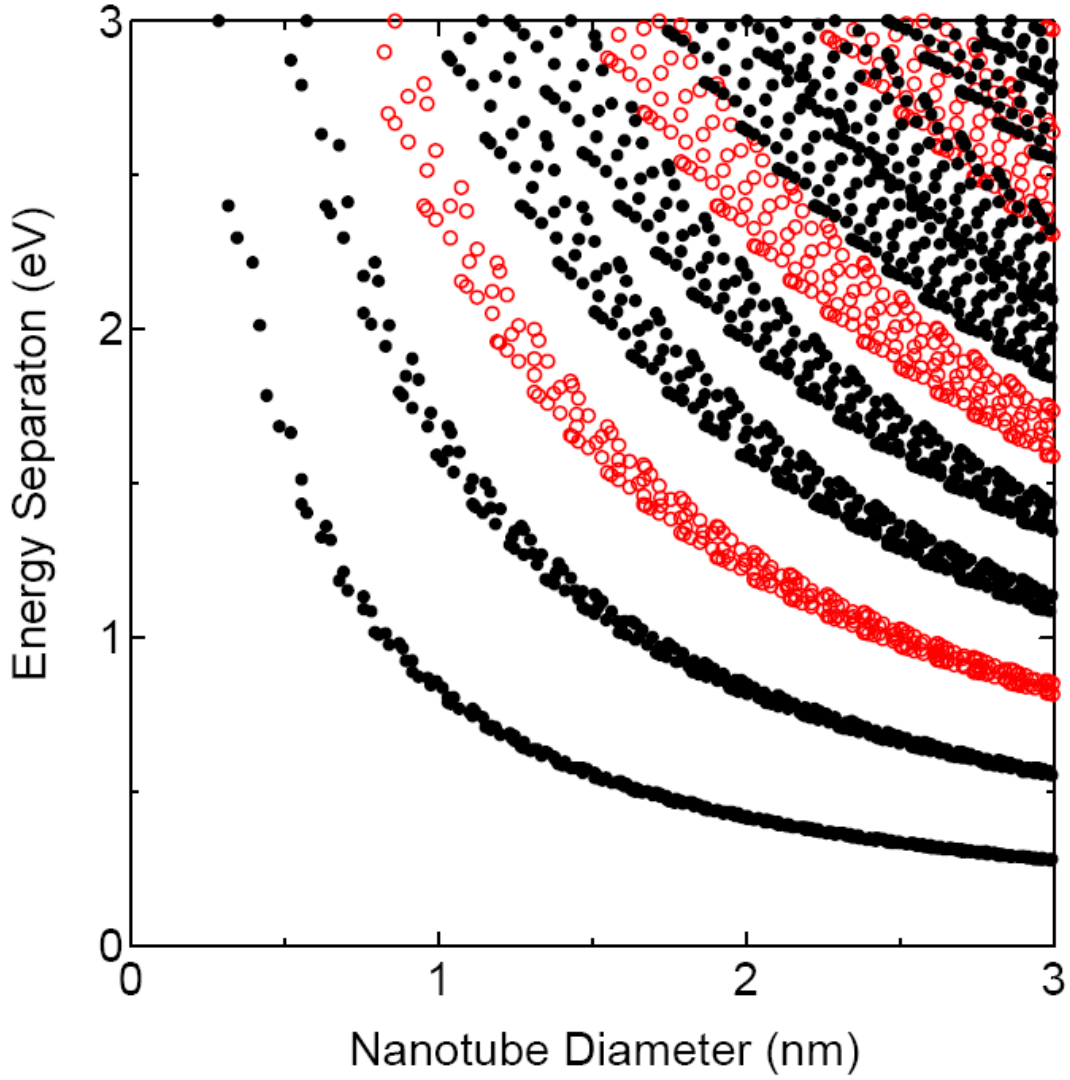

Figure 2-16 Kataura plot. Optical transition energy E_{ii} between van Hove singularities for all the (n,m) plotted against diameter. Red symbols correspond to metallic nanotubes and black to semiconducting ones. After 23.

One of the key features of the Raman spectra of SWCNTs are the radial breathing modes (RBM) which is depicted in Figure 2-17. They appear at the lower frequency (in Raman spectroscopy by convention all wavelength shifts with respect to the laser wavelength are presented in wavenumbers and are called frequencies) side and in the

range between 120 cm^{-1} and 250 cm^{-1}. This shift is due to the vibration of the carbon atoms along the radial direction[42]. From the frequency position of the RBM it is possible to calculate the diameter of the corresponding SWCNT from the following empirical equation:

$$\omega_{RBM} = \frac{A}{d_t} + B \qquad (32)$$

where ω_{RBM} is the frequency of the RBM, d_t the diameter of the nanotube and A, B two parameters which are determined experimentally. For isolated nanotubes on a SiO_2 surface[43] $A = 248\,cm^{-1}$ and $B = 0$. When the nanotubes are in bundles there is an upshift due to tube – tube interaction and is expressed[44] by $B = 10\,cm^{-1}$. In the same case[44] $A = 234\,cm^{-1}$. These two sets of parameters give similar d_t in the range of diameters of 1 nm to 2 nm. For diameters smaller than 1 nm equation (32) is not valid
anymore due to lattice distortion which gives rise to chirality dependence of the RBM shift[39]. For nanotubes of diameters larger than 2 nm the intensity of the RBM peak is very weak and hardly observable[46]. This due to the fact that the intensity of the mode depends on the carrier – phonon matrix element (equation (29)) which increases[45] with the transition energy, E_{ii}. However E_{ii} is reverse proportional with the nanotube diameter as it can be derived from equation (6) (see also the relevant section above).

It is clear from the above that by calculating the nanotube diameter from the RBM frequency and by using the Kataura plot (Figure 2-16) the metalicity of the nanotube can be determined. However Figure 2-16 implies also that in order to characterise a sample consisting of nanotubes of different diameters by means of resonant Raman scattering it is necessary to acquire multiple Raman spectra using several excitation wavelengths. This requirement arises from the fact that nanotubes with different diameters will exhibit resonances at different energies.

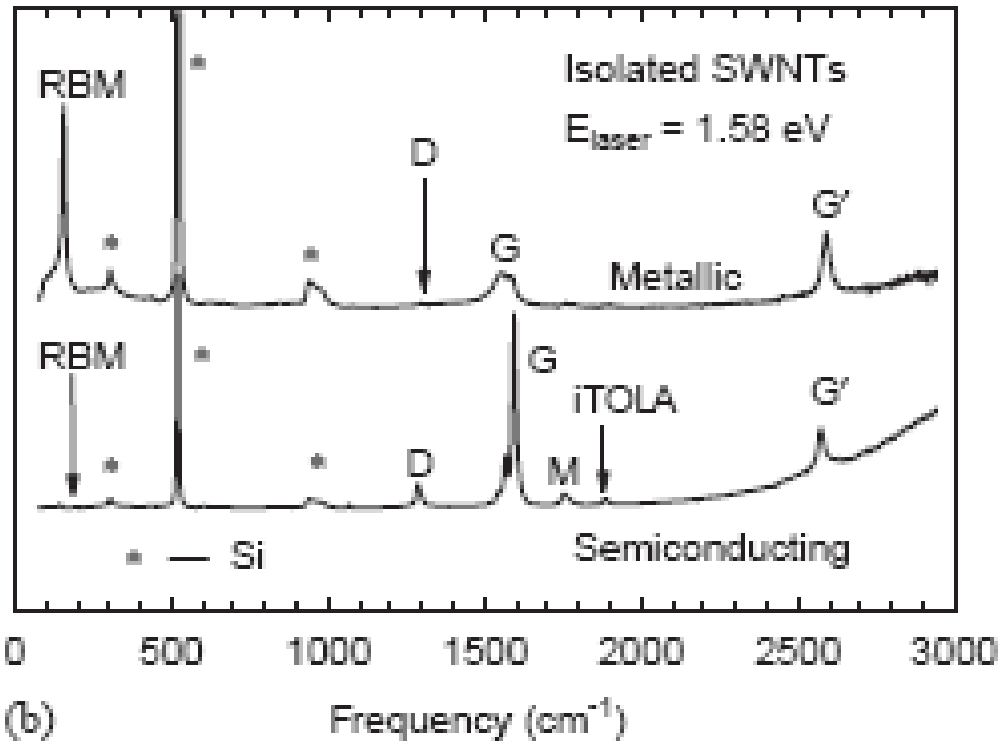

Figure 2-17 Raman spectra of an isolated metallic and an isolated semiconducting single walled carbon nanotubes (top and bottom respectively) on the oxidized surface of Si substrate. The characteristic modes of the SWCNTs are depicted as well as the ones of Si . After [46]

Around $1580\,cm^{-1}$ (Figure 2-17) the G-band can be observed which is related to the tangential modes of the graphene lattice. This mode has been observed as a single peak in graphite (hence the G) and is present also in SWCNTs. However in SWCNTs it gets the form of a multiple peak feature (up to six peaks can be observed). The main two peaks of the G-band (Figure 2-18) are the ones associated with the tangential modes along the nanotube axis (G^+, higher frequency mode) and along the nanotube circumference (G^- lower frequency mode). The G^+ and G^- modes are the most commonly observed peaks of the G-band.

The frequency of the G^- is lower than that of the G^+, due to the nanotube curvature. For this reason the frequency of G^- depends on the nanotube diameter. Therefore the difference $\Delta\omega_G = \omega_{G^+} - \omega_{G^-}$ can be used for diameter characterisation.

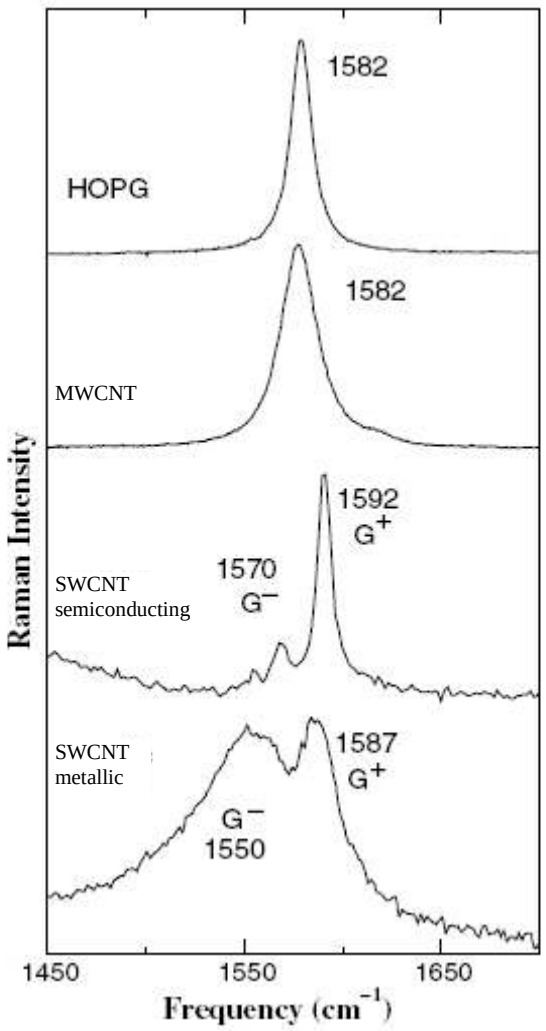

Figure 2-18 The G-band (shift due to tangential mode of lattice vibration) for high order pyrolytic graphite (HOPG), bundles of multi – walled carbon nanotubes MWCNT, an isolated semiconducting single walled carbon nanotube (SWCNT) and an isolated metalic single walled carbon nanotube (SWCNT). Two peaks can be clearly distinguished in the cases of the isolated SWCNT while in the case of the MWCNT the individual peaks are not clear due to the large diameters of the tubes. After 39

However this is valid only in the case of an isolated nanotube while in the case of a bundle it is related with the maximum of the size distribution but using $\Delta\omega_G$ for dermining the diameter of a SWCNT in a bundle is not accurate.

The lineshapes of the G^- mode are different for semiconducting and metallic nanotubes (and therefore they can be used for characterisation of the nanotubes over their metallic character). For semiconducting naotubes the G^- peak can be fitted by a relatively sharp Lorentzian (Figure 2-18) whilst for metalic nanotubes the peak is much broader. The BWF lineshape has been also observed in other graphite-like materials with metallic behaviour (n-doped graphite intercalations, n doped fullerenes). The reason for the broad shape of the G^- peak is a matter of a current debate.

The G^+ peak of an isolated nanotube exhibits a linewidth of $5 - 15 cm^{-1}$. The same linewidths are exhibited from the G^- peaks of isolated semiconducting nanotubes. Bundles of semiconducting nanotubes exhibit inhomogeneous broadening of the G^- peak as this is the one that depends upon the nanotube diameter. Significant broadening of the G^- occurs in metallic nanotubes with strong dependence on diameter while the broadening of G^+ is minor. Linewidths bigger than 70 cm^{-1} of the G^- peak for isolated metallic SWCNTs have been reported[47].

Another feature which often occurs in the Raman spectra at around 1350 cm^{-1} (Figure 2-17), is the disorder induced mode or D – band. It is a double resonance process in which apart from phonon scattering also a scattering on a defect is needed in order to conserve momentum[48]. This feature appear also in graphite and in the case of nanotubes the corresponding shift depends on diameter and chirality since due to the double resonance process there is strong dependence on how the 2-dimensional electronic and phonon structure is folded into a 1-dimensional structure[46].

The D – band due to its association with defects can be used as a first evaluation of the quality of the nanotubes[46]. However it has not yet been understood with which particular defects (e.g. hetero-atoms, vacancies, kinks, e.t.c) the D – band is connected[39].

An overtone of D – band appears at around 2600 cm^{-1} (Figure 2-17) and it is called G' – band. It is a double resonance second order process (two phonon process unlike with the combination of phonon – defect scattering process)[46]. Due to momentum conservation the phonons participating in this process are of opposite wavevector therefore there is no need of defect for the G' – band to occur. For similar reasons as for the D – band the frequency of the G' band depends upon the diameter and the chiral angle of the nanotube[46].

2.8 Growth of Carbon Nanotubes

In the following section the growth of carbon nanotubes will be discussed. Due to its vital importance this subject has been intensively studied and there is extensive literature on it. Here will be presented in brief only the aspects relevant to the studies of this thesis. More extensive information can be found in references [49], [50], [51], [52], [53], [54] which were the main sources for this section.

2.8.1 Methods of Growth

There is a number of methods that can be used for carbon nanotube growth. The growth methods can be distinguished[54] into physical and chemical ones according to the methods used in order to extract carbon atoms from the precursor that contains them. In the physical methods the carbon atoms are released by using a high energy input. The most important physical methods are the arc discharge[9] and the laser vapourization[55]. In the chemical methods the carbon atomization takes place on the surface of transition metals via catalytic decomposition. The most important chemical growth methods are: Chemical Vapour Deposition (CVD), Pyrolysis or Vapour Phase Deposition, CoMoCat Process, High – pressure CO Disproportionation (HiPco). The chemical methods can be divided further into chemical vapour deposition (i.e. CVD can be considered as a whole category of methods[54]) that the precursor decomposition takes place on to the surface of previously prepared catalyst and aerosol or gas phase synthesis where the whole process

takes place in the gas phase as the catalyst particles are formed in-situ during the carbon nanotube synthesis (e.g. Pyrolysis or Vapour Phase Deposition).

The most commonly carbon nanotube growth methods reported in the literature are the Arc discharge, Laser Vapourization, CVD and HiPco. During the experiments for the purposes of this thesis the CVD method (and more specifically thermal CVD) was deployed and thus some more details about this method will be given below.

2.8.2 Chemical Vapour Deposition

There different varieties of the CVD method such as Thermal CVD, Plasma Enhanced CVD (PECVD), Alcohol Catalytic CVD, Aerogel – supported CVD, Laser – assisted CVD. As it was mentioned above in the following discussion the focus will be placed on the Thermal CVD.

2.8.3 Growth Apparatus and Procedure

The general apparatus (Figure 2-19) used for growing nanotubes with the method of Thermal CVD as this is reported in the literature (which is identical with the one used in the experimental part of this thesis) is relatively simple. A quartz tube usually of 2 inches in diameter has been inserted into a tubular furnace. The furnace temperature can be maintained within ±1 ^{o}C over a 25 cm area. It can be considered as a hot wall system that operates at atmospheric pressure and therefore it does not require pumping. Gasses are provided into the quartz tube and their flux is regulated through mass flow controllers. The outlet gases are taken to a cooling bath and then vented in to a fume extract. The length of the tube and the flow rate of the gasses prevent the back flow of oxygen. The substrates (usually smaller than 1x1 in.) coated with catalyst or the catalyst on a support in powder form, are placed inside an open-top ceramic container which is then placed inside the quartz tube.

The growth process consists of three stages; a pre-anneal, nanotube growth, and cool down. In the pre-anneal stage the sample is heated up at the desired temperature while the quartz tube is purged with an inert gas like Ar or a mixture of an inert gas and a reduction agent like H_2 depending on the catalyst type. Then (growth stage), a flow of carbon feedstock is added or the whole flow is switched to the carbon feedstock only. This is the step that the actual growth takes place and it can last from few minutes to

hours depending on catalyst, growth recipe, aimed nanotube quality, density and length. During the growth time the oven temperature remains constant. Finally in the cool down stage the flow is switched to the inert gas only and the sample is let to cool down usually to room temperature. In general the sample must not be exposed to the air while the temperature is above 300 ^{o}C as this will damage the nanotubes and reduce the quality of the sample (defects) due to oxidation.

As it is obvious from the above the catalyst is of major importance for the growth process and as such a brief overview of its properties is given below.

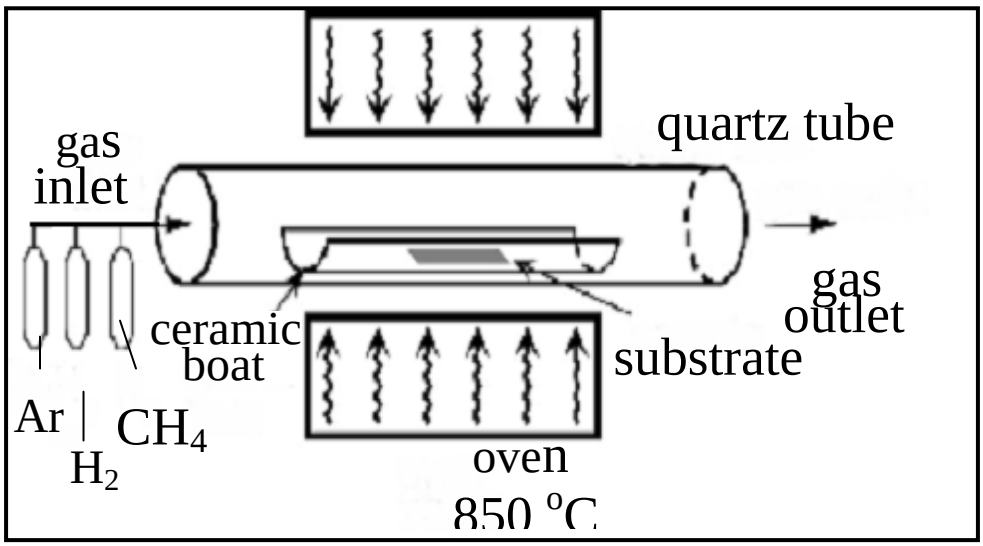

Figure 2-19 The Thermal CVD apparatus.

2.8.4 Catalyst Properties

The catalyst is used in the form of nanoparticles as nanotube growth has not been reported in the case of a catalyst in the form of a continuous film[51]. In all cases of CVD growth apart from the type of CVD growth reported later in this thesis the catalyst consists of nanosized transition metal particles[49-54] in oxide or metallic form and sometimes in a mixture of both. The key property of the transition metals relevant to the growth of carbon nanotubes is that they can decompose catalytically gaseous molecules that contain carbon. Other important properties of the transition metals that are related to the nanotube formation such as melting point, equilibrium vapour pressure, solubility of carbon, carbon diffusion rate in the metal are given in

Table 2-2. These metals exhibit relatively similar properties apart from the high melting point and low equilibrium vapour pressure of molybdenum and the low carbon solubility in copper.

Table 2-2 Physico-chemical properties of selected transition metals. N/A = data not available. After 54.

Macroscopic property	Iron	Cobalt	Nickel	Palladium	Copper	Molybdenum
Density[56], at 20 °C (kg m^{-3})	7874	8900	8902	12020	8960	10220
Melting temperature (T_{melt}) (°C)	1536	1495	1453	1553	1083	2617
Surface tension[57] at 20 °C (at 2000 °C) (N m−1)	1.95 (1.72)	2.1 (1.68)	1.86 (1.57)	2.1 (1.72)	1.75 (0.95)	2.2 (N/A)
Equilibrium vapour pressure[58] (at t = 1216 °C) (Pa)	5.5×10^{-3}	4.7×10^{-3}	4.0×10^{-3}	2.1×10^{-2}	7.1×10^{-1}	7.6×10^{-11}
Carbon solubility[59] (at.%) at T_{melt}	20.2	13.9	10.7	~5	2×10^{-4}	Up to 60–70%
Carbon diffusion coefficient in metal[60] (m^2 s^{-1}) (at t = 1000 °C)	1.5×10^{-11}	1×10^{-11}	2×10^{-11}	6×10^{-11}	N/A	N/A

2.8.5 Catalyst Preparation

The transition metal nanoparticles can be applied on the substrate in various ways.[51] Two common[51] approaches are the use of solutions that contain them or the deposition through physical means. In the first approach there are several methods for catalyst synthesis from solutions. Salts of transition metals (e.g. ferric nitrate – nonahydrate) can be dissolved in organic solvents and applied on the substrate by dip coating (see chap. 3 and corresponding references for more details). The substrate is then placed in the furnace and heated up in an atmosphere of inert gas and hydrogen. The latter will reduce the salt to its metallic form producing thus the active catalyst. Another method[61] (in the solution approach) is the precipitation of the metal salt on to a support which in this case is in a form of powder (e.g. alumina). This is followed by drying, calcining and grinding. An oxide form of the catalyst is obtained after calcining. The supported catalyst is then placed in the furnace for a reduction step as described above.

In the second approach a number of techniques[51] such as electron gun evaporation[62,63], thermal evaporation[64,65], pulsed laser deposition, ion-beam sputtering[66,67], and magnetron sputtering[68,69]. These techniques are easier and quicker[51] in most of the cases than the solution based methods. However they require sophisticated and expensive equipment. One of their advantages is that with good resolution they can patterned the catalyst on to a substrate something which is not possible with the solution based techniques. They deposit a thin film of catalyst on the substrate whose thickness affects the final nanoparticle size. The nanoparticles are created by heating.

Finally another approach utilizes the application of organic carriers[70] such as feritin which can possibly yield a relatively unifom size of nanopartices. A calcination step must be taken when the sample is inserted into the furnace in order to remove the organic shell.

2.8.6 Effect of the catalyst particle size

The size of the catalyst nanoparticle is expected to have an effect on the nanotube type (single or multi walled) and diameter. A general scheme[71] that relates the catalyst nanoparticle size and the formed nanostructures is shown in Figure 2-20. This should not be considered as a general rule but as what is likely to be expected as a product of a CVD nanotube growth process from particles of certain size. Observations that do not follow the above scheme as for instance multi-walled carbon nanotubes with diameters larger than 50 nm have been reported[52]. In general though there appears to be an agreement in the literature about the relation of the catalyst particle size and the nanotube diameter which accepts that small particle sizes are likely to yield nanotubes of small diameters[72,73,74,75].

Another issue related with the catalyst particle size is the diameter distribution of the produced nanotubes. In order to narrow the later the catalyst particle size distribution has to be controlled and its spread has to be minimized. Precipitation methods give relatively wide particle size distributions[54]. In contrast organic carrier methods such as apoferritin[70,76] and polyamidoamine dendrimers[77] reported to yield catalyst particle size

distribution in the range of 1 – 3 nm. Molybdenum oxide caged molecules have given similar distributions[78].

One of the difficulties that prevent an accurate correlation between catalyst particle size and nanotube diameter is the precise determination of the former. The difficulty arises from the fact that the determination of the nanoparticle size takes place before the actual growth process. Change of the particle size distribution is inevitable as different phenomena occur at the elevated temperature that is needed in order to accelerate the decomposition of the carbon precursor molecules on the catalyst surface. The metal nanoparticles may collide due to surface diffusion and subsequent sintering leads to an increase of the average particle size[79]. Evaporation of the metal nanoparticles with relatively small diameters might also happen. This will also contribute towards an increase of the average diameter. The particles that have been evaporated might nucleate and form secondary metal particles away from the surface of the substrate that was initially hosting them. Catalytic decomposition may then happen in the gas phase on the surface of the newly formed particles. The product of this process is eventually deposited on the walls of the reactor. Such an effect has been reported for a CVD process in which ruthenium was used as a co-catalyst[80].

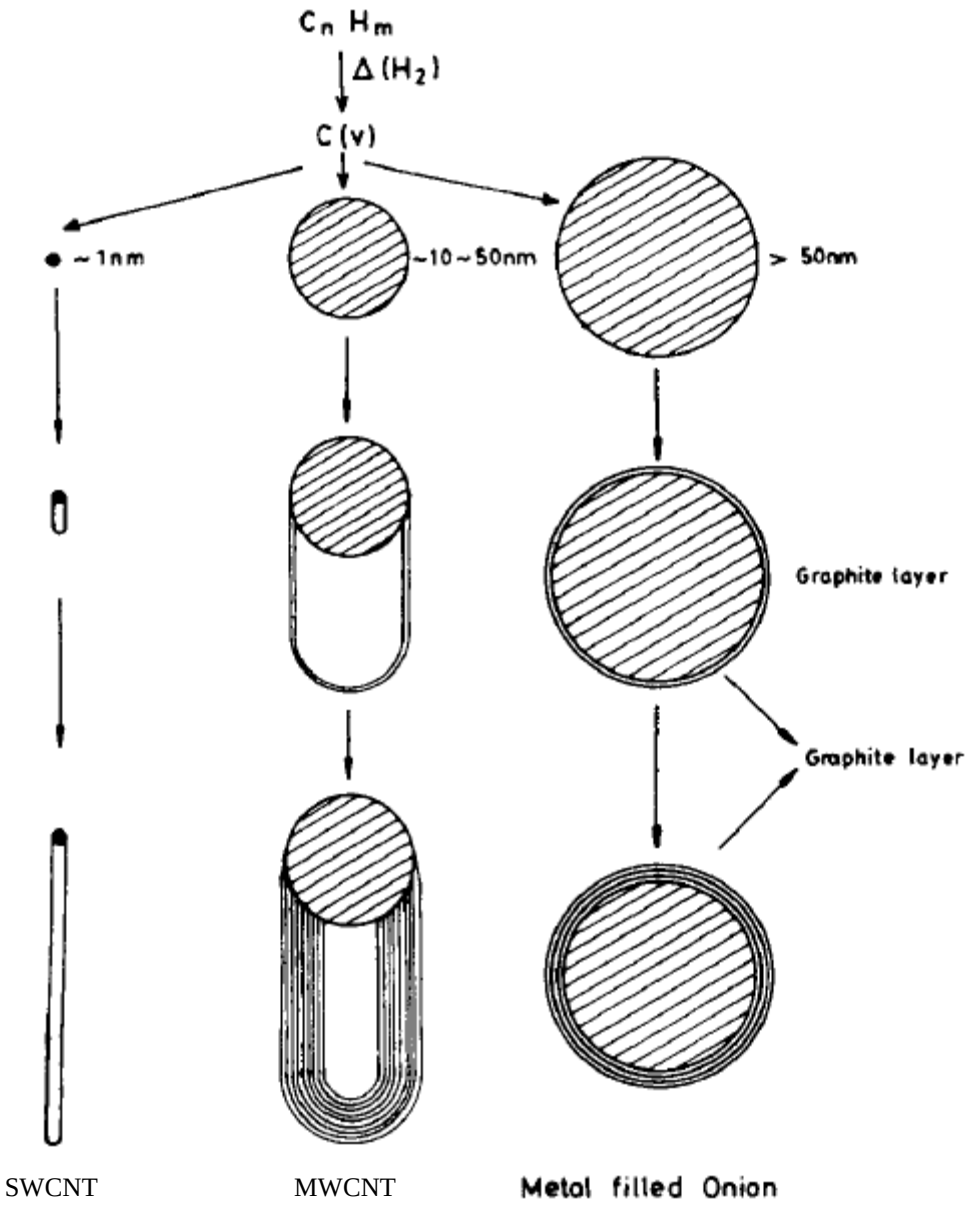

Figure 2-20 A general scheme showing the dependence of the formed carbon nanostructure upon the size of the catalyst particle. This schematic has not the character of a rule but is rather a lead of what is likely to be expected from particles of a particular range of size. Observations that do not follow this scheme have also been reported[52]. After 71.

2.8.7 Formation mechanism

There is a general agreement[81] of how a nanotube grow in length since it has been nucleated. A molecule of the carbon containing precursor decomposes when it impinges on the metal catalyst. The released carbon atom then diffuses either on the surface or in the bulk and reaches the open end of the nanotube which is chemisorbed into the catalyst. Then it gets bonded into the nanotube network as this will minimize the energy of the system. If the adhesion of the metal particle with the support surface is strong then the carbon precipitates from the top of the particle and the nanotube will continue to grow with the particle attached to the support surface. This type of growth is called base growth[51]. In the opposite case that the particle is weakly attached to the surface then there is a possibility that the carbon will precipitate from the bottom surface of the particle. As the nanotube continues growing it lifts the catalyst particle. This is called tip growth[51]. In this type of growth the top end of the nanotube contains the metal particle. Both of those types of growth have been observed[51,82].

The above picture of growth is compatible with the model of growth of carbon filaments which had been developed in the past[83]. The observation of the two types of growth (tip and base) in the case of carbon nanotubes agrees with the observation of similar types of growth in the case of carbon filaments indicating that the same model could apply for the carbon nanotube growth. The carbon filament growth model is using the concepts of the vapour – liquid – solid (VLS) theory that had been developed in the past for describing the growth of silicon whiskers[84]. The adaption[82] of this model in the case of carbon nanotubes consists of the following steps; i) adsorption and decomposition of the carbon precursor on the surface of the transition metal nanoparticle, ii) diffusion of carbon atoms into the catalyst bulk from the supersaturated surface, iii) precipitation of the nanotube network out of the supersaturated particle.

The VLS model (and its variances) for the nanotube growth considers the catalyst as being in the liquid phase[85] during the actual growth time. Although this seems unnatural due to the fact that the melting point of transition metals is well above the CVD growth temperatures (typically 900 ^{o}C), it is something that might be expected as the physical properties of nanoparticles can be different than those of the bulk. In Figure 2-21

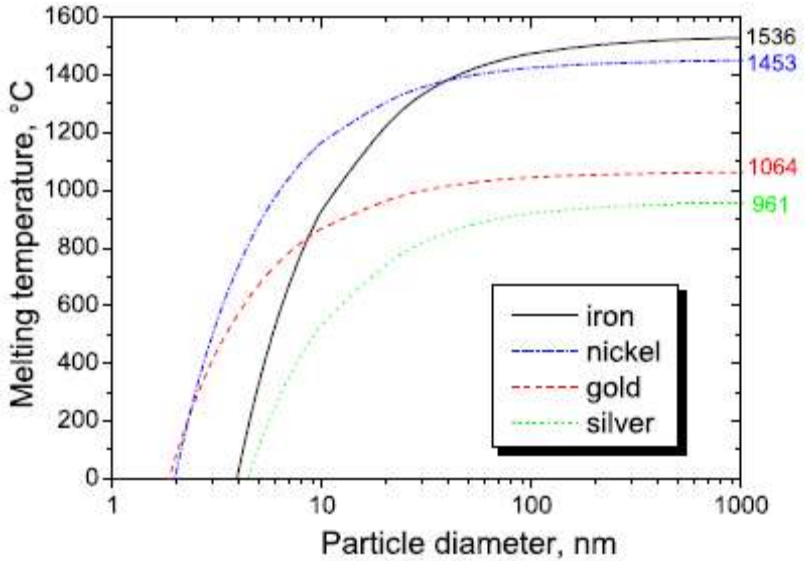

Figure 2-21 The melting temperature of selected metals as a function of particle diameter. After 54

the melting temperature of selected metals as a function of their particle size is shown. It can be seen that nanoparticles of Fe or Ni with diameters around 7 nm are expected to be close to their melting at CVD temperatures. The liquid phase of catalyst during growth has also been supported by experimental[86] evidence in the case of Co through transmission electron microscopy (TEM) observations.

Although the VLS model can describe how the nanotube growth evolves it does not give information of how the initial nucleation of the nanotube network happens. A modelled called “Yarmulke mechanism” has been proposed[81]. According to this model in order to minimise the total surface energy, the excess carbon forms a graphene cap on the surface of the metal particle, since graphene sheet has 10–20 times smaller surface energy than most metals. Important features of this mechanism are the strong chemisorption of the graphene cap to the particle in a way that avoids any open graphene edges and the equal diameters of the catalyst particle and the carbon nanotube.

The above models for the nanotube formation through catalytic growth are the most dominant once in the literature. There are also other models with similarities with the ones presented here but also differences. Their presentation here though would be beyond the scope of this section. The presented models contribute towards a basic understanding of the nanotube formation mechanism which was the aim of this section.

References:

[1] R. Saito, G. Dresselhaus, M. S. Dresselhaus, "Physical Properties of Carbon Nanotubes", Imperial College Press, (1998).

[2] T.W. Ebbesen, "Carbon Nanotubes", Edited by T.W. Ebbesen, Chapter I, CRC Press, (1997).

[3] B. McEnaney, "Carbon Materials for Advanced Technologies", Edited by T.D. Burchell, Chapter I, Pergamon 1999.

[4] E.A. Rohlfing, D.M. Cox, A. Kaldor, "Production and characterization of supersoninc carbon cluster beams", J. Chem. Phys. 81, 3322 (1984).

[5] G. Helden, M. T. Hsu, P. F. Kemper, M. T. Bowers, "Structures of carbon cluster ions from 3 to 60 atoms: Linears to rings to fullerenes", J. Chem. Phys. 95, 385, (1991).

[6] H.S. Carman Jr., R.N. Compton, " Electron attachement to C_n clusters ($n \leq 30$)", J. Chem. Phys. 98, 2473 (1993).

[7] M.S. Dresselhaus, G. Dresselhaus, P.C. Eklund, "Science of Fullerenes and Carbon Nanotubes", Chapter XIX, Academic Press (1996).

[8] H.W. Kroto, J.R. Heath, S.C. O'Brien, R.F. Curl, R.E. Smalley, "C60: Buckminsterfullerene", Nature 318, 162 (1985).

[9] S. Iijima, " Helical microtubules of graphitic carbon", Nature, 354, 56, (1991).

[10] M.S. Dresselhaus, G. Dresselhaus, R. Saito, Carbon 33, 883 (1995).

[11] L.F. Sun, S.S. Xie, W. Liu, W.Y. Zhou, Z.Q. Liu, D.S. Tang, G. Wang, L.X. Qian, Nature 403, 384 (2000).

[12] L.C. Qin, X. Zhao, K. Hirahara, Y. Miyamoto, Y. Ando, S. Iijima, Nature 408, 50 (2000).

[13] N. Wang, Z.K. Tang, G.D. Li, J.S. Chen, Nature 408, 50 (2000).

[14] M. J. O'Connell, S. M. Bachilo, C. B. Huffman, V. C. Moore, M. S. Strano, E. H. Haroz, K. L. Rialon, P. J. Boul, W. H. Noon, C. Kittrell, J. Ma, R. H. Hauge, R. B. Weisman, R. E. Smalley, "Band Gap Fluorescence from Individual Single – Walled Carbon Nanotubes", Science, 297, 593, (2002)

[15] M. Zheng, A. Jagota, M. S. Strano, A. P. Santos, P. Barone, S. G. Chou, B. A. Diner, M. S. Dresselhaus, R. S. Mclean, G. B. Onoa, G. G. Samsonidze, E. D. Semke, M. Usrey, D. J. Walls," Structure-Based Carbon Nanotube Sorting by Sequence-Dependent DNA Assembly", 302, 1545, (2003).

[16] S. Iijima, Mater. Sci. Eng. B19, 172 (1993).

[17] M. S. Dresselhaus, G. Dresselhaus, A. Jorio, "Unusual Properties and Structure of Carbon Nanotubes", Annu. Rev. Mater. Res. 34, 247, (2004).

[18] R. Saito, M. Fujita, G. Dresselhaus, M. S. Dresselhaus, "Electronic structure of chiral graphene tubules", Appl. Phys. Lett. 60, 2204, (1992).

[19] P. R. Wallace, "The Band Theory of Graphite", Phys. Rev. 71, 622, (1947).

[20] C. T. White, J. W. Mintmire, "Density of states reflects diameter in nanotubes", Nature, 394, 29, (1998).

[21] S. Reich, C. Thomsen, J. Maultzsch, "Carbon Nanotubes: Concepts and Physical Properties", Wiley – VCH, 2004.

[22] Ashcroft, Mermin, "Solid State Physics".

[23] R. Saito, H. Kataura, "Optical Properties and Raman Spectroscopy of Carbon Nanotubes" in Topics in Applied Physics vol. 80 "Carbon Nanotubes Synthesis Structure Properties and Applications" ed. M. S. Dresselhaus, G. Dresselhaus, Ph. Avouris, Springer, (2001).

[24] M. S. Dresselhaus, "New tricks with nanotubes", Nature 391, 19, (1998).

[25] J. C. Charlier, Ph. Lambin, "Electronic structure of carbon nanotubes with chiral symmetry", Phys. Rev. B 57, R15037, (1998).

[26] J. W. Mintmire, C. T. White, "Universal Density of States for Carbon Nanotubes", Phys. Rev. Lett. 81, 2506, (1998).

[27] J. W. G. Wildöer, L. C. Venema, A. G. Rinzler, R. E. Smalley, C. Dekker, "Electronic structure of atomicaly resolved carbon nanotubes", Nature, 391, 59, (1998).

[28] T. W. Odom, J-L. Huang, P. Kim, C. M. Lieber, "Atomic structure and electronic properties of single-walled carbon nanotubes", Nature, 391, 62, (1998).

[29] N. Hamada, S. sawada, A. Oshiyama, "New One-Dimensional Conductors: Graphitic Microtubules", Phys. Rev. Lett. 68, 1579, (1992).

[30] C. L. Kane, M. J. Mele, "Size, Shape, and Low Energy Electronic Structure of Carbon Nanotubes", Phys. Rev. Lett. 78, (1997).

[31] M. Ouyang, J. L. Huang, C. L. Cheung, C. M. Lieber, "Energy Gaps in "Metallic" Single-Walled Carbon Nanotubes", Science, 292, 702, (2001).

[32] D. E. Long, "The Raman Effect. A Unified Treatment of the Theory of Raman Scattering by Molecules", John Wiley & Sons Ltd, England, (2002).

[33] J. A. Koningstein, "Introduction to the theory of the Raman effect", D. Reidel Publishing Company, Holland, (1972).

[34] Editor: M. Cardona, "Light Scattering in Solids I. Introductory Concepts" ,2nd Ed., Topics in Applied Physcis, vol. 8, Springer – Verlag , Berlin – Heidelberg – New York, (1983).

[35] Editors: M. Cardona, G. Güntherodt, "Light Scattering in Solids II. Basic Concepts and Instrumentation", Topics in Applied Physcis, vol. 50, Springer – Verlag , Berlin – Heidelberg – New York, (1982).

[36] D. C. Smith, "Measurements of Ultrafast Dynamics, in a Superconductor, $YBa_2Cu_3O_{7-\delta}$, and a Semiconductor, GaSb", Ph. D. Thesis, University of Oxford, (1998).

[37] P. Y. Yu, M. Cardona "Fundamentals of Semiconductors: Physics and Materials Properties", Springer – Verlag, Berlin, Heidelberg, New York, (1996).

[38] R. Loudon, "Theory of the first – order Raman effect in crystals", Proc. Roy. Soc. (London) A 275, 218, (1963).

[39] A. Jorio, M. A. Pimenta, A. G. Souza Filho, R. Saito, G. Dresselhaus, M. S. Dresselhaus, "Characterising carbon nanotube samples with resonance Raman scattering", New J. Phys., 5, 139.1, (2003).

[40] M. A. Pimenta, A. Marucci, S. A. Empedocles, M. G. Bawendi, E. B. Hanlon, A. M. Rao, P. C. Eklund, R. E. Smalley, G. Dresselhaus, M. S. Dresselhaus, "Raman modes of metallic carbon nanotubes", Phys. Rev. B, 58, R16 016, (1998).

[41] P. M. Rafailov, H. Jantoljak, C. Thomsen, "Electronic transitions in single-walled carbon nanotubes: A resonance Raman study", Phys. Rev. B, 61, 16 179, (2000).

[42] A. M. Rao, E. Richter, S. Bandow, B. Chase, P. C. Eklund, K. A. Williams, S. Fang, K. R. Subbaswamy, M. Menon, A. Thess, R. E. Smalley, G. Dresselhaus, M. S. Dresselhaus, "Diameter-Selective Raman Scattering fromVibrational Modes in Carbon Nanotubes", Science, 275, 187, (1997).

[43] A. Jorio, M. A. Pimenta, A. G. Souza Filho, R. Saito, G. Dresselhaus M. S. Dresselhaus, Phys. Rev. Lett. 86, 1118, (2001).

[44] M. Milnera, J. Kürti, M. Hulman ,H. Kuzmany, Phys. Rev. Lett. 84, 1324, (200).

[45] J. Jiang, R. Saito, A. Grüneis, S. G. Chou, Ge. G. Samsonidze, A. Jorio, G. Dresselhaus, M. S. Dresselhaus, "Intensity of the resonance Raman excitation spectra of single-wall carbon nanotubes", Phys. Rev. B, 71, 205420, (2005).

[46] M. S. Dresselhaus, G. Dresselhaus, R. Saito, A. Jorio, "Raman spectroscopy of carbon nanotubes", Physics Reports, 409, 47, (2005).

[47] A. Jorio, C. Fantini, M. S. S. Dantas, M. A. Pimenta, A. G. Souza Filho, Ge. G. Samsonidze, V. W. Brar, G. Dresselhaus, M. S. Dresselhaus, A. K. Swan, M. S. U ¨ nlu¨, B. B. Goldberg, R. Saito, "Linewidth of the Raman features of individual single-wall carbon nanotubes", Phys. Rev. B, 66, 115411, (2002).

[48] M. L. Sanjuán, A. Ansón, M. T. Martínez, "Double resonance features in the Raman spectrum of carbon nanotubes", Phys. rev. B, 70, 201404(R), (2004).

[49] H. Dai, "Nanotube Growth and Characterisation" in Topics in Applied Physics vol. 80 "Carbon Nanotubes Synthesis Structure Properties and Applications" ed. M. S. Dresselhaus, G. Dresselhaus, Ph. Avouris, Springer, (2001).

[50] J-C. Charlier, S. Iijima, "Growth Mechanisms of Carbon Nanotubes" in Topics in Applied Physics vol. 80 "Carbon Nanotubes Synthesis Structure Properties and Applications" ed. M. S. Dresselhaus, G. Dresselhaus, Ph. Avouris, Springer, (2001).

[51] M. Meyyappan, "Growth: CVD and PECVD", in "Carbon Nanotubes science and applications", ed. M. Meyyappan, CRC PRESS Boca Raton, London, New York, Washington, D.C. (2005).

[52] C.N.R. Rao FRS, A. Govindaraj, "Nanotubes and Nanowires", RSCPublishing, (2005).

[53] P. J. F. Harris, "Carbon Nanotubes and Related Structures: New Materials for the Twenty-first Century", Cambridge University Press, (1999).

[54] A. Moisala, A. G. Nasibulin, E. I. Kauppinen, "The role of metal nanoparticles in the catalytic production of single-walled carbon nanotubes—a review", J. Phys.: Condens. Matter, 15, S3011, (2003)

[55] T. Guo, P. Nikolaev, A. Thess, D.T. Colbert, R.E. Smalley, "Catalytic growth of single-walled manotubes by laser vaporization", Chem. Phys. Lett. 243, 49, (1995).

[56] J. Emsley, "The Elements", Oxford: Clarendon, p. 264, (1991).

[57] R. M. German "Sintering Theory and Practice", Wiley–Interscience, p. 550, New York, (1996)

[58] I. S. Kulikov, "Termodinamika Oksidov (Thermodynamics of Oxides)", Metallurgija, Moscow, p. 344, (1986).

[59] I. S. Kulikov, "Termodinamika Karbidov i Nitridov (Thermodynamics of Carbides and Nitrides)", Metallurgija, Chelybinsk, p.149, (1988).

[60] H. Yokoyama , H. Numakura, M. Koiwa, "The solubility and diffusion of carbon in palladium", Acta Mater. 46, 2823, (1998).

[61] J-F Colomer, G. Bister, I. Willems, Z. Konya, A. Fonseca, G. Van Tendeloo, J. B . Nagy, Chem. Commun. 1343–4, (1999).

[62] V.I. Merkulov et al., Appl. Phys. Lett., 76, 3555 (2000).

[63] V.I. Merkulov et al., Appl. Phys. Lett., 79, 1178 (2001).

[64] M. Chhowalla et al., J. Appl. Phys., 90, 5308 (2001).

[65] L. Valentini et al., J. Appl. Phys., 92, 6188 (2002).

[66] C. Bower, W. Zhu, S. Jin, and O. Zhou, Appl. Phys. Lett., 77, 830 (2000).

[67] K. Matthews, B. Cruden, B. Chen, M. Meyyappan, and L. Delzeit, J. Nanosci. Nanotech., 2, 475, (2002).

[68] G.W. Ho, A.T.S. Wee, J. Lin, and W.C. Tjiu, Thin Solid Films, 388, 73 (2001).

[69] Y.H. Wang et al., Appl. Phys. Lett., 79, 680 (2001).

[70] Y. Li, W. Kim , Y. Zhang, M. Rolandi, D. Wang, H. Dai, J. Phys. Chem. B, 105, 11424, (2001).

[71] C. N. R. Rao, B. C. Satishkumar, A. Govindaraj, M. Nath, "Nanotubes", ChemPhysChem, 2, 78, (2001).

[72] C. L. Cheung, A. Kurtz, H. Park, C. M. Lieber, "Diameter-Controlled Synthesis of Carbon Nanotubes", J. Phys. Chem. B.(Letter), 106, 2429, (2002).

[73] Y. Li, W. Kim, Y. Zhang, ; M. Rolandi, D. Wang, H. Dai, "Growth of Single-Walled Carbon Nanotubes from Discrete Catalytic Nanoparticles of Various Sizes", J. Phys. Chem. B. 105, 11424, (2001).

[74] G.-H. Jeong, S. Suzuki, Y. Kobayashi, A. Yamazaki, H. Yoshimura, Y. Homma, "Effect of Nanoparticle Density on Narrow Diameter Distribution of Carbon Nanotubes and Particle Evolution during Chemical Vapour Deposition Growth," J. Appl. Phys., 98, 124311, (2005).

[75] D. Kondo, S. Sato, and Y. Awano, "Low-temperature Synthesis of Single-walled Carbon Nanotubes with a Narrow Diameter Distribution Using Size-classified Catalyst Nanoparticles," Chem. Phys. Lett., 422, 481, (2006).

[76] Y. Zhang, Y. Li, W. Kim, D. Wang, H. Dai, "Imaging as-grown single-walled carbon nanotubes originated from isolated catalytic nanoparticles",Appl. Phys. A 74, 325, (2002).

[77] H. C. Choi, W. Kim, D. Wang, H. Dai, "Delivery of Catalytic Metal Species onto Surfaces with Dendrimer Carriers for the Synthesis of Carbon Nanotubes with Narrow Diameter Distribution", J. Phys. Chem. B. (Letter), 106, 12361, (2002).

[78] L. An, J. M. Owens, L. E. McNeil, J. Liu, "Synthesis of Nearly Uniform Single-Walled Carbon Nanotubes Using Identical Metal-Containing Molecular Nanoclusters as Catalysts", J. Am. Chem. Soc. (Communication), 124, 13688, (2002).

[79] W. E. Alvarez, B. Kitiyanan , A. Borgna, D. E. Resasco, Carbon, 39, 547, (2001).

[80] A. M. Cassell , J. A. Raymakers, J. Kong, H. Dai, J. Phys. Chem. B 103, 6484, (1999)

[81] H. Dai, A. G. Rinzler, P. Nikolaev, A. Thess, D. T. Colbert, R. E. "SmalleySingle-wall nanotubes produced by metal-catalyzed disproportionation of carbon monoxide", Chem. Phys. Lett., 260, 471, (1996)

[82] J. Kong, H. T. Soh, A. M. Cassell, C. F. Quate, H. Dai, "Synthesis of individual single walled carbon nanotubes on patterned silicon wafers", Nature, 395, 878, (1998).

[83] R. T. K. Baker, "Catalytic growth of carbon filaments", Carbon, 27, 315, (1989).

[84] R. S. Wagner, W. C. Ellis, "Vapour – Liquid – Solid Mechanism of Single Crystal Growth", Appl. Phys. Lett., 4, 89, (1964).

[85] J. Gavillet, A. Loiseau, C. Journet, F. Willaime, F. Ducastelle, J.-C. Charlier, "Root-Growth Mechanism for Single-Wall Carbon Nanotubes", Phys. Rev. Lett., 87, 275504, (2001).

[86] A. R. Harutyunyana, T. Tokune, E. Mora, "Liquefaction of catalyst during carbon single-walled nanotube growth", Appl. Phys. Lett. 86, 153113, (2005).

Chapter 3 Metal – Free – Catalyst Growth of Single Walled Carbon Nanotubes

In this chapter a method of growing single walled carbon nanotubes by the means of chemical vapour deposition without the need of metal catalyst is described.

Contributions

K. N. Bourdakos suggested the Chemical Vapour Deposition recipe for SWCNTs growth, established the existence of single walled carbon nanotubes (SWCNTs) on the substrates after the growth and further characterised the samples through the means of Raman and AFM measurements. Dr T. Ushino conceived the idea of carbon nanotube (CNT) growth on carbon ion implanted nanostructured substrates, performed the growth and the scanning electron microscopy (SEM) measurements. The substrates were prepared by G. D. Dilliway. The carbon ion implantation was carried out by the ion beam centre of the University of Surrey. The SIMS measurements were carried out by the Charles Evans company. The TEM was carried by Dr. S.Wang

3.1 Introduction

Carbon nanotubes due to their quasi-one-dimensional molecular structure have semiconducting or metallic properties that make them promising material for future electronic applications[1,2]. The research in this domain has yielded several achievements from which the most important ones are the fabrication of one of the smallest ever field effect transistor (FET) devices (Infineon 18 nm channel FET)[3], a light emitting FET[4], non volatile electromechanical memory devices of comparable density and higher speed of the current flash memory devices[5].

However the large scale integration of carbon nanotube FET devices has not yet been achieved due to some serious obstacles. One is the positioning (or growth) of cnts of specific diameter and chirality on specific points of a patterned substrate. This requires either control of the diameter and chirality during the growth process as well as of the position and the direction of the growth in a large scale or selection of the cnts according to their chirality and diameter and a method of positioning also in large scale.

Another serious obstacle is the incompatibility of the current growth methods of SWCNTs with the front end silicon processing technology. The reason for the latter is the need of metal nano-particles which act as catalyst for the growth of SWCNTs[6]. This consist a significant contamination hazard for the silicon processing facilities. The presence of metal nanoparticles (or conducting nanoparticles in general) on the surface of a wafer might result in their encapsulation in the structure of the integrated circuit. This might lead to short circuits by bridging interconnect lines in the circuit or by assisting electrical breakdown of the insulating oxide between the interconnect lines[7]. The part of the circuit that suffers from this kind of contamination will function in an unpredictable way resulting to the failure of the whole circuit[7].

The current work establishes experimentally a new method of growth of SWCNTs that does not use metal particles as catalyst[8,9]. This method reveals another aspect of the nanotube growth process while simultaneously opens up the prospect of merging CNTs with the front end silicon processing. This metal-catalyst-free growth method uses chemical vapor deposition (CVD) of CNTs and has been found that it can be applied in three different types of substrates i) carbon implanted SiGe islands on Si substrates, ii) carbon implanted Ge dots on Si substrates iii) non carbon implanted Ge dots on Si substrates with lower yield of carbon nanotube growth. The existence of SWCNTs on the above substrates (after CVD growth) was established by means of Raman spectroscopy. Information about the diameter and metalicity of the as grown NTs was also extracted from the Raman Spectra. Further information about the yield, substrate coverage and possible mechanisms of growth was acquired by performing SEM and AFM measurements.

3.2 Metal-free-catalyst growth of CNTs. An overview

There are two methods that have been reported so far in the literature which enable the growth of SWCNTs without the use of metal catalyst[10,11,12,13]. In the first method[10,11] carbon nanotubes are produced by low velocity spraying of carbon nanosized particles on a heated Si substrate. The growth parameters of this method are: Ar carrier flow at 300 sccm (standard cubic centimeters per minute), ambient pressure of 0.04 atm, substrate temperature of 800 ^{o}C to 1100 ^{o}C and deposition time of 30 min. The produced nanotubes have perpendicular orientation to the substrate, forming bundles with diameters from 30 to 90 nanometers. From Raman measurements single walled carbon nanotubes were detected among the observed nanotubes with diameters of 0.85 to 1.33 nm. However from the same measurements the presence of quantities of amorphous carbon, graphitic particles and multiwall carbon nanotubes was revealed. The fact that this method, produces bundles of nanotubes of relatively large diameter with perpendicular orientation to the substrate, makes it improper for application in nanotube electronics.

The second method[12,13] employs hexagonal silicon carbide (6H-SiC) substrates which are annealed in high temperature (above 1500 C) in vacuum (10^{-8} Torr). The method has been found to yield a mixture of SWCNTs on the Si face of the SiC. The orientation of the nanotubes is parallel to the surface of the substrate and they form a hexagonal network. From scanning tunneling microscopy (STM) measurements[12,13] the nanotubes were found to be single walled with diameters in the range of 1.2 to 1.6 nm. However in this method of growth only part of the CNTs lays on the surface of the substrate. The growth of nanotubes takes place in several atomic layers, and the network of CNTs is composed of tubes from different depth connected together. This makes difficult the fabrication of nanotube devices on such substrates due to the high probability of short-circuits caused by random nanotubes at different depths on the substrate (for instance diffusion of metal contacts even in small depth inside the substrate might give rise to contacts with nanotubes laying in the same depth thus leading to an unpredictable behaviour of the device). Additionally the use of expensive SiC substrates makes this method unsuitable for large scale production.

Therefore the method presented here is the only one (to the knowledge of the author) that achieves horizontal surface growth of SWCNTs without the need of metal catalyst.

3.3 Growth on SiGe substrates

Growth of SWCNTs was achieved on substrates with SiGe nano islands as it was mentioned above. The growth was carried by means of CVD and without the use of any metal catalyst. The as fabricated substrates were characterized with Raman spectroscopy and SEM.

3.3.1 Substrate preparation and growth

A 50 nm-thick SiGe (30% Ge) layer was deposited by CVD on Si (001) wafers after the growth of a thin Si buffer layer. To accommodate the stress as a result from the lattice mismatch between Si and Ge, the SiGe layer forms islands on top of a thin wetting layer. The height of the islands ranges from 20 to 50 nm. Subsequently, the islands were doped with carbon using ion implantation. A dose of 3310^{16} cm^{-2} was implanted at an energy of 30 keV.

In order to evaluate the carbon content at the SiGe-Si interface secondary ion mass spectrometry (SIMS) was preformed. For those measurements 1.5 keV Cs negatives at 60 degrees angle of incidence were used. They were run on a Phi Adept 1010 Quadrapole SIMS instrument. The depth of the created craters was measured using surface profilometry. The implanted SiGe layer was found to contain 2% carbon at the SiGe-Si interface (Figure 3-1). The SiGe(C) substrates were cut in 537 mm pieces and dipped in buffered HF solution to remove the native oxide. Chemical oxidation was performed using a 30% hydrogen peroxide (H_2O_2) solution at room temperature. The thickness of the chemical oxide layers on the bumpy SiGe surface was estimated to be around 0.5 nm from similar experimental results on Si substrates[14].

The as prepared substrates (two for each growth session) were laid at the bottom of a ceramic boat container with their nanostructured surface facing upwards. The loaded container was inserted inside a quartz tube furnace. The temperature was ramped in 30 minutes to 1000^{o}C in an atmosphere of Ar (1.0 standard litre per minute (SLM)) and H_2

(0.4 SLM). After 10 min anneal at 1000 ^{o}C the temperature was ramped down to 850^{o}C in 5 min. At this temperature growth took place for 10 min in an atmosphere of 1 SLM CH_4 and 0.4 SLM H_2. After this step the substrates were left to cool down to room temperature in Ar atmosphere (1.4 SLM) in about 40 min.

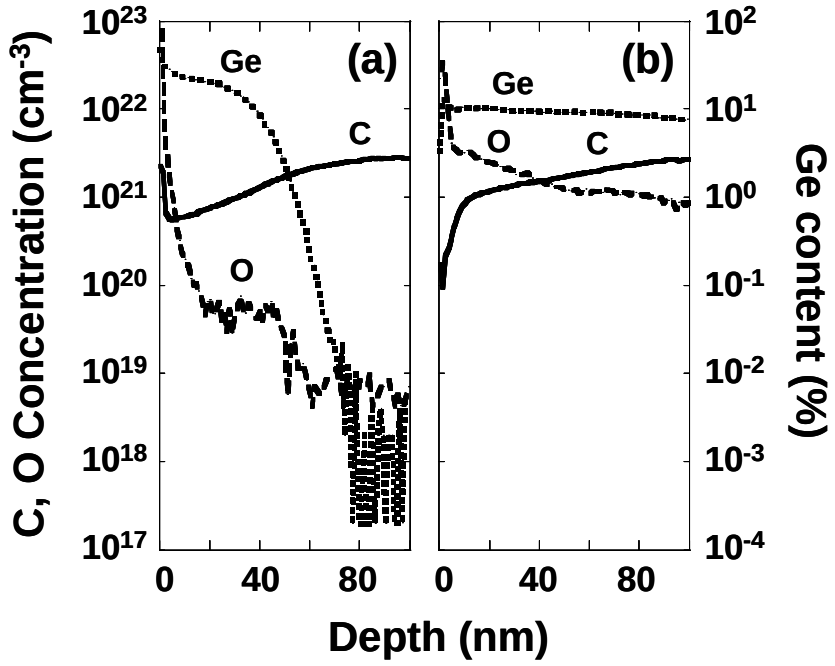

Figure 3-1 SIMS measurements on the carbon implanted SiGe substrate before (a) and after annealing and cnt growth (b).

3.3.2 Scanning Electron Microscopy measurements on the SiGe substrates after CVD growth.

After the growth the substrates were imaged by means of field-emission scanning electron microscopy (FE-SEM). A JSM 6500F thermal FE-SEM was used. At a magnification of 30,000 times (x30,000), beam energy 10 keV and working distance (WD) 13.7 mm clear images of the nanostructured surface of the samples were obtained. Two types of nanofibers (Figure 3-2) were intermingled in most of the samples. The first type comprises curly and thick fibres with around 20 nm diameter and 1 μm length. The second type comprises straight and thinner fibers with less than 10 nm diameter and 5 μm length.

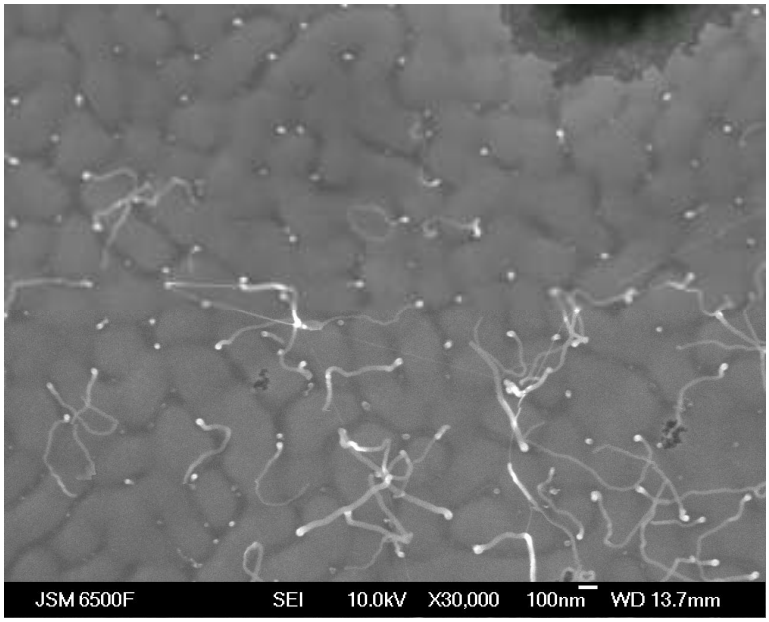

Figure 3-2 FE-SEM micrograph of SiGe substrate after CVD growth. Two kind of fibres can be distinguished.

The chemical composition was analyzed by energy-dispersive x-ray spectroscopy (EDS). The EDS system which was incorporated with the FE-SEM in use was an INCA 300 from Oxford Instruments. For the EDS measurements a beam with energy of 10 keV and integration time of 2 sec were used. The beam spot size at the surface of the sample was approximately 2 nm. It is expected with the above settings that quantities of Fe, Ni and Co as less as 0.1% could be detected within the detection volume. An average of ten points per 1 μm^2 were probed at the areas covered with fibres. With the above settings no gross metal contamination was detected in any of the 34 SiGe samples on to which surfaces fibres had been observed. A typical EDS spectrum is depicted in Figure 3-3b while in Figure 3-3a is shown the point on the sample that this spectrum was derived from.

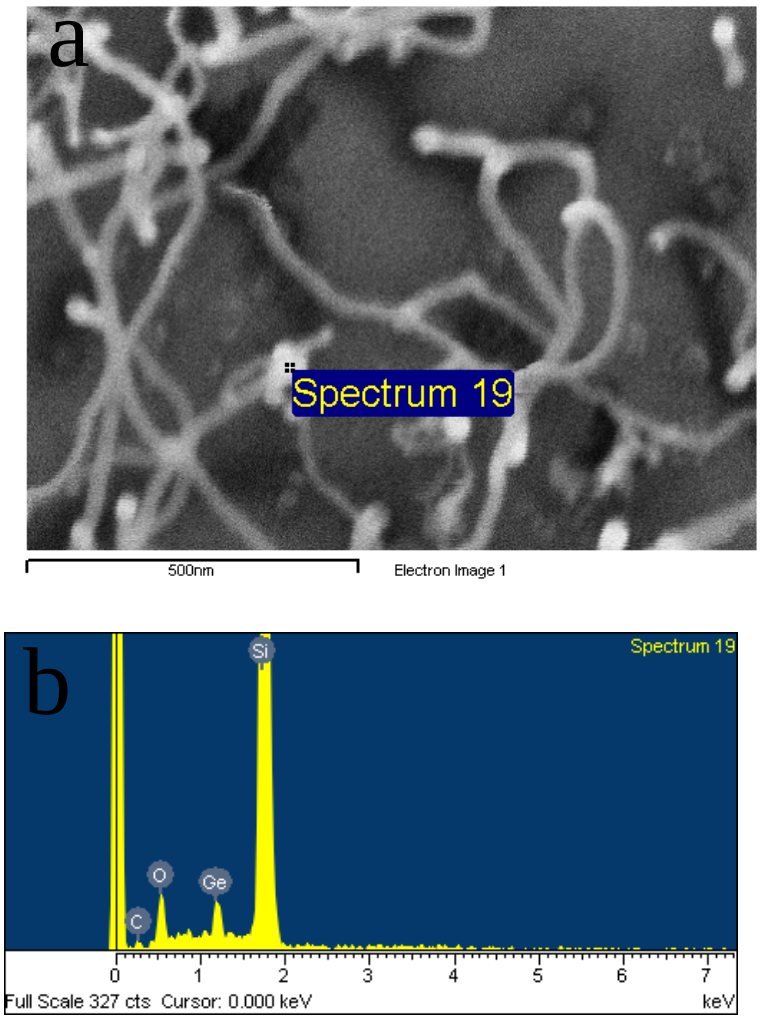

Figure 3-3 EDS measurements on a SiGe substrate after CVD growth. a) SEM image of a SiGe sample with as grown fibres on to which the point of the EDS measurement is depicted. b) EDS spectrum of the obtained from the point depicted in a).

3.3.3 SEM measurements on the SiGe substrates after CVD growth and vapour HF etching.

To distinguish between the two kinds of fibres, the substrates were subjected to HF vapour etching. Figure 3-4(b) shows clearly that only the thin fibres survive the processing, and that thick fibres were dissolved in the HF treatment.

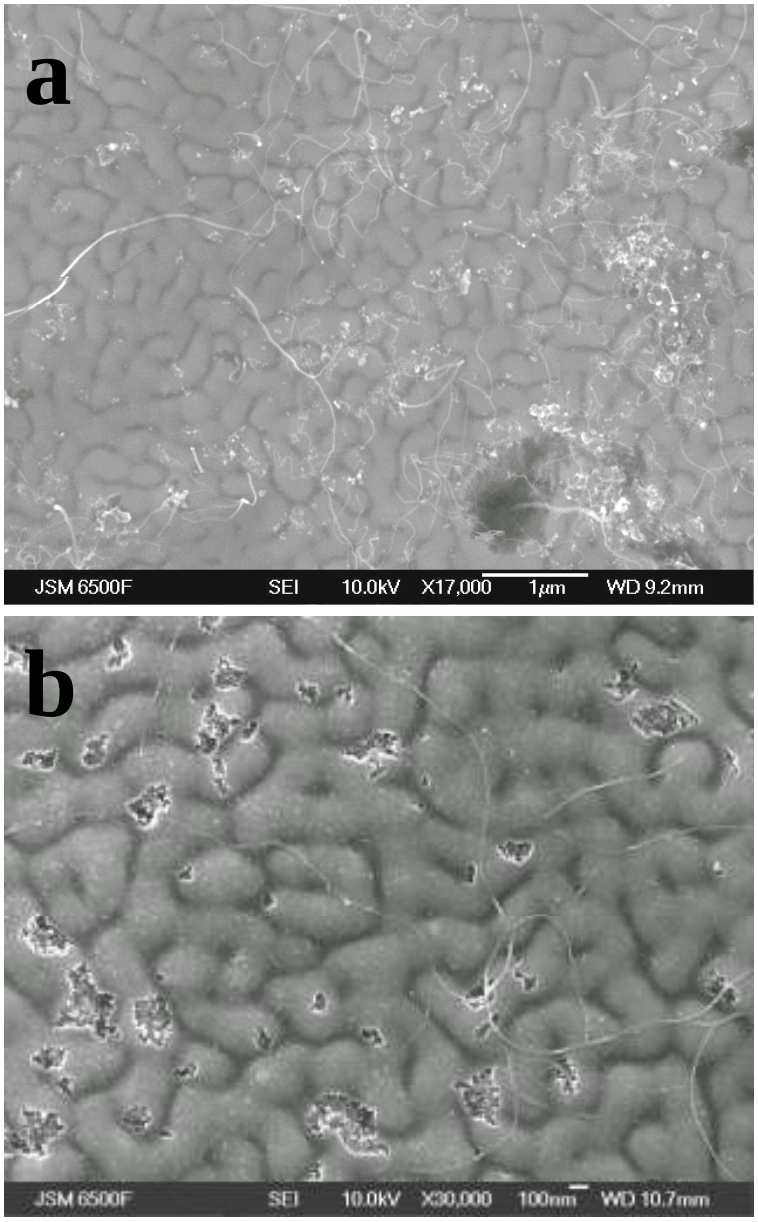

Figure 3-4 SEM images of the fabricated nanofibers on SiGe islands. (a) As-grown fibers; oxide nanofibers (short, curly, thick and bright) and SWNTs (long, straight, thin and dark) were observed. (b) After HF vapor etching only SWNTs were observed.

3.3.4 SEM measurements on the SiGe substrates after CVD growth and air annealing.

The thick fibres, however, survive after the atmospheric annealing at 900°C, while the thin ones were burnt out. These last two observations indicate that the thick fibres consist of Si and Ge oxide embedded in an amorphous carbon matrix.

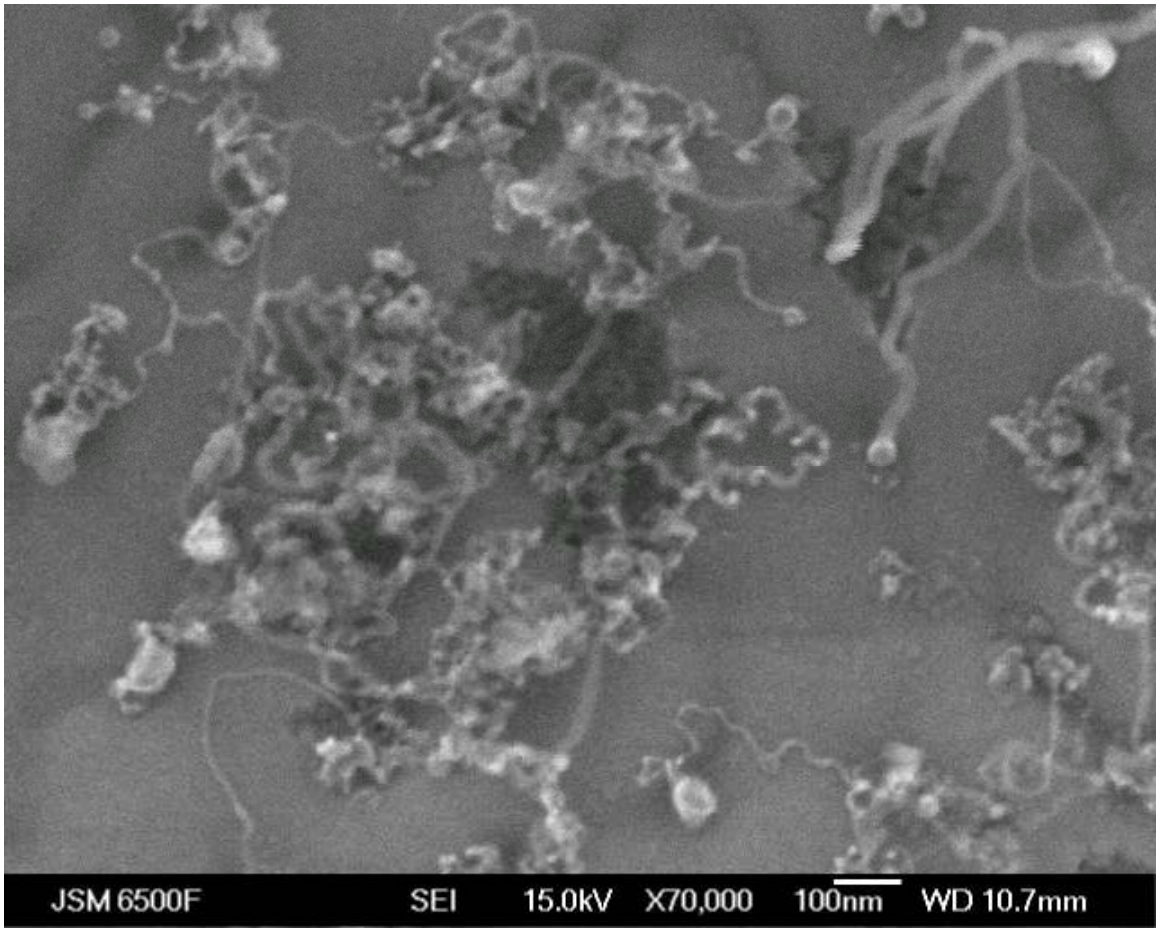

Figure 3-5 SiGe sample after CVD growth and air annealing at 900 ^{o}C. Only thick fibres have survived. Sample 28_AA01.

3.3.5 Effect of H_2 on the growth of Carbon Nanotubes.

The effect of H_2 on the CNT growth has been studied in the case of catalytic CVD growth. It is mainly the reduction of the metal salts (for instance in the case of $Fe(NO_3)_3$ the H_2 will reduce during annealing to Fe, which is going to be the active catalyst. From this point of view it is not clear what the role of H_2 is in the current method as the above model does not comply with the materials involved in this case. Performing CVD on the SiGe nanostructured substrates as it was described above, but without using H_2 was found to give reduced yield of CNT growth (Figure 3-6). This indicates that H_2 still affects the CNT growth process in the case of the SiGe nanostructured substrates although the underlying mechanism of this effect is not clear.

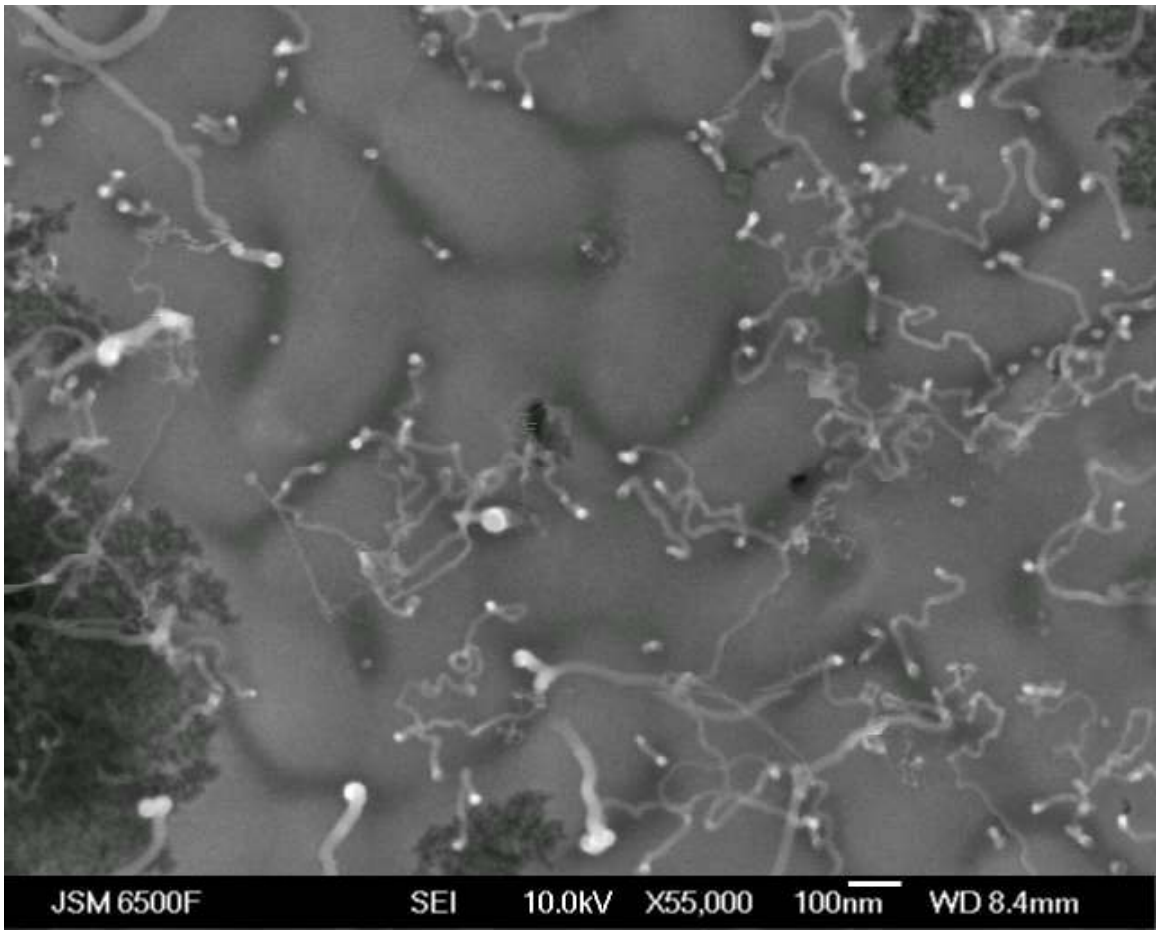

Figure 3-6 Lack of H_2 during CVD growth results in poor carbon nanotube growth. Sample 39_3

3.3.6 Raman measurements on the SiGe substrates after CVD growth

Although the SEM images provided valuable information about the growth, they could not give any knowledge about the nature of the observed fibres. In order to get this information the as-grown nanofibres were characterised by means of micro-Raman spectroscopy. The Raman measurements were performed on a Renishaw system, (consisting of an Olympus microscope, a monochromator with a 1200 grooves/mm grating, a 512 3256 ccd, a holographic notch filter, He-Ne (632.8 nm) laser with power of 12mW, Ar^+ laser (488 nm, 30mW) . The samples were excited using the HeNe laser which was focused through a 503 objective and the signal was collected in a backscatter geometry. After passing through a holographic notch filter (which rejects the laser wavelength) it was dispersed through 1200grooves/mm grating onto a 512×256 charge coupled device (CCD) operating at room temperature. The tuning of the notch filter was such that the frequency cut off ranges from -100 to 200 cm^{-1} and for this reason only the anti-Stokes shifts could be obtained for signals in the range between 100 and 200 cm^{-1}.

Many of the Raman spectra obtained from the areas where the density of the thin nanofibres is higher exhibited an asymmetric double peak around 1590 cm^{-1}(Figure 3-7 b). This double peak resembles very well to the G-band of SWCNTs[15]. In some cases the low frequency peak is relatively broad (Figure 3-7d) and can be fitted with Lorentzian and Breit-Wigner-Fanno functions[16] (Figure 3-7e). The latter is an evidence of the existence of a metallic SWCNT in the sample[16]. Furthermore in many cases spectra exhibiting peaks in the range of -100 to -200 cm^{-1} (anti-Stokes) were obtained (Figure 3-7f). These peaks are spectrally located in the range of the radial breathing mode (RBM) of SWCNTs[15] and they appear only at the points of the sample from which the spectra with the double peak around 1590 cm^{-1} were obtained. Therefore it can be safely concluded that these spectra originate from SWCNTs whose existence on the nanostructured Si-Ge face of the substrates is now well established.

The peaks of -197 cm^{-1} and -155 cm^{-1} are assigned to metallic and semiconducting SWNTs with diameters of 1.26 nm and 1.60 nm, respectively[15]. The peak of 303 cm^{-1} comes from the Si substrate. In the high frequency region, the G-band feature around 1600 cm^{-1} is observed and in most of the spectra the disorder induced D-band feature around 1350 cm^{-1} is not present. Many of the measured CNTs show the three

intense peaks in G-band. These multiple splitting peaks are characteristic of semiconducting SWNTs and the diameter can be estimated from the peak frequencies[16]. The diameter of the SWNTs was found to be 1.6 nm, which is consistent with the result from RBM.

A broad peak at 1450 cm^{-1} was also observed (Figure 3-7a). Although there are no conclusive data about the origin of this feature, two possible explanations are presented here. The first one has to do with CNTs. It has been observed that a similar feature appears in the Raman spectra of SWCNTs when they are not in resonance with the excitation energy of the laser[15]. The fact though that there are no other characteristic spectral features from SWCNTs in the spectrum presented in Figure 3-7a (G-band features) makes this case quite unlikely.

The other possibility is that this signal originates from a carbon amorphous phase[17]. A similar signal had been observed by Rugeiro et.al[17]. In this paper it was shown by means of x-ray measurements that this signal corresponds to a carbon amorphous phase. In the case of the current samples the amorphous carbon might have been deposited on the surface during the growth process, or consists one of the components of the thick nanofibres.

Raman measurements carried out on the substrates that had undergone HF-etching (which eliminated the thick nanofibres) showed the characteristic G-band of SWCNTs. This confirms that the observed thin nanofibres are SWCNTs bundles. Also this finding along with the observations on the air annealed samples (shown above) consist strong evidence that the thick nanofibres are composed by an oxide which contains Si, Ge and possibly C.

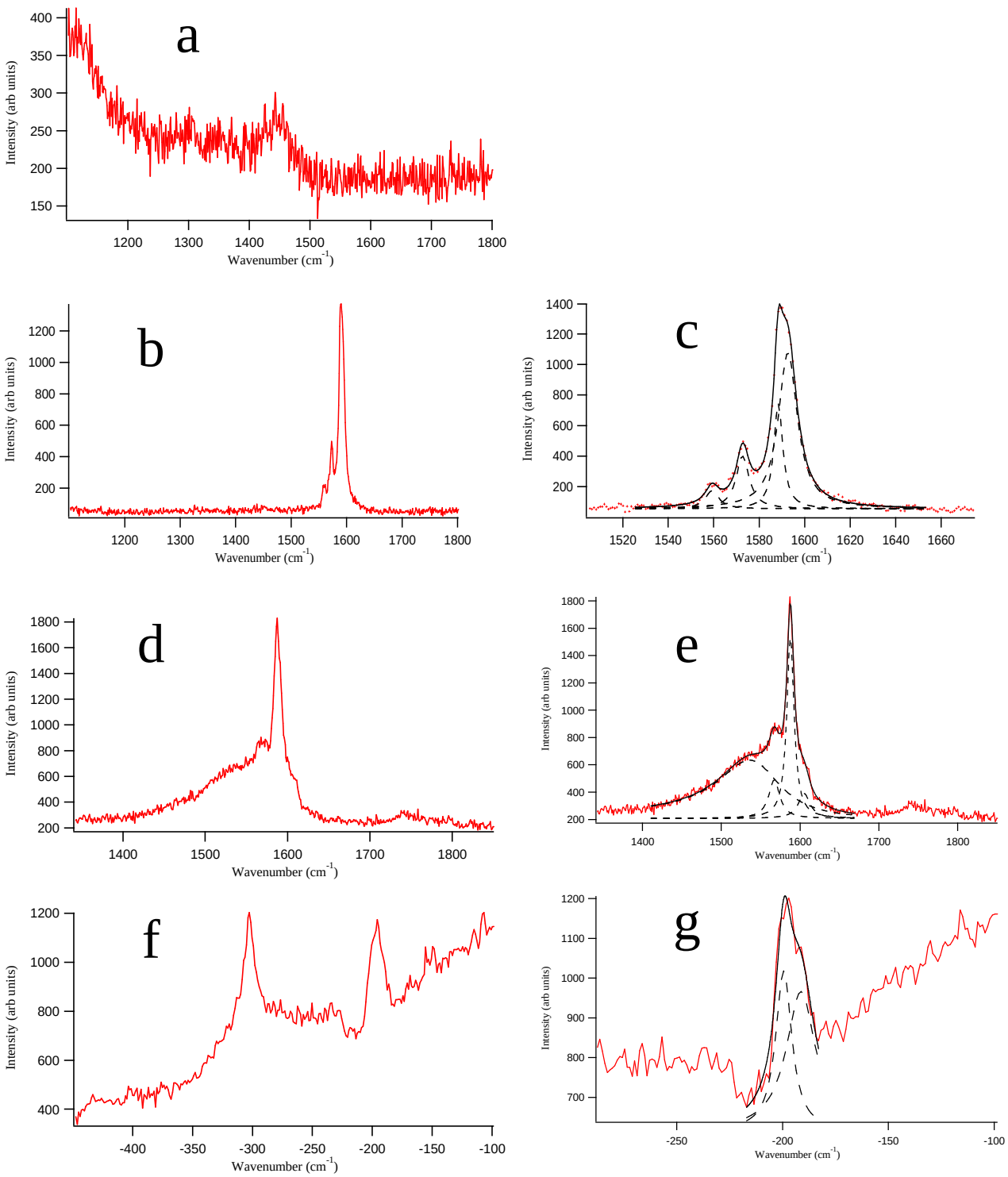

Figure 3-7 Raman spectra of the as-grown fibres on SiGe/Si substrates using 633 nm (1.96 eV) laser excitation. a) Signal possibly originating from Oxide nanofibers. b) G band signal from SWCNT and c) the same signal fitted with 4 Lorentzian curves. d) G band signal from SWCNT at another point of the sample e) the same signal fitted with 3 Lorentzian and 1 BWF curves. f) RBM signal (- 198 cm^{-1}) and Si signal (-300 cm^{-1}) (obtained from the same point of the sample as b)). g) the RBM signal fitted with 2 Lorentzian curves.)

3.3.7 Summary of growth experiments on SiGe substrates and conclusions

The main experimental findings concerning the CNT growth were summarised below in Table 3-1. It can be seen that C ion implantation and $HF+H_2O_2$ pre-treatment are essential steps for the growth of CNTs on the nano-structured SiGe substrates. The same steps are necessary for the growth of the oxide fibres (thick nanofibres). However in the latter case growth can take place without the need of any carbon feedstock (sample 3 in Table 3-1).

Table 3-1 Summary of CNT growth

Sample	Doping	Pre-treatment	Growth gas	CNT growth	Thick nanofibres
1	C ion implantation	$HF+H_2O_2$	CH_4, H_2	Yes	Yes
2	C ion implantation	HF	CH_4, H_2	Yes, reduced density	Yes
3	C ion implantation	$HF+H_2O_2$	Ar, H_2	No	Yes
4	No	$HF+H_2O_2$	CH_4, H_2	No	No
5	No	HF	CH_4, H_2	No	No

3.4 Growth on Si substrates with Ge dots

Growth was also achieved without the use of metal catalyst on Si substrates with Ge dots. As it will be shown below growth of CNTs took place on carbon ion implanted surfaces as well as on non carbon ion implanted surfaces of such substrates.

3.4.1 Substrate preparation and growth

The method starts with Si (001) wafers on which Ge dots are formed by CVD on top of a thin Si buffer layer. Next, parts of each wafer were implanted with carbon ions (energy 30 keV, dose 3×10^{16} cm^{-2}). The wafers were cut into 5 × 7 mm pieces and dipped in buffered HF solution to remove the native oxide. Chemical oxidation was performed using a 30% hydrogen peroxide solution at room temperature for 20 min followed by immediate drying without water rinse, as GeO_2 is dissolved by water treatment. It was expected this to produce a 0.5 nm-thick oxide on the Si and a 2 nm-thick oxide on the

Ge[18,19]. These substrates were transferred to an atmospheric pressure CVD furnace and annealed at 1000 °C in argon (1000 sccm) and hydrogen (300 sccm) for 10 min. The anneal was immediately followed by CNT growth at 850 °C for 10 min in a mixture of methane (1000 sccm) and hydrogen (300 sccm). It should be noted that energy dispersive X-ray spectroscopy measurements on both the implanted and un-implanted substrates before and after growth show no gross metal contamination.

3.4.2 SEM and TEM measurements

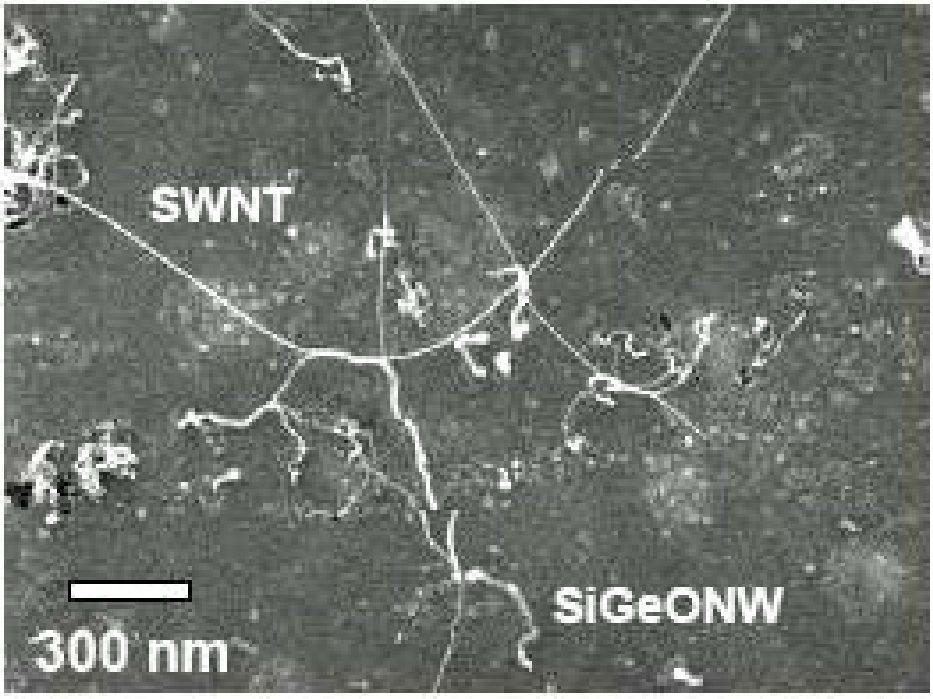

Figure 3-8 A typical field-emission SEM image of as-grown single walled carbon nanotubes (SWNTs) and SiGe oxide nanowires (SiGeONWs**).**

Figure 3-8 shows field-emission scanning electron microscopy (FE-SEM) images of carbon-implanted samples. There are two types of fibers, thick curly fibers which evidence indicates are amorphous SiGe oxide wires and thin straighter fibers which evidence indicates are SWNTs. There is a clear association between the straighter fibers and the curly fibers, i.e. the straighter fibers intersect with curly fibers at many points along their length. However, there are also isolated curly fibers, which do not intersect with the straighter fibers. The curly fibers, which were also observed on CNT growth

from SiGe layers, can be removed using HF vapor treatment, which strongly suggests they are mostly composed of an amorphous SiGe oxide.

The identification of the two types of fibers is supported by transmission electron microscopy (TEM) of fibers, which hang over the edge of the substrate. Figure 3-9(a) shows a TEM image of a straighter fiber, which is consistent with a bundle of SWNTs. Figure 3-9(b) shows a TEM image of the curly fibers and shows that they have a much larger diameter than the straight fibers and that they have an amorphous structure.

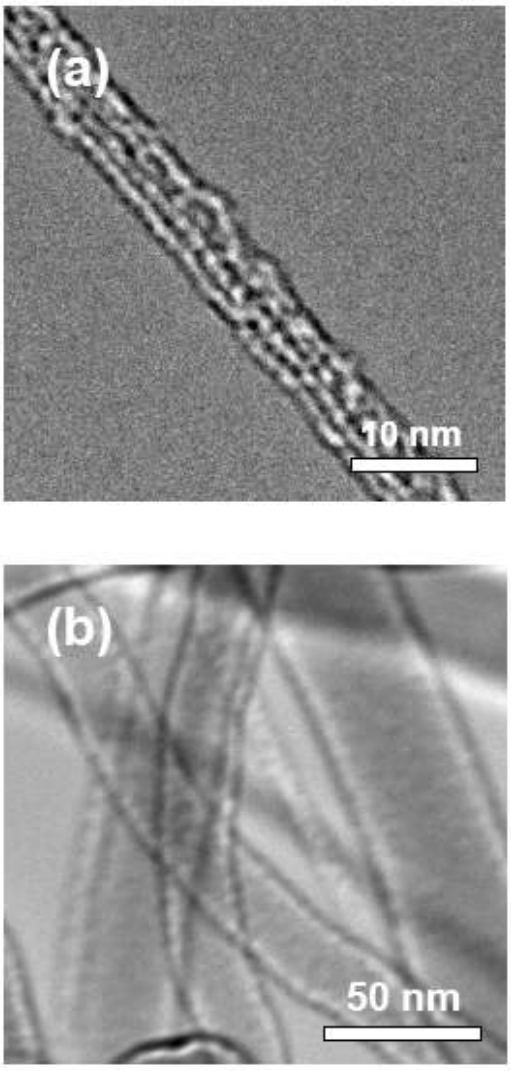

Figure 3-9 High resolution TEM images of the grown nanofibers. (a) A bundle of single walled carbon nanotubes and (b) amorphous oxide nanowires.

From the experiments and discussion so far it is implied that the carbon ion implantation is required for successful growth of CNTs. However, there exist small

fractions of the un-implanted wafer (around 1%, predominantly near the edge of the wafer) in which CNTs are present, as shown in Figure 3-10, and confirmed by Raman spectroscopy. As Figure 3-10 shows, these parts of the un-implanted wafer do not have the expected smooth topography of a Si wafer, but instead contain a large amount of trenches. This trenching was only observed in association with CNT growth on un-implanted substrates, and not at all on carbon ion implanted wafers.

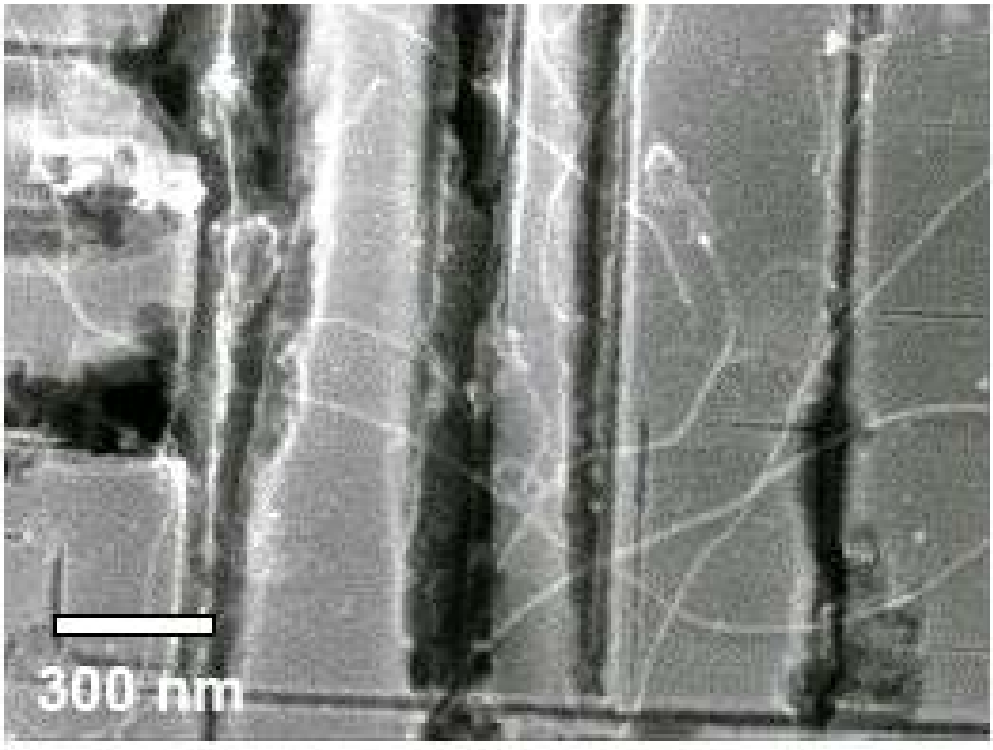

Figure 3-10 Field-emission SEM image of single walled carbon nanotubes on samples prepared without carbon implantation.

In order to understand the different stages of CNT growth, FE-SEM and atomic force microscopy (AFM) studies were carried out on as-grown, post oxidation, post anneal and post growth substrates. The as-grown substrates (Figure 3-11(a)) show Ge dots in the form of cones with diameters in the range 20 to 250 nm and heights in the range 10 to 25 nm. The oxide formation changes the contrast of the dots as observed by FE-SEM (Figure 3-11(b)), however it makes little difference to the morphology of the dots. The anneal occurs at a temperature above the melting point of Ge (938 °C) and the post anneal substrates (Figure 3-11(c)) show considerable changes due to the anneal and

in particular the formation of the curly fibers. In addition to the curly fibers the substrates also show features reminiscent of Ge dots and much smaller nanoparticles. At the end of the growth process (Figure 3-8) there is a clear association between the curly fibers and the CNTs.

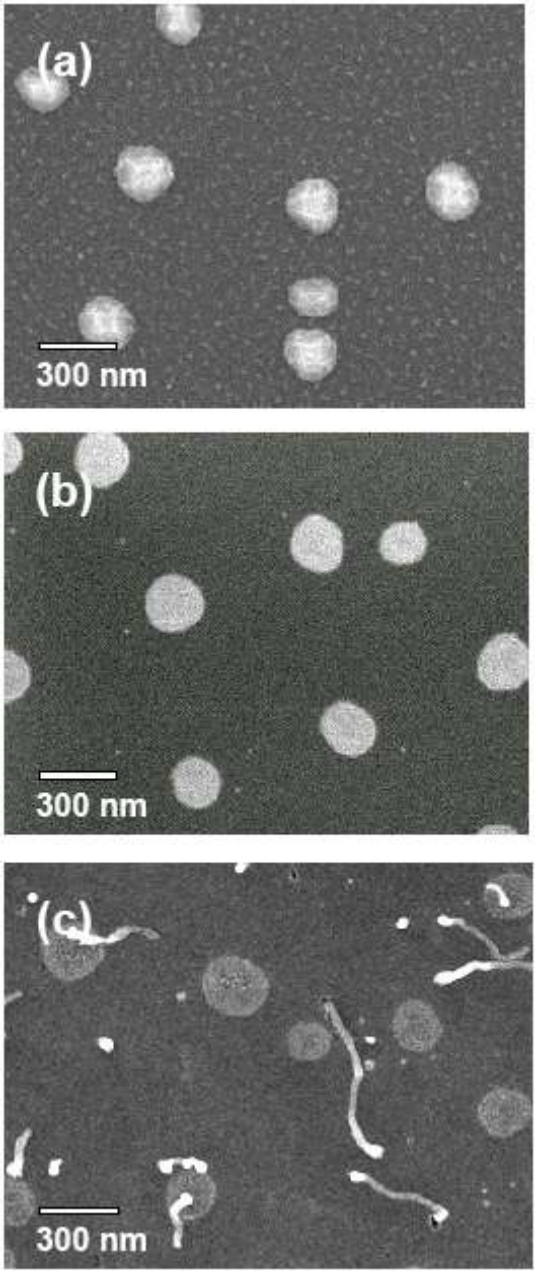

Figure 3-11 Field-emission SEM images of Ge dots corresponding to the following process steps. (a) as-grown Ge dots, (b) after chemical oxidation with hydrogen peroxide, and (c) after argon anneal at 1000 °C

3.4.3 AFM measurments

AFM images of samples (Figure 3-12 (a)) that have been treated with HF vapor to remove

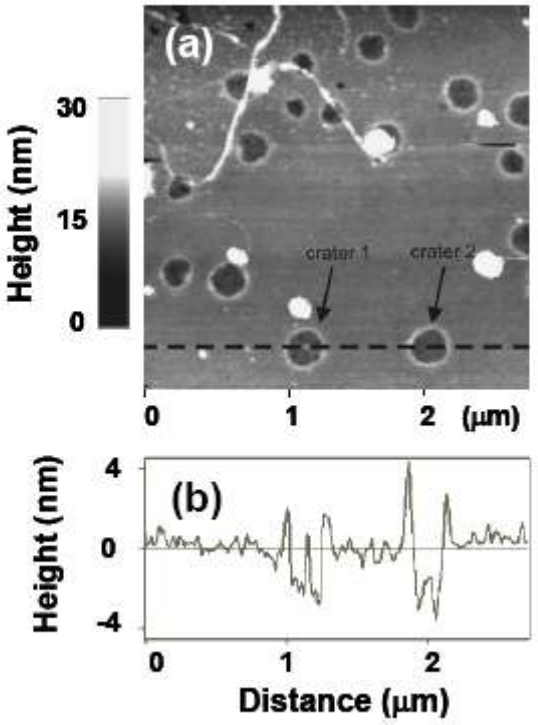

Figure 3-12 (a) AFM image of substrate after nanotube growth and HF vapor etch to remove curly fibers. The image shows single walled carbon nanotubes bundles, crater-like remains of Ge dots and some remaining Ge dots. (b) Topographical section along the dashed line in Fig. 13(a), showing the profile of two of the crater-like features.

the curly fibers confirm that the diameters of the straighter fibers are consistent with bundles of SWNTs. They also show that many of the Ge dots have become crater-like features (Figure 3-12 (b)), with the crater height being approximately 4 nm. The total volume of material present in the walls of these craters is considerably less than that of the as-grown Ge dots. The FE-SEM and AFM images both show that within some of these craters are nanoparticles. Whilst these nanoparticles vary in size at least some have dimensions in the few nanometer range. For instance, the nanoparticle shown in the

middle of the first crater shown in Figure 3-12 (b) is 3.4 nm high; its lateral dimension cannot be determined due to limitations of the AFM tip size. As expected only CNTs were observed on substrates that have been all the way through the process. Whilst it was attempted to determine where the CNTs start growing on the substrate it was not possible to do so due to the fact that the CNTs in general are bundled and the length of the bundles means that they intersect with many features on the surface (Figure 3-8 and Figure 3-12).

3.4.4 Raman measurements

The existence of SWNTs on the substrates is unambiguously determined by performing micro Raman spectroscopy using a He-Ne laser (632.8nm). The Raman spectra (Figure 3-13) clearly show the radial breathing mode (RBM) and G band features expected for SWCNTs[20]. The RBM modes indicate that the diameters of SWCNTs are in the range 1.6 to 2.1 nm[15], which are slightly larger than those on SiGe islands[8]. In the high frequency region, the G-band shows twin peaks at 1590 and 1573 cm^{-1} which are well fitted by Lorentzian functions and can be attributed to semiconducting SWCNTs[16]. Despite considerable effort it was not possible to detect the disorder induced D-band feature[20] at around 1350 cm^{-1}. This indicates that the CNTs produced with this method, have a low defect density and can thus be described as high quality. It was also observed a feature at 2653 cm^{-1} which is attributed to G'-band[20]. This feature does not show the characteristic double peak of double and multi-walled CNTs[21]. In addition, no RBM[22,23] features at energies above 160 cm^{-1} were observed, which would be expected for double walled CNTs due to the small inner nanotubes. Therefore it is believed that the CNTs produced by this process are mostly SWCNTs. The same Raman features are observed on samples which have been HF vapor treated to remove the curly fibers leaving only the straighter fibers, which is clear evidence that these straighter fibers are the SWNTs.

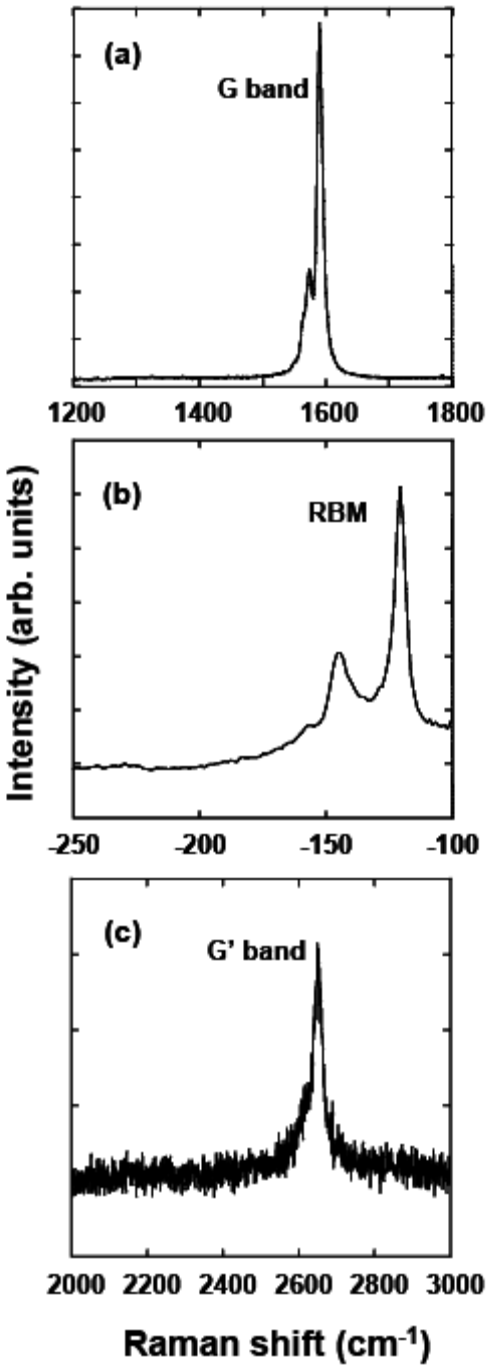

Figure 3-13 Raman spectra of as-grown fibres using 633 nm (1.96 eV) laser excitation. (a) G-band, (b) anti-Stokes spectrum of the radial breathing mode (RBM) of single walled carbon nanotubes, and (c) G'-band.

3.4.5 Discussion

The above observations have led us to form a preliminary hypothesis concerning the mechanism responsible for growth of CNTs from these substrates. However further studies will be required to confirm this. The results suggest that during the anneal, possibly due to the formation of the oxide fibers, the Ge dots decompose to form nanoscale Ge particles, i.e. those observed with AFM. Due to the effects of surface energy[24], these will have a reduced melting temperature compared with bulk Ge and it is hypothesized that they remain liquid at the CNT growth temperature. These nanoscale Ge particles might act as seeds for VLS growth of the CNTs. If this hypothesis is correct then it may be possible to obtain the seeds by another route removing the need for an anneal step and allowing an increase in the density of seeds and CNTs.

The above results show that CNT formation is aided by the carbon ion implantation, but is not essential to CNT growth, as the results in Figure 3-10 demonstrate. It is not clear what the role of the ion implanted carbon is. The implantation of carbon ions clearly alters the processes happening during the anneal step. It may be that it aids the formation of the seeds from which the CNTs grow, either chemically or by the amorphisation of the substrate during ion bombardment. It is possible that the presence of the carbon lowers the melting temperature of any Ge nanoparticles, which are formed during the anneal allowing them to be molten during the growth phase. It is also possible that the carbon directly produces seeds from which CNTs grow and that the Ge plays the role of host to the carbon allowing the formation of these seeds.

The formation of the trenches associated with CNT growth in un-implanted substrates is also not understood. Although considerable effort was made it was not possible to find any literature on the formation of such trenches in Si substrates in the presence of Ge, carbon and hydrogen during CVD of carbon doped SiGe layers.

3.4.6 Conclusions

In conclusion, a new method is presented, which enables the growth of high quality single walled carbon nanotubes (SWNTs) without the need for a metal catalyst using equipment and techniques standard to a silicon foundry. Extensive characterisation is presented of the effect of each stage in the growth process. Using this evidence, it is

proposed that the growth mechanism is vapor-liquid-solid growth with nanoscale Ge seeds. This method will require further development before it could be used in an industrial process. In particular, it will be necessary to increase the uniformity and density of the growth. However, these preliminary studies show good promise and indicate that further efforts to develop this method are likely to be very worthwhile. It has also been shown that it is possible to grow SWNTs from Ge containing substrates without carbon ion implantation.

References:

[1] "Carbon Nanotubes: Synthesis, Structure, Properties and Applications", edited by M. Dresselhaus, G. Dresselhaus, Ph. Avouris (Springer – Verlag, Berlin, 2001).

[2] Ph. Avouris, R. Martel, V. Derycke, J. Appenzeller, "Carbon nanotube transistors and logic circuits", Physica B 323, 6, (2002).

[3] "Infineon Unveils World`s Smallest Nanotube Transistor", http://www.infineon.com

[4] J. A. Misewich, R. Martel, Ph. Avouris, J. C. Tsang, S. Heinze, J. Tersoff, "Electrically Induced Optical Emission from a Carbon Nanotube FET", Science 300, 783, (2003).

[5] Nantero, Inc. "Nanotube device structure and methods of fabrication", U.S. Patent, 4 July 2006.

[6] N. Grobert, "Carbon nanotubes becoming clean", Materials Today, 10, 1-2, 28, (2007).

[7] R. J. Bolam, A. J. Gregortisch, "Method for charge enhanced defect breakdown to improve yield and reliability", U.S. Patent 5,804,459, Sep. 8, 1998.

[8] T. Ushino, K. N. Bourdakos, C. H. de Groot, P. Ashburn, M. E. Kiziroglou, G. D. Dilliway, D. C. Smith, "Metal catalyst-free low-temperature carbon nanotube growth on SiGe islands", App. Phys. Lett. 86, 233110, (2005).

[9] T. Ushino, K. N. Bourdakos, C. H. de Groot, P. Ashburn, D. C. Smith, International Patent application

[10] S. Botti, R. Ciardi, M. L. Terranova, S. Piccirillo, V. Sessa, M. Rossi, M. Vittori-Antisari, "Self-assembled carbon nanotubes grown without catalyst from nanosized carbon particles adsorbed on silicon", Appl. Phys. Lett., 80, 1441, (2002).

[11] S. Botti, R. Ciardi, M.L. Terranova, S. Piccirillo, V. Sessa, M. Rossi, "Carbon nanotubes and nanowires grown from spherical carbon nano-particles", Chem. Phys. Lett. 355, 395, (2002).

[12] V. Derycke, R. Martel, M. Radosavljevic´, F. M. Ross, Ph. Avouris, "Catalyst-Free Growth of Ordered Single-Walled Carbon Nanotube Networks", *Nano Lett.*, 2, 1043, (2002).

[13] P. Avouris, J. Appenzeller, R. Martel, S. J. Wind, "Carbon Nanotube Electronics", Proc. IEEE, 91, 1772, (2003).

[14] U. Neuwald, A. Feltz, U. Memmert, R. J. Behm, "Chemical oxidation of hydrogen passivated Si(111) surfaces in H_2O_2", J. Appl. Phys. 78, 4131 (1995).

[15] A. Jorio, M. A. Pimenta1, A. G. Souza Filho, R. Saito, G. Dresselhaus, M. S. Dresselhaus, "Characterizing carbon nanotube samples with resonance Raman scattering", New J. Phys. 5, 139.1, (2003).

[16] S. D. M. Brown, A. Jorio, P. Corio, M. S. Dresselhaus, G. Dresselhaus, R. Saito, K. Kneipp, "Origin of the Breit-Wigner-Fano lineshape of the tangential G-band feature of metallic carbon nanotubes", Phys. Rev. B, 63, 155414, (2001).

[17] M. N. Regueiro, L. Abello, G. Lucazeau, J-L. Hodeau, "Diamond from fullerenes: Evidence from Raman measurements", Phys. Rev. B 46, 9903 (1992).

[18] U. Neuwald, A. Feltz, U. Memmert, R. J. Behm, " Chemical oxidation of hydrogen passivated Si(111) surfaces in H_2O_2", J. Appl. Phys. 78, 4131 (1995).

[19] T. Akane, J. Tanaka, H. Okumura, S. Matsumoto, " Preparation of high-quality Ge substrate for MBE", Appl. Surf. Sci. 108, 303 (1997).

[20] M. S. Dresselhaus, G. Dresselhaus, R. Saito, and A. Jorio, "Raman spectroscopy of carbon nanotubes", Phys. Rep. 409, 47 (2005).

[21] R. Pfeiffer, H. Kuzmany, F. Simon, S. N. Bokova, E. Obraztsova, "Resonance Raman scattering from phonon overtones in double-wall carbon nanotubes", Phys. Rev. B 71, 155409 (2005).

[22] A. Rahmani, J. L. Sauvajol, J. Cambedouzou, C. Benoit, "Raman-active modes in finite and infinite double-walled carbon nanotubes", Phys. Rev. B 71, 125402 (2005).

[23] L. J. Ci, Z. P. Zhou, X. Q. Yan, D. F. Liu, H. J. Yuan, L. Song, Y. Gao, J. X. Wang, L. F. Liu, W. Y. Zhou, G. Wang, S. S. Xie, P. H. Tan, "Resonant Raman scattering of double wall carbon nanotubes prepared by chemical vapor deposition method", J. Appl. Phys. 94, 5715 (2003).

[24] A. R. Harutyunyan, T. Tokune, and E. Mora, "Liquid as a required catalyst phase for carbon single-walled nanotube growth", Appl. Phys. Lett. 87, 51919 (2005).

Chapter 4 Utilization of Single Walled Carbon Nanotubes as high resolution probes in Atomic Force Microscopy

In the following chapter the work that was carried out for the fabrication of Atomic Force Microscopy (AFM) tips with Single Walled Carbon Nanotubes (SWCNT) will be presented. Initially the reasons that prevent conventional AFM tips from achieving high resolution will be discussed and the fact that SWCNTs AFM tips have the potentional of overcoming those obstacles will be shown. The results of two methods of growth of SWCNTs AFM tips will be presented and the advantages and drawbacks of each method will be discussed. The need of further engineering of the SWCNTs AFM tips as a consequence of their mechanical properties will be shown as well as the limitations and possibilities of those tips. Finally the application of the SWCNTs AFM tips in high resolution imaging of the surfaces of mesoporous materials which led to a publication[1] will be exhibited.

4.1 Introduction

Since its invention in the mid eighties[5] AFM has played an important role in the exploration and characterisation of surfaces and nanostructures. It is a unique non destructive technique for imaging bio – molecules, nanoparticles, surface features with high resolution, little sample preparation, and at low cost. However the precision of this imaging is limited due to the geometrical shape and the size of its tip. SWCNTs due to their shape, size and mechanical properties have a great potential as AFM probes. SWCNTs AFM tips can achieve ultra high resolution and minimum distortion of the image of the probed features. Furthermore, due to their elastic properties they are unique in imaging soft and delicate structures without damaging them. Their high aspect ratio allows them to image deep features on a surface a process that is not possible with the conventional AFM tips and which is very important in front end silicon electronics[20]. So far they have been exploited in imaging biomolecules with high resolution[2], as

conductive nanoprobes[3], as functionalised probes in Chemical Force Microscopy[25], to mention some of their spectacular applications. They are one of the first nanotechnology products to be commercialised and can be purchased from several AFM firms[4].

4.2 Tip convolution error

The main application that AFM was meant to fulfil in the early years of its invention[5] was the imaging with atomic resolution of atomically flat surfaces[6]. In this process only the very end point of the AFM tip interacts with the surface and in the case that this tip is atomically sharp, no matter how irregular the rest of the tip is the acquired images will give a faithful representation of the surface[7]. Furthermore, by using proper techniques such as Frequency Modulation (FM) AFM, that reduces the tip wearing and improves the signal to noise ratio, it was made possible to achieve subatomic resolution[8,9]. It was also soon realised that AFM could be used to image mesoscopic features. Nanoscale features like biological molecules, corrugated surfaces and semiconductor devices could be imaged without additional preparation and without being destroyed by the imaging process as in the case of Scanning Electron Microscopy (SEM). However, it was also soon understood that the finite size and shape of the tip was posing a considerable obstacle in the correct imaging of nanoscale objects and in the acquisition of precise quantitative information from those images.

In reality the image of an object acquired through the means of AFM contains information for both the object as well as the AFM tip. To make that more clear, one could consider the extreme case of a sharp feature imaged by an AFM tip of pyramidal shape with size considerably bigger than that of the feature as (Figure 4–1).In this case the acquired image resembles merely the tip and much less the object (reverse imaging)[10].

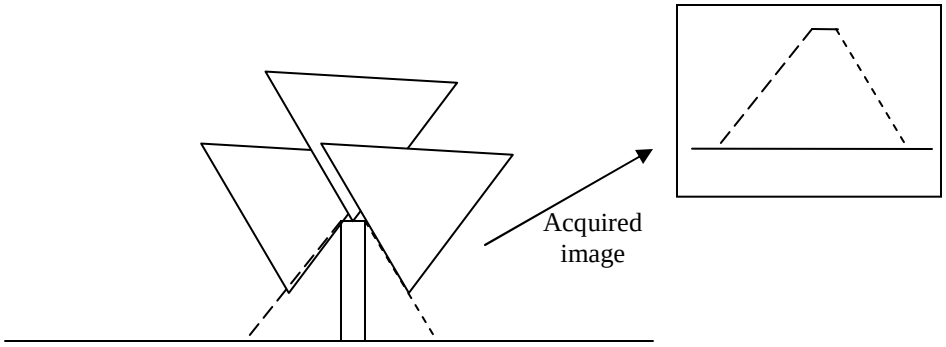

Figure 4-1 Principle of reverse imaging in AFM.

In the general case, the acquired image is a convolution of the sample and tip shapes and in most of the cases the sample dominates the image[11]. The situation is obviously reversed when the size of the sample is smaller than that of the tip. If the shape of the tip is known then the shape of the sample can be reconstructed from the acquired image by a deconvolution procedure as it will be shown below. A more thorough analysis than the summarised one presented below can be found in references [12], [13]).

If the slope of the surface of the sample is high then the AFM tip "touches" (touches here has the meaning of interacts) the sample at a different point than the recorded tip position (Figure 4-2). The acquired image profile is then shifted with the respect to the true profile of the sample and the corners of the image profile are more rounded than those of the true sample. The true sample profile can be reconstructed from the distorted image if the real point of contact (again here "point of contact has the meaning of point of interaction) of the tip and sample surfaces can be calculated from the image surface and the tip shape. This can be done if two quantities are known: i) the lateral distance Δx between the true contact point x and the apparent contact point x' and ii) the corresponding vertical distance Δs.

From Figure 4-2 it can be seen that the tip shape and the sample have the same slope at the true contact point. The image surface at the corresponding apparent point of contact has also the same slope as is shown below.

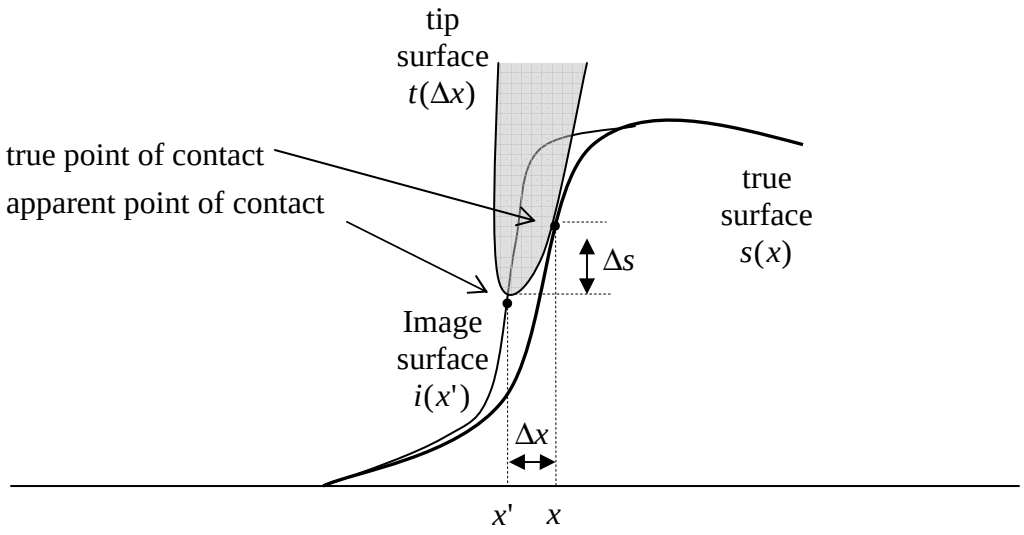

Figure 4-2 AFM tip – sample convolution. The impact of the AFM tip finite size on the imaging of a high aspect ratio shape.

From Figure 4-2 it can be seen that:

$$\frac{dt(\Delta x)}{d\Delta x} = \frac{ds(x)}{dx} \qquad \textbf{(33)}$$

where $t(\Delta x)$ is the surface that describes the tip ($t(\Delta x)$ is a function of Δx only since the tip moves relative to the sample) and $s(x)$ is the true surface of the sample. In Figure 4-2 $i(x')$ is the surface of the image reported by the tip. Equation (33) states that the slopes of the tip and sample surfaces are equal at the point of contact (true contact point). Because movement of the tip will cause change of x', and this will affect the value of Δx the latter can be considered as a function of x': $\Delta x = \Delta x(x')$. By definition holds that: $\Delta x = x - x'$ therefore it can be written that:

$$x = x' + \Delta x(x') \qquad (34)$$

As it has already mentioned above Δs is the vertical distance between the apparent and the true point of contact therefore

$$s(x) = i(x') + \Delta s(x') \qquad (35)$$

It can easily be seen from Figure 4-2 that:

$$\Delta s(x') = t[\Delta x(x')] \qquad (36)$$

By differentiating equation (34) it turns out:

$$\frac{dx}{dx'} = 1 + \frac{d\Delta x(x')}{dx'} \qquad (37)$$

From equations (33), (35), (36) and (37) comes out:

$$\frac{di(x')}{dx'} = \frac{ds(x)}{dx}\frac{dx}{dx'} - \frac{dt(\Delta x)}{d\Delta x}\frac{d\Delta x(x')}{dx'} = \frac{ds(x)}{dx}\left[\frac{dx}{dx'} - \frac{d\Delta x(x')}{dx'}\right] = \frac{ds(x)}{dx} \qquad (38)$$

Equation (38) states that the slope of the image and the true sample surface at the apparent and true contact points respectively is the same. The quantity $\frac{d\Delta x}{dx'}$ is a measure of the distortion of the acquired image due to the finite size of the tip. The closer its value is to zero the smaller the difference of the image and the true sample. By differentiating the above equation gives:

$$\frac{d\Delta x}{dx'} = \frac{d^2 i / dx'^2}{d^2 t / d\Delta x^2}$$

The latter states that the higher the curvature of the tip the smaller the distortion of the acquired image. Therefore an image acquired with a sharp tip is much closer to the true image.

Substituting equation (33) in equation (38) gives:

$$\frac{dt(\Delta x)}{d\Delta x} = \frac{di(x')}{dx'} \qquad (39)$$

If equation (39) is inverted then $\Delta x(x')$ can be found when $t(\Delta x)$ and $i(x')$ are known. Once $\Delta x(x')$ is found it can be substituted in equation (34) in order to find x' as a function of x. Then $x'(x)$ can be used in equation (35) from which the true shape of the sample $s(x)$ can be extracted. This procedure can be applied through a Legendre transform[14] as it will be shown below.

The definition of Legendre transform of a function $f(x)$ is as follows: it is the intercept on the y-axis of the line tangent of that function at x:

$$L[f(x)] = b(m) = f(x(m)) - mx(m) \qquad (40)$$

In the above equation m is the value of the slope of the function $f(x)$ at x. The value of x can be deduced by inverting the derivative of $f(x)$:

$$m = \frac{df(x)}{dx} \qquad (41)$$

The Legendre transform $b(m)$ of the function $f(x)$ can be considered as an equivalent representation of the $f(x)$ curve. Therefore $f(x)$ can be extracted from $b(m)$ through the means of the inverse Legendre transform:

$$f(x) = m(x)x + b(m(x)) \qquad (42)$$

Here $m(x)$ can be found by the inversion of the derivative of $b(m)$:

$$-x = \frac{db(m)}{dm} \qquad (43)$$

The Legedre transform of $t(\Delta x)$, $i(x')$ and $s(x)$ are related as it can be seen from Figure 4-3 by the equation:

$$L[s(x)] = L[i(x')] + L[t(\Delta x)] \qquad (44)$$

According to the above equation the Legendre transform of the true sample is the sum of the Legendre transforms of the tip and the image surfaces. Therefore by finding the reverse Legendre transform of equation (44) one can get extract the true surface of the sample.

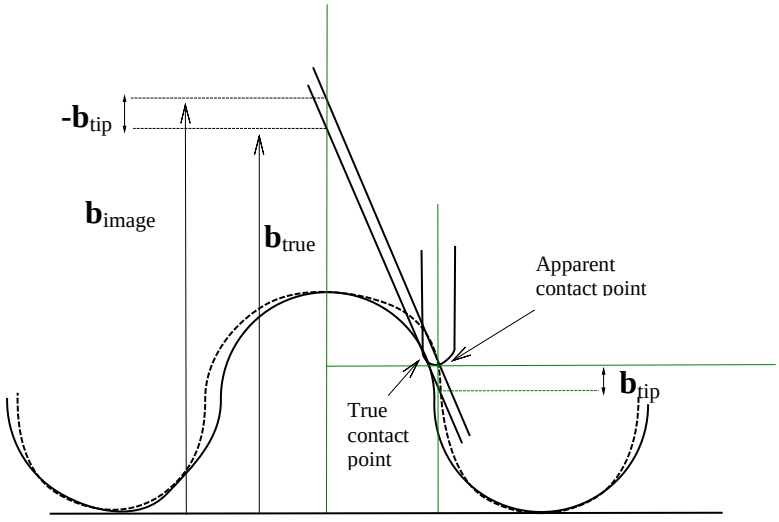

Figure 4-3 The Legendre transforms of the true, image and tip surfaces are related as $L[s(x)] = L[i(x')] + L[t(\Delta x)]$ (in the figure $L[s(x)] = \mathbf{b}_{true}$, $L[i(x')] = \mathbf{b}_{image}$, $L[t(\Delta x)] = \mathbf{b}_{tip}$). After 12.

The true surface however is not always possible to be reconstructed from the acquired image and the tip shape[12]. This is true when the curvature of the sample exceeds the one of the tip (Figure 4-4). In this case there would be regions of the sample that the tip touches two points simultaneously. For those regions it is not possible to calculate Δx and Δs therefore the previous method cannot be applied. Only a sharper tip can resolve regions as those.

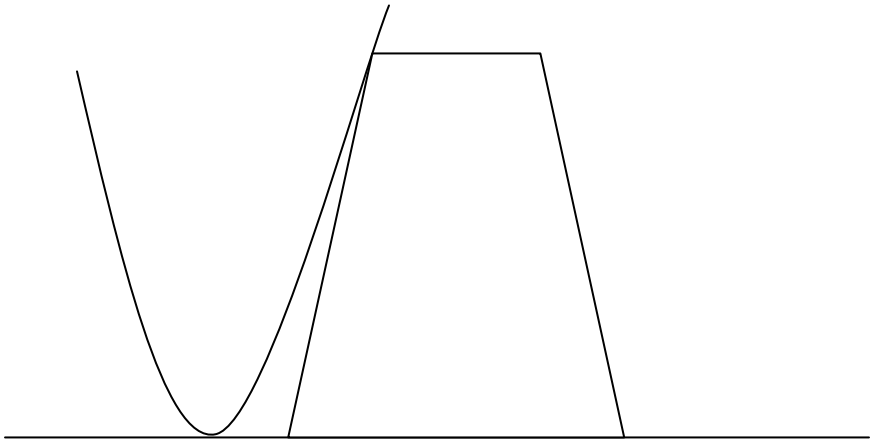

Figure 4-4 In the case of double contact the acquired image does not contain information about the region between these contact points. After 12

Furthermore the application of the reconstruction method requires the knowledge of the precise tip shape. This can be done by using scanning electron microscopy (SEM) or transmission electron microscopy (TEM) imaging of the tip. It is also possible to use specific samples of well known geometry to reconstruct the tip shape from their AFM images[10]. However, what is really needed is the shape of the tip at the time of the AFM scan. This is not always possible as the tip very often wears out during an AFM scan and therefore the image of the tip which is acquired before or after the AFM scan is only an approximation of the real tip shape during the AFM scan.

4.3 The Ideal Tip

The convolution error is in fact due to the limited resolution of the conventional AFM when scanning surfaces with mesoscopic features such us biomolecules (DNA, ptoteins, e.t.c) and not atomically flat surfaces. This is due to their size and shape as it was explained above (section 2.). The conventional tips have large radius of curvature (5

– 10 nm for Si tips) in comparison with the mesoscopic features they have to image. They usually have conical shape with cone angles of 10^o – 30^o. Although subnanometer resolution has been reported in some cases of AFM imaging of biomolecules[15,16] by using conventional tips this has not been done in a controllable manner. The achieved resolution, which was smaller than the radius of curvature of the tip, was probably due to nano – protrusions at the end of tip. However, those features were not fabricated deliberately but they were a form of side effect of the fabrication process. Therefore one has to rely on luck in order to pick a proper tip. An effort in improving the AFM resolution was made by fabricating Si sharp tips by means of chemical etching or by using focus ion beam etching. Both of these methods are very expensive and the fabricated tips although sharp are also very brittle.

Another kind of technique uses the electron beam of an SEM to deposit a carbon tip[17] at the end of a commercial tip. The main achievement of this technique is to increase the aspect ratio and durability of the tip but the achieved radius of curvature is rather large (30 nm).

The above discussion demonstrates that the ideal AFM tip should have high aspect ratio with 0^o cone angle, with a radius of curvature as small as possible (and in this case "as small as possible" means less than 5 nm and ideally subnanometer), exhibit mechanical and chemical robustness so that its structure does not undergo alterations during the scans in air or fluid environments. All of the above features are among the unique properties of carbon nanotubes making them one of the most promising materials for substantially improving AFM imaging.

4.4 Current status and achievements of the field of Carbon Nanotubes AFM tips

The fabrication of the first cnt tip was reported around ten years ago[18]. Since then new methods for their fabrication have been developed and are described further below. Some of them have progressed towards the mass production of cnt – tips[19,20] which is going to drop their price considerably and increase their availability. However, since no

growth technique that can yield nanotubes of specific diameter and chirality has been developed so far, the control on the type of cnt tips that those methods produce is still low.

In the terms of resolution and imaging there are major achievements mainly in the field of biological systems. It must be mentioned here that carbon nanotube tips have an additional strong advantage in the imaging of such kind of systems. Smaller adhesive forces have been observed[24] with cnt tips which are about 2 – 5 times smaller than those that have been measured with relatively sharp Si tips.. This is probably due to two reasons, the one being the smaller tip radius and the other the lower surface energy. Both of them are smaller when compared with the ones of Si. The lower adhesion forces make possible the use of cantilever with smaller spring constant in tapping mode reliably without the need to apply large driving amplitudes. This can result in a considerable reduction of the sample deformation which is extremely important in the case of soft samples such as the biomolecules.

By using carbon nanotube tips it was made possible to image a series of protein molecules as GroES[21], IgG and IgM antibody proteins[22,23], the amyloid proteins[24] Aβ40 and Aβ42 which is related to Alzheimer's disease with resolution similar to that of cryogenic electron microscopy (EM). Apart from the advantage of the simplicity of sample preparation with respect to the cryogenic EM, imaging with cnt – tips enables scanning without sample fixation on the substrate which opens up the prospect of in – vitro imaging[22]. Also high resolution imaging of molecules in solutions where the ionic concentration can be well defined is possible with the cnt – tips, while only dried samples can be imaged with cryogenic EM.

Furthermore the well defined chemistry of carbon nanotubes allows functionalisation of cnt – tip at its very end by a few molecules and in some cases by only one. With such kind of tips, chemical force microscopy (CFM) can be performed, which enables the probing of the chemistry of surfaces in a molecular level[21,22,25].

4.5 Fabrication of Carbon Nanotube AFM tips

Below the various methods of fabrication of carbon nanotube AFM tips are described emphasising the ones that were used in the current project.

4.5.1 Manual assembly of carbon nanotube AFM tips

In this approach a multi walled carbon nanotube (MWNT) is attached manually at a conventional AFM tip. It is the method with which the first ever carbon nanotube AFM tip was fabricated[18]. In this technique micromanipulators are used to control the position of a commercial AFM tip and the nanotubes. Both of them are observed through an optical microscope under dark field illumination and with a magnification of 500 – 1000 x. MWNTs have been attached on an adhesive tape. First the tip will be coated with some adhesive by simply pressing it on the above mentioned adhesive tape. Then the tip is pressed on a MWNTs and the latter is stuck on it. Micromanipulators are used to correct the position of the tube in such a way that it is parallel with the tip. Further process to stabilise nanotube is applied like electrical etching which is going to be presented further below.

4.5.2 Surface Growth of Carbon Nanotube AFM tips

This method[26] of fabrication is based on the fact that carbon nanotubes grow in such a way that minimizes their potential energy due to strain and surface interactions with the substrate. It is one of the methods that have been used in the current project.

Carbon nanotubes usually prefer to grow along a surface due to van der Waals and chemical interactions[27]. In that way they minimize their potential energy. However when as they grow they reach an edge of the surface then the minimization of energy again will determine whether they will bend in order to stay on the substrate or they will grow out of the edge (Figure 4-5a). There are two quantities that must be taken into account: one is the cohesive energy of the nanotube with the surface E_c and the other is the energy due to the strain on the nanotube E_{st} as it bends when it reaches the edge of the surface in order to grow parallel to it (Figure 4-5b). Those energies can be determined by the following equations[28,29]:

$$E_c = -2\pi R \frac{\theta}{360^o} K \qquad (45)$$

(where R is the radii of curvature of the nanotube bent, and θ is the corresponding angle of the bent (Figure 4-5b), K is the cohesive energy per unit length of the nanotube with the substrate)

$$E_{st} = \frac{\pi}{8}\theta_1^{\,2}\,\mathrm{Y}t\frac{r}{L}\left(4r^2 + t^2\right) \qquad (46)$$

(where Y is the Young's modulus, θ_1 the bending angle in radians, t the wall thickness, r the radii of the nanotube, L the length of the part of the nanotube that has been bent). Equation (46) has been derived by continuous mechanics calculations in reference 29 and corresponds to a shell that simulates a SWCNT with the same diameter and bending length. For this reason some quantities in equation (46) as the thickness t, and the Young modulus Y, correspond to this continuous model and might differ from similar quantities of the real nanotube that this model simulates. The comparable quantity[29] of this model and a real nanotube is the stretching modulus $\mathrm{Y}t$ which as it will be shown below is in good agreement with experimental results reported in the literature. The model is valid for relatively small curvatures and does not give information for the buckling and post buckling regime of the nanotubes.

The bending angle can be converted in degrees by the simple formula:

$$\theta_1 = \frac{\theta}{360^o}2\pi \quad (47)$$

where θ_1 is the bending angle in radians and θ is the bending angle in degrees. The bending length can be given as a function of the radii of curvature R and the bending angle θ by:

$$L = \frac{\theta}{360^o}2\pi R \quad (48)$$

By replacing (47) and (48) into (46) yields:

$$E_{st} = \frac{\pi^2}{4}\frac{\theta}{360^o}\mathrm{Y}\,t\frac{r}{R}(4r^2 + t^2) \quad (49)$$

Considering now that the bending of the nanotube will start at a distance d from the edge of the substrate then the radii of the bending curvature can be expressed as a function of this distance and the bending angle θ:

$$R = \frac{d}{1-\cos(\theta)} \quad (50)$$

(a geometrical proof of this expression is given in 4.8 . Appendix I)

Replacing equation (50) in (45) and (49) gives:

$$E_c = -2\pi \frac{d}{1-\cos(\theta)} \frac{\theta}{360^o} K \quad (51)$$

$$E_{st} = \frac{\pi^2}{4} \frac{\theta}{360^o} \mathrm{Y} t \frac{r(1-\cos(\theta))}{d} (4r^2 + t^2) \quad (52)$$

In Table 4-1 are given some values of the sum of the cohesive and strain energies for different values of the bending angle. These results were obtained by considering a [10,10] SWCNT that starts to bend at a distance $d \sim 20\,nm$ from the edge and were calculated by using $K = 3eV/nm$ (value extracted from Figure 3a of reference [30]), $r = 0.7nm$, $t = 0.08nm$, $E = 6.85TPa$. The values of E, t were obtained from reference 29 and as it was mentioned before correspond to a continuous shell that simulates a [10,10] SWCNT. Their product $\mathrm{Y}t = 510\,Pa\ m$ which is the stretching modulus is within the range of the experimental data reported in the literature[29,31].

Figure 4-5 Concept of surface growth

It is obvious from Table 4-1 that if a nanotube grows towards the apex of the tip when it reaches there it is going to protrude out of the tip as the apex curvature is relatively big and the strain energy overwhelms the cohesive energy of the substrate. Furthermore it is believed[26] that some of the nanotubes that grow on the faces of the

pyramidal tips will not protrude at the edges but will continue to grow towards the apex where they will join to form a nanotube rope protruding out of the apex.

$\theta(^o)$	$E_{st}(J)$	$E_c(J)$	$E_{st}+E_c(J)$
30	6.24642E-18	-6.24897E-18	-2.55113E-21
60	2.88397E-17	-5.41387E-18	2.34259E-17

Table 4-1 Balance of cohesive and strain energies of a SWCNT for different angles and radii of curvature.

Growth of carbon nanotubes has been achieved on the top of silicon AFM tips with the means of Chemical Vapour Deposition (CVD). The procedure for growth is as follows: The tips are dip coated for about 1 min in a catalyst solution (5mg of catalyst in 5ml CH_3OH). The catalyst powder consists of ferric nitrate nonahydrate, molybdenyl acetylacetonate and fumed alumina. After the dip coating the CVD growth takes place in a furnace where the tips were put in batches of five each time.

Two different growth recipes have been used. In **recipe A** the tips were ramped to 800 ^oC in 30 min in 0.6 SLM[iv] Ar and 0.4 SLM H_2 atmosphere. Then they were kept at this temperature for another 10 – 20 min in order to allow stabilisation of the temperature. Growth took place for 3 min in 0.6 SLM Ar, 0.4 SLM H_2, 2 SCCM[v] C_2H_4. After this the tips were left to cool down in 1 SLM Ar for about 80 min. In **recipe B** the tips were ramped to 900 ^oC in 30 min in 1.12 SLM Ar and 0.3 SLM H_2 and were kept for 10 – 20 min in order to allow stabilisation of the temperature. Then growth took place for 3 min in 0.3 SLM H_2, 12.5 SCCM C_2H_4 and 1SLM H_2. After that the samples were let to cool down in 1.42 SLM Ar for about 80 min.

Both of the recipes were found to yield nanotube growth on the tips (Figure 4-6) although there were a number of batches in whic***)*** no growth was observed at all. A crucial parameter of the whole growth process was found to be the quality of the catalyst. Fresh catalyst (fresh here means that it was used within one or two weeks after its container was opened for first time) gave rise to relatively good growth. Also another important parameter appeared to be the time between the dip coating and the CVD

[iv] Standard Litre per Minute
[v] Standard Cubic Centimetre per Minute

growth. The batches on to which the CVD process was applied within the same day that they had been dip coated gave higher percentage of tips with nanotubes on their surface. It is possible that atmospheric moisture deactivates the catalyst and therefore the longer the catalyst is exposed to the air the higher the probability not to yield any growth. In each batch of tips the growth was not homogeneous as there were tips with vast growth and others with none. This probably has to do with the statistical character of the dip coating process. Due to the mesoscopic size of the tip surface relatively important variations are expected on the number of the catalyst particles that have been attached on it and the tips with low catalyst density gave poor or no growth. Other conditions such as catalyst aggregation might have played some role as it reduces the catalyst active surface and therefore makes the catalyst particles less effective.

The CVD growth parameters described above for recipes A and B were found to be the minimum ones for obtaining growth on the tips. Variations towards reducing the carbon feedstock or the growth time resulted in no growth or extremely low percentage of tips with carbon nanotubes on their surface. The minimum growth parameters were preferred because they have higher probability to give rise to small diameter ropes of SWCNTs or even individual SWCNTs. Furthermore the minimum parameters are less likely to give long nanotubes protruding from the tip apex which might result in their bending and the formation of loops (Figure 4-6c,d) which are more difficult to etch electrically and convert them into useful probes. Additionally high rate of carbon feedstock might result in saturation of the catalyst particles with amorphous carbon which has as a consequence their deactivation. The growth temperatures of recipes A and B were the optimum ones for temperatures within ± 50 ^{o}C from the given ones above practically no growth was observed.

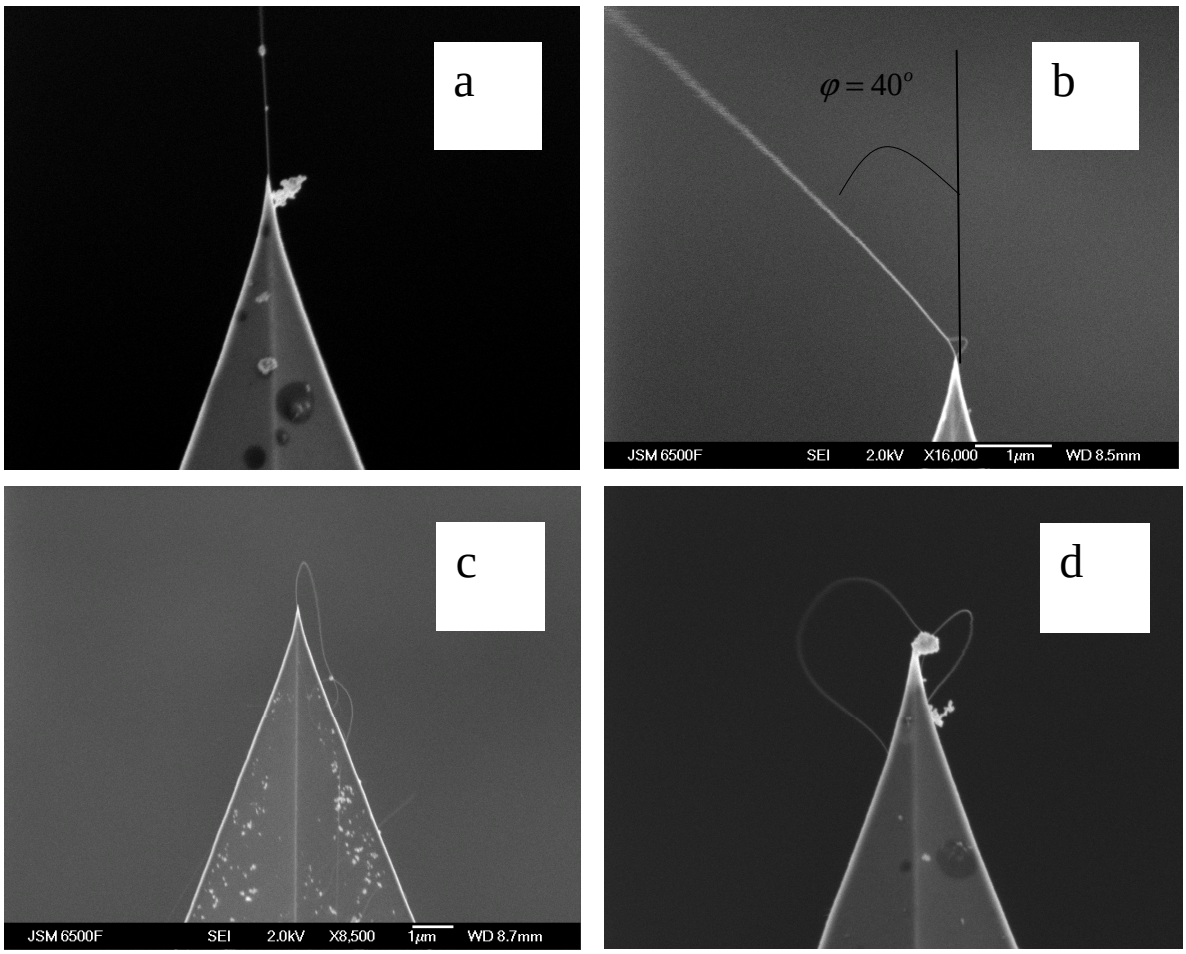

Figure 4-6 SEM images of carbon nanotubes on the top of AFM tips. **a**) a vertical grown tube on the tip. **b**) a bundle of probably two ultra long tubes **c**) and d) nanotubes which have folded back

An average of about 20% of the tips that went through the CVD process had nanotubes protruding out of their apex (Figure 4-6). Although the SEM cannot be used for precise measurement of the nanotube diameter a rough evaluation can be made from the obtained images. In most of the cases the protruding nanotube had a diameter more than 5 nm which is the resolution limit of the instrument. Not all of these tips had the protruding nanotubes aligned along the pyramid axis but some of them had grown at an angle (Figure 4-6b) with it or had folded back to the tip forming a loop (Figure 4-6c). In the first case the angle that the nanotube forms with pyramid axis (angle φ in Figure 4-6b) affects the imaging capabilities as it gives rise to big lateral forces on the nanotube and therefore to distorted images as will be explained below[32,33]. In the second case the electrical etching might break the loop producing thus a useful probe.

All of the tips that have a nanotube (or a nanotube rope) at their apex have to be etched electrically in order to reduce the length of the nanotube and thus to minimise its thermal vibrations which are a major source of noise. An image of a nanotube tip that has been electrically etched is shown in Figure 4-7.

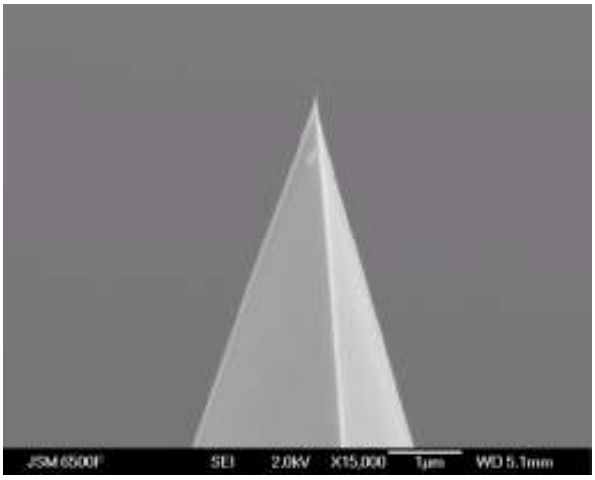

Figure 4-7 Nanotube tip after being electrically etched.

The overall performance of the surface growth is relatively low. The 20% of the tips with a nanotube at their apex is further reduced due to tips with a nanotube at a relatively big angle with the pyramid axis and mainly due to the electrical etching which some times might deplete the tip apex from the nanotube. The tips can be re –used[23,26] by oxidising them at 500 ^{o}C and then applying the whole growth procedure (apart from the dip coating stage). However the probability to achieve growth of nanotubes at their apex drops considerably (there were batches of recycled tips that after growth no nanotubes were observed). This is probably due to contamination of the catalyst by amorphous carbon (that the oxidation process can only partially remove) and absorption of moisture.

4.5.3 Pick – up Substrates

The main disadvantages of the previous two methods are the large diameter of the nanotubes that have to be used in "Manual assembly" (see 4.5.1) in order to be visible through the optical microscope and the low yield of tips with small diameter nanotubes at their apex (and the correct direction) in the "Surface Growth" method (see 4.5.2). Another approach that exploits both CVD growth and mechanical assembly has a potential of a very high yield (almost 100%) of tips with small diameter nanotubes at their apex. This method comprises CVD growth of vertically aligned carbon nanotubes on a flat substrate (pick-up substrate) and then mechanical picking up of a vertically aligned nanotube with the AFM tip[34,35,36,37].

The fabrication of a pick-up substrate is not a trivial process as the reasons and conditions under which carbon nanotubes are grown vertically on the substrate are not yet well understood. It seems that the effect has a statistical character and a number of growth experiments are needed in order to be realised. In our case apart from repeating the same recipe in order to fabricate a pick-up substrate there was need to test also a variety of recipes in order to produce a pick-up substrate with a good distribution of small diameter (nanometer or subnanometer) SWCT.

A number of different catalyst recipes have been tried that can give quite small particles on the substrate (nanometer or subnanometer) and therefore can yield small diameter SWCNT which in the case that they can be exploited as AFM tips will increase further the lateral resolution. For this reason a number of different catalysts and coating techniques were tried such as dip coating of the substrates in ferric nitrate solution in isopropanol, drop casting of a ferritine solution on a piranha-cleaned substrate, or the dip coating of the previous substrates in the ferritine solution, the spin coating or dip coating of piranha-cleaned substrates with or in a solution of bi-metallic (Ru-Fe or Pt-Fe) catalyst.

After the substrates had been coated they were placed in a 1 inch diameter quartz tube furnace. In all of the cases but the one of the ferric nitrate the samples are first annealed in air so as to burn the organic layer that contains the metal particles. Then annealing in Ar takes place, followed by 10 min reduction in H_2 at an elevated temperature and finally doing the growth in CH_4 and H_2 at the same temperature. The recipe differs a bit in the

case of bimetallic catalyst because the reduction of the metal particles has been carried out in advance during the preparation of the solution and MnO promoter is used for the growth. Substrates with carbon nanotubes have been produced with all of the above methods however not always successfully. The reason that the same method does not work every time has probably to do with the moisture in the catalyst, which gets higher with time.

A large number of substrates underwent CVD growth. The ones that had been coated with ferric nitrate gave the highest density of growth. It was assumed that the likelihood of carbon nanotubes growing vertically on the substrate increases with the density of the growth. Because of this assumption the effort for the fabrication of a pick-up substrate was focused on the substrates that had been coated with ferric nitrate. Strong indication that the latter assumption is correct came later from the experimental data that will be presented below. The density of the catalyst solution was optimised in order to give as dense growth of nanotubes as possible and also a good distribution of small diameters. For these reasons the catalyst solution density should have been adequately high in order for the surface density of the catalyst particles to be high on the substrate but also it must be kept low in order to prevent the formation of aggregates. Catalyst aggregates have smaller active surface and therefore keep the growth density low and also give rise to the growth of nanotubes with bigger diameters[37,38,39]. The ferric nitrate solutions were always sonicated in order to break the catalyst aggregates and centrifuged in order to remove the big catalyst particles. The SiO_2/Si substrates were cut from a 5 inches wafer in 1cm x 1cm squares. The thickness of the oxide layer was evaluated from reflectance measurements[40] and was found to be more than 300 μm which is enough in order to prevent diffusion of the catalyst particles in the silicon[41]. The substrates were sonicated in acetone in order to remove organic contaminants then in deionised (DI) water to remove any remains of acetone and non organic particles and then in methanol in order to remove the water. During sonication each substrate was kept in a separate container in order to prevent fracturing of the substrates and contamination of their surfaces. After the sonication the substrates were dried under air spray. Then they were dip coated in the catalyst solution for a short time (from 10 sec to 120 sec) and after that they were rinsed with plenty of hexane in order to rinse off any excess catalyst that is not attached to the

surface. The growth recipe that was followed for these substrates was recipe B as it has been described in section 4.5.2 apart from the growth time which was optimised to give the highest growth density (optimum value was found around 10 min). The substrates were put in the CVD furnace in batches of two.

After the growth the substrates were topographically imaged in ambient conditions with a Multimode Digital Instruments AFM system in tapping mode. The AFM imaging of those substrates apart from giving valuable information about the density of the growth and the diameter distribution can provide also with indirect and quick information about the existence of vertically aligned nanotubes. Sudden distortion of the topography image could be caused by one or more vertically aligned nanotubes that have been attached on the tip during scanning. Whether there is a nanotube attached on the tip or not can be further investigated by observing the force calibration (FC) curves[34].

Figure 4-8a shows the AFM topography image of a substrate that has gone through the growth process and it is a pick up substrate, as will be shown below. In Figure 4-8c a cross section analysis of that image is presented. The diameters of some nanotubes were measured (by measuring their height) and they were found to be in the range of 1 to 4 nm (Figure 4-8c). The density of the growth on this substrate is quite high as can be seen more clearly in Figure 4-8b where an improved contrast image of that substrate is displayed. From this image a rough evaluation of the nanotube density can be done and it is about 50 nanotubes / μm^2. In order to allow comparisons a low density substrate is depicted in Figure 4-9c with a density of about 1 nanotube / μm^2. No nanotubes could be picked up from the low density substrates while they could relatively easily be picked from the high density one depicted in Figure 4-8a. This indicates that the initial assumption that the higher the nanotube density on the substrate the higher the probability that there are vertically aligned nanotubes was correct for the range of densities covered in this study. It has to be clarified though that the higher nanotube density increases only the probability of the occurrence of vertically aligned nanotubes but it does not necessarily mean that any substrate with dense growth is a pick-up one. For example the substrate depicted in Figure 4-9d although the growth is relatively dense it was not possible to pick up any nanotube from this substrate.

The strong statistical character of the fabrication process of a pick up substrate has also to be reported. It was observed that substrates that they were dip coated in the same solution for the same amount of time and had identical parameters of growth exhibited very different growth densities. Three such substrates are shown in Figure 4-8a Figure 4-9a and Figure 4-9b. The first and the last one exhibited vast growth and were found to be pick-up ones while the second exhibited no growth at all. The overall process has very low yield as from the 150 substrates that went through the fabrication process only three became pick-up substrates (yield = 2%). However although it seems difficult to fabricate a pick-up substrate as long as one is produced it can be used to fabricate a very large number of nanotube tips. For example in the fabricated pick-up substrate (Figure 4-8a) it was possible to pick – up one nanotube in every 10 x 10 μm^2. This means that for the 1 x 1 cm^2 substrate about one million nanotubes have been grown vertically (as a very rough evaluation). If it is assumed that the substrate stops being functional when the density of the vertically aligned nanotubes falls to a 30% of its initial value **(,)** about**( )**700,000 nanotube tips could have been fabricated by then. Assuming even a two orders of magnitude error in the above evaluation could mean that a potential number of 7000 nanotube tips could be fabricated from one substrate.

A first indication that a substrate which has gone through the carbon nanotube growth process, might accommodate vertically aligned nanotubes on its surface**(,)** is some broad area image distortions when scanning with the AFM (Figure 4-8a and Figure 4-9b). Those distortions indicate that there is something affecting the tip and forcing it out of its regular mode. The cause of the distortion could be dust particles attached to the tip that might come from the air or the substrate, damage on the tip, or in this case one or more nanotubes that have been picked up. By going into FC mode the tip goes out of the raster scanning and oscillates above the same point of the sample. The z –piezo scans the distance between the sample and the tip and the amplitude of the oscillation is recorded versus the separation distance of the tip and the sample (Figure 4-10a). As it can be seen in Figure 4-10a initially the tip – substrate distance is longer than the range of the attractive forces (van der Waals and capillary forces)[35] between them and the tip oscillates at a constant amplitude. As the separation distance becomes smaller the attractive forces between the tip and the substrate become more important affecting the

elastic constant of the cantilever by making it weaker and thus changing its natural frequency. Because the drive frequency of the cantilever is constant and has been set at the natural frequency (or eigen frequency) of the cantilever the effect of the above change is the decrease of the oscillation amplitude as the resonance has been shifted away from the driving frequency. This effect increases as the sample – tip separation distance becomes shorter and results in a linear decrease of the oscillation amplitude. At a certain point (which is at about 8 nm in Figure 4-10a) the protruding nanotube touches the substrate and starts bending. This exerts a repulsive force on the tip which makes smaller the weakening of the cantilever's elastic constant due to the attractive forces and therefore "pushes" the resonance closer to the driving frequency. This has as an effect, an increase of the oscillation amplitude of the cantilever, as it can be seen in Figure 4-10a. Further bending causes the nanotube to buckle and therefore a decrease in the elastic force that the nanotube exerts on the tip. Once more the increase of the attractive forces will shift the resonant away from the driving frequency with a consequent decrease of the oscillation amplitude[35] (point at about 3.9 nm in Figure 4-10a). The shape of the FC curve as the one depicted in Figure 4-10a can be explained very well by taking into account the elastic properties of carbon nanotubes and for this reason consists a "signature" that a nanotube is attached on the tip.

The final confirmation that a nanotube has been attached on the AFM tip is given from Transmission Electron Microscopy (TEM) images. In Figure 4-10b can be seen a TEM image of an AFM tip with a nanotube attached to it. It is clear from that image that the attached nanotube is a single walled one and that it is very well aligned with the tip. The diameter of the nanotube is 4 nm which is very close with the diameters of nanotubes on the substrate as they were measured by AFM (Figure 4-8c). It can also be seen that the attachment length on the tip is more than 70 nm. Considering that for a 4 nm SWCNT the cohesion energy with silicon is 0.67 eV/Å (see FIG. 3a in reference 30) this means that the cohesive energy between the nanotube and the tip is more than 466 eV which can explain the robust attachment of the nanotube on the tip.

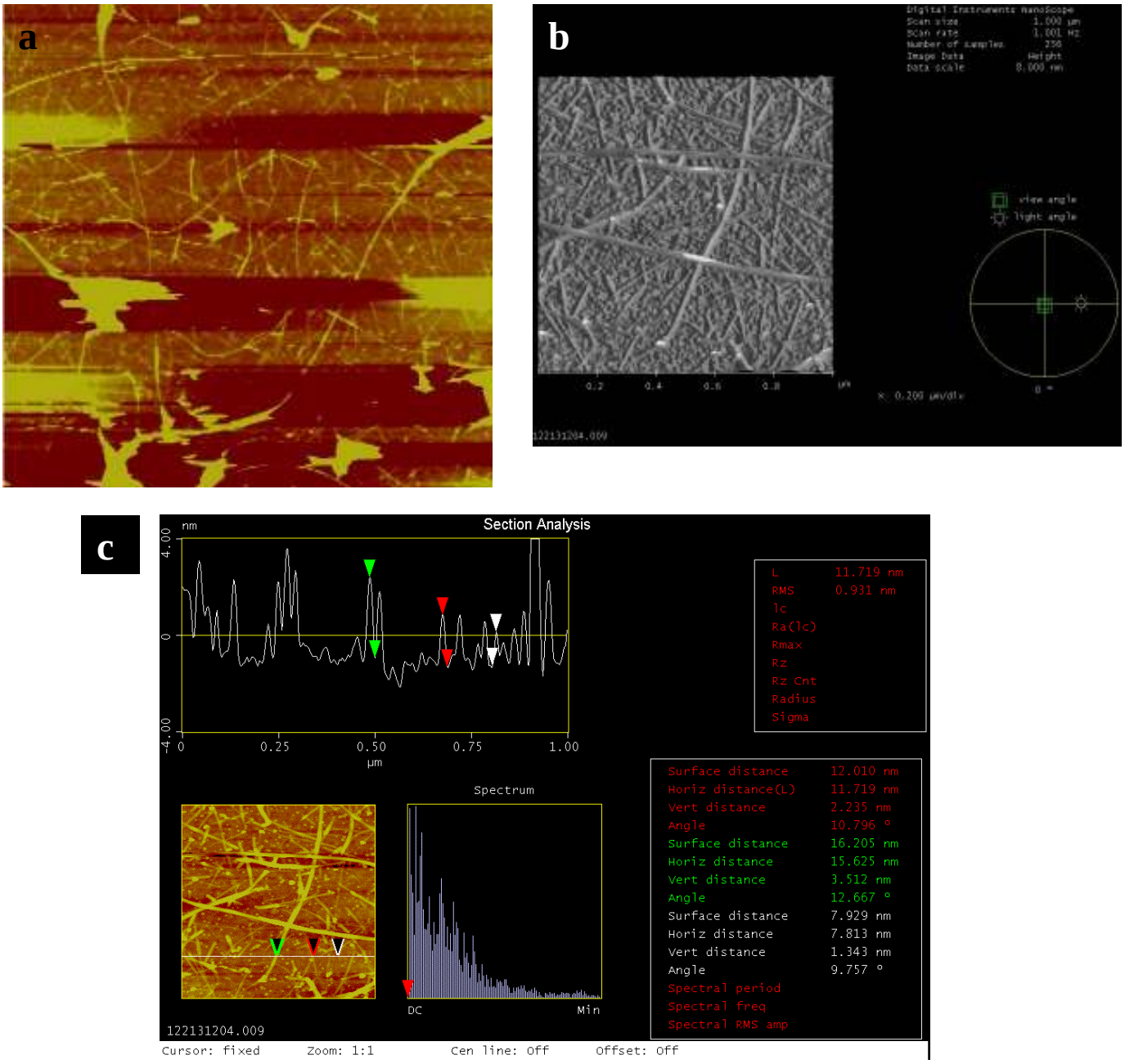

Figure 4-8 Pick-up substrate. a) topography image (5 µm each side) b) Light and angle of adjustments for improved contrast of topography image c) cross section of the image with measurements of nanotube diameters.

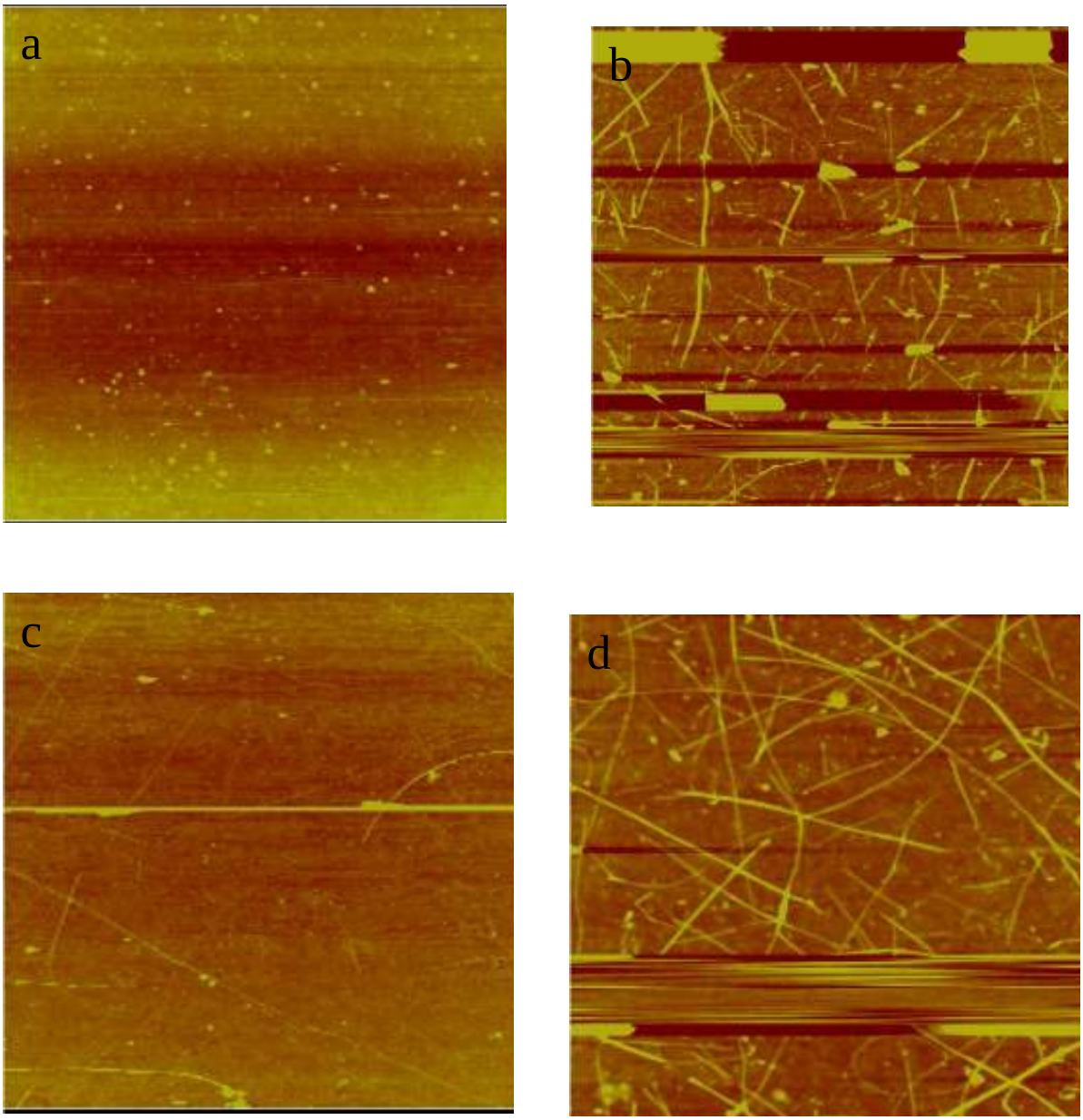

Figure 4-9 a) substrate from the same batch as the pick-up substrates (6 μm scan) **b**) the second pick-up substrate from the same batch (5 μm scan) **c**) a substrate grown with the same process as **a** and **b** but from another batch exhibits relatively sparse growth (5 μm scan) **d**) substrate grown as the previous three with relatively dense growth (2 μm scan)

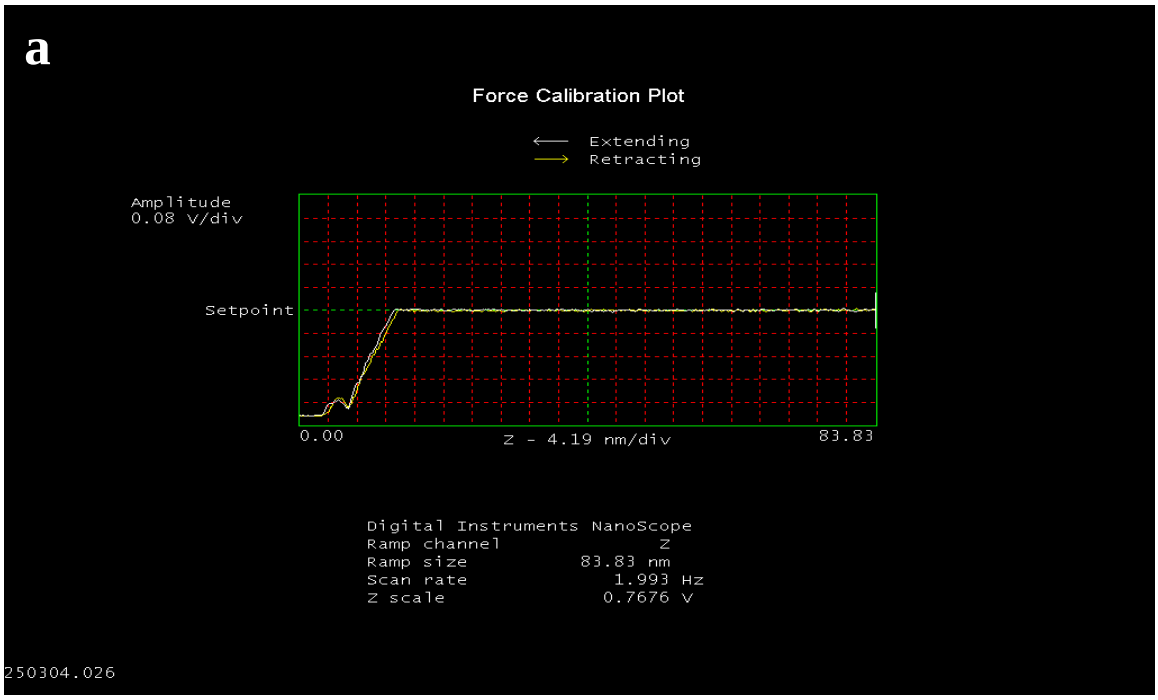

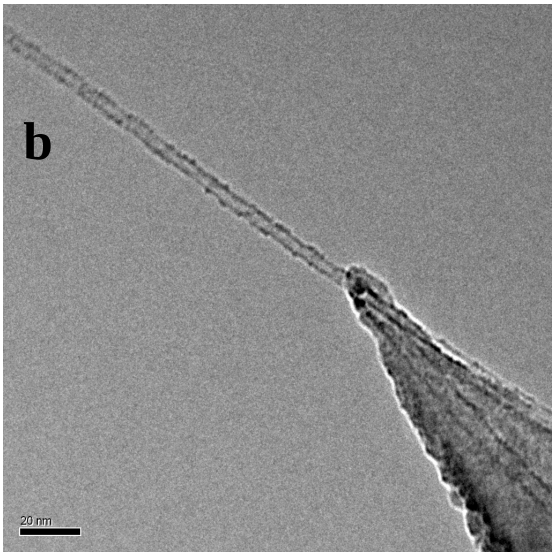

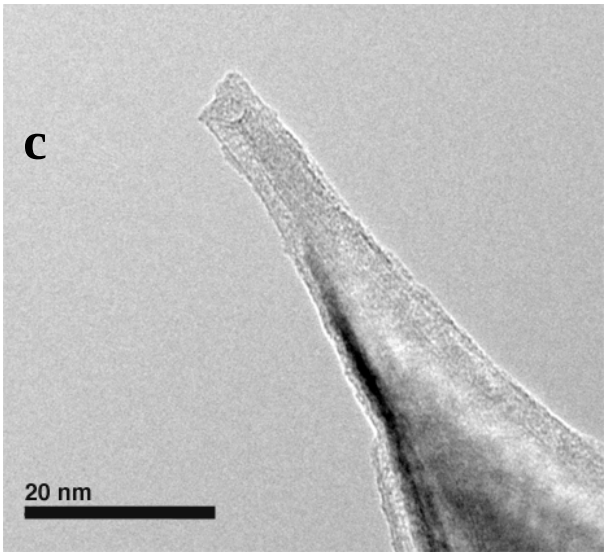

Figure 4-10 a) Force calibration curve of the amplitude of AFM tip with a carbon nanotube attached to its apex picked up from a pick-up substrate. **b**) TEM image of an AFM tip with a nanotube at its apex attached through the pick up method. **c**) TEM image of an AFM tip with a nanotube after being electrically etched.

4.5.4 Electrical etching of CNT AFM tips

In order to make the nanotube tips efficient it is necessary to shorten them. There are two main reasons for this. The first is that the nanotubes vibrate thermally and the amplitude of this vibration is proportional to $\mathbf{l}^{3/2}$ where **l** is the length of the tube[34]. The second is that the force constant for lateral bending of the tube is proportional[34] with $\mathbf{l}^{-3}$. This means that long tube tips introduce noise to the imaging as well as distortion, which is due to their high flexibility. If the nanotube, at the top of the tip, has folded back to form a loop (Figure 4-6c,d) then shortening will make it functional.

The shortening process[1,26,34,37] is carried out by mounting the tube tips on the AFM head and using as a sample a heavily doped silicon substrate. When the tip has approached the substrate a pulse voltage is applied between the tip and the substrate. The produced spark will burn out a part of the nanotube, thus shorten it.

4.6 Application of CNT AFM tips in Imaging of Mesoporous Materials[1]

The manufacturing of new functional metamaterials with improved or even new properties has been enabled through three dimensional nanostructuring of mesoporous materials metals and semiconductors. The method for realising such nanostructuring is by using liquid crystal templates[42,43,44,45]. The nanostructured materials due to their high specific area and mechanical robustness have a wide range of potential applications such as catalysis, batteries, fuel cells, sensors and optical devices. The characterisation of mesoporous materials have been carried out so far through the means of standard techniques such as TEM and small-angle x-ray scattering (SAXS) . However these techniques have some disadvantages which are the difficult sample preparation for the TEM and the non-local character of SAXS measurements from which only information on average spatial ordering can be acquired. More specifically in the case of TEM, the mesoporous film must be scraped on to a copper grid. This destroys the film's surface

and therefore apart from the information of the existence or not of the nanopores it is not possible to obtain information about the surface topography which is very important for understanding the properties of those materials. Although this problem can be overcome by using focused ion beam (FIB) milling of the sample to this is extremely expensive, time consuming and results in the destruction of the film.

On the contrary as it has already been explained above AFM (and also scanning tunneling microscopy (STM) in the case of conductive samples) can be used for high resolution imaging without the need of difficult and expensive sample preparation. Additionally as it has also been explained above it is not destructive and can be operated under ambient conditions. Furthermore the wide field of view of the AFM technique can reduce considerably the time needed for imaging the surface of mesoporous film and consequently it drops significantly the cost. However the size and the geometry of conventional AFM tips poses an obstacle in the high resolution imaging of the mesoporus surfaces. This obstacle as it will be shown below can be overcome by the use of CNT AFM tips.

Nanostructured films of mesoporous titanium dioxide (TiO_2) on conducting glass slides of fluorine doped tin oxide (FTO) have been prepared by using a liquid crystal template as described in reference 1. The method that was used for the above preparation is analogous to that described in reference [46]. The conducting glass slides that were used were Asahi, textured F-doped SnO_2, 2.5x3.5x0.1 cm^3.

The samples were first imaged with SEM. The SEM images revealed uniform film thicknesses of 0.5 μm and macroscopically smooth surfaces. The films were well adhered on to the FTO substrates. They were also found to be homogeneous in cross section as well as in surface profile.

The mesoporous films were then imaged with AFM by using a SWCNT AFM tip (Figure 4-10c). One of the acquired AFM images of the mesoporous films is shown in Figure 4-11a). An ordered array of nanometer-sized pores can be clearly distinguished. From cross sectional analysis (Figure 4-11b) it was found that the pores diameters were between 7 - 12 nm and the repeat distance between the pores was approximately 15 - 18 nm. From this information the pore volume fraction was calculated to be equal to 0.3. From the same analysis the pore depth was determined to be between

4-5 nm. Because the film thickness is 0.5 μm it is very likely that not the whole depth of the pore is probed probably due to the short length of the nanotube tip.

The SWCNT AFM tip that was used for the imaging of the mesoporous films were fabricated with the pick up method as it was described in section 4.5.3 . The effective lateral resolution of the tip that was used was 5 nm. It was determined by analyzing images recorded on 5nm gold colloid standards deposited on mica[47]. From the TEM image of Figure 4-10c it can be seen that the nanotube tip consists of a bundle of two SWNTs with a total diameter of 6.6 nm. Surprisingly the measured nanotube tip diameter is larger that the observed lateral resolution of the tip. This effect has been reported in the literature[48]. The possible explanations of this improved resolution are that an asperity or an edge of the nanotube bundle interacts with the sample[48]. It is very likely that the same reasons hold also for the improved lateral resolution observed when imaging the mesoporus surfaces. In addition the relatively large diameter of the bundle and its small length could also contribute to the improved resolution due to the high stiffness of the nanotube tip. The latter eliminates or minimizes the deformation of the tip due to lateral forces caused by the van der Waals interaction of the nanotube tip with the sample which results in the reduction of the nanotube tip's lateral resolution and imaging artefacts[33]. In order to allow comparisons an effort was made to visualise the pores with a conventional tip. However this was not possible due to the very corrugated sample surface. Finally the pore diameter and repeat distance were measured with field emission SEM and were found in good agreement with the data obtained with the AFM.

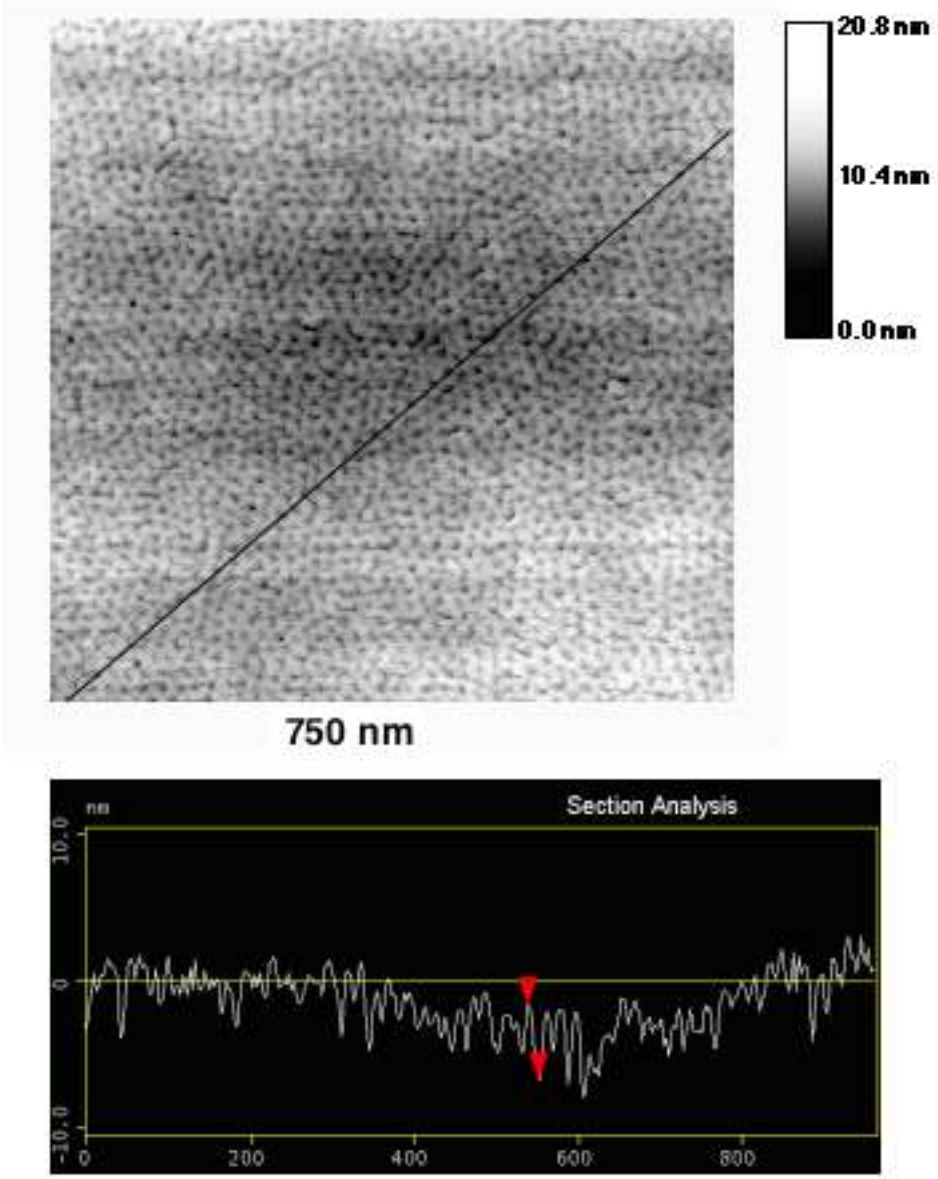

Figure 4-11 (a) High-resolution tapping mode AFM image of mesoporous TiO_2 film. (b) Cross section along the line shown in Fig.1 (a).

4.7 Conclusions

In the current work the effect of the size and shape of the probe on the imaging capabilities of the AFM was described. It was shown that carbon nanotubes are ideal probes for AFM imaging. Those probes were fabricated with two different methods and the advantages and disadvantages of each one were exhibited. Although the surface growth method for fabrication of nanotube tips is promising for automated mass production and therefore commercialisation of those tips it was found to be impractical for laboratory capabilities (small diameter furnace, no possibility of wafer production). On the contrary the pick up method was found to be able to yield a practically infinite number of nanotube tips fulfilling easily the needs in probes of an average lab although they have be produced one per time (no mass production).

It was exhibited that AFM imaging of highly corrugated surfaces such as the ones of mesoporous materials is possibly when nanotube tips are used. This demonstrates the superiority of the nanotube tips over the conventional AFM tips while simultaneously opens up the prospect of imaging the entire mesopore range by means of AFM. The latter is expected to have a great impact in the understanding and controlling the properties of the mesoporous materials in the nanometer scale.

4.8 Appendix I

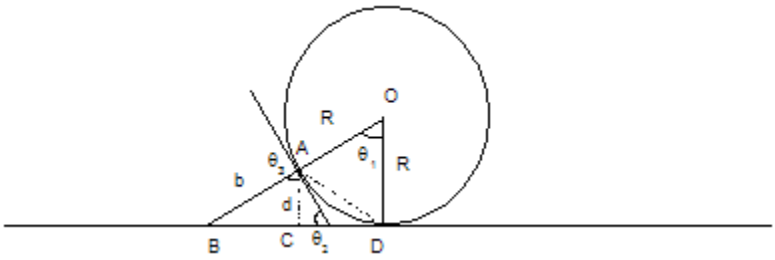

Figure 4-12 Geometrical proof for equation **50**

$\theta_1 = \theta_2 = \theta_3 = \theta$ (θ_1, θ_3 have parallel sides, θ_1, θ_2 have their sides perpendicular)

$$b = \frac{d}{\cos(\theta)} \quad (53)$$

Because OBD, ABC triangles are similar as they have their sides parallel it holds:

$$\frac{d}{b} = \frac{R}{R+b} \Rightarrow R = \frac{d\,b}{b-d} \quad (54)$$

From (53), (54) turns out: $R = \dfrac{d}{1-\cos(\theta)}$ which is equation (50)

References:

1 I. S. Nandhakumar, T. J. Gordon-Smitha, G. S. Attarda, D. C. Smith, "Application of Carbon Nanotube AFM Probes to the Characterization of Mesoporous Materials", small, 1, 406, (2005).

[2] J. Li, A. M. Cassel, H. Dai, "Carbon Nanotubes as AFM Tips : Measuring DNA Molecules at the Liquid/Solid Interface", Surf. Interface Anal. 28, 8, (1999).

[3] N. R. Wilson, J. V. Macpherson, "Single-Walled Carbon Nanotubes as Templates for Nanowire Conducting Probes", Nano Lett. 3, 1365, (2003).

[4] Product list from manufacturer website: http://www.nanoscience.com/

[5] G. Binnig, C. F. Quate, Ch. Gerber, "Atomic Force Microscope", Phys. Rev. Lett. 56, 930, (1986).

[6] P. K. Hansma, J. Tersoff, J. Appl. Phys. 61, (1987) R1.

[7] F. F. Abraham, I. P. Batra, "Effect of Tip Profile on Atomic – Force Microscope Images: A model Study", Phys. Rev. Lett. 60, 1314, (1988).

[8] F. J. Giessibl, "Advances in atomic force microscopy", Rev. Mod. Phys. 75, 949, (2003).

[9] F. J. Giessibl, C. F. Quate, "Exploring the nanoworld with atomic force microscopy", Phys. Today, ?, 44, (2006)

[10] L. Montelius, J. O. Tegenfeldt, "Direct observation of the tip shape in scanning probe microscopy", Appl. Phys. Lett. 62, 2628, (1993).

[11] J. O. Tegenfeldt, L. Montelius, "Image widening not only a question of tip sample convolution", Appl. Phys. Lett. 66, 1068, (1995).

[12] D. Keller, "Reconstruction of STM and AFM images distorted by finite-size tips", Surf. Sci. 253, 353, (1991).

[13] D. Keller, "Envelope reconstruction of probe microscope images", Surf. Sci. 294, 409, (1993).

[14] H. B. Callen, "Thermodynamics" 2nd ed. (Willey, New York, 1985) ch. 5.

[15] D. J. Muller, D. Fotiadhs, A. Engel, " Mapping flexible protein domains at subnanometer resolution with atomic force microscope", FEBS Lett. 430, 105, (1998).

[16] D. J. Mü ller, D. Fotiadis, S. Scheuring, S. A. Müller, A. Engel, "Electrostatically Balanced Subnanometer Imaging of Biological Specimens by Atomic Force Microscope", Biophys. J. 76, 1101, (1999).

[17] D. J. Keller, C. Chih – Chung, "Imaging steep, high structures by scanning force microscopy with electron beam deposited tips", Surf. Sci. 268, 333 (1992).

[18] H. J. Dai , J. H. Hafner, A. G. Rinzler, D. T. Colbert, R. E. Smalley, "Nanotubes as nanoprobes in scanning probe microscopy", Nature, 384, 147, (1996).

[19] E. Yenilmez, Q. Wang, R. J. Chen, D. Wang, H. Dai "Wafer scale production of carbon nanotube scanning probe tips for atomic force microscopy", Appl. Phys. Lett. 80, 2225, (2002).

[20] C. V. Nguyen, Q. Ye, M. Meyyappan, "Carbon nanotube tips for scanning probe microscopy: fabrication and high aspect ratio nanometrology", Meas. Sci. Technol. 16, 2138, (2005).

[21] J. H. Hafner, C. –L. Cheung, A.T. Wooley, "Structural and functional imaging with carbon nanotube AFM probes", Prog. Biophys. Mol. Biol. 77, 73, (2001).

[22] A. Alessandrini, P. Facci, "AFM: a versatile tool in biophysics", Meas. Sci. Technol. 16, R65, (2005).

[23] J. H. Hafner, C. L. Cheung, C. M. Lieber, "Growth of nanotubes for probe microscopy tips", Nature, 398, 761, (1999).

[24] S. S. Wong, J. D. Harper, P. T. Lansbury, C. M. Lieber, "Carbon Nanotube Tips: High – Resolution Probes for Imaging Biological Systems", J. Am. Chem. Soc. 120, 603, (1998).

[25] S. S. Wong, E. Joselevich, A. T. Woolley, C. L. Cheung, C. M. Lieber, "Covalently functionalized nanotubes as nanometer sized probes in chemistry and biology", Nature, 394, 52, (1998).

[26] J. H. Hafner, C. L. Cheung, C. M. Lieber, "Direct Growth of Single-Walled Carbon Nanotube Scanning Probe Microscopy Tips", J. Am. Chem. Soc. 121, 9750, (1999).

[27] T. Hertel, R. Martel, P. Avouris, "Manipulation of Individual Carbon Nanotubes and Their Interaction with Surfaces", J. Phys. Chem. B 102, 910, (1998).

[28] C. L. Cheung, "Carbon Nanotubes as Molecular Probes for Scanning Probe Microscopy", Ph. D. Thesis , Harvard University, Cambridge, Massachusetts, U.S.A. (2001).

[29] X. Chen, G. Cao, "A structural, mechanics study of single-walled carbon nanotubes generalized from atomistic simulation", Nanotechnology, 17, 1004, (2006).

[30] T. Hertel, R. E. Walkup, P. Avouris, "Deformation of carbon nanotubes by surface van der Waals forces" Phys. Rev. B, 58, 13870, (1998).

[31] E. W. Wong, P. E. Sheehan, C. M. Lieber, "Nanobeam Mechanics, Elasticity Strength and Toughness of Nanorods and Nanotubes", Science, 277, 1971, (1997).

[32] M. C. Strus, A. Raman, C-S. Han, C. V. Nguyen, "Imaging artefacts in atomic force microscopy with carbon nanotube tips", Nanotechnology, 16, 2482, (2005).

[33] E. S. Snow, P. M. Campbell, J. P. Novak, "Single-wall carbon nanotube atomic force microscope probes", Appl. Phys. Lett. 80, 2002, (2002).

[34] J. H. Hafner, C-L. Cheung, T. H. Oosterkamp, C. M. Lieber, "High-Yield Assembly of Individual Single-Walled Carbon Nanotube Tips for Scanning Probe Microscopies", J. Phys. Chem. B, 105, 743, (2001).

[35] L. Chen, C-L. Cheung, P. D. Ashby, C. M. Lieber, " Single-Walled Carbon Nanotube AFM Probes: Optimal Imaging Resolution of Nanoclusters, and Biomolecules in Ambient and Fluid Environments", Nano Lett. 4, 1725, (2004).

[36] N. R. Wilson, D. H. Cobden, J. V. Macpherson, "Single-Wall Carbon Nanotube Conducting Probe Tips", J. Chem. Phys. B, 106, 13102, (2002).

[37] J. H. Hafner, C. L. Cheung, C. M. Lieber, "Fabrication of nanotube microscopy tips", United States Patent, (6,716,409), April 6, 2004.

[38] O. A. Nerushev, S. Dittmar, R.-E. Morjan, F. Rohmund, E. E. B. Campbell, "Particle size dependence and model for iron-catalyzed growth of carbon nanotubes by thermal chemical vapor deposition", J. Appl. Phys. 93, 4185, (2003)

[39] Yoshikazu Homma,a) Yoshihiro Kobayashi, and Toshio Ogino, Takayuki Yamashitab), "Growth of suspended carbon nanotube networks on 100-nm-scale silicon pillars", Appl. Phys. Lett., 81, 2261, (2002).

[40] R. Swanepoel, "Determining refractive index and thickness of thin films from wavelength measurements only", J. Opt. Soc. Am. A, 2, 1339, (985).

[41] A. Cao, P. M. Ajayan, G. Ramanath, R. Baskaran, K. Turner, "Silicon oxide thickness-dependent growth of carbon nanotubes", Appl. Phys. Lett. 84, 109, (2004).

[42] G.S. Attard, J.C.Glyde, Göltner, C.G, *Nature* **1995**, *378*, 366.

[43] G.S. Attard, P.N. Bartlett, N.R.B.Coleman, J.M. Elliott, J.R. Owen, J.H. Wang, *Science* **1997**, *278*, 838.

[44] I.S.Nandhakumar, J.M. Elliott, G.S. Attard, *Chemistry of Materials* **2001**, *13*, 3840.

[45] T. Gabriel, I. Nandhakumar, G.S. Attard, Electrochem. Comm. 2002, 4, 610.

[46] E.L. Crepaldi, G.J. de A.A. Soler-Illia, D. Grosso, F. Cagnol, F. Ribot, C. Sanchez, C. J. Am. Chem. Soc. 2003, 125, 9770.

[47] J.Vesenka, S. Manne, R. Giberson, T. Marsh, E. Henderson, *Biophys. J.* **1993**, *65*, 992.

[48] L. A. Wade, I. R. Shapiro, Z. Ma, S. R. Quake, C. P. Collier, "Correlating AFM Probe Morphology to Image Resolution for Single-Wall Carbon Nanotube Tips", Nano Lett. 4, 725, (2004).

Conclusions of Part I

In the first part of the thesis two aspects of the field of carbon nanotubes were studied. First a novel method of carbon nanotube growth without the need of metal catalyst was demonstrated. Overwhelming data from characterisation by means of Raman Spectroscopy (RS), Scanning Electron Microscopy (SEM), Transmission Electron Microscopy (TEM) and Atomic Force Microscopy (AFM) show that products of this method of growth are single walled carbon nanotubes (SWNTs). Further evidence from the RS data show, that very likely, these SWNTs are very low in defects and therefore of high quality. Essential steps of the method are the preparation of Si substrates with Stranski – Krastanow Si-Ge islands or Ge dots, carbon ion implantation of those substrates and growth of carbon nanotubes on those substrates through chemical vapour deposition. Some of the characterisation data though indicate that it might be possible for growth of carbon nanotubes on such substrates without the need of carbon ion implantation. No metal particles are employed in any of these steps therefore this method is fully compatible with the front end silicon processing facilities. AFM data indicate that the growth mechanism of carbon nanotubes on the Ge dots substrates follow the vapour-liquid-solid growth with nanoscale Ge seeds. In order for this method to have industrial applications further work must be done to improve the uniformity and the density of the carbon nanotube growth.

Second carbon nanotubes were utilized as AFM probes. Different methods for the fabrication of carbon nanotube AFM probes were applied. It was found that the surface growth method although is promising for commercial application and mass production it is rather impractical for laboratory use. The pick up method from the other hand has the potential to supply a practical infinite number of carbon nanotube AFM probes which can easily suffice the needs of an average laboratory in a cost effective way. The latter method is probably not ideal for mass production as the probes have to be fabricated one per time. It was also shown that the as fabricated probes (with either of the above methods) need further engineering in order to reduce the effects of thermal noise and to increase stiffness. The fabricated carbon nanotube AFM probes were used in AFM

imaging of surfaces of mesoporous materials proving that this imaging is possible with this kind of probes which shows their advantage in comparison with the conventional AFM probes. Furthermore it indicates the possibility of AFM imaging of the entire mesopore range which is expected to extend down to the nanometer scale the knowledge and the control of such materials.

PART II

Quantum Dots

Chapter 5 Physical Properties of Quantum dots

5.1 Introduction

Quantum dots are zero dimensional nanostructures into which charge carriers are confined in all three dimensions. Their physics, properties and applications are fascinating with the latter ranging from quantum information processing, to biological marking. In the following sections some aspects of quantum dots such as their growth and their physical will be discussed to an extent that covers the needs of this thesis. The material presented here is a brief compilation from references [1], [2], [3], [4], [5], [6], [7], [8], [9], [10] and more extended information about the topics of quantum dot physics presented here can be sought there and references therein.

5.2 Fabrication of Quantum Dots

The fabrication of quantum dots is challenging technologically as control over the shape and dimensions are required at the nanometer range. The requirement for three dimensional confinements sets the size upper and lower limits. The lower limit is dictated by the requirement of at least one bound electron (hole) level. In the simple case for instance of a spherical potential well with infinite barriers the energy of the electronic levels E_{nl} is given by the equation[2,3,11]:

$$E_{nl} = \frac{\hbar^2 \chi_{nl}^2}{2m_e^* R^2} \qquad (55)$$

where m_e^* is the effective electron mass, R the radius and χ_{nl} is n-th zero of the spherical Bessel function of the order l. The energy E_{10} of the lowest energy state must be smaller than the conduction band offset energy which for an InAs/GaAs system[12] is 0.69eV. This leads to a minimum radius of approximately 3nm.

In order to determine the upper limit of the quantum dot size the requirement that the quantum effects should remain important at room temperature must be taken into account. This means that the spacing of the energy levels must such that minimizes the effect of thermal excitation of the carriers. It can be taken as a rule of thumb that[6] $E_{11} - E_{10} = 3K_B T$ (where E_{11} is the first excited state and T the temperature). This requirement for the InAs/GaAs system leads (by using equation (55)) to an upper limit of

14 nm when the electron levels are considered and 7 nm when the hole levels are considered.

Several techniques have been developed for the fabrication of quantum dots and the most important ones will be described in brief.

5.2.1 Fabrication by lithographic techniques[2]

In this group of techniques the quantum dots are fabricated by lithographically patterning quantum well hetero-structures. Techniques such as optical lithography, X – ray lithography, electron beam and ion beam lithography (EBL, FIBL) have been employed. The main advantages of those techniques are that the shape, size and arrangement of the fabricated quantum dots can be controlled with the precision of the resolution limit of each technique, they can produce integrated arrays of quantum dots and they are generally compatible with the VLSI (very large scale integrated) semiconductor technology.

The general process for the lithographic techniques (Figure 5-1) consists of the following steps[1]: The surface of a quantum well sample is coated with a polymer mask. The mask is being exposed partially and a pattern is formed on its surface which defines the shape of the nanostructure to be fabricated (Figure 5-1a). Then the exposed part of the mask is removed (Figure 5-1b) and the whole surface is coated with a thin metal layer (Figure 5-1c). The whole polymer film along with the metal layer on its surface is removed by applying the appropriate solvent. The part of the metal film that had covered the previously exposed area remains on the surface of sample as there was no polymer under it to be dissolved (Figure 5-1d). Through the means of chemical etching the area which is not protected by the metal film is removed (Figure 5-1e) and a pillar is created which contains a cut-out fragment of the quantum well (Figure 5-1f). Thus the motion of carriers is confined laterally by the nanoscale dimensions of the pillar (typical sizes are of the order or 10 – 100 nm) and vertically by the quantum well layer.

There are two important disadvantages associated with the lithographic techniques[2]. The one is the limitation on sizes that the resolution of the lithographic techniques imposes which restricts the lower[2] size limit to around 10 nm. The second one has to do with the side effects of etching on the optical properties of the as fabricated quantum dots. A

highly damaged or even amorphized layer is formed at the surface of the lithographically fabricate quantum dots due to etching (edge effects). In this layer non – radiative recombination is predominant reducing considerably the internal quantum efficiency of the dots. The influence of this layer increases as the dot size decreases. Furthermore charged impurities may also lead to "blinking" effects in the dots[3].

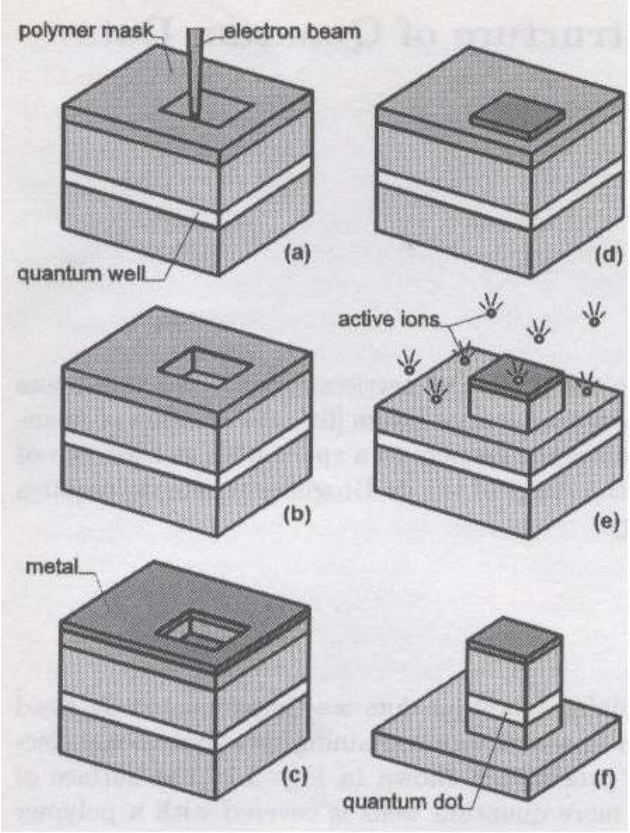

Figure 5-1 Fabrication of quantum dots by using lithographic techniques. After 1.

5.2.2 Modulated Electric Field

Quantum dots can also be fabricated through the patterned formation of miniature electrodes via lithographic means on the surface of a quantum well structure[1] (Figure 5-2). By applying appropriate voltages at the electrodes lateral confinement of the carriers in the quantum well layer can be achieved.

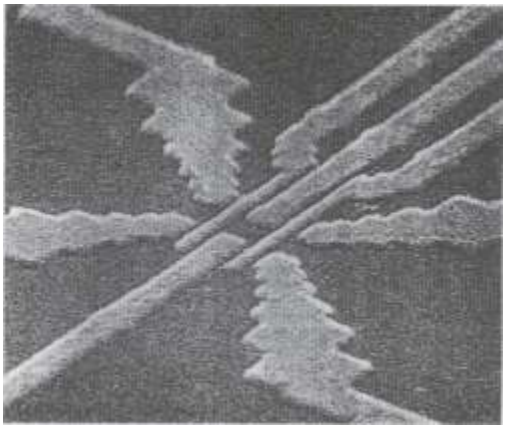

Figure 5-2 Modulated Electric Field quantum dot. The quantum dot is formed at the intersection area of the four inner electrodes whose voltages confine the electrodes. The outer four electrodes are used as contacts for electron tunnelling from the dot.After 1.

This kind of quantum dots does not suffer from edge effects[1]. However their main disadvantage is their large size which is in the range of hundreds[13] of nanometers and as such it does not allow for room temperature applications.

5.2.3 Colloidal Quantum Dots

Colloidal quantum dots or nanocrystals[3] are compounds of II-VI materials such as CdSe, PbS, CdS, CdTe, e.t.c. They are usually grown in a solution or as inclusions in a glass matrix. In the case of solution the nanocrystals are produced[14] from reagents containing the nanocrystals constituents. One reagent contains the metal ions (e.g. Cd^{2+}) and the other provides the chalcogenide (e.g. Se^{2-}). The size of the nanocrystals is controlled by the temperature of the solutions and the concentrations of the reagents and the stabilizers. Their shape is almost spherical displaying faceted surfaces due to anisotropic growth rates along different crystal axis[15,16]. The nanocrystals have diameters in the range[17] of 1 to 10 nm. Subsequent chemical and physical processing may be used to select a subset of the crystallites which display good size uniformity[17]. It is obvious that this kind of nanoparticles would exhibit a high fraction of atoms at the surface with many of them possessing dangling bonds. These dangling bonds are passivated by the use of organic ligands such as tri-octylphosphine oxide (TOPO). However even after the passivation of the dangling bonds holes can interact with uncoordinated selenium atoms giving rise to photo-oxidation[15]. Addition[18,19] of a thin layer (a few mono-layers thick) of

a wider bandgap material such as ZnS can confine the holes into the core due to the band offset.

This kind of quantum dots exhibit very high photoluminescence efficiency (a typical range is between 60 to 90%) and are relatively easy to process (solution processable). Thus they have a big number of potential as well as current applications that extend from biological tagging up to solar cells and hybrid organic infrared emmiters[20].

5.2.4 Self Assembled Quantum Dots

By means of means of epitaxial techniques such as molecular beam epitaxy (MBE) and metal – organic chemical vapour deposition (MO-CVD), quantum dots can form under certain epitaxial conditions. More specifically these conditions have to do with the lattice constants of the substrate and the epitaxial deposited crystalline material. When those two constants differ considerably (e.g. 7% as in the case of InAs and GaAs) then only the first deposited mono-layers crystallize as epitaxial strained layers whose lattice constant is equal with the one of the substrate[1]. However if the thickness of the deposited layer become bigger than a critical value then significant strain is induced in this layer resulting in its break – down and to the spontaneous formation of 3-dimensional islands of similar size and shape. The distribution of the islands on the substrate is random. The phase transition from the epitaxial structure to the randomly distributed islands is known as Stranski – Krastanow transition[21]. The critical value of the thickness above which the Stranski – Krastanow transition occurs depends upon the lattice mismatch and decreases as the latter increases[22].

The shape and the average size of the as formed islands depend upon parameters such as degree of the lattice mismatch, growth temperature and growth rate[1,2,3,4,17]. Of similar importance[4] are the annealing times after the growth and prior to capping (see below). In general there have been reported dots with pyramid shapes[23] of 2.8 nm height with square base of 24 nm side (with about 15% fluctuations from these values), lens shape[24] with height around 4.4 nm and diameter about 36 nm (deviations from this values were between 5 and 10%), as well as truncated pyramids and cones[2] of similar sizes.

The as formed islands sit on a thin interface layer of the deposited material and the substrate, called the wetting layer. After the end of the growth the islands and the wetting layer are passivated by another layer which is usually from the same substance as the substrate. The obtained quantum dots have perfect crystal structure[1], small sizes, relatively good size homogeneity and they emit quite efficiently from the visible up to the near infrared[6].

5.3 Electronic structure of Quantum Dots

Due to the 3-dimensional confinement of the electronic motion, quantum dots are characterised by a discrete density of states. For this reason quantum dots are also called artificial atoms. However a closer examination of the electronic structure of quantum dots reveals fundamental differences with the one of real atoms. The lay – out of the energy levels in quantum dots is affected by a number of parameters such their size, shape, composition, strain distribution and matrix effects[1,2,3,4,5,6]. Furthermore few body effects influence the electronic structure of quantum dots and have to be taken into account. The real electronic structure of quantum dots is a complicated problem that cannot be solved analytically leaving space only for approximations. In the text that follows an outline of the theory of the quantum dot electronic structure will be presented. This outline applies mainly on self – assembled quantum dots of pyramidal shape as those where the subject of the corresponding experimental part of this thesis.

5.3.1 The single particle picture

It is necessary for the understanding of the electronic structure of quantum dots to have realistic calculations of the single – particle energy levels that can be compared with the experiment[4]. As quantum dots consist typically of 100,000 atoms it is obvious that even for single particle levels only approximation methods can be used.

An intuitive picture of the single particle energy levels of a quantum dot can be gained by considering an idealized system of a cuboidal[25] dot. This system has the same .four fold rotation symmetry about an axis in the growth direction through the centre of the base as the pyramidal dot. For simplicity the barriers at the hetero-interface are assumed infinite. Unlike the pyramidal dot, separation of variables can be applied when

solving the Schrödinger equation for the cuboidal dot. The side of the square base of the dot has length L and its height is $H << L$. In this case the wavefunctions of the electron are sinusoidal inside the dot and vanish outside. They can be written in the form of:

$$\Phi_{lmn} = \Phi_l(x)\Phi_m(y)\Phi_n(z) \qquad (56)$$

where:

$$\Phi_l(x) = \left(\frac{2}{L}\right)^{\frac{1}{2}} \sin(k_x x), \qquad \Phi_m(y) = \left(\frac{2}{L}\right)^{\frac{1}{2}} \sin(k_y y), \qquad \Phi_n(z) = \left(\frac{2}{H}\right)^{\frac{1}{2}} \sin(k_z z)$$

(57)

In equations (57) $k_x = \frac{l\pi}{L}$, $k_y = \frac{m\pi}{L}$, $k_z = \frac{n\pi}{H}$ due to the boundary conditions of the system $(l, m, n = 1, 2, 3, \ldots)$. This leads to a discrete energy spectrum, with the energy given by the following equation:

$$E_{lmn} = E_g + E_l + E_m + E_n \qquad (58)$$

where E_g is the bandgap energy of the semiconductor of which the dot is made of, and E_l, E_m, E_n are given by the equations:

$$E_l = \left(\frac{\pi l}{L}\right)^2 \frac{\hbar^2}{2m_e}, \quad E_m = \left(\frac{\pi m}{L}\right)^2 \frac{\hbar^2}{2m_e}, \quad E_n = \left(\frac{\pi n}{H}\right)^2 \frac{\hbar^2}{2m_e} \qquad (59)$$

The energy separation between states with different z quantum number (n) is relatively large due to $H << L$ and therefore only states with $n = 1$ will be considered. From equations (4) and (5) is obvious that the ground state level $(l = m = n = 1)$ is only two fold degenerated due to spin while the first excited level $(l = 1, m = 2, n = 1$ or $l = 2, m = 1, n = 1)$ is four fold degenerate. In most of the cases there are only two electronic levels bound in the dot. Classifying the electronic levels according to the nodal points of their wavefunction, one can consider the ground state as an s – like state, and the first excited state as a p – like state. This nomenclature is the most commonly used one in the quantum dot literature and it will be followed in this thesis as well.

The above model of the cuboidal quantum dot can only be used as an intuitive representation of the single particle picture of a quantum dot and by no means can it be considered that it yields an accurate approximation of the single particle states. Furthermore while this model can not be used for the hole states as in this case the single

band approximation is completely invalid due to the valence band mixing. For example the lowest lying hole state has been found to be predominantly heavy hole like (as expected) but with a 10% light hole admixture[26]. Obviously other methods are needed in order to derive an accurate picture of the single particle states of a quantum dot.

Furthermore it has to be taken into account that the quantum dots produced with the Stranski – Krastanow method are strained structures. As it has been analyzed in reference [27] the strain modifies the local band gap. The strain induced shift of the conduction band depends only upon the hydrostatic component of the strain. The three valence bands (heavy hole, light hole, split-off bands) are also affected by the presence of strain. The light hole and the split-off bands are split far from the valence band edge and their impact in the electronic structure is reduced.

The shear strains induce a piezoelectric polarization which creates fixed charges which reside close to the pyramid's edges and have opposite signs for adjacent edges. Due to the fact that the piezoelectric module of InAs is smaller by a factor of 4 than the one of GaAs the resulting potential is mainly present in the barrier. This potential reduces the symmetry of the pyramidal dot about the axis in the growth direction and through the centre of the pyramid from four fold to two fold thus leading to a lift of degeneracies.

There are two main methods[2,6] for the approximation of the strain field which are the continuum elasticity model (CET) and the valence force field (VFF). In many cases both of these methods give similar results.

One of the most often used methods for the approximation of the single particle levels is the $\mathbf{k}\cdot\mathbf{P}$ method[2,4,5,6]. It allows a relatively accurate calculation of the single particle levels for an arbitrary confinement potential. This method can be easily modified to include changes in composition and strain across the structure.

According to the $\mathbf{k}\cdot\mathbf{P}$ method[25,28,29] one can solve the Schrödinger equation at the Γ point where the term $\mathbf{k}\cdot\mathbf{P}$ vanishes and then treat this term as a perturbation for other points around the Γ point. In the case of quantum dots an eight – band $\mathbf{k}\cdot\mathbf{P}$ (including the conduction band, light and heavy hole band and split off band) is used. However in many cases one band might be sufficient.

The validity of the $\mathbf{k}\cdot\mathbf{P}$ calculations has been confirmed from experimental observation in many cases. For instance the hole mass measured through the means of

magneto-optical measurements is in good agreement[30] with the one derived from the $\mathbf{k}\cdot\mathbf{P}$ method. The predictions of $\mathbf{k}\cdot\mathbf{P}$ theory have been further compared with experimental observations from Photoluminescence Excitation Spectroscopy (PLE) measurements on quantum dot ensembles and have been found in good agreement mainly for larger quantum dots ($E_{\det} \le 1.1eV$, pyramid base ≈ 17 nm) as it has been shown in reference [31]. The predicted excited state absorption is in the same energy region in which excitation resonances appear in the PLE spectra. The predicted separations of the energy levels though, were systematically larger than the ones observed experimentally. The agreement between the predictions of $\mathbf{k}\cdot\mathbf{P}$ theory and experiment worsens for smaller dots. The discrepancies probably arise[31] from uncertainties in the size and growth dependent variations of the quantum dot shape and composition and possible Coulomb-induced localised wetting layer states.

More specifically quantum size effects as they are included in the $\mathbf{k}\cdot\mathbf{P}$ theory predict an increase in the energy separation between the ground state and the excited states. Although this has been experimentally confirmed[31,32] for quantum dots with ground state energy below 1.2 eV it was also experimentally observed that this energy separation decreases[32] with increasing ground state energy above 1.2 eV. The latter was attributed to quantum shape effects (aspect ratio of the pyramidal dots) and agrees well with the predictions of the empirical pseudopotential method[32,33].

Apart from the $\mathbf{k}\cdot\mathbf{P}$ method also other atomistic methods such as the empirical pseudopotential method (EPM) have been employed[34]. The single particle wavefunctions derived with EPM for a pyramidal quantum dot with tetragonal base is shown in Figure 5-3**.**

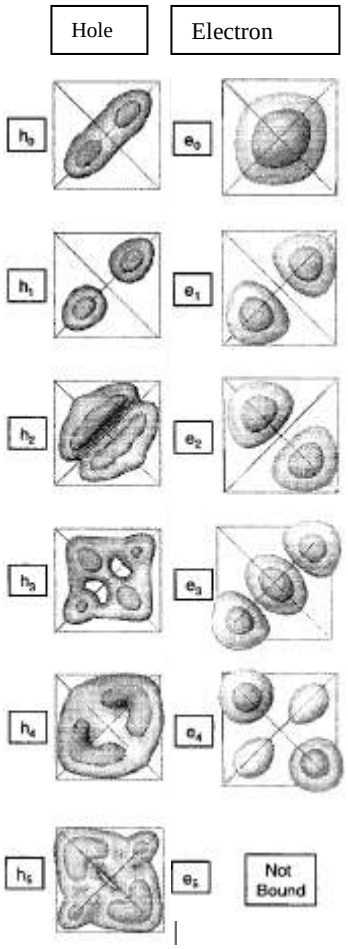

Figure 5-3 Single particle states calculated with the EPM method for a pyramidal quantum dot. After 34.

5.3.2 Excitons in quantum dots

The simplest optical exitation of the system is an electron hole pair which interact via Coulomb interaction and they form bound states called excitons. The Coulomb interaction and the corresponding contribution to the energy of the system due to this interaction is $W_{ij}\left(\mathbf{r}_i,\mathbf{r}_j\right)=\frac{1}{4\pi\varepsilon_r\varepsilon_o}\frac{q_i q_j}{\left|\mathbf{r}_i-\mathbf{r}_j\right|}$ assuming that ε_r is considered as uniform and isotropic.

The impact of the Coulomb interaction between an electron and a hole in a quantum dot can be classified in three regimes[2]:

1. The strong confinement regime in which the Coulomb interaction is small compared with the quantization of the kinetic energy due to the imposed confinement. An estimate[4] for when this happens is the dimensions of the dot with respect to the exciton bulk Bohr radius. According to this strong confinement is expected for small quantum dots whose radius is smaller than the Bohr radius in the bulk. The wavefunctions of the electron and hole are largely uncorrelated.
2. The weak confinement regime in which the Coulomb interaction is comparable or larger than the sublevel separation caused by the confinement. In this case the centre of the mass motion of the as formed electron hole pairs is quantized by the confinement potential. Weak confinement is expected for quantum dots with radius small than the Bohr radius of the exciton in the bulk.
3. In the intermediate regime the Coulomb interaction is much smaller than the electronic sublevel separation due to confinement but much bigger than the corresponding hole separation. This happens due to the different masses of electrons and holes. In this regime the hole energy is quantized by the electrostatic potential of the electron orbital.

Because[2] the Coulomb energy depends strongly on the value of the dielectric constant, dots of the same size but with different composition (and therefore different value of the dielectric constant) might belong to different regimes. For example as the dielectric constant of III-V compounds is relatively small, the bulk exciton Bohr radius is bigger than 10 nm. Consequently dots with similar dimensions and enough deep potential are expected to be in the strong confinement regime[4]. However in II-VI compounds due to relatively large dielectric constant strong confinement is expected only for dots with radius smaller than a few nanometres.

Considering now the case of a spherical quantum dot, it can be shown that its lowest state is eight fold degenerate[2,]. There is a number of mechanisms that can lift this degeneracy resulting in an exciton fine structure. Such mechanisms can be the internal crystal structure, the shape of the quantum dot, the electron – hole exchange interaction which depends on the overlap of the electron and hole wavefunctions. The states of the

exciton $|N, N_m\rangle$ can be described using the total angular N momentum and its projection N_m. The total angular momentum is $N = F + s$ where $F = 3/2$ is the momentum of the hole whose projections are $m_F = \pm 3/2, \pm 1/2$ and $s = 1/2$ is the electron spin with projections $m_s = \pm 1/2$. According to this description the states of the exciton are $|1,1\rangle$, $|1,0\rangle$, $|1,-1\rangle$, $|2,2\rangle$, $|2,1\rangle$, $|2,0\rangle$, $|2,-1\rangle$, $|2,-2\rangle$. Due to photon spin preservation no radiative recombination is allowed for the states $|2,2\rangle$, $|2,0\rangle$, $|2,-2\rangle$. For this reason these states are called dark states or dark excitons[2].

5.3.3 Excitonic Complexes

Apart from excitons there is a possibility of formation in the dot of other entities involving a larger number of charge carriers than an electron hole pair. Of those, species of particular interest for the purposes of this thesis are the charged exciton and the biexciton which are expected to emit at approximately the energy of the exciton[35]. This is due to the fact that the exciton is a charged neutral complex and intracts weakly with other excitons or charges[35].

Charged Excitons

Charged excitons are formed in the quantum dot when the exciton is bound with one or more extra charge carriers of the same kind (either electrons or holes). The number of the extra carriers defines the net charge of the charged exciton. The extra charged carriers can be injected in the dot electrically or optically. Photoluminescence emission of charged excitons with net charge of -6, -5, -4, -3 -2, -1, +1,+2 has been observed[36,37,38]. From the above charged excitons the simplest ones _(net charge ±1) are called trions as they involve three carriers in their formation. Trions due to their simplicity in comparison with other excitonic charged complexes have been studied theoretically more extensively[2,35,39].

The binding energies of trions have been found to strongly depend upon the size and shape and chemical composition of the quantum dot[39] as well as on the on the ratio of

the effective masses of the electron and the hole[35] . Thus for instance[2] the positive trion in a flat InAs/GaAs cone was calculated to be 2meV for a diameter of 12 nm while dropping to zero for a diameter of 7nm. For the same range of radius the negative trion was found to be unbound[2]. The situation is reversed for hemispherical InGaAs/GaAs caps in which the bound trion is the negative one[2].

As it can be seen from the above example negative and positive trions in the same dot are not expected to exhibit equal binding energies as the Coulomb correlation and exchange interactions for electrons are predicted to be different than the ones for the holes[39]. Furthermore a trion can be found in an anti-binding state, i.e. at a higher energy than an exciton, in a quantum dot[39]. Such state cannot exist in the bulk or in a quantum well or in a quantum wire[40]. It is the lack of continuum which prevents anti-binding multi-particle complexes from disassociation[39]. The three dimensional confinement in quantum dots allows the formation energetically unfavourable states[39,40].

In the case of pyramidal InGaAs quantum dots the photoluminescence emission of trion has been observed within a 2 meV range around the exciton line[41,42]. The emission line corresponding to the trion is expected to have linear dependence upon excitation intensity as the one of the exciton due to the fact that both arise from the single exciton occupancy of the dot[41].

Biexciton

In the cases that the single particle ground state for electrons as well as the one for holes is occupied by two particles each, this leads to the formation of a biexciton instead of two excitons[2]. This can be achieved for instance in photoluminescence experiments for the proper values of excitation intensity[41,42,43]. The energy E_{XX} of the biexciton is different than the one of two excitons ($2E_x$) by an amount of energy E_{BX}, which accounts for the binding between the two excitons[2] and is called biexciton binding energy. It is defined as $E_{BX} = 2E_X - E_{XX}$.

A biexciton in the bulk can disassociate into two excitons when its constituent excitons separate spatially far enough from each other that the interaction between them

vanishes[2]. Similar disassociation of a biexciton cannot take place in a quantum dot due to the three dimensional confinement[2].

Exact calculation of a value for the biexciton binding energy is relatively difficult[44]. Analytical calculations of the biexciton binding energy in a spherical quantum dot[44] have shown that the first perturbation theory term vanishes while there is a strictly positive second perturbation theory term. The range of values for this term was found to depend on relative ratio of the dielectric constants of the quantum dot and the surrounding material[44]. It has also been shown[2] that the biexciton binding energy is independent of the ratio of the electron and hole masses and increases with decreasing dot radius.

Through the means of approximate methods (variational calculations) a biexciton binding energy value of 1.5 meV was predicted[2,45] for flat cones of InAs/GaAs with a diameter of 8 nm. Furthermore in the case of pyramidal quantum dots the biexciton is predicted to be anti-binding or binding depending on their geometry, composition and size[39]. This is due to the piezoelectric effects in the quantum dot. More specifically as it has been discussed in reference 39 the piezoelectric quadrupole potential separates electrons and holes which has as an effect the reduction of the electron – hole attraction whilst simultaneously increases the pairwise Coulomb repulsion leading to an antibinding biexciton. However the piezoelectric effect scales linearly with the dot size and depends on the composition and geometry of the dot. Therefore in smaller pyramids or in pyramids that consists of less piezoelectric materials, or they are less strained, or they have less developed facets the quadrupole potential is weaker. This gives rise to weaker electron – hole separation thus enabling the exchange and correlation interactions to overcome the net Coulomb repulsion allowing the formation of binding biexcitons. Evidence for the validity of the above predictions are the experimental observation of antibinding biexcitons with binding energy of approximately -0.7 meV in 12 nm large InAs/GaAs quantum dots[46] while binding biexcitons with binding energy 3 meV were observed in 20 nm large $In_{0.4}Ga_{0.6}As$/GaAs quantum dots[47].

Multi-excitons

Apart from excitons and biexcitons quantum dots can accommodate excitonic complexes consisting of a larger number of excitons which are commonly referred to in the literature as multiexcitons[26,48]. The neutral charge of the excitons allows the dots to be occupied by a high number of electron - hole pairs with typical numbers reported in literature varying form six[49] to several tens[50].

The number of excitons in the dot depends on the optical excitation intensity with the excitation energy being tuned at the barriers or the wetting layer[49,51]. As the excitation intensity increases more carriers are generated populating initially the ground state of the dot and consequently due to the Pauli exclusion filling the states of higher energy[26,52]. The observed spectra (from single dot spectroscopy) exhibit usually a complex structure consisting of sharp features which dominate the spectrum for a specific range of excitation intensities but disappear or become weak for other values of the excitation intensity[26,49,50,51,52].

These features cannot be explained in the frame of the single particle picture[48]. Instead it is necessary to consider the Coulomb interactions among the constituent electrons and holes in each excitonic complex which give rise to a set of characteristic spectral features for each complex[26]. For example[48] the ground state of a triexciton (3X) consists by two excitons with their carriers (electrons and holes) in the single particle ground state forming a biexciton and one more exciton whose electron and hole are in the first single particle excited state. In this configuration there are two electrons with parallel spin as well as two holes. This leads to an energy difference of approximately 10 meV in comparison with the one expected from the single particle energies. Furthermore in this configuration if one of the ground state excitons recombines radiatively the final state of the system will be an excited biexciton (one exciton in the ground state and one exciton in the excited state) and the energy of the emitted photon will be different than the biexciton recombination energy without the presence of the exciton in the excited state[48].

The above example indicates that the electronic structure of a quantum dot is strongly affected by the presence of carriers due to the Coulomb interactions between them. Consequently the resulting optical properties differ than the ones of an empty dot.

5.4 Theory of coherence in matter

In the following a brief presentation of the theory of coherence in matter will be given. Initially the coherent properties of a two level system will be described and then some more general examples will be presented. Finally some main coherent phenomena will be outlined. The treatment presented here is semiclassical. Only a very basic description of the above will be presented here and more details as well as description of other aspects of coherence theory can be seek in references [53], [54], [55].

5.4.1 Coherence of a two - level system

One of the simplest systems in quantum mechanics is a two level system whose eigenstates are $|a\rangle$ and $|b\rangle$. The respective eigenenrgies of this system are E_a and E_b with the latter being greater but close to the former. This system is not just a theoretical abstraction but can be found in nature, for example two close but isolated (from the others) levels of an atom, the two levels of electronic spin in a magnetic field etc.

An excitation of the two level system is considered as being coherent if the wavefunctions of each level are in phase during the excitation time. In this case the wavefunction $|\Psi\rangle$ of the system is a linear combination of $|a\rangle$ and $|b\rangle$ and the system is considered as being in a coherent superposition of those two eigenstates. Thus the wavefunction of that describes the state of the system can be written as:

$$|\Psi\rangle = a(t)\, e^{-iE_a t/\hbar}\, |a\rangle + b(t)\, e^{-i(E_b t-\Phi)/\hbar}\, |b\rangle \quad (60)$$

where $|a(t)|^2 + |b(t)|^2 = 1$ and Φ a phase factor. Such a state is called "pure state"[56,57] and the meaning of this term will be clarified below. All of the properties of the system (described by eq. 6) can be calculated by finding the expectation values of the corresponding operators.

An alternative way of describing observable quantities for the above system is through the density matrix formalism. The density matrix ρ of the system described by eq. 6 can be constructed by using the state vectors as follows:

$$\rho = |\Psi\rangle\langle\Psi| = \begin{pmatrix} |a(t)|^2 & a(t)b(t)\,e^{-i[(E_a-E_b)t+\Phi]/\hbar} \\ a(t)b(t)\,e^{i[(E_a-E_b)t+\Phi]/\hbar} & |b(t)|^2 \end{pmatrix} = \begin{pmatrix} \rho_{aa} & \rho_{ab} \\ \rho_{ba} & \rho_{bb} \end{pmatrix} \quad (61)$$

In this formalism the expectation value of an observable corresponding to an operator $\wp$ can be calculated from:

$$\langle\wp\rangle = Tr(\rho\wp) \qquad (62)$$

where Tr denotes the trace of the quantity in parenthesis. The diagonal elements, of the density matrix ρ_{aa} and ρ_{bb}, give the probability of finding the system in the eigenstates $|a\rangle$ and $|b\rangle$ respectively.

The meaning of the non diagonal elements can be understood by considering an ensemble of systems with two levels each and all of them described by state vectors $|\Psi_k\rangle$ similar to the one of equation (6). However the these wavefunctions are not identical as they may vary in their phase factor. The fraction of systems in a specific $|\Psi_k\rangle$ state is described by a probability distribution P_k over the ensemble. If P_k =1 for $k = k_o$ and zero fro any other k then the ensemble is considered as being in a "pure state". I a different case though where P_k is non zero for a number of values of k then the ensemble is considered as being in a statistical mixture of states[56,57]. Considering the ensemble as consisting of an infinite number of systems according to the ergodic hypothesis[58] the same description holds for a single system considered in an infinite period of time. By taking into account the probability distribution of the density matrix of the ensemble can be written as:

$$\rho = \sum_k P_k \begin{pmatrix} |a(t)|^2 & a(t)b(t)\,e^{-i[(E_a-E_b)t+\Phi]/\hbar} \\ a(t)b(t)\,e^{i[(E_a-E_b)t+\Phi]/\hbar} & |b(t)|^2 \end{pmatrix} = \begin{pmatrix} \rho_{aa} & \rho_{ab} \\ \rho_{ba} & \rho_{bb} \end{pmatrix} \qquad (63)$$

In this case if the distribution of values of Φ is random for this ensemble (i. e. the phase factors corresponding to the individual systems of the ensemble are completely uncorrelated), then the non diagonal elements average to zero and the system is considered as incoherently excited. Under this circumstances the density matrix will be:

$$\rho_{inc} = |\Psi\rangle\langle\Psi| = \begin{pmatrix} |a(t)|^2 & 0 \\ 0 & |b(t)|^2 \end{pmatrix} \quad (64)$$

However if the phase factors Φ of the ensemble are related then the non diagonal elements of ρ do not vanish and the system is considered as being in a coherent state. In this case the non diagonal elements of the density matrix describe the degree of coherence of the system. An example of a system in a coherent state is the case of a system interacting with a strong electromagnetic field. If all of the dipole moments induced by the field oscillate in phase then the result a macroscopic oscillating dipole moment D.

The equivalent of Schrödinger equation in the density matrix formalism is the Liouville's equation:

$$i\hbar\dot{\rho} = [H, \rho] \quad (65)$$

where $\dot{\rho}$ is the time derivative of the density matrix and H the Hamiltonian of the system. The Hamiltonian can be separated into several contributions such as $H = H_o + H_I + H_R$ where H_o is the Hamiltonian of the unperturbed isolated system, H_I is the interaction term (which in the case that is considered here is the interaction with the electromagnetic field) and H_R is the relaxation term. All of the processes that return the system to thermal equilibrium[54] such as spontaneous emission, collisions, coupling between rotational, vibrational and electronic excitations (in molecules) and others are described by the relaxation Hamiltonian.

By using the relaxation Hamiltonian the decay process from level $|b\rangle$ to level $|a\rangle$ can be described from the relaxation operator matrix element[53,54,59,60]:

$$\frac{-\rho_{bb}}{T_b} = \frac{1}{i\hbar}[H_R, \rho]_{bb} \quad (66)$$

with T_b being the lifetime of the excited state $|b\rangle$ (T_b is also called by some authors[67] as longitudinal lifetime). The decay of the off – diagonal elements of the density matrix decay toward equilibrium is described by the equations[53,54,60,61]:

$$\frac{-\rho_{ab}}{T_2} = \frac{1}{i\hbar}[H_R, \rho]_{ab} \qquad \frac{-\rho_{ba}}{T_2} = \frac{1}{i\hbar}[H_R, \rho]_{ba} \quad (67)$$

The decay of ρ_{ab} and ρ_{ba} describes the decay of coherence which can be viewed in the frame of the polarisation example given above as the decay of the phase relations between the dipoles of the system. The decay time T_2 is called transverse relaxation or dephasing time. It is related with lifetimes of levels $|a\rangle$ and $|b\rangle$ by the equation[53,54]:

$$\frac{1}{T_2} = \frac{1}{2}\left(\frac{1}{T_a} + \frac{1}{T_b}\right) + \gamma_\Phi \qquad (68)$$

In eq. (14) T_a is the lifetime of level $|a\rangle$ and γ_Φ which is called pure dephasing rate is the decay rate due to mechanisms that affect only the phase of the wavefunctions without causing population decay (for example elastic collisions). In a closed two level system the lifetime T_a can be considered as infinite[54] therefore $\frac{1}{T_2} = \frac{1}{2}\frac{1}{T_b} + \gamma_\Phi$.

The above description of the decay rates applies to systems for which the condition $\rho_{aa} + \rho_{bb} = 1$ is valid[54]. For open systems[54] where the $|a\rangle$ and $|b\rangle$ sates are allowed to interact with a reservoir of levels of similar energies a more complicated treatment is needed.

5.4.2 The optical Bloch equations and the rotating wave approximation

When all of the components of the Hamiltonian are known then from eq. (11) the equations of motion of the density matrix elements can be derived known as master equations[54,62]. Although these equations can be solved analytically, more physical insight can be achieved with a simpler approximation, the rotating wave approximation[54,63,64,65]. This approximation will be used below for the description of the interaction of a two level system with an incident electromagnetic field[66,67].

The interaction Hamiltonian in this case will be:

$$H_I = -\mathbf{p}\cdot\mathbf{E} \qquad (69)$$

where $\mathbf{p}$ is the electric dipole moment of the charge particle and $\mathbf{E}$ is the incident electric field. In an atomic two level system the electric dipole moment of the charge particle is given by the equation:

$$\mathbf{p}_{ij} = \int d\mathbf{r}\, \varphi_i^* (-e\mathbf{r}) \varphi_j \qquad (70)$$

where $-e$ is the charge of the particle, $\mathbf{r}$ the position vector of the particle with the origin of the coordinates taken on the nucleus, φ_j the $j(=a,b)$ eigenfunction of the unperturbed system. Since the eigenfunctions of such a system[67,68] have a definite parity and since $\mathbf{r}$ has an odd parity the diagonal elements given by eq. (16) and consequently the diagonal elements of the interaction Hamiltonian will vanish.

In the following two vectors will be introduced:

$$\mathbf{s} = (s_1, s_2, s_3) = (\rho_{ab} + \rho_{ba},\ i(\rho_{ab} - \rho_{ba}),\ \rho_{bb} - \rho_{aa}) \qquad (71)$$

$$\mathbf{\Omega} = \left(\frac{(\mathbf{p}_{ab} + \mathbf{p}^*_{ab}) \cdot \mathbf{E}}{\hbar}, i\frac{(\mathbf{p}_{ab} - \mathbf{p}^*_{ab}) \cdot \mathbf{E}}{\hbar}, -\omega_o \right) \qquad (72)$$

In eq. (17) the vector $\mathbf{s}$ is called Bloch vector and ρ_{ij} are the density matrix elements with $i, j = a,b$. The Bloch vector has unitary modulo for a closed two – level system (i.e. a two level system fro which the condition $\rho_{aa} + \rho_{bb} = 1$ is valid). In eq. (18) vector $\mathbf{\Omega}$ is known as pseudofield vector and $\omega_o = (E_b - E_a)/\hbar$ where E_a and E_b are the eigenenergies of levels $|a\rangle$ and $|b\rangle$ respectively. If momentarily the relaxation terms are ignored, it can be shown that the equations of motion of the density matrix can be expressed[54] by using vectors $\mathbf{s}$ and $\mathbf{\Omega}$ as follows:

$$\frac{d\mathbf{s}}{dt} = \mathbf{\Omega} \times \mathbf{s} \qquad (73)$$

Equation (19) along with eq. (18) are known as optical Bloch equations[67]. They describe the interaction of a two – level system with the electromagnetic field. The fact that $\mathbf{\Omega}$ is time dependent makes the general solution of eq. (19) complicated.

Instead, the simpler case (but very important as it covers a wide range of experiments) of linearly polarised transitions of the two-level system due to the interaction with a linearly polarised nearly monochromatic light field can be considered. In this case the form of excitation is $\mathbf{E} = \boldsymbol{\varepsilon}(t)\cos\omega t$, where $\boldsymbol{\varepsilon}(t)$ is the envelope function of the electric field (defined here as a vector in the direction of the electric field) and ω the angular frequency of the electric field. Furthermore because linearly polarised transitions (i.e. transitions with $\Delta m = 0$) are considered $\mathbf{p}_{ab} = \mathbf{p}^*_{ab} = \boldsymbol{\mu}$. Then the solution

of eq. (19) can be further simplified by applying a unitary transformation that introduces a reference frame which rotates about the z –axis with angular frequency ω. In this new frame equation (19) can be rewritten as:

$$\frac{d\mathbf{s}'}{dt} = \mathbf{\Omega}' \times \mathbf{s}' \qquad (74)$$

where:

$$\mathbf{\Omega}' = \left(\frac{\boldsymbol{\mu} \cdot \boldsymbol{\varepsilon}(t)(1+\cos 2\omega t)}{\hbar}, \frac{-\boldsymbol{\mu} \cdot \boldsymbol{\varepsilon}(t)\sin 2\omega t}{\hbar}, \omega - \omega_o \right) \qquad (75)$$

$$\mathbf{s}' = (s_1', s_2', s_3') = (s_1 \cos \omega t + s_2 \sin \omega t, \quad -s_1 \sin \omega t + s_2 \cos \omega t, \quad s_3) \qquad (76)$$

Under the condition that $\boldsymbol{\mu} \cdot \boldsymbol{\varepsilon}(t)/\hbar << \omega$ and also by considering averaged effects over time periods which are much longer than the period $2\pi/\omega$ of the optical wave (which for the visible has a typical value of 1 fsec), the oscillating terms with frequency 2ω can be neglected. This approximation is known as the rotating wave approximation[54,64,65,67]. Under this approximation $\mathbf{\Omega}'$ takes a simple and time independent form:

$$\mathbf{\Omega}' = (\omega_R, 0, \omega - \omega_o) \qquad (77)$$

where $\omega_R = \boldsymbol{\mu} \cdot \boldsymbol{\varepsilon}(t)/\hbar$ and the quantity $\omega - \omega_o$ is called detuning. Equations (20) and (23) lead to the following system of differential equation:

$$\frac{ds_1'}{dt} = -(\omega - \omega_o)s_2', \quad \frac{ds_2'}{dt} = (\omega - \omega_o)s_1' - \omega_R s_3', \quad \frac{ds_3'}{dt} = -\omega_R s_2' \qquad (78)$$

The physical significance of the quantities s_1', s_2', s_3' can be sought back in equations (22), (17) and the definition of the density matrix. It can be seen from those that s_3' expresses the population difference of the two levels and can take values from 1 to -1, with 1 meaning fully inversion of the population to the upper level, while -1 means that all the population is in the ground state. In a similar way it can be seen that s_1' and s_2' are the amplitudes of the components of the dipole moment which are in phase and in quadrature with the driving field $\mathbf{E}$. The third from the left of the equations (24) shows further, that s_2' is the component effective in coupling to the driving field to produce energy changes[65]. Thus s_2' is the absorptive component of the dipole moment and s_1' the dispersive one.

It can be shown[65] that for zero detuning the solution of system (24) is:

$$s_1'(t) = s_{1o}' \qquad (79a),$$

$$s_2'(t) = s_{3o}' \sin(\theta(t)) + s_{2o}' \cos(\theta(t)) \quad (25b),$$

$$s_3'(t) = -s_{2o}' \sin(\theta(t)) + s_{3o}' \cos(\theta(t)) \quad (25c)$$

where $s_{1o}' = s_1'(t=0)$, $s_{2o}' = s_2'(t=0)$, $s_{3o}' = s_3'(t=0)$. The quantity $\theta(t)$ is called input area and is defined by the relation:

$$\theta(t) = \int_{-\infty}^{t} \frac{\boldsymbol{\mu}}{\hbar} \boldsymbol{\varepsilon}(t')dt' \qquad (80)$$

Considering an excitation with a CW laser beam then $\boldsymbol{\varepsilon}(t) = \mathbf{E}_o$ for $t > 0$ and thus eq. (26) yields:

$$\theta(t) = \boldsymbol{\mu}\mathbf{E}_o t/\hbar \qquad (81)$$

For a system which at time $t = 0$ is in its ground state (i.e. only the lower level of the system is populated) the corresponding initial conditions for s_1', s_2', s_3' are:

$$s_{1o}' = s_{2o}' = 0, \quad s_{3o}' = -1 \qquad (82)$$

Using equations (25c), (27), (28) the solution for the s_3' can be written as $s_3'(t) = -\cos(\omega_r t)$ where $\omega_r = \boldsymbol{\mu}\mathbf{E}_o/\hbar$ is known as the Rabi frequency. Taking also into account the definition s_3' as well as that the system under consideration conserves probability the above solution for s_3' leads to an expression for the time evolution of the population of the upper level which is $\rho_{bb} = \sin^2(\omega_r t/2)$. It can been seen from this expression (Figure 5-4) that under resonant CW excitation the probability of populating the upper level is oscillating with time between one and zero (the same obviously holds for the lower level with a phase difference of π).

The system of differential equations (24) can be solved for non –zero detuning for the case of CW excitation (eq. 27) and for the initial conditions (28). The expression of ρ_{bb} (which is more general) becomes[65,67]:

$$\rho_{bb} = \frac{\omega_r^2 \sin^2\left(\frac{\sqrt{(\omega-\omega_o)^2 + \omega_r^2}}{2} t\right)}{(\omega-\omega_o)^2 + \omega_r^2} \qquad (83)$$

As it can be seen from Figure 5-4 the further away from resonance the excitation the smaller the amplitude of the oscillation becomes. As it was expected the probability of populating the upper level gets reduced as the energy of the excitation differs from resonance.

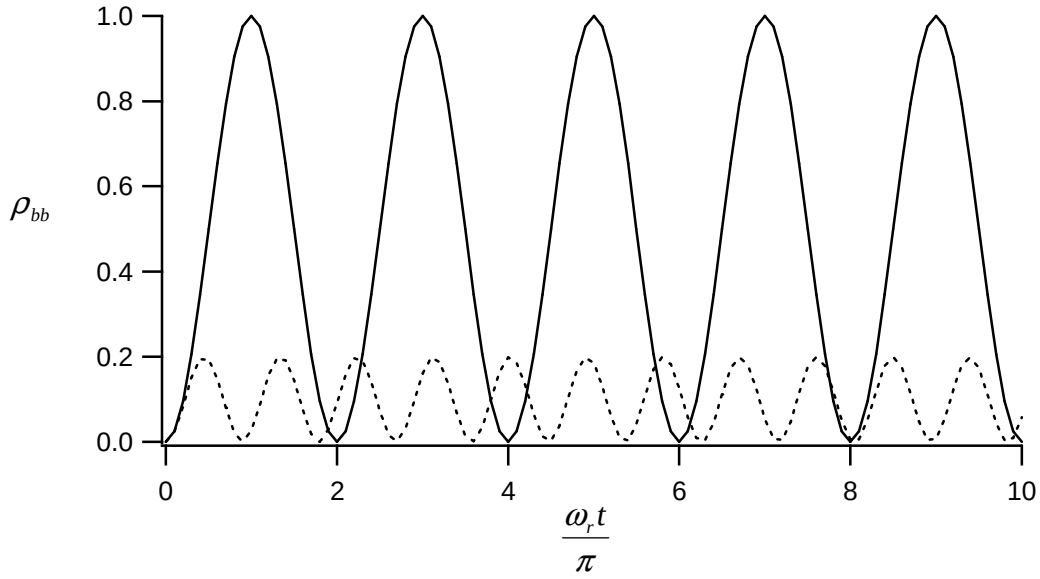

Figure 5-4 Rabi oscillations of the upper level population of a two level system under resonant cw excitation for zero detuning (solid line) and for detuning equal to $2\omega_r$ (dashed line).

Under pulsed excitation and for zero detuning the population can be coherently controlled[69]. If the temporal width τ_p of the pulse is much smaller than the dephasing time[70] and the initial conditions of eq. 28 hold then according to eq. 25c, 26, the population of the upper level can be controlled by exciting with a pulse of the appropriate input area. As θ increases from zero the population of the upper level increases, and for $\theta = \pi$ reaches full inversion. By increasing θ further the population of the upper level drops and becomes zero for $\theta = 2\pi$. The latter is a remarkable result; it means that pulses with resonant frequency will be transmitted through the system unattenuated[54]. This will happen because the first half of the pulse will give rise to a full population inversion while the second half leads to the stimulating emission of the inverted population[69]. If for example the envelope function of a pulse has a secant form $E(t) = E_o \sec h(t/\tau_p)$ then the input area for this pulse is[70] $\mu E_o \int_{-\infty}^{t} dt \sec h(t/\tau_p)/\hbar = \pi\mu E_o \tau_p/\hbar$. This suggests that input

area of the pulse can be controlled by varying its intensity as $E_o \approx \sqrt{I_o}$ where I_o is the peak intensity of the pulse. This kind of population oscillations as a function of the input pulse area have been observed for atomic systems such as an Rb atomic beam[71] as it can be seen in Figure 5–5. The same effect has also been observed in quantum dots as it will be presented below.

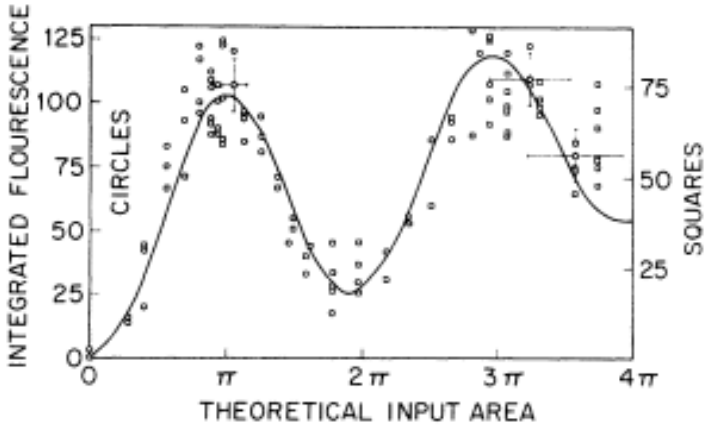

Figure 5-5 Oscillations of the population of an excited state of a Rb atomic beam probed through the means of time – integrated photoluminescence. After 71.

References:

[1] L. Jacak, P. Hawrylak, A. Wójs, "Quantum Dots", Springer Verlag, Berlin, Heidelberg, (1998).

[2] D. Bimberg, M. Grundmann, N. N. Ledentsov, "Quantum Dot Heterostructures", John Wiley & Sons, Chichester, New York, (1999).

[3] U. Woggon, "Optical Properties of Semiconductor Quantum Dots", Springer Verlag, Berlin, Heidelberg, New York, (1997).

[4] G. W. Bryant, G. S. Solomon, (editors), "Optics of Quantum Dots and Wires", Artech House, Inc., Boston, London, (2005).

[5] F. Rossi (editor), "Semiconductor Macroatoms: Basic Physics and Quantum – device Applications", Imperial College Press, London, (2005).

[6] R. Oulton, "Optical spectroscopy of single self-assembled InGaAs/GaAs quantum dots", Thesis (Ph.D.), University of Sheffield, (2003).

[7] P. W. Fry, "Optical spectroscopy of InGaAs GaAs self assembled quantum dots", Thesis (Ph.D.), University of Sheffield, (2001).

[8] P. Michler (editor), "Single Quantum Dots: Fundamentals, Applications and New Concepts", Springer Verlag, Berlin, Heidelberg, (2003).

[9] P. Borri, "Coherent Light – Matter Interaction in Semiconductor Quantum Dots", Habilitationsschrift, University of Dortmund, (2004).

[10] Y. Masumoto, T. Takagahara (editors), "Semiconductor Quantum Dots: Physics Spectroscopy and Applications", Springer Verlag, Berlin, Heidelberg, (2002).

[11] L. Bányai, S. W. Koch, "Semiconductor Quantum Dots", World Scientific, Singapore, New Jersey, London, Hong Kong, (1993).

[12] R. Colombelli, V. Piazza, A. Badolato, M. Lazzarino, F. Beltram, W. Schoenfeld, P. Petroff, "Conduction-band offset of single InAs monolayers on GaAs", Appl. Phys. Lett., 76, 1146, (2000).

[13] T. Kita, D. Chiba, Y. Ohno, H. Ohno, "(In,Ga)As gated-vertical quantum dot with an Al2O3 insulator", Appl. Phys. Lett. 90, 062102, (2007).

[14] J.M. Martínez-Duart, R.J. Martín-Palma, F. Agulló-Rueda, "Nanotechnology for microelectronics and optoelectronics", Elsevier, Amsterdam, (2006).

[15] C. E. Finlayson, " Optical Characterisation of Semiconductor Nanocrystals", Thesis (Ph.D.), University of Cambridge, (2001).

[16] J.J.Shaing, A.V.Kadavanich, R.K.Grubbs, A.P.Alivisatos, "Symmetry of Annealed Wurtzite CdSe Nanocrystals: Assignment to the C3v Point Group" J. Phys. Chem., 99, 17417 (1995).

[17] R W. Kelsall, I. W. Hamley, M. Geoghegan (editors), "Nanoscale Science and Technology", John Wiley & Sons Ltd, Chichester, (2005).

[18] X.Peng, M.C.Schlamp, A.V.Kadavanich, and A.P.Alivisatos, J. Am. Chem. Soc., 119, 7019 (1997).

[19] B.O.Dabbousi, J.Rodriguez-Viejo, F.V.Mikulec, J.R.Heine, H.Mattoussi, R.Ober, K.F.Jensen, and M.G.Bawendi, J. Phys. Chem. B, 101, 9463 (1997).

[20] K.N. Bourdakos, D.M.N.M. Dissanayake, T. Lutz, S.R.P. Silva, R.J. Curry, "Highly Efficient Near-Infrared Hybrid Organic-Inorganic Nanocrystal Electroluminescence Device", Appl. Phys. Lett. (to be published).

[21] I. N . Stranski., L. Krastanow, Akad. Wiss. Let. Mainz Math. Natur K1 IIb 146, 797 (1939).

[22] P. M. Petroff, S. P. Denbaars, "MBE and MOCVD growth and properties of self-assembling quantum-dot arrays in III-V semiconductor structures", Superlattices and Microstructures, 15 (1): 15-21 (1994).

[23] J. -Y. Marzin, J. -M. Gérard, A. Izraël, D. Barrier, G. Bastard, "Photoluminescence of Single InAs Quantum Dots Obtained by Self-Organized Growth on GaAs ", Phys. Rev. Lett. 73, 716, (1994).

[24] S. Raymond, S. Fafard, P. J. Poole, A. Wojs, P. Hawrylak, S. Charbonneau, D. Leonard, R. Leon, P. M. Petroff, and J. L. Merz, "State filling and time-resolved photoluminescence of excited states in InxGa1-xAs/GaAs self-assembled quantum dots",Phys. Rev. B 54, 11548, (1996).

[25] P. K. Basu, “Theory of Optical Processes in Semiconductors: Bulk and Microstructures”, Oxford University Press, New York, 1997.

[26] G. Bastard, E. Molinari, “Fundamentals of Zero – Dimensional Nanostructures”, in "Semiconductor Macroatoms: Basic Physics and Quantum – device Applications", ed. F. Rossi, Imperial College Press, London, (2005).

[27] M. Grundmann, O. Stier, D. Bimberg, "InAs/GaAs pyramidal quantum dots: Strain distribution, optical phonons,and electronic structure", Phys.Rev. B, 52, 11969,(1995).

[28] P. Y. Yu, M. Cardona, “Fundamentals of Semiconductors: Physics and Material Properties”, Springer – Verlag, Berlin, Heidelberg, New York, (1996).

[29] T. Wenckebach, “Essentials of Semiconductor Physics”, John Wiley & Sons Ltd, Chichester, New York, Weinheim, Brisbane, Singapore, Toronto, (1999).

[30] L. R. Wilson, D. J. Mowbray, M. S. Skolnick, M. Morifuji, M. J. Steer, I. A. Larkin, "Magneto-optical studies of self-organized InAs/GaAs quantum dots", Phys. Rev. B, 47, R2073, 1998.

[31] R. Heitz, O. Stier, I. Mukhametzhanov, A. Madhukar, D. Bimberg, "Quantum size effect in self-organized InAs_GaAs quantum dots",Phys. Rev. B, 62, 011017,2000.

[32] M. Bissiri, G. Baldassarri Höger von Högersthal, M. Capizzi, P. Frigeri, S. Franchi, "Quantum size and shape effects on the excited states of $In_xGa_{1-x}As$ quantum dots",Phys. Rev. B, 64, 245337,2001.

[33] J. Kim, L. W. Wang, A. Zunger, "Comparison of the electronic structure of InAs/GaAs pyramidal quantum dots with different facet orientations", Phys. Rev. B 57, R9408 (1998).

[34] A. J. Williamson, “Energy States in Quantum Dots”, in “Quantum dots”, ed. E. Borovitskaya, M. S. Shur, Selected Topics in Electronics and Systems - Vol. 25, World Scientific Publishing Co. Pte. Ltd., New Jersey,London,Singapore, Hong Kong, (2002).

[35] P. Hawrylak, M. Korkusiński, “Electronic Properties of Self-Assembled Qauntum Dots”, in P. Michler (editor), "Single Quantum Dots: Fundamentals, Applications and New Concepts", Springer Verlag, Berlin, Heidelberg, (2003).

[36] P. M. Petroff, “Epitaxial Growth and Electronic Structure of Self-Assembled Qauntum Dots”, in P. Michler (editor), "Single Quantum Dots: Fundamentals, Applications and New Concepts", Springer Verlag, Berlin, Heidelberg, (2003).

[37] A. Hartmann, Y. Ducommun, E. Kapon, U. Hohenester, E. Molinari, "Few-Particle Effects in Semiconductor Quantum Dots Observation of Multicharged Excitons", Phys. Rev. Lett. 84, 5648, (2000).

[38] D. V. Regelman, E. Dekel, D. Gershoni, E. Ehrenfreund, A. J. Williamson, J. Shumway, A. Zunger, W. V. Schoenfeld P. M. Petroff, "Optical spectroscopy of single quantum dots at tunable positive neutral and negative charge states", Phys. Rev. B,64, 165301, (2001)

[39] O. Stier, "Electronic and Optical Properties of Quantum Dots and Wires", Berlin Studies in Solid State Physics 7,(ISBN 3-89685-366-X),Wissenschaft & Technik Verlag, Berlin 2000.

[40] S. Rodt, A. Schliwa, R. Heitz , V. Turck, O. Stier,R. L. Sellin, M. Strassburg, U. W. Pohl, D. Bimberg, "Few-Particle Effects in Self-Organized Quantum Dots",phys. stat. sol. (b) 234, 354, (2002).

[41] J. J. Finley, A. D. Ashmore, A. Lemaitre, D. J. Mowbray, M. S. Skolnick, I. E. Itskevich, P. A. Maksym, M. Hopkinson, T. F. Krauss,"Charged and neutral exciton complexes in individual self-assembled In(Ga)As quantum dots" Phys. Rev. B, 63 073307,(2001).

[42] L. Besombes, J. J. Baumberg, J. Motohisa,"Coherent Spectroscopy of Optically Gated Charged Single InGaAs Quantum Dots", Phys. Rev. Lett. 90, 257402, (2003)..

[43] J.J. Finley, A. Lemaitre, A.D. Ashmore, D.J. Mowbray, M.S. Skolnick, M. Hopkinson, T.F. Krauss,"Excitation and Relaxation Mechanisms in Single In(Ga)As Quantum Dots", phys. stat. sol. (b), 224, 373, (2001).

[44] L. Bányai, "Asymptotic biexciton "binding energy" in quantum dots", Phys. Rev. B, 39, 8022, (1995).

[45] P. Lelong, G. Bastard, In Proceedings of 23rd International Conference on the Physics of Semiconductors, Berlin, Germany, (eds.) M. Scheffler, R. Zimmermann, (1996), World Scientific, Singapore.

[46] L. Landin, M.-E. Pistol, C. Pryor, M. Persson, L. Samuelson, M. Miller, "Optical investigations of individual InAs quantum dots: Level splittings of exciton complexes", Phys. Rev. B, 60, 16640, (1999).

[47] M. Bayer, A. Kuther, F. Scha¨fer, J. P. Reithmaier, A. Forchel, "Strong variation of the exciton g factors in self-assembled $In_{0.60}Ga_{0.40}As$ quantum dots", Phys. Rev. B, 60, R8481, (1999).

[48] F. Troiani, U. Hohenester, E. Molinari, "Few – Particle Effects in Semiconductor Macroatoms/Molecules", " in "Semiconductor Macroatoms: Basic Physics and Quantum – device Applications", ed. F. Rossi, Imperial College Press, London, (2005).

[49] M. Bayer, O. Stern, P. Hawrylak, S. Fafard, A. Forchel, "Hidden symmetries in the energy levels of excitonic 'artificial atoms'", Nature, 405, 923, (2000)

[50] R. Rinaldi, S. Antonaci, M. DeVittorio, R. Cingolani, U. Hohenester, E. Molinari, H. Lipsanen, J. Tulkki, "Effects of few-particle interaction on the atomiclike levels of a single strain-induced quantum dot", Phys. Rev. B, 62, 1592, (2000).

[51] E. Dekel, D. Gershoni, E. Ehrenfreund, D. Spektor, J. M. Garcia, P. M. Petroff, "Multiexciton Spectroscopy of a Single Self-Assembled Quantum Dot", Phys. Rev. Lett. 80, 4991, (1998).

[52] E. Dekel, D. Gershoni, E. Ehrenfreund, J. M. Garcia, P. M. Petroff, "Carrier-carrier correlations in an optically excited single semiconductor quantum dot", Phys. Rev. B, 61, 11009, (2000).

[53] W. Demtröder, "Laser Spectroscopy: Basic Concepts and Instrumentation ", (3d) Edition, Springer-Verlag, Berlin, Heidelberg, (2003).

[54] M. D. Levenson, S. S. Kano, "Introduction to Nonlinear Laser Specroscopy", (Revised Edition), (ISBN: O-12-444722-8), Academic Press, Inc. San Diego, London, (1988).

[55] J. T. Verdeyen, "Laser Electronics", (3d) Edition in "Prentice Hall Series in Solid State Physical Electronics", N. Holonyak, Jr., Series Editor, Prentice Hall, New Jersey, (1995).

[56] S. Mukamel, "Principles of Nonlinear Optical Spectroscopy", p. 47, Oxford University Press, (1995).

[57] C. Cohen-Tannoudji, B. Diu, F. Laloe, "Quantum mechanics",p.253-259,Wiley,New York, London, (1977).

[58] A. Isihara, "Principles of Statistical Mechanics",p.24,Academic Press,New York, London, (1971).

[59] C. Cohen-Tannoudji, J. Dupont-Roc, G. Grynberg, “Atom – Photon Interactions: Basic Processes and Applications”, p.283, J. Wiley, New York, (1992).

[60] P. W. Milonni, J. H. Eberly, "Lasers", p.203, Wiley, New York, Chichester, 1988.

[61] C. Cohen-Tannoudji, J. Dupont-Roc, G. Grynberg, “Atom – Photon Interactions: Basic Processes and Applications”, p.602, J. Wiley, New York, (1992).

[62] S. Mukamel, “Principles of Nonlinear Optical Spectroscopy”, p. 177, Oxford University Press, (1995).

[63] C. Cohen-Tannoudji, J. Dupont-Roc, G. Grynberg, “Atom – Photon Interactions: Basic Processes and Applications”, J. Wiley, New York, (1992).

[64] P. W. Milonni, J. H. Eberly, "Lasers",, Wiley, New York, Chichester, 1988.

[65] L. Allen, J. H. Eberly, “Optical Resonance and Two - Level Atoms”, Dover Publications, New York, (1987).

[66] A. Yariv, “Quantum Electronics”, 3d edition, John Wiley and Sons, New York, (1989).

[67] P. Borri, W. Langbein, “Dephasing Processes and Carrier Dynamics in (In, Ga)As Quantum Dots” in "Single Quantum Dots: Fundamentals, Applications and New Concepts", P. Michler (editor), Springer Verlag, Berlin, Heidelberg, (2003).

[68] L. I. Schiff "Quantum mechanics", p.74, 1st edition, McGraw-Hill, New York (1949).

[69] H. Htoon, C-K. Shih, “Ultrafast Coherent Dynamics in Semiconductor Quantum Dots”, in “Ultrafast Dynamical Processes in Semiconductors”, K-T. Tsen (ed.), Topics in Applied Physics, vol. 92, Springer-Verlag, Berlin, Heidelberg, (2004).

[70] H. Kamada, H. Gotoh, J. Temmyo, T. Takagahara, H. Ando,"Exciton Rabi Oscillation in a Single Quantum Dot", Phys. Rev. Lett. 87, 246401, (2001).

[71] H. M. Gibbs, “Incoherent Resonance Fluorescence from a Rb Atomic Beam Excited by a Short Coherent Optical Pulse”, Phys. Rev. A, 8, 446, (1973).

Chapter 6 Single Quantum Dot Optical Spectroscopy

6.1 Introduction

In this chapter is reported the work that was done on single dot spectroscopy. Our initial aim was to investigate the coherence of the ground state by applying a two colour pumped time resolved photoluminescence technique. The reason for applying the aforementioned technique was to tackle the bad signal to noise ratio of the conventional pump and probe method (which in any case was applied on the same sample without any success in previous work). Although the final aims of this project were not completely achieved, the Photoluminescence Excitation spectroscopy and the resonant power dependence measurements revealed features of the single quantum dot system which to our knowledge have not been reported in the literature.

6.2 Sample

The sample[1] was prepared by the group of Professor Junishi Motohisa at the university of Hokkaido in Japan. It was grown according to the Stranski –Krastanow[2,3] method by the means of Metal Organic Chemical Vapour Deposition (MO – CVD)[3]. An undoped GaAs substrate was used. A buffer layer of GaAs was grown on the top of the substrate. On the buffer a thin layer of 1.8 monolayers of InAs was deposited. The InAs layer formed islands - dots in order to accommodate the strength due to the lattice mismatch (Stranski –Krastanow mechanism). The as formed dots are of near - pyramidal shape[4] with heights between 5 and 8 nm and lateral sizes between 10 and 40 nm. All of the pyramidal dots sit on an InGaAs wetting layer. A GaAs capping layer of 300 nm was deposited by means of low temperature growth[5] on the top of the dots. The average density of dots is between 1 and 5 3 10^9 cm^{-2}.

On the surface of the capping layer an aluminium mask with circular and square apertures of various sizes (300 nm to 5 μm) was fabricated (Figure 6-1). The mask was fabricated with standard photolithography and lift off techniques. The various size apertures are needed in order to characterise the sample as a whole and also to allow single dot spectroscopy. The big apertures enable a relatively quick characterisation of the different areas on the sample. The small apertures will be used for the micro

photoluminescence measurements. They mean that only a small area of the sample is exposed on the beam. Because the density of the dots on the sample is low and also not completely homogenous there are some apertures with very few dots. Single dot spectroscopy can be performed by applying spectral filtering on the photoluminescence[vi] emitted by the dots of those apertures.

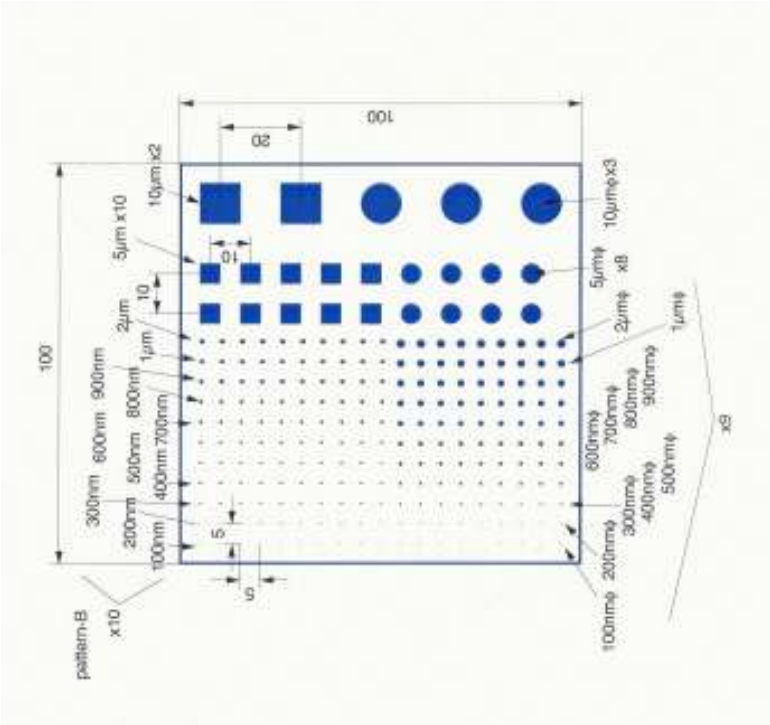

Figure 6-1 One of the repeated patterns of the aluminium mask that covers the quantum dot substrate.

6.3 Initial Pump and Probe Experiments

Before the start of the work discussed here a first attempt to study the coherence of the ground state of a single quantum dot on the above sample was made by means of a pump and probe technique. In this specific technique we used three pulses; two probes and one pump all of them tuned at the energy of the dot ground state. The first probe arrives at the sample before the pump and it has vertical polarisation. This pulse will be used as a reference for the second probe. The second pulse is the pump and it excites

[vi] The random dot size allows the dots o be filtered spectrally, i.e. the likelihood of two dots having exactly the same size and shape and therefore the same spectrum is extremely low.

resonantly the ground state. The third pulse is the second probe which arrives at the same time or later than the pump. The spot size of the probes is about 10μm in diameter. Assuming that the spot is perfectly centred on the quantum dot only a small fraction of it will be absorbed (first probe) which corresponds to a disc of at most 40nm in diameter (i.e. a disc with a diameter equal to the lateral size dot). The second probe will find the ground state of the dot occupied and therefore it will not be absorbed. The difference between the two probes is the signal and corresponds to the fraction of the probe that has been absorbed when the pump is not present. By taking into account an exciton lifetime of the order of 1 ns and assuming that one photon per pulse is absorbed by the quantum dot, one would expect that the absorbed power would be equal with a few tens of pW. Considering now a background of the order of 1mW the resulting S/N is of the order of 10^{-8} which is at the limit of detection. However those ideal values of the signal might be decreased by practical difficulties such as the impossibility of centring the beam exactly on the dot, the non perfect Gaussian shape of the beam and the tiny amount of power that corresponds at the component of the pulse which is exactly equal with the energy of the ground state. The 10^{-8} S/N ratio is at the limit of detectability and it was found the experiments were unable to detect any effect[vii]. This first attempt failed to produce any results and the next alternative was to apply a two colour pump time resolved photoluminescence experiment.

6.4 Two colour Pump Time Resolved Photoluminescence

To resolve some of the problems observed with experiments discussed above a new experiment was proposed. This is a two colour two pulse experiment. The one pulse is tuned exactly at the energy of the ground state of the dot (first pulse) and the other one is the second harmonic of the first pulse and pumps the GaAs barriers exciting the dot non-resonantly. As the carriers relax they fill the states of the dot. However the occupation of the p-state is strongly depend upon the occupation of the s-state which is controlled by the first pulse. Therefore the p photoluminescence should provide a useful

[vii] Also a variant of the pump and probe experiment where the pump was tuned at the energy of the p – state of the dot did not yield any results.

probe for the s state whose coherence now can be studied by means of coherent control[6,7] or Rabi oscillations[8,9] experiments.

The advantage of this technique in comparison with the pump and probe experiment above is the zero background to the signal and therefore the improvement of the S/N by many orders of magnitude.

6.5 Spectroscopic characterisation

6.5.1 Non resonant Photoluminescence experimental setup

The setup which was used to acquire non resonant photoluminescence spectra is depicted in Figure 6-2. Picosecond pulses at 935 nm from a Ti:Al_2O_3 laser were frequency doubled by a BBO crystal. Their energy was controlled by a liquid crystal modulator and they were focused on the sample by x50 long working distance microscope objective with 0.45 NA. The sample was held in a continuous flow He

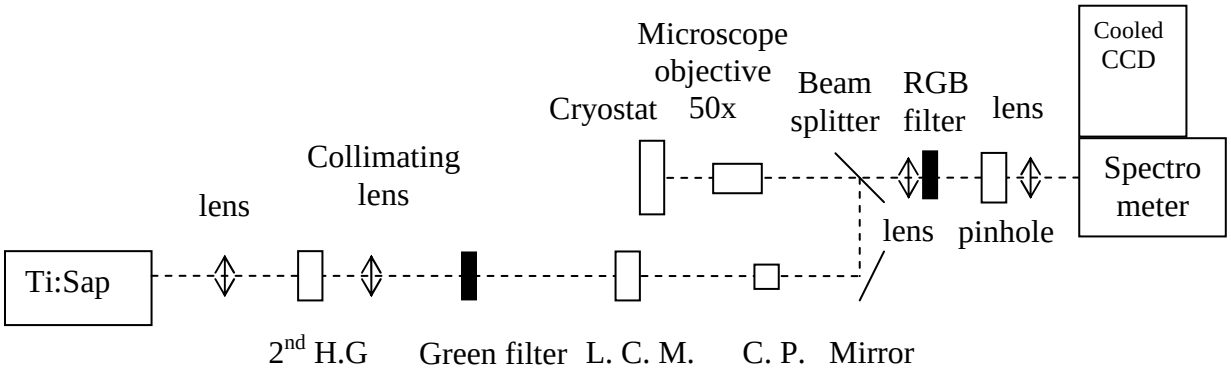

Figure 6-2 Setup for non-resonant Photoluminescence measurements (H.G. = Harmonic Generation, L.C.M.= Liquid Crystal Modulator, C.P.= cube polarizer). The microscope objective (NA=0.45 – check) is corrected to infinity and the lens after has 20 cm focal length and works as a tube lens.

cryostat at a temperature of 6K. The photoluminescence of the sample was collected by the same objective and dispersed by a 1200 grating on a 1024 x 256 nitrogen cooled CCD array. The back reflection of the excitation was cut by an RGB filter. A pinhole was used for spatial filtering so that the luminescence of only one aperture of the mask reached the spectrometer.

6.5.2 Non resonant Photoluminescence measurements

In order to be able to distinguish clearly the p-state photoluminescence of a single dot a low density area of the sample is needed. The reason is that it is desired to have a low density of lines on which it will be possible to apply spectral filtering (with a band pass filter) so as to isolate the line that will be used as a probe (the p-state line in this case). An aperture with the above features was found and its non resonant photoluminescence spectrum is shown in Figure 6-3. This aperture will be referred to from now on as aperture 6 (ap6). In the graph of Figure 6-3 there are two prominent lines at the low energy side (long wavelengths), at 934.8nm and 935.2nm which have been assigned to exciton and biexciton lines of a single quantum dot (which will be referred from now on as quantum dot 6 - qd6). Further evidence to support this assignment will be presented in the power dependence measurements.

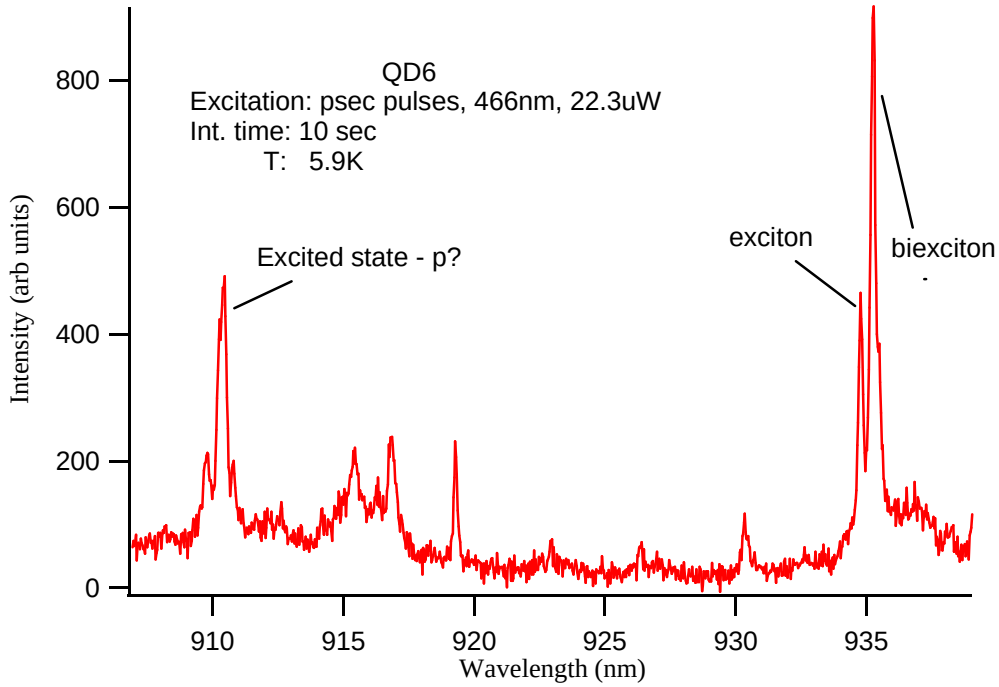

Figure 6-3 Ground state and possible first excited state of quantum dot 6. Non resonant excitation at 466nm by psec pulses.

At the high energy side of the graph there is another prominent line at 910nm. This line is about 35 meV above the energy of the s – exciton transition. In previous measurements on other parts of the sample this separation was attributed to the separation between p and s states (Figure 6-4). Therefore was considered as the most likely to be the p-state of the quantum dot.

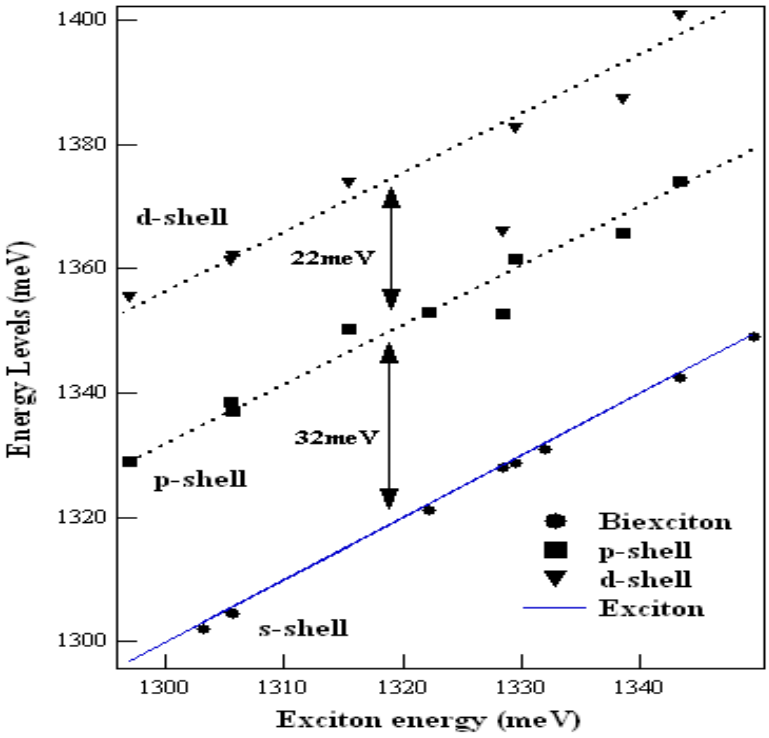

Figure 6-4 Energy separaton of s,p and d shells for eight different quantum dots on the sample. It appears that the energy difference between the s and the p shells is around 32meV (research carried out by Dr. L. Besombes).

6.5.3 Power dependence of non-resonant photoluminescence

Below are presented the power dependence photoluminescence measurements which were acquired by the means of the setup of Figure 6-2. In these scans the power ranges five orders of magnitude from 0.03 up to 300 μW.

As it can be seen in Figure 6-5 in the spectral window of the measurements eleven spectral lines could be observed. Three of them (lines 1, 2, 3) can be distinguished by their strength. Especially at the low excitation powers (<2.25μW) they are the only lines observed. By examining the evolution of those lines as the excitation power rises it can be seen that line 1 is the only line observed for very low powers (0.55 μW). It evolves faster and reaches saturation at about 3μW as it is shown in Figure 6-6 where the power profiles of the most prominent spectral lines have been plotted. Line 1 seems to have a linear dependence upon the excitation power. Line 2 appears at the low energy side of line 1 and at very close proximity with it. The energy separation between the two lines is 0.7 meV (Figure 6-7). The strength of

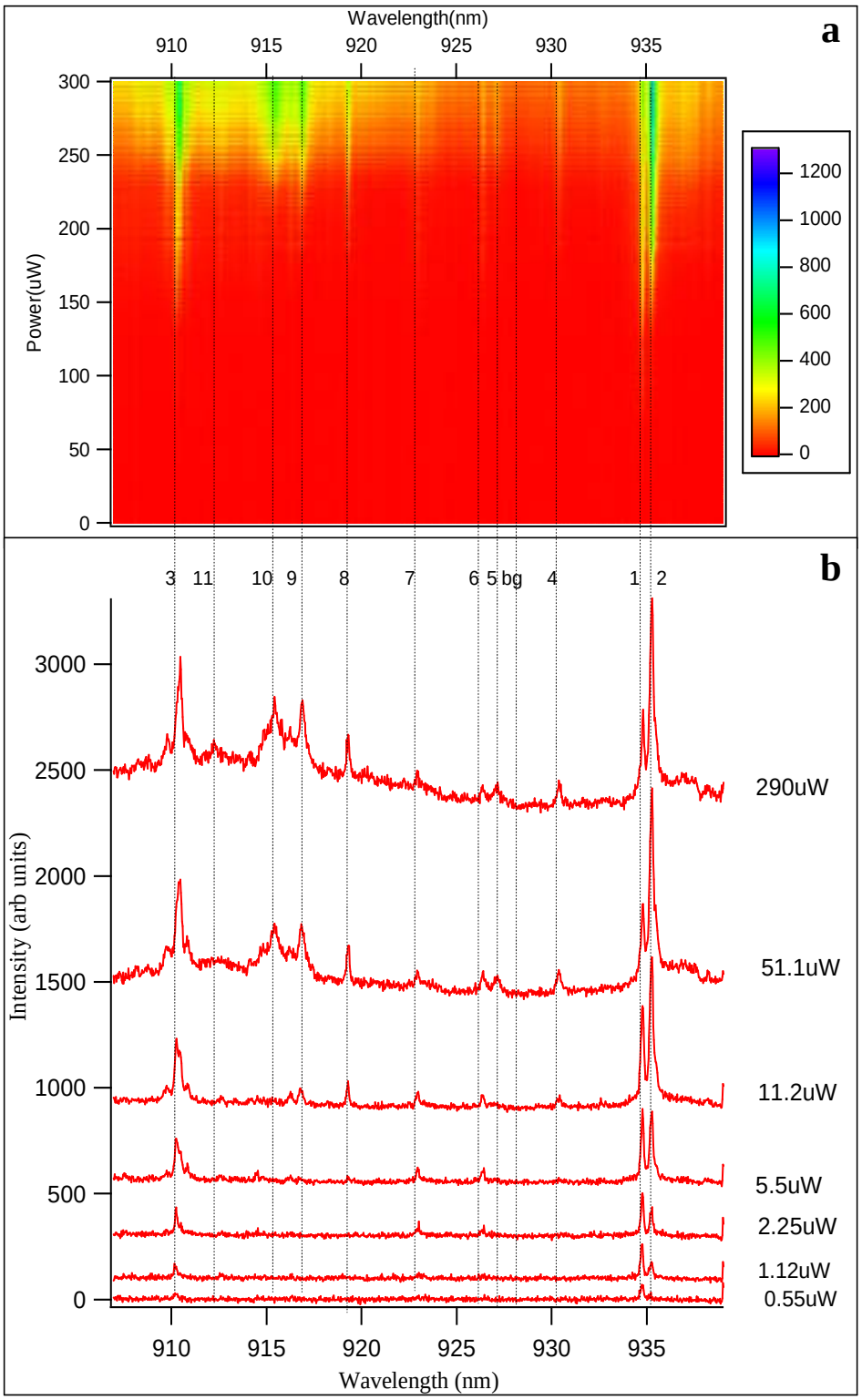

Figure 6-5 a) A map of the PL intensity (colour scale) obtained from **aperture 6** as a function of wavelength (horizontal axis) and excitation power (vertical axis). Picosecond pulses at 467 nm were used and the sample was kept at a temperature of 6 K. **b)** Horizontal slices from the map above which show the pl spectra for various powers. The slices have been offset for clarity.

line – 2 is enhanced considerably after line – 1 reaches saturation and it saturates at the excitation power of 20μW (Figure 6-6). Its dependence on power is superlinear. The power dependence of lines 1 and 2, lead to the identification[10,11,12] of those lines as the exciton (line 1) and biexciton (line 2) recombinations of the s-shell of quantum dot– 6.

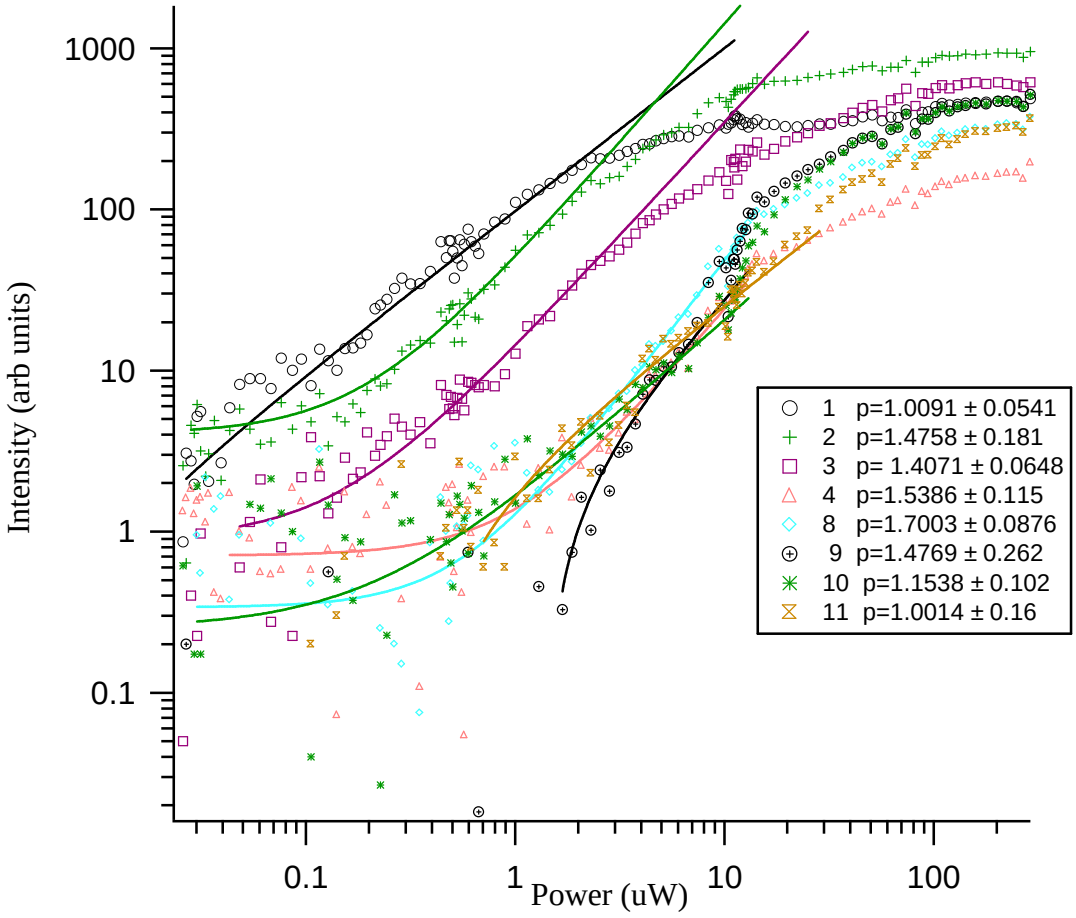

Figure 6-6 Power dependence profiles (markers) of the lines depicted in fig.5. Each line is the corresponding vertical slice of fig. 5a. In the inset are given the power law fit exponents for each power profile respectively.

Line – 3 of Figure 6-5 appears at approximately the same power as the biexciton. This is something expected for the recombination from the p-shell and it is a consequence of the Pauli exclusion – principle. Photo-excited electrons and holes with the same spin as those occupying the ground state can only populate the p-shell excited state as their relaxation to the ground state has been blocked. Furthermore when the ground shell will be fully occupied with electron – hole pairs with spin – up and spin – down, all other

excitons must then populate the fourfold (including a factor of 2 for spin) degenerate p – shell[12,13,14].

The power dependence features of line – 3 are in a striking agreement with the above physical mechanisms. First as it has already mentioned above PL signal from line – 3 was recorded at almost the same power as for the biexciton (Figure 6-5 a) and b) for the spectral trace which corresponds at 1.12μW excitation power). It has super – linear behaviour as a function of excitation power which is expected as its PL strength would depend also on the occupation of the s –shell which has super – linear dependence upon excitation power as it has already been shown above. Finally it reaches saturation at even higher power (~50μW Figure 6-6) than line – 2 (biexciton) which is a consequence of the further filling of the p – shell after the s – shell has been fully occupied.

Furthermore line – 3 is 35.4meV higher in energy than the exciton (line – 1) (Figure 6-7) which is in the close vicinity of the GaAs LO phonon energy[15,16]. Therefore relaxation of carriers from that level to the ground state by LO phonon emission or through two phonon (LO+LA) mechanisms is possible[17]. This is also consistent with the PLE data for this quantum dot (Figure 6-8 a) and b)) which show a strong resonance close to the energy of line – 3. Finally it is also very close to the 32meV (within a standard deviation of a few meV) energy spacing between the s- and the p- shells (Figure 6-4) of a good[viii] set of quantum dots of this sample. Those facts strongly suggest the possibility that line – 3 is the exciton recombination in the p-shell.

[viii] "Good" here with the meaning of adequate number.

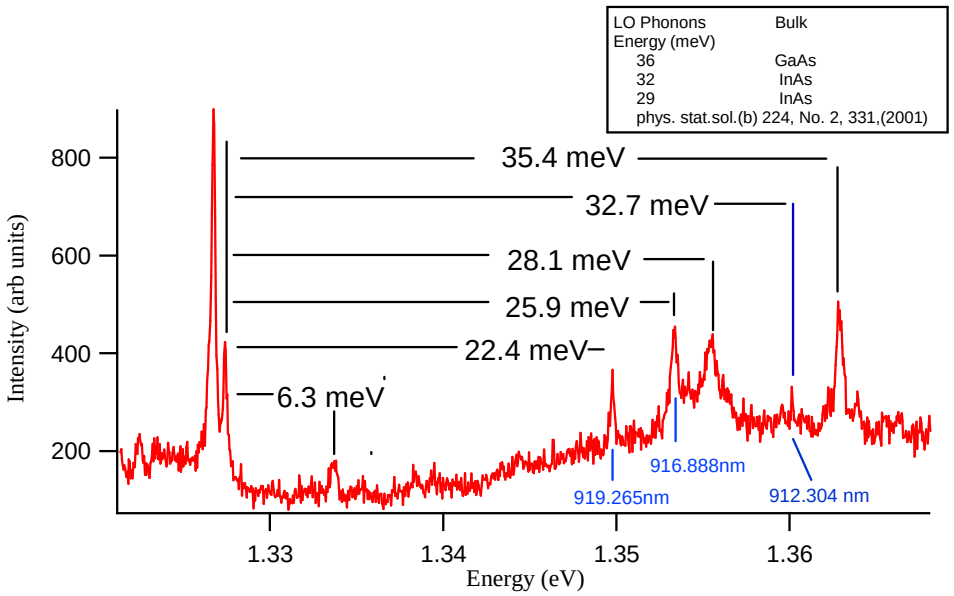

Figure 6-7 Energy separation of the spectral lines observed in fig.5 Inset the LO phonons' energy of GaAs and InAs bulk

The rest of the lines exhibit linear or superlinear dependence on the power, which is always smaller than quadratic. The power profiles of all of the lines as well as the fit parameters are presented in Appendix I. The origin of those lines is not clear. They could either be emission lines due to excited stated of another quantum dot or the effect of higher multiexcitons[18] (4X, 5X, etc.) due to state filling of the excitonic shells of quantum dot – 6 with increasing power or a combination of both. The case that all of the observed PL lines are originated from only one quantum dot is indicated (without being conclusive) by the following facts: i) At very low power only a single narrow line is observed (Figure 6-5) which according to Landin et al (ref. 19) is evidence of single dot emission. ii) Those lines are observed at powers that the exciton, biexciton, and p – exciton lines show considerable strength which indicates the possibility of the dot being occupied by more than two excitons. iii) Some of those lines are clearly connected with quantum dot – 6 by their PLE traces (data shown in section "Photoluminescence Excitation Spectroscopy for different values of laser power.").

6.5.4 Photoluminescence excitation spectroscopy of qd6

In order to further characterise quantum dot 6 photoluminescence excitation spectroscopy (PLE) was performed. A narrow band pass filter was put in front of the spectrometer slit so as to isolate only a narrow spectral area around the ground state exciton and to reduce the effect of laser scatter into the detector. The filter had FWHM of 10 nm and was centred at 940 nm. Because the emission of the dot's exciton ground state is at the edge of this filter the later was angle tuned in order to allow good transmission at this wavelength. The laser was turned into cw mode for achieving maximum resolution. Additionally the auxiliary cavity was used and all of the dispersive items (in this case the GTI[ix]) were removed in order to avoid mode jumping and lasing of multiple modes. The range between 926nm down to 900nm was scanned with an average resolution of 0.2nm. The laser beam was focused through a 5 cm focal length lens from one side of the microscope objective in order to reduce the laser scatter collected by the objective (it is necessary to use all the possible ways to reduce the laser scatter in the collection line in order to allow laser wavelengths close to the low edge of the band – pass filter). The laser spot size on the sample was evaluated by its image using the objective and it was around 15μm. The focusing of the beam was adjusted for the optimum PL signal. The laser power was kept low (5.6mW) as this was the best compromise between signal and laser scatter. The collection optics were as depicted in Figure 6-2. The integration time for the spectrometer – ccd system was 5 sec for each wavelength step of the laser and the temperature of the sample was 6 K.

The acquired data (PL spectra for each excitation wavelength of the laser) are presented in the form of a map in Figure 6-8a. There are three lines that can be clearly distinguished on the map of Figure 6-8a. The two of them have been detected at identical wavelengths as lines 1 and 4 in Figure 6-5 (934 nm and 930 nm respectively). Line 1 which is the most prominent line on the map of Figure 6-8a has been already identified in the previous section (section 6.5.3 *)* and corresponds to the s-shell exciton recombination

[ix] Gires Turnois Interferometer (GTI): an optical standing – wave cavity used to generate chromatic dispersion. In ultrafast lasers is used as a dispersive item for creating negative Group Velocity Dispersion (GVD) and therefore compensating for the dispersion caused by the other optical elements of the cavity.

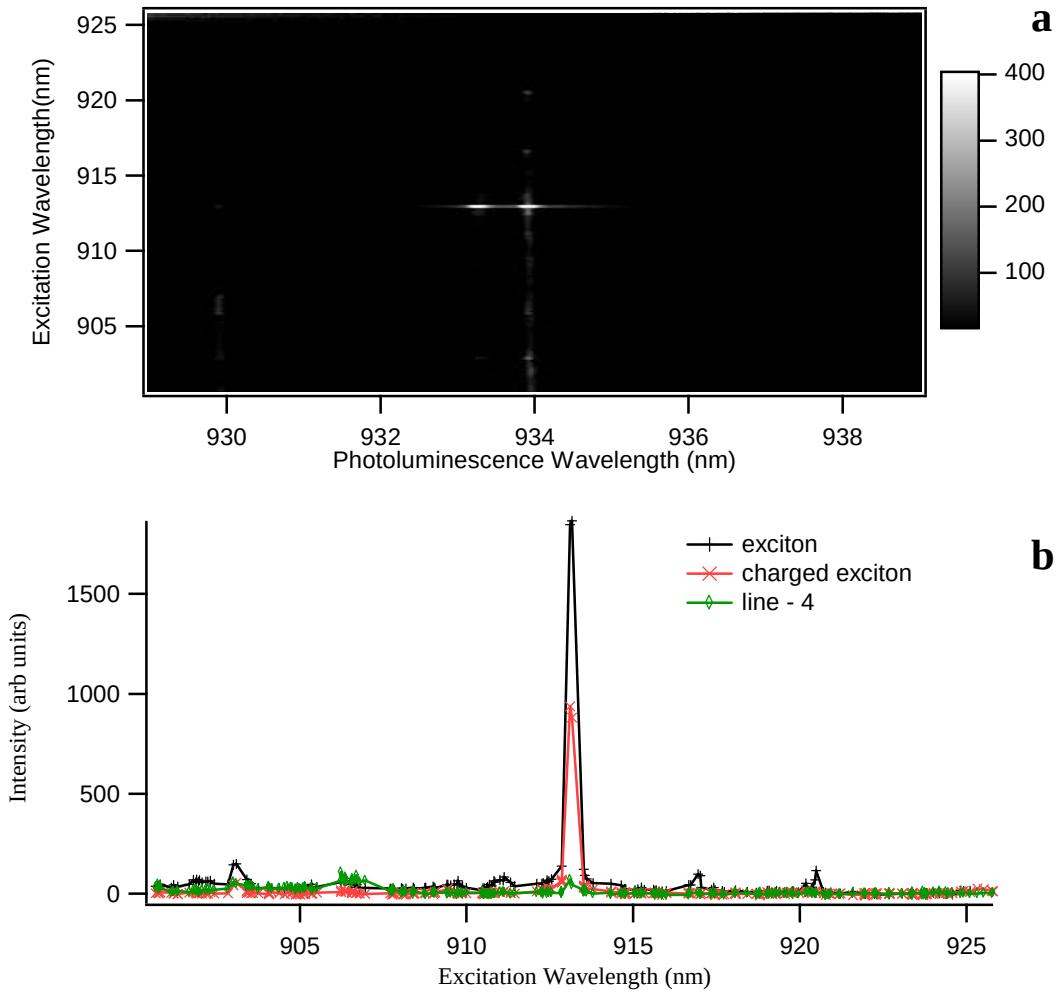

Figure 6-8 a) Map of the PLE data. PL spectra (horizontal slices) and excitation spectra (vertical slices). The colour scale indicates the PL intensity. It has been deliberately suppressed in order to allow the visualization of the two higher energy spectral lines which otherwise would have been obscured by the brightness of the excitonic ground state spectral line. **b)** The PLE profiles of the observed lines in the PLE map.

The PLE profile of the exciton ground state which is a vertical slice of the map in Figure 6-8a along this line is showed in Figure 6-8b. It is apparent that the excitation spectrum is dominated by a very strong resonance at 913.17nm. There are also some other resonances which are at least an order of magnitude smaller than the one at 913.17nm. For clarity Figure 6-8b has been magnified close to the base – line in Figure 6-9. It can be seen that there are two smaller resonances on the low energy side of the main resonance at 913.17 nm and five features that resemble resonances (although some of them are relatively broad) on the high energy side which appear to lie on a weak continuous background.

At the 933.3 nm (emission wavelength in the map of Figure 6-8) another bright spectral line can be distinguished. It appears at 0.9 meV (0.62 nm) higher energy than the exciton and it is not present in the PL spectra under non – resonant excitation (Figure 6-5). This line has been attributed to the emission from the charged exciton and evidence about this will be presented later in this section. Its excitation spectrum is dominated by a strong resonance at the same wavelength as for the exction (Figure 6-8). It exhibits also a number of weaker resonances which appear at the same wavelengths as for the exciton.

The third line that appears in the PL spectra (Figure 6-8) has identical emission wavelength with line – 4 in the non – resonant PL spectra of Figure 6-5 (930 nm). It emits at an energy 6meV (4.3 nm) higher than the exciton. It exhibits 3 resonances (Figure 6-9) at similar wavelength as the exciton and their strength does not vary

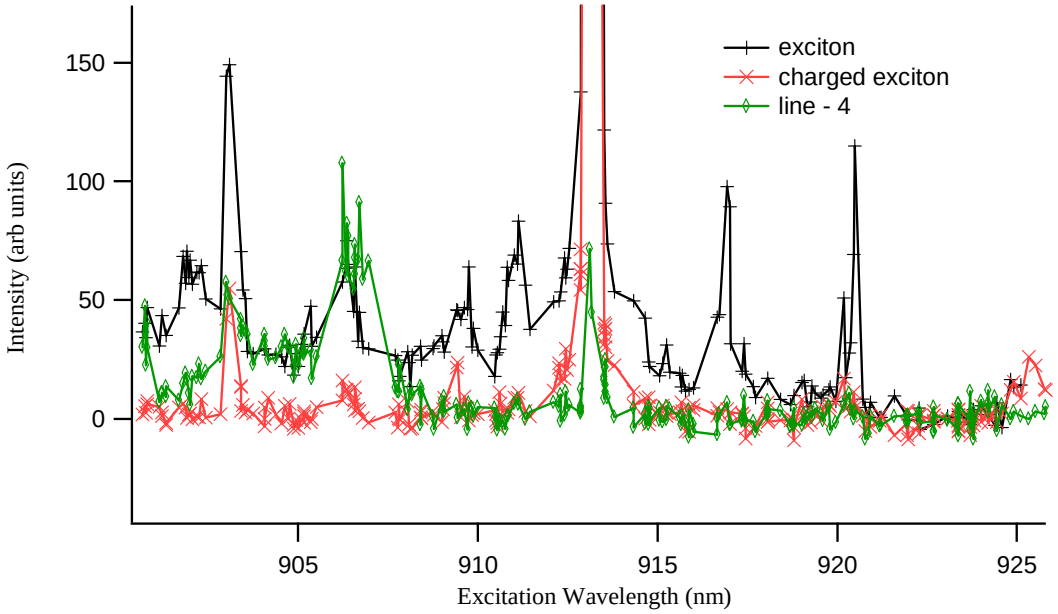

Figure 6-9 Blown up Figure 6-8b close to the baseline in order to show smaller features which have been obscured due to large magnitude of the exciton resonance at 913.17 nm.

considerably. Although the nature of the transition that gives rise to this emission line is not clear its excitation spectrum suggests that it originates from the same quantum dot.

An attempt to interpret the PLE spectra will be started by justifying the attribution of the emission line at 933.3 nm to the charged exciton. Similar lines have occurred under resonant excitation also in other quantum dots on this sample[1]. This line as it has already been mentioned can be observed only under resonant excitation. Simultaneous non-

resonant pumping (Figure 6-10) quenched this line something which is in agreement with reference 1. The charged exciton is created by charge transfer from a weak background doping in the barriers[5]. Therefore the charged exciton is formed only when pumping at lower energies than the wetting layer. The simultaneous non- resonant pumping at high energies gives rise to the creation of e-h pairs which disassociate in the space charge region between the charged quantum dot and ionised impurities. In that case charge can be attracted into the charged quantum dot and recombine with the extra carrier thus neutralising it.

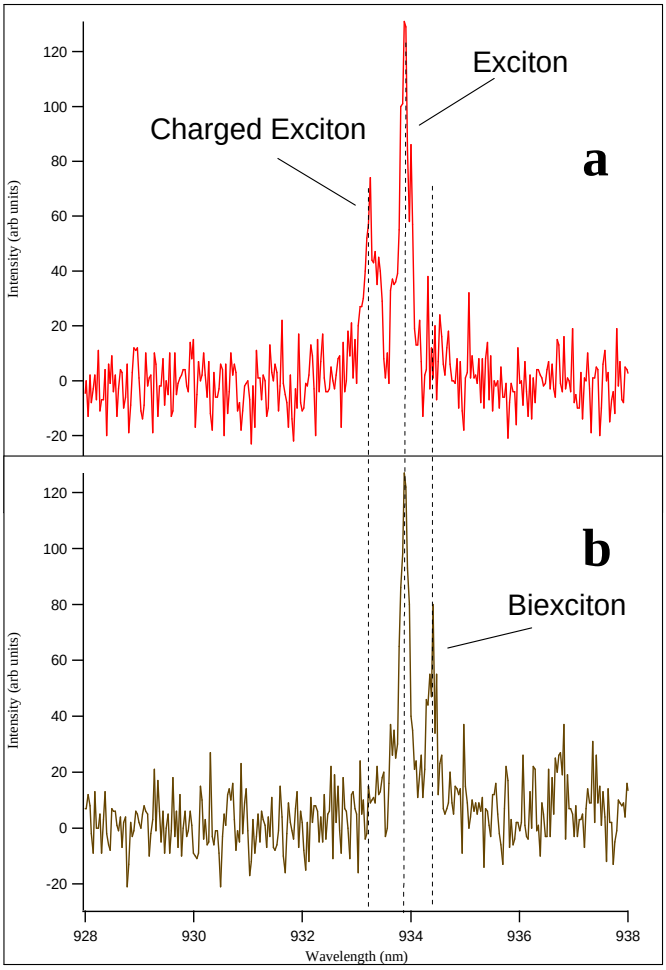

Figure 6-10 a) Photoluminescence spectrum produced by resonant pumping at 913.8 nm. The line at the high energy side of the exciton has been assigned to the charged exciton. **b)** Photoluminescence spectrum by simultaneous resonant and non-resonant pumping. The charged exciton has been photo – depleted and the biexciton at the low energy side of the exciton can be observed.

The main resonance, which appears in the excitonic PLE spectrum, at 913.17nm, does not coincide in energy with any of the observed emission lines under non-resonant excitation. Furthermore at the same energy the main resonance for the charged exciton appears as well (Figure 6-8b).

There is a possibility that during the emission the energy of the state has been shifted due to the fact that the occupation in the dot is different than when exciting in resonance. When the dot is pumped non resonantly at the barriers the filling of the p shell will start when the s shell has been completely filled and cannot accommodate any more excitons according to the Pauli exclusion principle. In this case the energy of the transition that corresponds to the recombination of an exciton in the p shell would be determined by the energy of the of the p state when only the single particle levels are considered, as well as by the Coulomb exchange interaction between the excitons that occupy the dot. On the contrary when the dot is pumped resonantly there are no other excitons but the one created in the p shell whose energy would correspond to the one of the single particle levels. Therefore it is not expected the energy of the p state emission under non resonant pumping and the energy of the PLE resonance to coincide. This means that the observed PLE resonance could correspond to absorption at the p state.

Another possible model that could explain the above effect is phonon assisted absorption[20,21] (Figure 6-11). According to this model a photon is absorbed into the state |GS+1LO> followed by creation of an exciton in the ground state |GS> and the simultaneous emission of 1 LO phonon. This mechanism could account for the exciton resonance but also for the one of the charged exciton considering that in the latter case the emitted phonon has a slightly different energy due to the small energy separation of the exciton and charged exciton states (0.9 meV).

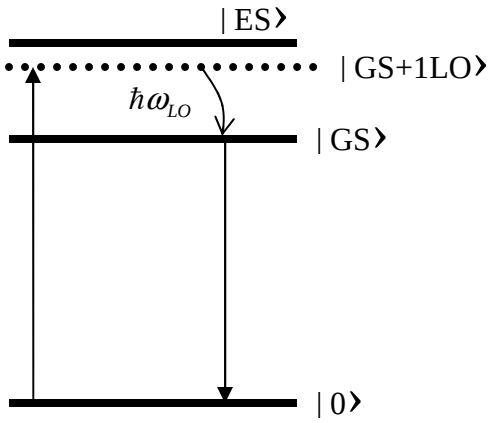

Figure 6-11 A possible mechanism that could explain the strong resonance at 913.17 nm is phonon assisted absorption.

There is also the possibility that the resonance at 913.17 is due to Raman scattering[22]. This process[x] is similar to the phonon assisted absorption with the difference being that involves excitation to virtual state and the fact that it is coherent leading to a polarization memory between incident and emitted photons. However, according to reference 21, such polarization memory was not found, in experiments on very similar quantum dots.

From the current data it appears that the first explanations are possible and there is no any strong indication to favour one of them. Both of them though do not contradict with the interpretation of the emission peak at 910 nm as luminescence from the p state (section 6.5.3). Later on in section 6.9 further data will be presented that indicate that this PLE resonance is probably due to an excited state.

The energy of the emitted LO phonon that corresponds to the resonance at 913.17nm) is about 30 meV and is probably InAs related[23]. There are also other smaller features which appear in the PLE spectra of the exciton at 19.36, 24.58, 33.2, 35.45, 40.4, 45.33 meV respectively (energy separation from the exciton ground state). Apart from the feature at 35.45 meV all of the other ones correspond probably to phonon features (the feature at 24.58 meV is probably InAs related[23] and the other ones are probably related

[x] The key difference between phonon assisted and Raman mechanisms for absorption is that the Raman virtual state is purely electronic (excitonic in the case of quantum dots) and does not include any phonon contribution.

with localised phonons). The reason that the feature at 913.17 nm (30.16 meV) is of much larger strength, has probably to do with the fact it is a few meV (~ 5 meV) close to an excited state and thus the transition probability will be enhanced by resonant coupling with excited state transitions as it is shown in Figure 6-11. However it is not clear why the feature at 911.13 nm (33.2 meV) does not behave in the same way[xi]. It is likely that the reason for this is due to scattering selection rules.

[xi] Could it be an acoustic phonon side band?

6.6 Time Resolved Two Colour Pump Photoluminescence Experiment

In order to study the coherent optical properties of the exciton ground state, a two colour pump experiment was performed on quantum dot 6. The laser was tuned at exactly the same wavelength as the exciton ground state and was set to work in picosecond mode at 76 MHz repetition rate. A fraction of the laser power was used for producing blue picosecond pulses by frequency doubling through a BBO crystal. The delay time between the blue and the infrared pulses was controlled by a translation stage with a retro-reflector. The power of the two beams was controlled by two different liquid crystal modulators in association with two cube polarizers. The spot size of the infrared pulses on the sample was around 10 μm and the one of the blue pulses about 5 μm. Using a band pass filter (in order to eliminate the laser scatter) centred at 910 nm with FWHM=10 nm, the photoluminescence spectrum around the p-state was collected. The p-state of dot was placed at the upper (long) wavelength side of the spectrometer spectral window so as to reduce further the laser scatter from the infrared pulses.

The ground state of the quantum dot was pumped with the infrared pulses and non-resonant pumping at the double energy was applied with the blue pulses. The power of the blue pulses was kept at 3.6 μW which is the point on the power dependence curve that one would expect to observe significant rise in the strength of the p state photoluminescence by increasing the occupation of the exciton ground state. The power of the infrared pulses was adjusted at 4.6 mW in order from the one hand to achieve strong pumping of the exciton ground state and from the other keep the laser scatter as low as possible and also to avoid other red shift effects which are going to be described further bellow. The blue pulse was delayed by 0.5 ns with respect to the infrared one. This delay was chosen in order to be shorter than the exciton lifetime[24] which is expected to be more than 1 ns in this type of quantum dots. With the above settings the photoluminescence spectrum around the p-state (at 910.5 nm) was obtained in two cases: i) when the quantum dot was only pumped non-resonantly with the blue pulses and ii) when it was pumped resonantly and non-resonantly with infrared and blue pulses respectively. As it can be seen in Figure 6-12 there is a clear rise in the p-state photoluminescence when the quantum dot is pumped with both kinds of pulses, infrared

and blue. This is in comparison to the p-state emission strength when the quantum dot is pumped only with the blue pulses. This rise is accompanied with a red shift in the energy of the p-state (Figure 6-12b) and also a rise of a spike at the low energy side of the p-line.

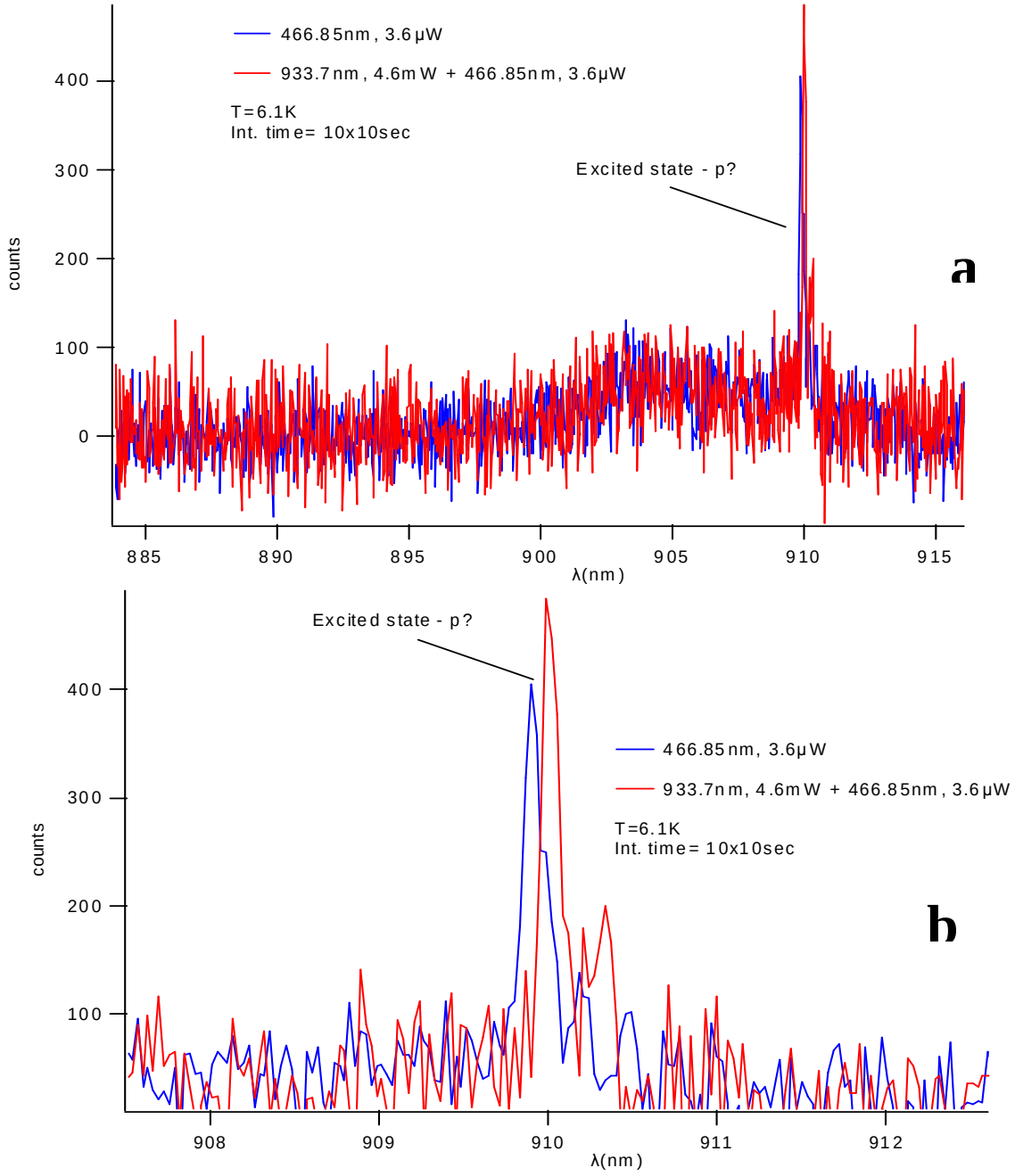

Figure 6-12 a) Photoluminescence spectrum around the p-state of the quantum dot at 910.5 nm acquired when pumping only with blue pulses (blue curve) and when pumping with both blue and infrared pulses. A clear increase in the p-state emission can be observed when pumping with both (infrared and blue) colours. **b)** The same spectrum as in a) but blown up in order to show the red shift in the energy of the p-state when pumping with both colours.

In order to study the effect of the infrared pulses on the p-state photoluminescence of the quantum dot a series of measurements were performed. First by using different band pass filters the photoluminescence spectrum of lines that had been observed in lower energies (Figure 6-5) than the p-state was collected for the cases i) and ii) stated in the above paragraph. Those measurements are presented in Figure 6-13 and it can be seen that there is no increase in the photoluminescence intensity of those lines when the quantum is pumped with pulses of both colours. There is, however, a clear red shift in their energy in the latter case.

Second a variety of measurements on different delay times between the infrared and blue pulses and for different energies of the infrared pulses (which were around the exciton ground state energy) as well as for different powers of the blue and the infrared pulses were performed. From those measurements it was found that the rise in the p-state photoluminescence could be observed for all of the different delay times[xii] between the blue and the infrared pulses, even in the case that the infrared pulse was delayed with respect to the blue one. This means that the effect of the additional infrared pulses affect the p-state photoluminescence not by increasing the occupation of the ground state but in a different way.

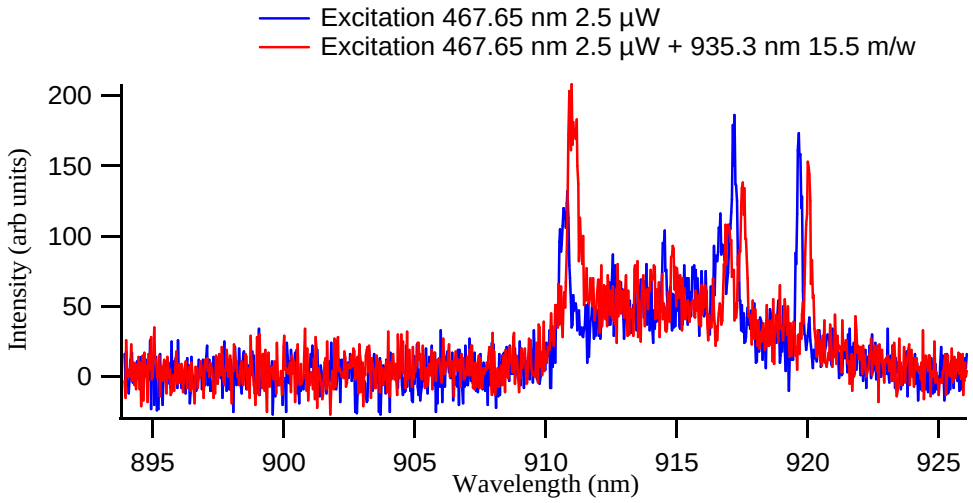

Figure 6-13 The two colour experiment by using filtered femtosecond pulses. Only the 910nm line exhibits significant increase when the ground state is pumped.

[xii] The accuracy of the delay times is limited from the fact that the zero time delay was determined just by measuring the length of the paths of the blue and the infrared pulses respectively. The precision of those measurements was ± 1 cm which corresponds to ± 33 picoseconds.

The measurements upon different energies of the infrared pulses lead to the same conclusion. The increase of the p-state photoluminescence was observed for higher as well as for lower energies than the ground state. For all those different conditions which are summarised in increase in photoluminescence intensity and red shift in the energy of the p-state were observed.

Studying in more detail the red shift of the photoluminescence of the p-state it was found to have almost linear dependence on the power (Figure 6-14).

Table 6-1

6.6.1 Different conditions for the 2 colour pump			
Wavelengths(nm)	Time delay (nsec)	Infrared Power (mW)	Blue power (uW)
927.2	~0.5	4.5	13
933.1	~0.5	5	13
933.2	~0.5	4.5	50
933.4	~0.5	4.5	3.2
933.5	~0.5	4.5	12
933.7	~0.5	4.5	3.2
933.9	~0.5	4.5	3.6
934.1	~0.5	4.5	3.6
935.6	~0.5	4.5	3.6
933.9	~-0.2(?)	4.5	3.9

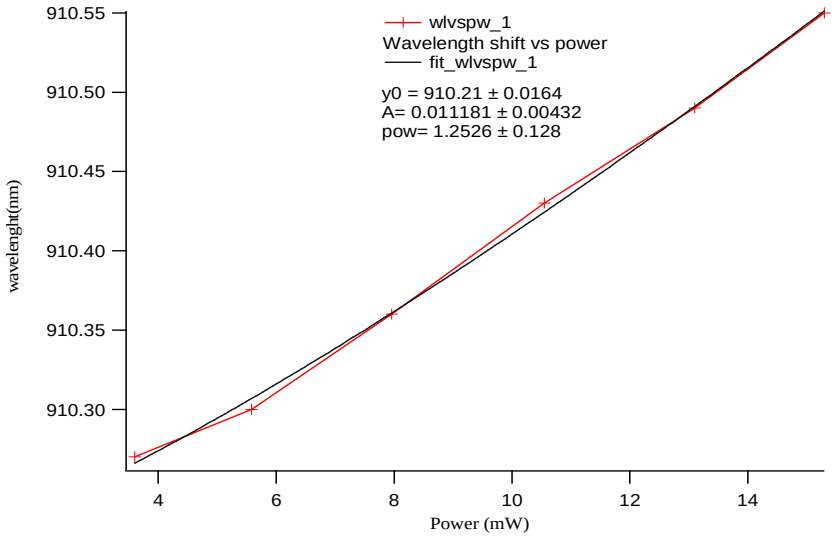

Figure 6-14 The red-shift of the p-state photoluminescence, data (red markers) and fit (black line) exhibits almost linear dependence on the power.

6.7 Temperature dependence of the quantum dot photoluminescence

In order to study and explain the effect of the infrared pulses on the p-state photoluminescence some further experiments were carried out. As red shift of PL lines can be caused by heating of the sample[25] some non resonant photoluminescence versus temperature measurements were performed.

The sample temperature was controlled using the heater of the cryostat and the photoluminescence spectrum was recorded for each temperature point. The temperature changes gave rise to small shifts of the sample position which was corrected for each temperature setting. The non-resonant excitation intensity was kept similar to the one used in the two colour pump experiment (5.3 μW) in order to allow some easy comparisons between the observed effects. The range of the scan temperatures was from 9.2 K up to 31.7 K. The increase step was adjusted each time to be less than 5% of the actual temperature of the sample.

The collected spectra are presented in Figure 6-15. From Figure 6-15b) where all the collected spectra are presented as a map it can be seen that lines 1, 2 and 3 which correspond to the exciton biexciton and p-state as it has already been explained, undergo a clear red shift as the temperature rises. The same holds as it is shown again in Figure 6-15b) for all of the intermediate spectral lines. The size of the shift depends only upon the temperature and not on the energy of the spectral lines and therefore it is the same for all spectral lines. Furthermore it appears to have a nonlinear dependence upon the temperature as it will be shown below.

The intensity of the spectral lines appears to increase with temperature as it can be clearly seen from Figure 6-15a). However this time the increase depends on the energy of the line. The strength of the exciton line increases relative to the biexciton.

The profile of the exciton line strength as well as its wavelength as a function of temperature, are presented in Figure 6-16a) and b). Both of them have a nonlinear behaviour as they seem to be fitted well by power law curves ($\boldsymbol{I}_{PL} = \boldsymbol{I}_{\boldsymbol{o}} + \boldsymbol{A} \cdot T^{a}$ for the PL intensity and $\lambda = \lambda_o + B \cdot T^{b}$ for the wavelength) with exponents 2.34 and 2.5 respectively.

The reasons for the red shift of the spectral lines are associated with the temperature behaviour of the band gap of the bulk material[25] which is mainly defined

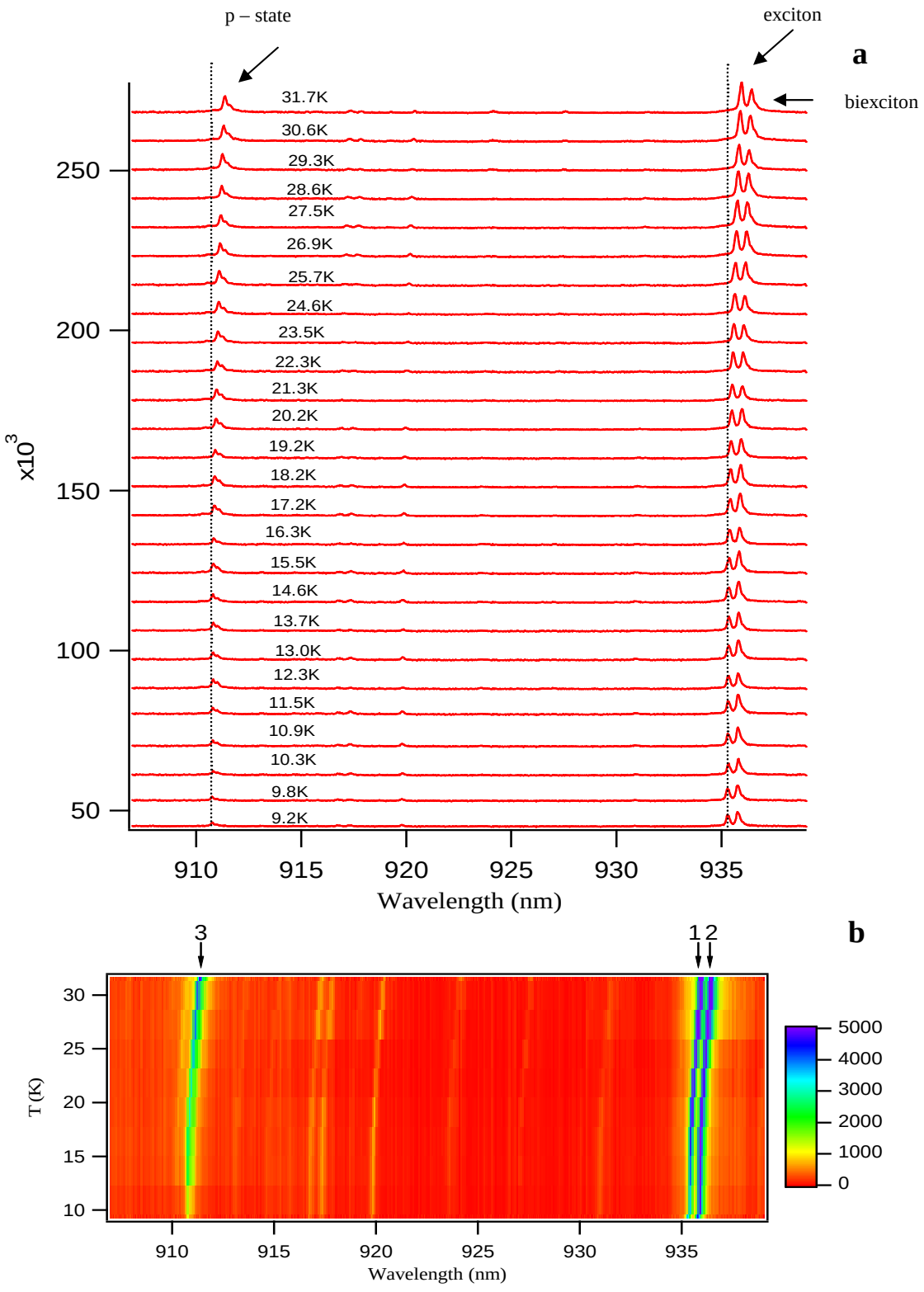

Figure 6-15 a) Photoluminescence spectra of quantum dot 6 for various temperatures. The excitation power was kept at 5.3 mW at 462nm and the integration time was 100sec. The spectra have been offset for clarity. **b)** The photoluminescence spectra of 13 a) for the various temperatures presented as a map. It is apparent that all the spectral lines between the s and the p – states undergo similar energy shifts as the temperature rises.

by two effects: scattering of electrons by phonons and thermal expansion of the lattice. In general this behaviour is described well by the Varshni's formula which assumes a quadratic dependence of the band – gap decrease over the temperature at cryogenic temperatures. In particular this quadratic temperature dependence appears to describe well also the shift of the excitonic energy in quantum dots.

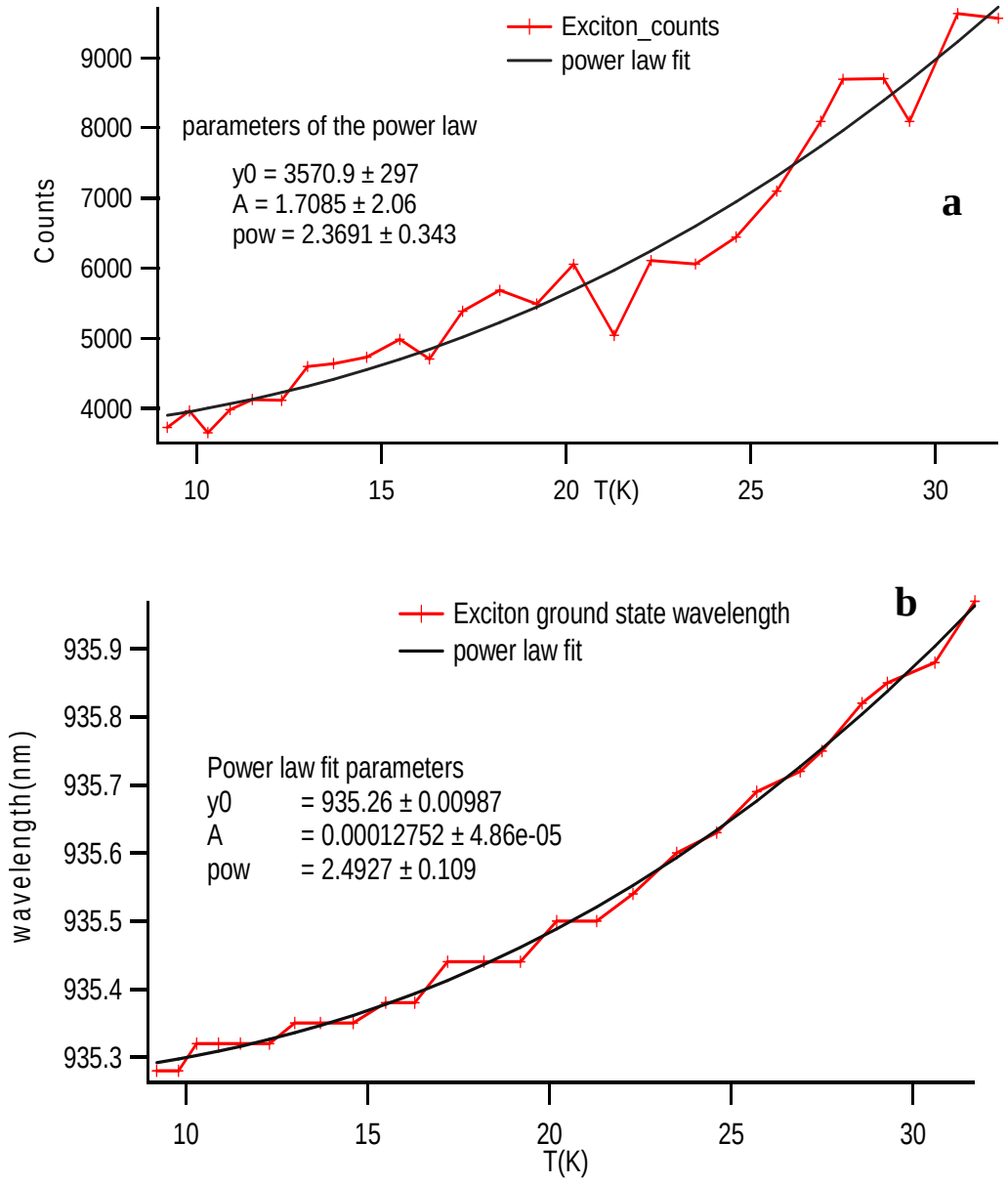

Figure 6-16 The exciton **a)** line strength and **b)** red shift as a function of temperature. Excitation at 462nm (psec pulses),with excitation density of 5.3μW. Integration time 10 sec.

However in the case of quantum dot 6 as it was mentioned above the dependence of the temperature was over – quadratic. It is not clear the origin of this difference. It has

to be mentioned though that the reported quadratic temperature dependence concerns dots which is occupied by only one exciton while it the case of the collected data for qd 6 clearly show that more than one excitons were occupying the dot. This fact might contribute to the divergence from the quadratic model.

The intensity increase with temperature of the spectral lines probably originates from the efficiency increase of the relaxation processes in the quantum dot. This is something to be expected as the phonon population increases with temperature.

Finally observed effects as the change of the intensity ratio of the exciton and biexciton are probably related with the different effect of the temperature on the different relaxation channels for the carriers into the exciton and biexciton states as well as with possible effects on the radiative lifetime of the two states.

6.8 Resonant Excitation

Further experiments were performed in order to study the behaviour of the system under resonant excitation as well as the effect of the laser excitation on the red shift of the quantum dot states. Those experiments consisted of four sets of measurements in which the power of the laser was varied by using a liquid crystal modulator. In the first three the laser was operated in picosecond mode and it was tuned at the wavelength of the p-state absorption (913.3 nm) of the quantum dot in the first set, at slightly longer wavelength (913.9 nm) in the second set and at slightly shorter (912.6 nm) in the third one. The full width half maximum (FWHM) of the picosecond pulses was about 0.8 nm. In the last set the laser was operated in continuous wave (cw) mode and it was tuned at the wavelength of the p-state absorption (913.3 nm).

The acquired data are presented below in figures Figure 6-17 and Figure 6-18

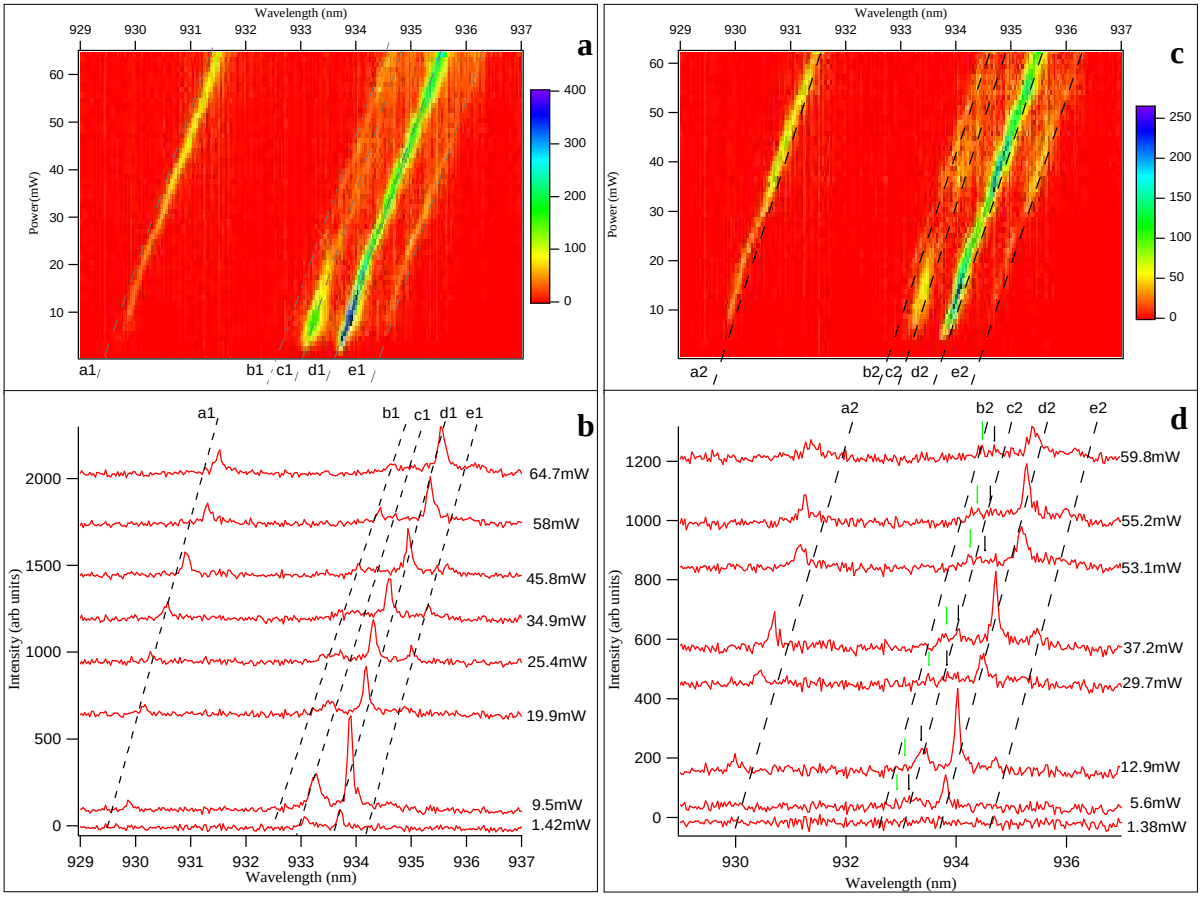

Figure 6-17 Maps of the photoluminescence strength versus wavelength (x-axis) and excitation density (y-axis) under resonant excitation (913.3nm) **a)**, and slightly above resonance (913.9nm) **c)**, by picosecond pulses. In **b)**, **d)** horizontal slices extracted from the respective maps, above, depicting the photoluminescence spectra for various values of the excitation power.

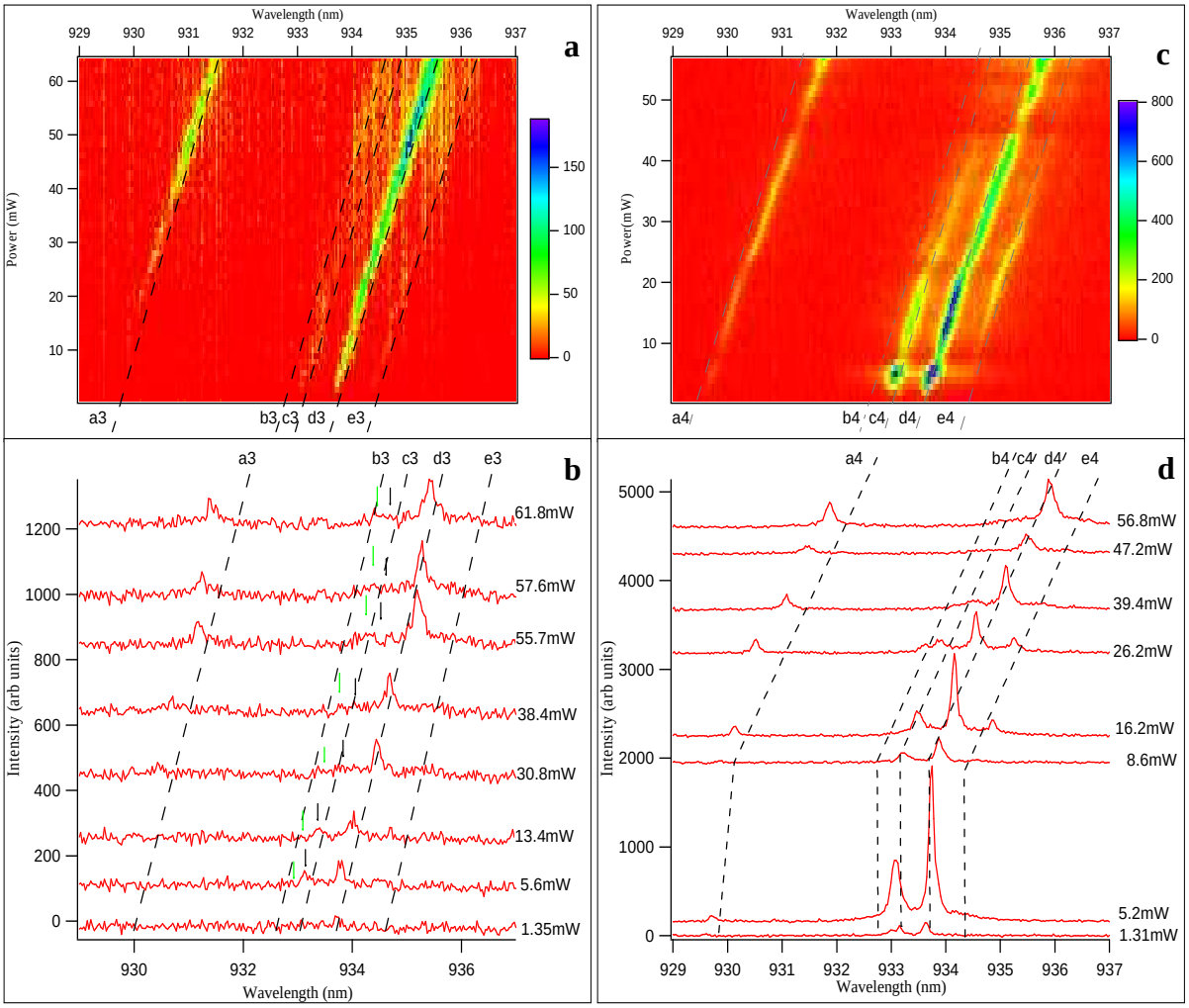

Figure 6-18 Maps of the photoluminescence strength versus wavelength (x-axis) and excitation density (y-axis) under excitation slightly below resonance (912.6nm) by picosecond pulses **a)**, and under resonant excitation in continuous wave (cw) mode **c)**. In **b)**, **d)** horizontal slices extracted from the respective maps, above, depicting the photoluminescence spectra for various values of the excitation power

in the form of maps (a, c - figures) (with the x-axis being the photoluminescence wavelength and the y-axis the laser power) and a number of offset spectra in each case (b, d – figures). Five lines appear in each one of the measurement sets which have been named as a, b, c, d, and e with “a” being the one corresponding to the shortest wavelength and “e” to the longest. On the right of each letter there is a number which represent the number of the measurement set (1, 2, 3, and 4). All but lines “a” and “b” have been identified from previous measurements. Line “c” corresponds to the emission from the charged exciton, line “d” to the emission of the exciton and line “e” to the biexciton.

As it can be seen from the maps in figures Figure 6-17 and Figure 6-18 all of the lines (a – e) undergo a red shift with increasing excitation density. All of them shift in parallel with each other as the energy spacing between them does not change. In Figure 6-19

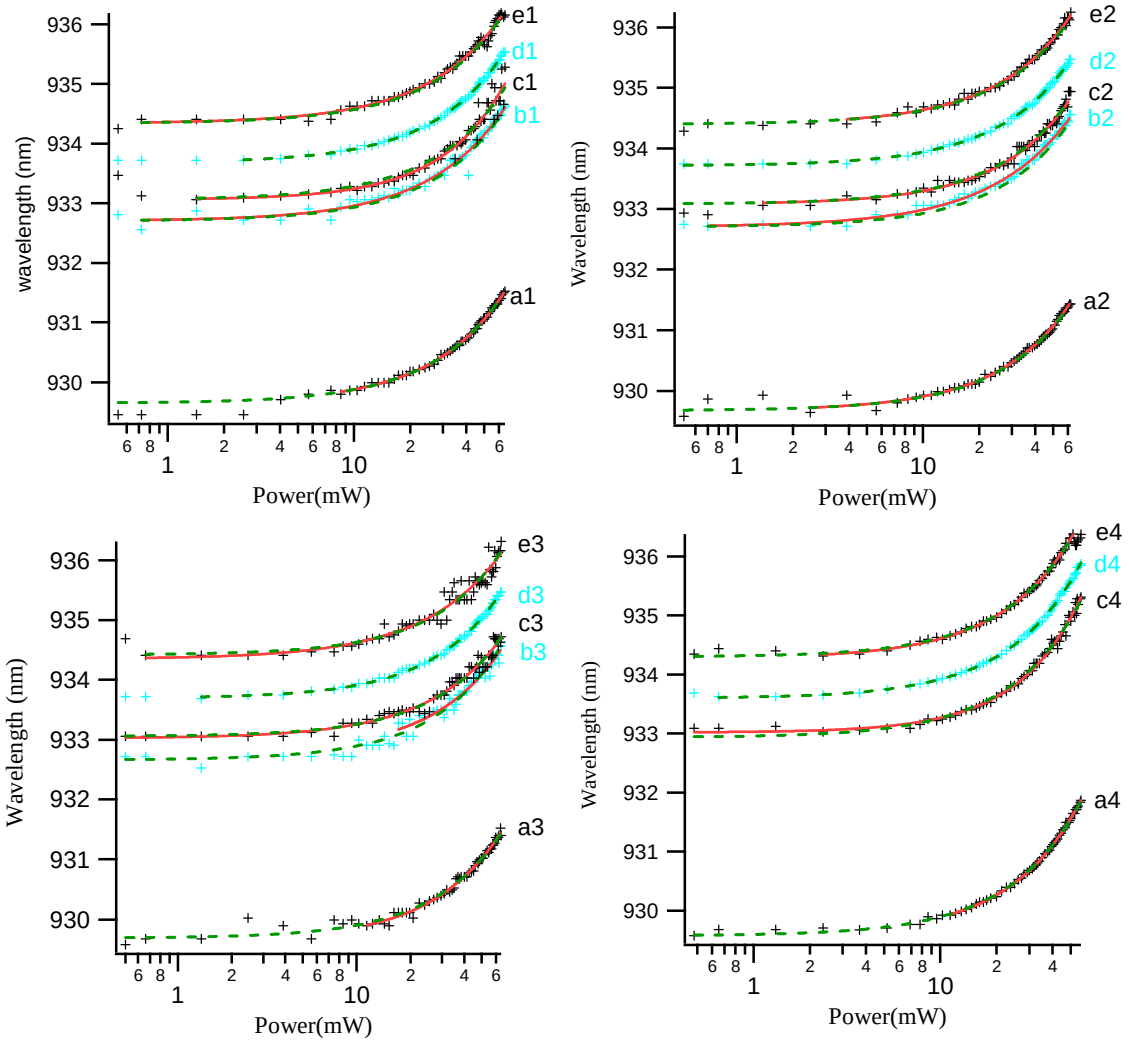

Figure 6-19 Wavelength shift versus excitation density of spectral lines a-e for all four sets of measurements. The shifts have been fitted with power law curves (red solid lines and green dashed line for spectral line d). Also on the wavelength shift of each spectral line the power law curve that fitted line d has been plotted (green dashed lines) after being appropriately offset, for comparison. The fitting parameters and their deviations are given in **Appendix II - Table 1**.

the wavelength of each line has been plotted against the excitation intensity. Each one of those data sets has been fitted with a power law curve ($\lambda=\lambda_o+A\,P^p$). The respective fitting curves are also depicted in Figure 6-19 (red solid lines and green dashed line for spectral line d). The fitting parameters λ_o, **A, p** are presented in Appendix II - Table 1. It appears

that the wavelength shift is slightly nonlinear with the excitation density (~$P^{1.13}$). As it was expected the parameters **A** and **p** have almost the same values (within a standard deviation) for all of the lines and in all of the measurement sets. Slight deviations that appear mainly for line "b" are due to the poor signal of the line which does not allow precise fitting. In order to enable comparisons the fitting curve of the d – line in each of the sets 1 – 4, has also been plotted (green dashed lines),after being properly offset, along with the wavelength versus excitation density plots and their fitting curves of each of the other spectral lines.

There are some features of this wavelength shift that can be deduced from the presented data. First it does not appear to be influenced by the excitation energy as it retains the same behaviour in all of the measurement sets. Second it is not affected by the laser being in pulsed or in continuous wave mode. The first feature indicates that the effect of the red shift due to excitation density is not related with absorption of light in the quantum dot. The second feature excludes the possibility of the effect being related with two photon absorption in the GaAs substrate.

The fact that all of the lines red – shift parallel to each other resembles the wavelength shift of the spectral lines due to temperature increase (Figure 6-15 b). Additionally the indication that the effect is not related to light absorption in the quantum dot (and therefore not to excitonic effects caused by light excitation) leads to the consideration that the shift is caused due to heating. From Figure 6-16b it can be deduced that wavelength shifts similar to the one appeared due to excitation density require temperatures of 32 K. Therefore if there is this kind of temperature increase should be located close to the surface of the sample as the temperature of cryostat's cold base was continuously monitored and it was stable at 6 K. The most likely candidates for light absorption are the aluminium mask (which reflects most of the light but also absorbs a small percentage of it) and defects in the wetting layer and/or in the GaAs substrate. In principle it should be possible to write down a model to determine the heating as a function of excitation intensity. This model would need to include where and how much light is absorbed, the heat capacity and thermal conductivity of all of the layers, the thermal impedance at the interfaces between layers and would have to have been solved in 3D, or possibly 2D if cylindrical symmetry was used. The complexity of the model and

the inability to be certain of important facts such as the site of the absorption means that it is unlikely that the results of such a model would be truly predictive and so the modelling was not undertaken. It is therefore difficult to be certain that heating was responsible for the spectral shifts of the lines however it seems most likely that heating is the cause.

The PL intensity profiles of the a-e spectral lines as a function of the excitation density for all sets of measurements are presented in Figure 6-20 (for clarity the PL

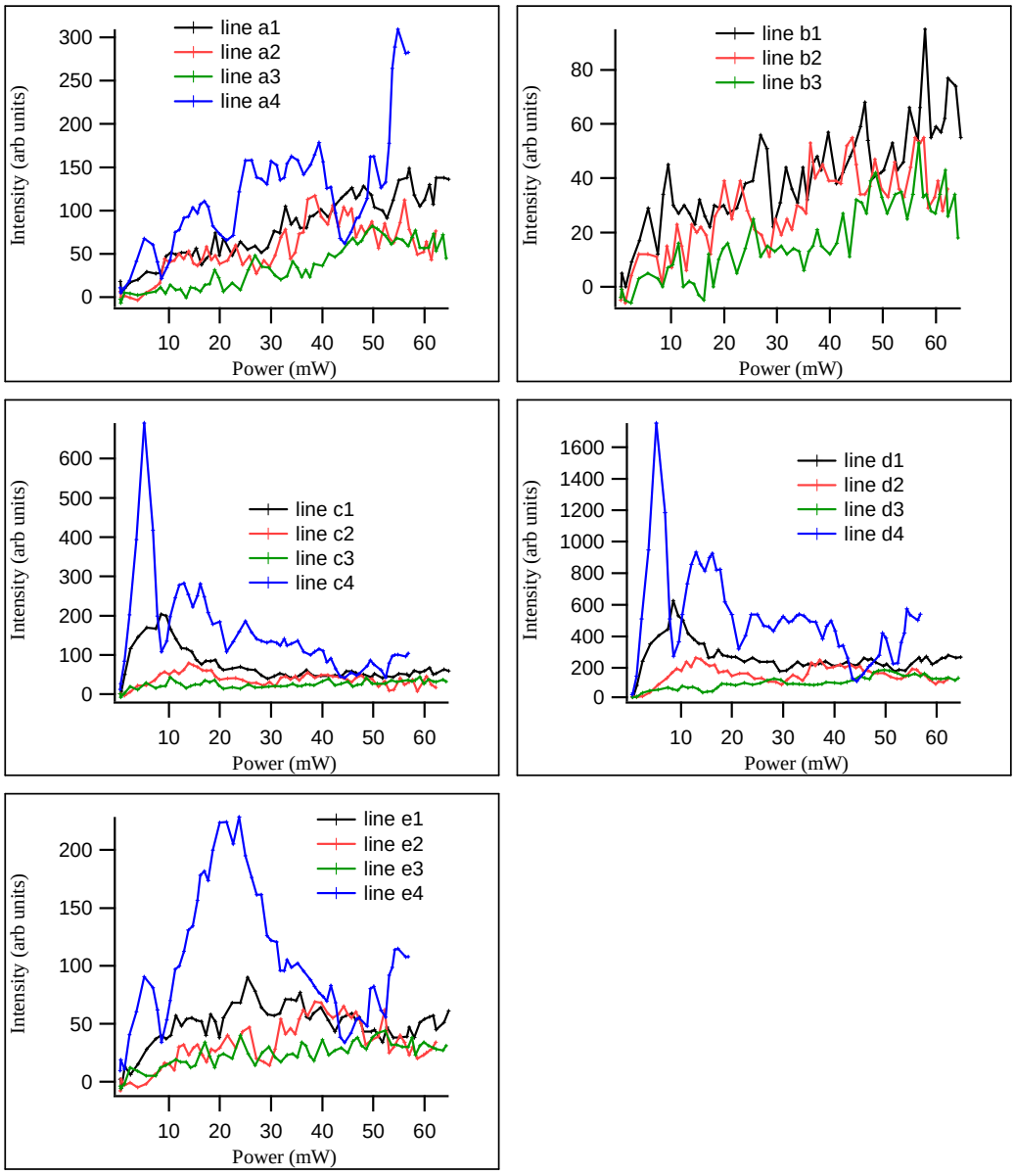

Figure 6-20 PL intensities of each of the a – e spectral lines versus excitation density for all of the measurement sets (1-4) in each of the graphs.

intensity profiles versus excitation intensity have been plotted in single line graphs in Appendix II). As it can be seen from those profiles (Figure 6-20) line “c” and “d” (charged exciton and single exciton respectively) have the same dependence on excitation intensity in all of the measurement sets (curves c1-4 and d1-4 in Figure 6-20). This is expected since both lines correspond to a dot with only one exciton. The different strength of their PL intensities which is in favour of the exciton has probably to do with the relative low probability for thermal excitation of the extra carrier at cryogenic temperatures. However the behaviour of both of them as a function of excitation intensity varies considerably in the different sets of measurements (1-4), although their behaviour with respect to each other is the same in each set. In set “1” a strong oscillation of their PL intensity appears which peaks at 8.5mW and then drops by more than 50% of the peak intensity and almost levels out at that value after 22mW. In set “2” their PL intensity exhibits two milder and broader oscillations which peak at 13mW and 37mw while their strength is considerably weaker. In set “3” the PL intensity of the two lines appears to rise mainly linearly with the excitation density although due to the low strength of the PL it is not possible to distinguish other features due to the background noise. Finally in set “4” the PL is significantly stronger than any of the previous sets. It exhibits at least three oscillations with the strength of the one that appears at low power to be the highest and that of the one at the highest power to be the lowest. From those oscillations only the first one exhibits a clear peak at 5.2mW while the other two exhibit a kind of plateau (or a double peak the second one as it appears in both exciton and charged exciton) and they are significantly broader than the first one with the last being the broadest.

The oscillations of the PL profiles described above cannot be attributed to random fluctuations of the excitation density. The monotonous wavelength shift of the PL lines towards longer wavelengths, with increasing excitation intensity in all of the measurement sets (Figure 6-19), shows that such fluctuations have not occurred. An obvious process which could lead to oscillations in the intensity of the lines is that it is likely that the absorption lines are shifted spectrally with increasing excitation intensity in the same manner as the emission lines. Thus if the system is excited with a fixed wavelength the absorption of the light will depend on an excitation intensity dependent

energy difference between the excitation energy and the absorption energy. The form of the intensity dependence of the emission intensity expected due to this model is presented in Figure 6-21. The equations plotted in this figure assume that the absorption line can be treated as a delta function with an energy which shifts linearly with excitation intensity and that the laser spectrum is a Gaussian. Clearly the absorption line has some spectral width which could be included in this model however the qualitative form of the results would be unchanged.

As it can been seen in Figure 6-21 this model predicts one oscillation of the PL intensity but cannot explain the multiple oscillations that occur in set 2 and 4. This suggests that there are also other mechanisms that contribute in the behaviour of the PL intensity of those lines. An attempt to explore the nature of those mechanisms will be presented in the next section.

Lines “a” and “b” (Figure 6-20) exhibit an almost linear and clear overall increase with the power in the measurement set 1 – 3. However due to the weak signal

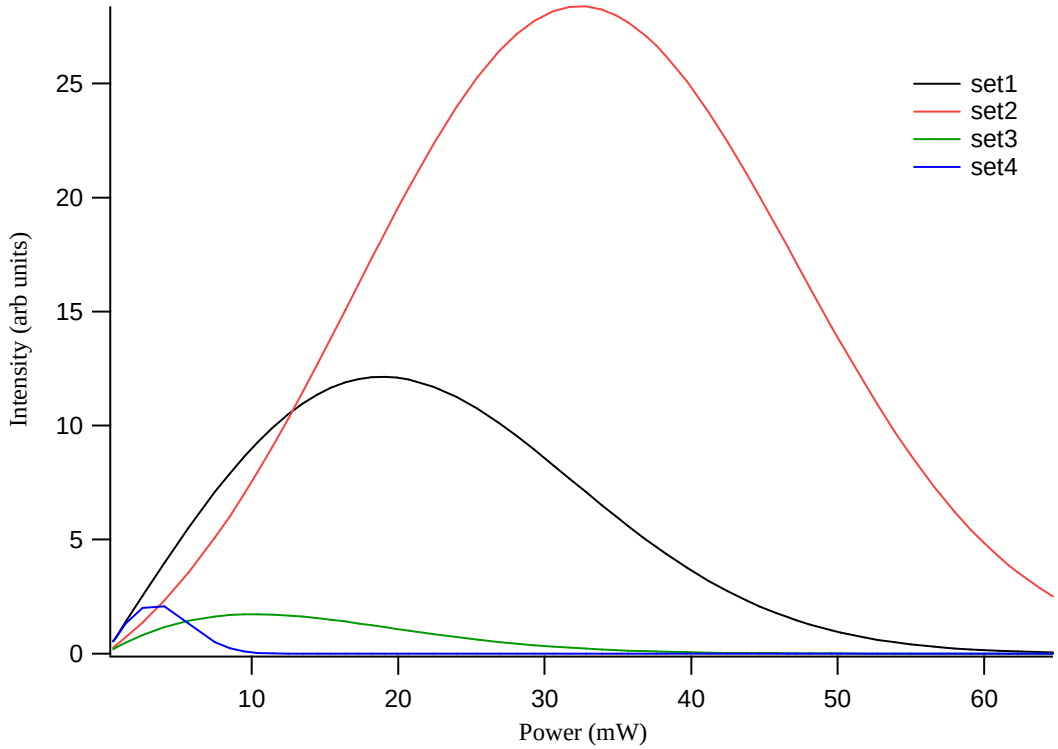

Figure 6-21 Predictions for the PL intensity of the exciton or the charged exciton as a function of excitation density. The predictions have been made for each set of measurements (sets 1 – 4). The model is based on the assumption that the absorption is a delta function over the wavelength and that the observed PL oscillations are the result of the convolution of the absorption and the excitation pulse spectral shape.

of

these lines the background noise might have hindered additional features of their power dependence. Line “a” shows a different behaviour in set 4 which is characterised by small oscillations (Figure 6-20). In the same set there is no adequate information for line “b” as its PL signal was close to the level of background noise and that of the PL pedestal of line “c”. Therefore it was not possible to be extracted from the data. From the above information it is not possible to determine if these lines originate from the studied quantum dot. However their independent behaviour with respect to the rest of the lines indicates that they do not.

The biexciton line (“e”) exhibits different behaviour than that of lines “c” and “d”(however it has been shown in figures Figure 6-5 and Figure 6-6 that it originates from the same quantum dot as line “c” and “d” and that it also has super-linear behaviour). In all of the measurement sets apart from set 3 it exhibits one broad oscillation which peaks at considerably higher excitation density than lines “c” and “d”. It is expected that the biexciton PL would behave in a different way than that of the exciton and the charged exciton as the quantum dot in this case is double excited (two excitons in the dot).

In conclusion in this section the wavelength red shift due to excitation density was studied. The collected data revealed that this shift is not related with light absorption in the quantum dot or two photon absorption in the GaAs substrate. All of the spectral lines shift equally which indicates along with the first conclusion above that the shift is caused due to heating. The PL profiles of the exciton and the charged exciton show oscillations with excitation density and this behaviour cannot be explained only as a convolution of a red shifting absorption and the spectral shape of the pulse. The confirmation of the red shift of the p – state as well as the possibility of other mechanisms involved in the formation of the above PL profiles will be the subject of the next section.

6.9 Photoluminescence Excitation Spectroscopy for different values of laser power

In order to verify if there is a wavelength shift of the absorption which was one of the main assumptions for the model of Figure 6-21 and also to explore further the behaviour of the of the observed PL, four Photoluminescence Excitation Spectroscopy

(PLE) scans were carried out at different excitation intensities. The laser was operated in continuous wave (cw) mode. The spectral width of the beam was less than 0.1 nm and the average step during the scan was 0.2 nm. The scanned wavelength range was from 920 nm to 907 nm. The power of the laser beam was regulated by using a liquid crystal modulator but it was not monitored during the scan. However the laser power for specific wavelengths was recorded after each scan (Figure 6-25).

Maps for each of the scans are presented in Appendix III and the extracted PLE profiles for lines a – f are presented in Figure 6-22. Lines a-d correspond to the same

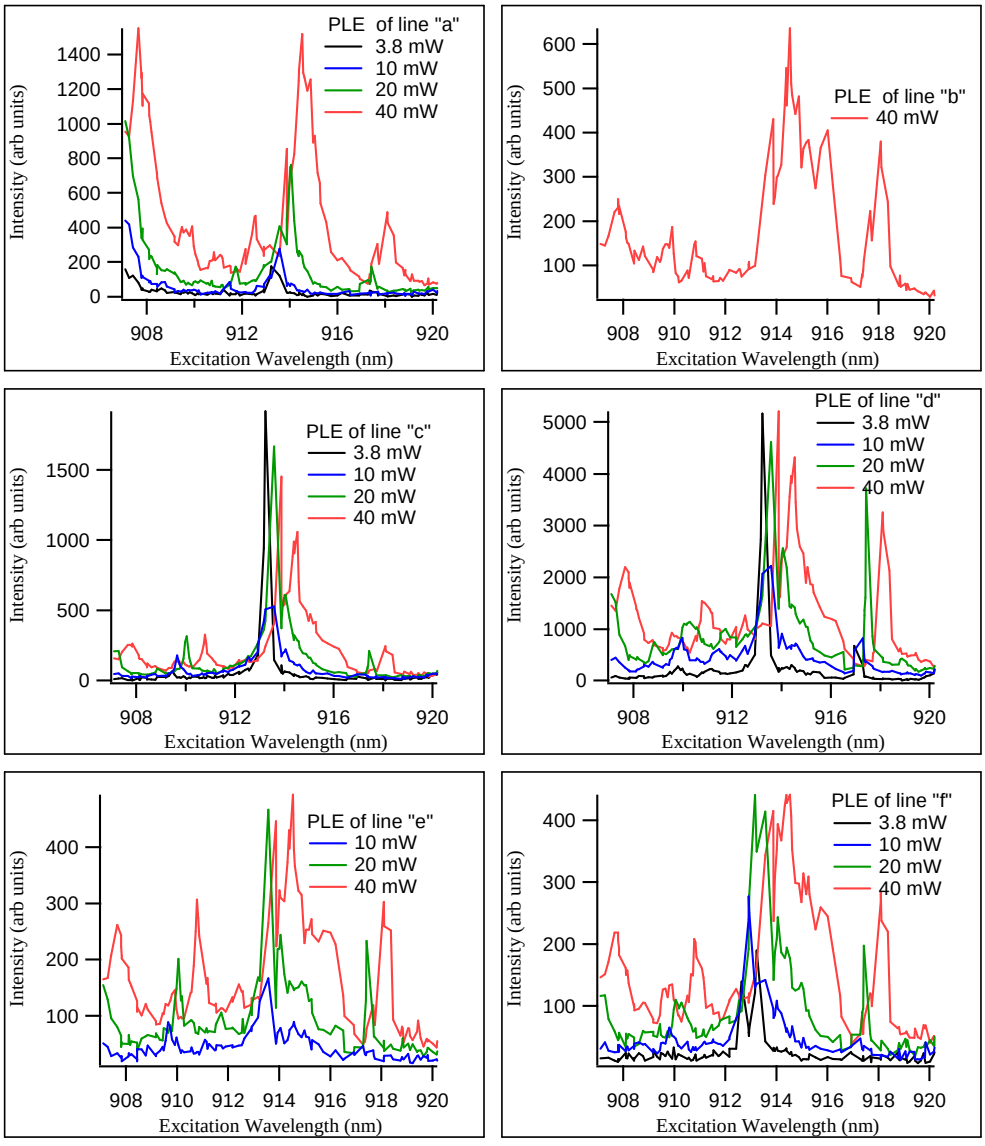

Figure 6-22 PL profiles of lines a-f against excitation wavelength and for various excitation densities.

wavelengths as in the previous section. Line “e” is attributed to the ground state biexciton as it has the same energy separation from the exciton as line 2 in Figure 6-5 which was identified as the s-shell biexciton in section 6.5.3 . Line “f” occurs at slightly longer wavelengths than the biexciton (Figure 6-23). A persistent feature with the same energy separation from the exciton has also been observed in the PL spectra under non – resonant excitation. The nature of this line is not clear. Whilst it may be possible to identify other features within the PL spectra, the PLE spectra of these have not been analysed as for the most part these features are of comparable magnitude as the noise and so the PLE spectra would contain very little useful information.

One of the most obvious features of the PLE spectra when plotted as a function of excitation wavelength is that all the obvious PLE features shift towards longer wavelengths with increasing power. These shifts mirror the wavelength shifts observed in the PL spectra (Figure 6-24). When the PLE spectra are plotted against the excitation energy relative to the energy of the exciton the features show no shift with

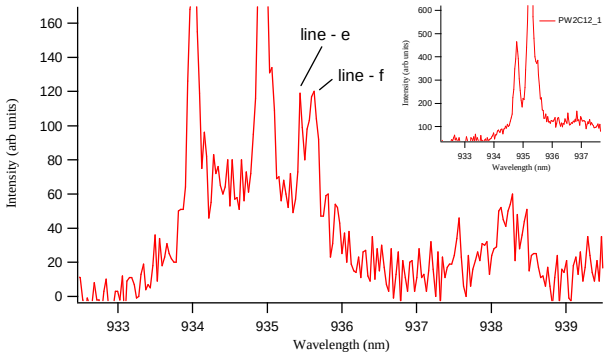

Figure 6-23 Lines e (biexciton) and f . In the inset a feature that appears consistently in the PL spectra under non – resonant excitation with the same energy separation form the exciton as line f

.

excitation intensity. Thus the shifts observed are presumably associated with some change in the bandgap of the InGaAs which as discussed before is probably due to heating. The observed shifts are in agreement with the assumptions of the model of the intensity dependence of the PL lines under resonant excitation discussed in the previous section.

The PL wavelengths of all of the lines are almost constant as a function of excitation energy for a fixed intensity for most of the scanned ranged for each of the PLE scans. However at specific excitation wavelengths (913 nm and 912 nm) a blue shift

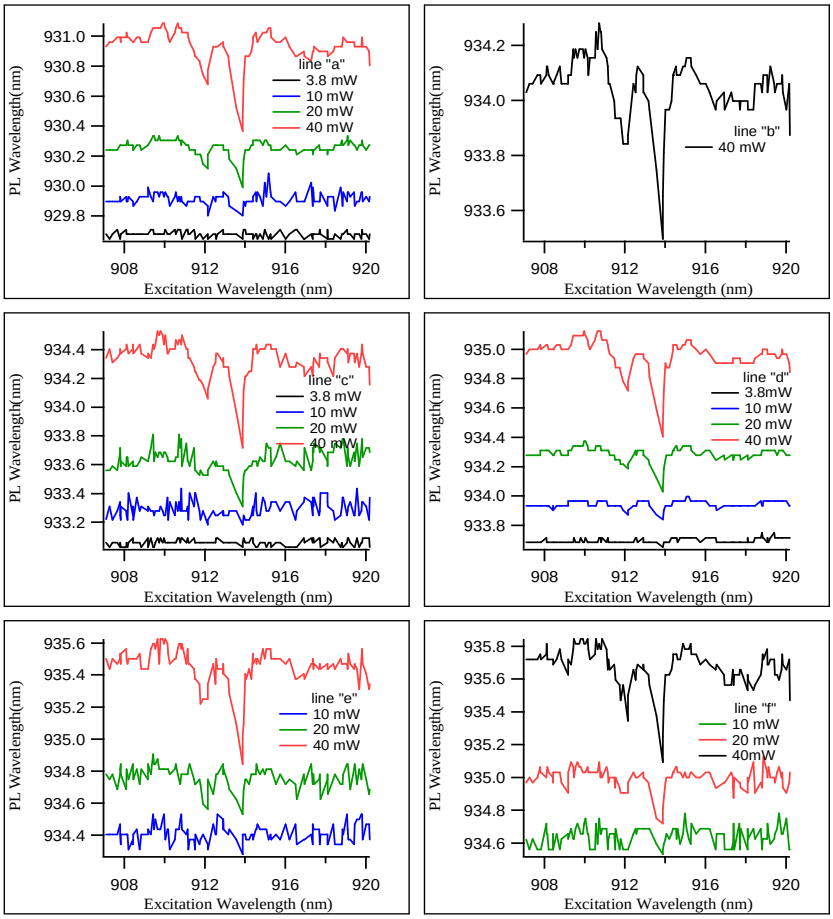

Figure 6-24 Wavelengths of the PL lines a-f during the PLE scans against excitation wavelength and for various excitation intensities (laser power).

occurs. This shift is due to a drop in the power of the laser at the same wavelengths due to atmospheric absorption (Figure 6-25). Whilst in principle it would have been possible to correct this effect it was not found until after the end of the available experimental time. Although this is not ideal it is still possible to obtain useful information from the experiments. One particularly unfortunate consequence of this problem is that it leads to a double peak in one of the main resonances in the PLE spectra. For example the main resonance of the exciton in Figure 6-22 exhibits a double peak when pumped with high power. In reality though, this double peak is the same resonance that appears two times. Once when the laser energy is tuned at the resonance and a second time because as the laser energy increases further, the laser output power drops (as explained above) which has as a consequence, less red shift of the resonance which makes it coincide again with the laser energy giving rise to a “second” absorption spike. This artefact disappears when

the PLE spectra are plotted as a function of the energy separation from the exciton (Figure 6-26).

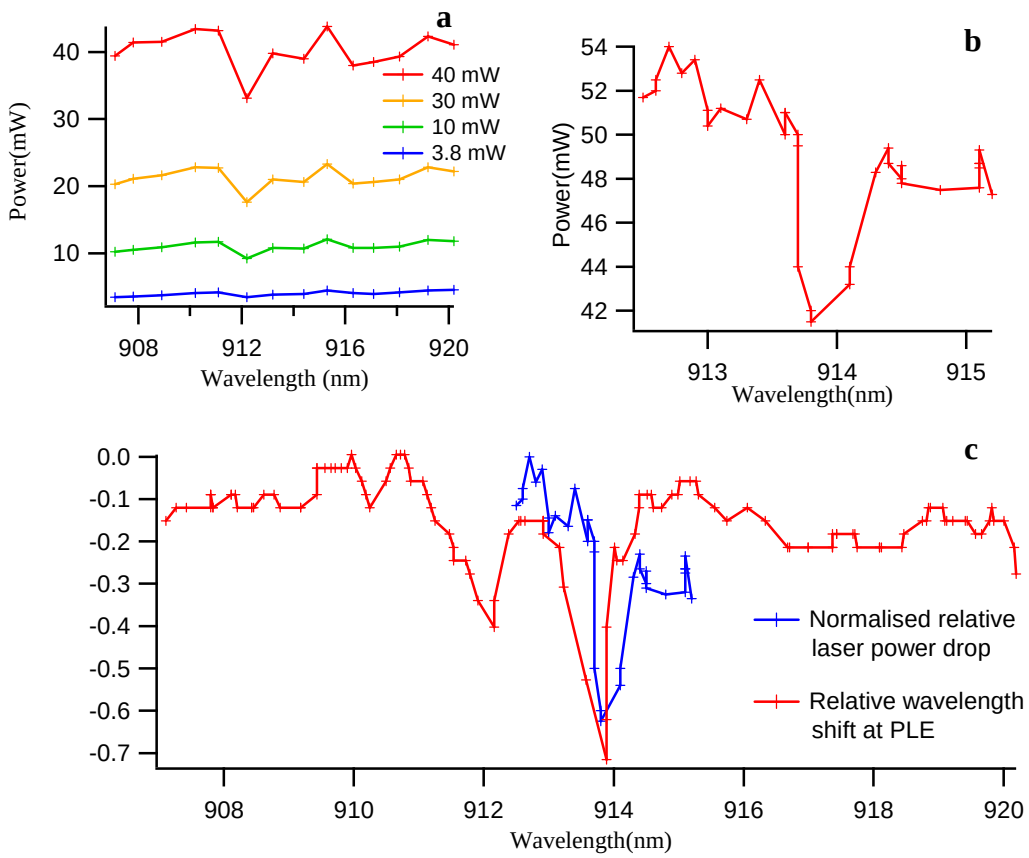

Figure 6-25 a) Laser power for the 4 different PLE scans versus laser wavelength. **b)** Laser power versus laser wavelength, around 913.8nm. **c)** Normalised excitonic wavelength shift and laser power drop around excitation wavelength of 913.8nm

The PLE spectra obtained for all of the PL lines show one strong resonance, at an energy relative to the exciton of 30meV (Figure 6-26), plus a number of subsidiary resonances. It can be observed in those spectra that the main resonances of all of the lines appear at about the same energy distance from the ground state exciton. This means that the resonance is not at a fixed energy relative to the energy of the PL line. In fact for line a, the difference in energy between the excitation and detection energies is 24 meV and for line f, the energy difference is 31 meV (for their main resonances). This suggests that the energy of the resonance is due to an excited state rather than a phonon replica of a ground state. In principle it might be possible for excitons produced in the ground state to transfer to another state giving a similar effect. However if our attribution of the trion line is correct then it seems very unlikely that it would be possible to pump the trion via the

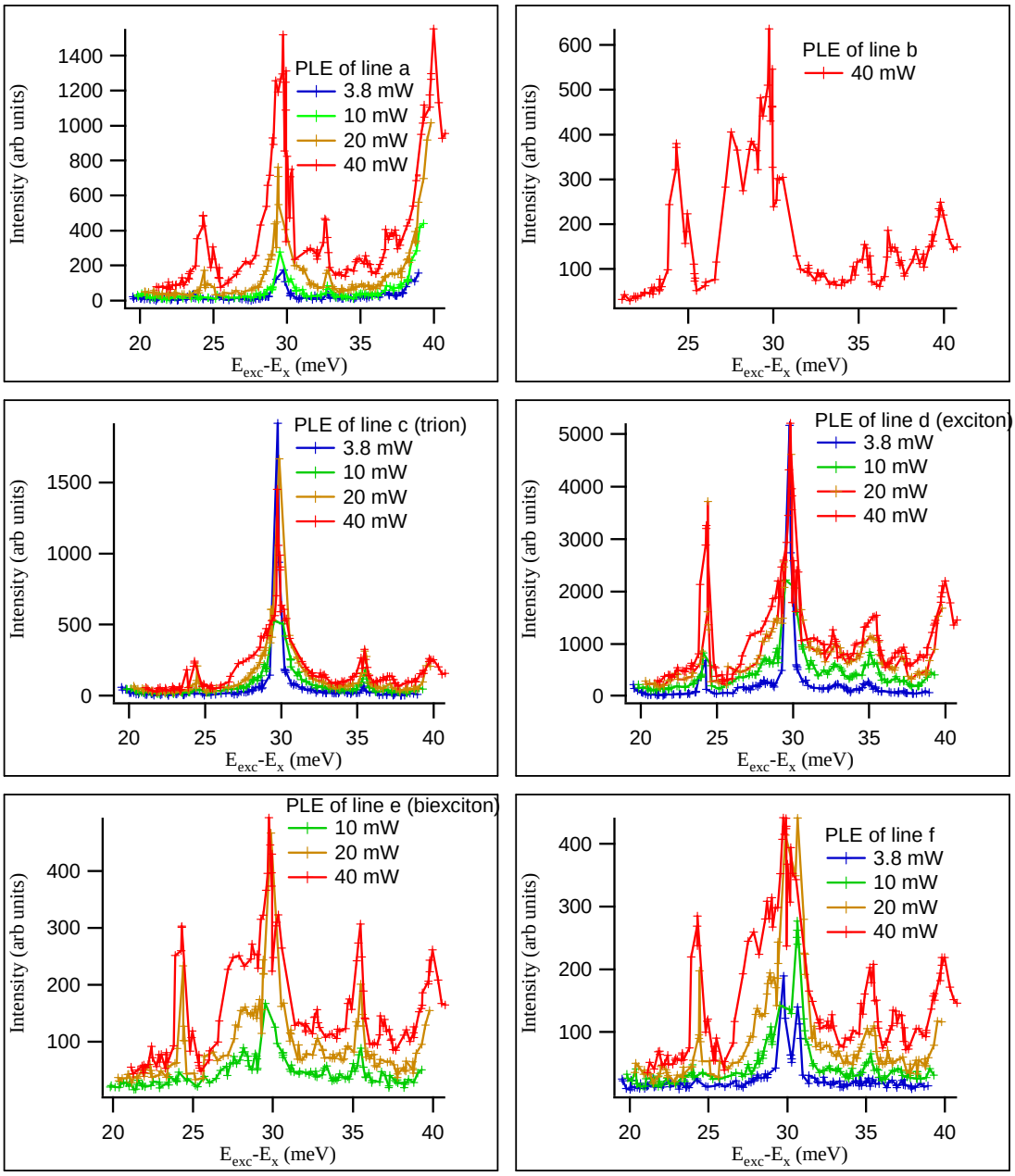

Figure 6-26 PLE spectra of lines a – f plotted as a function of the energy difference between the excitation energy and the energy of the exciton.

exciton line or vice versa which argues against this interpretation. Having said this since there is no detectable emission line at the energy where the resonances have been observed it still leaves open the possibility that the resonances are due to phonon assisted absorption as described in section 6.5.4 .

The strength of some weak resonances (at 918 nm, 910 nm and 908 nm in Figure 6-22) gets considerably enhanced (in contrast with that of the main resonance of each PL

line occurring at ~30 meV in Figure 6-26) at higher laser power and becomes comparable with that of the main resonance. Similarly to what it was mentioned above for the main resonance those secondary resonances do not appear at a constant relative energy with respect to the corresponding PL line. Since the separation of the energy levels of the dot is around 30 meV (section 6.5.2 Figure 6-4) those resonances probably cannot originate from absorption in excited states of the dot. PLE features that have similarities with the secondary resonances presented here have been reported in the literature (see ref 22,23). In those references the secondary PLE resonance had been attributed to Raman scattering due to localised phonons[22] or due to a reduced symmetry of the dot which alters the structure of the excitonic energy levels, making it much more complicated than for dots of high symmetry[23].

Additionally an increase of the PL background can be observed at the high laser power for some of the resonances. It is puzzling why the PL background is enhanced with excitation intensity for some resonances for instance the exciton (line d in Figure 6-26) and not for others as the trion (line c). This absorption background is reported widely in the literature and its origin has been attributed to electronic transitions from electronic levels of the dot to the wetting layer holes[26,27].

Another striking observation from the PLE spectra of Figure 6-26 is the apparent broadening of the resonances as the excitation intensity increases. This broadening occurs mainly as a big enhancement of the pedestal of the resonances. Although by plotting the PLE spectra as a function of the energy separation from the exciton ground state cancels the effect of the wavelength shift (due to the fluctuations of the laser power), on the broadening of the main resonance, the same cannot be assumed for the strength of absorption. It could be that the strength of the main absorption point (the sharp line of the resonance) would have been much higher with respect to the strength of the pedestal but it is not, because the pedestal is pumped with higher power and therefore it looks broader (more enhanced with respect to the sharp line where the main absorption occurs). However in the case of the exciton main resonance (Figure 6-26) the main absorption appears to be saturated and this is not an artefact due to laser power fluctuations. The highest power PLE scan (40 mW) at its highest attenuation does not drop more than 20% (down to 32 mW). Even in this case the excitation intensity of the highest power PLE

scan is still almost one order of magnitude higher than that of the lowest power PLE scan (3.8 mW). The strengths of the respective absorption resonances have not the above ratio and on the contrary appear to be almost equal. Therefore the fluctuation of the laser power does not play any role or does not play any important role to the relative strength of the main resonance and its pedestal which means that the observed broadening is a real effect.

A possible cause of this broadening could be heating. It would be expected though that heating would affect in a similar way the emission lines. For this reason the PL spectra of the main resonance have been plotted for the highest and the lowest excitation intensities in Figure 6-27. Some slight broadening can be observed but it is much smaller than that of absorption. However the latter observation cannot be

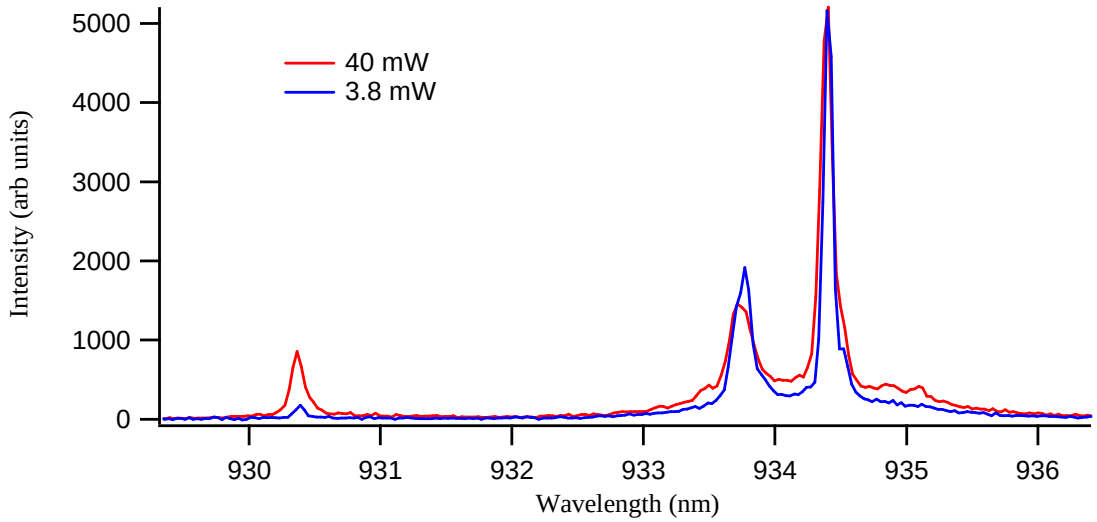

Figure 6-27 The PL spectra when exciting at the main resonance for the highest (red) and lowest (blue) power. Although some broadening can be observed it is much smaller than the one observed for the absorption.

conclusive as the emission lines of Figure 6-27 are those of the ground state so no direct comparisons can be done. Some more insight into the effect of the absorption broadening could be acquired from the data of the temperature dependence of the PL lines which were presented in section 6.7 . It can be seen from Figure 6-24 that the wavelength shift of the exciton emission (line d) between the lowest power PLE scan (3.8 mW) and the one with power 20 mW is at most 0.7 nm. Such wavelength shift is induced when the temperature of the sample increases from 5.7 K to 31.7 K according to the temperature dependence of the exciton wavelength shift which is given by the power law presented in

Figure 6-16b. A comparison of the broadening due to temperature increase of PL lines with energies close to the one that the main exciton absorption occurs is presented in Figure 6-28. It is obvious that temperature induced broadening on its own cannot give rise to the broadening observed for the high power pump (inset of Figure 6-28 and Figure 6-26).

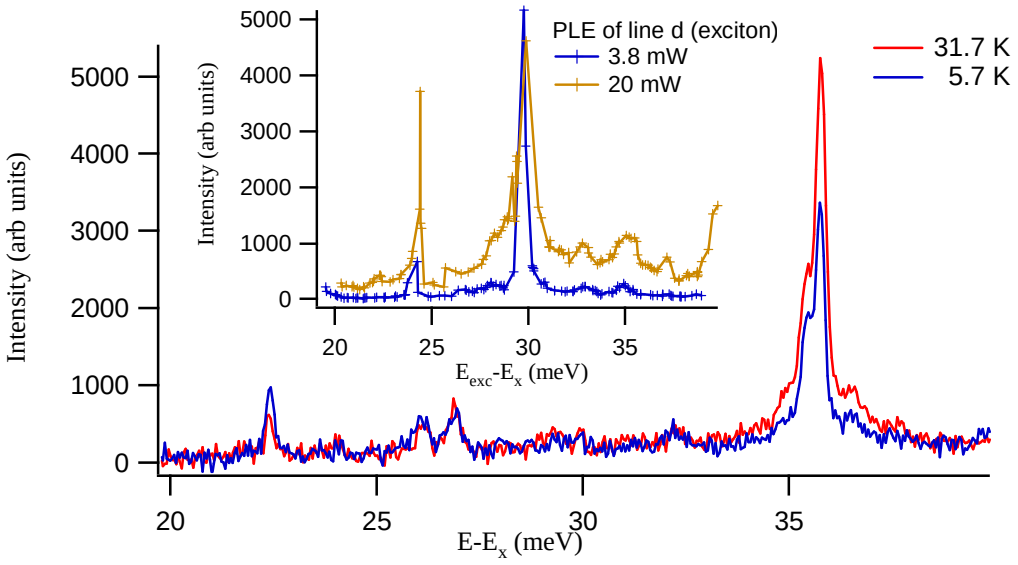

Figure 6-28 Comparison of the emission line at 36 meV higher than the exciton (possible emission from the p shell). The 5.7 K temperature PL has been horizontally shifted in order to overlap with the PL spectrum at 31.7 K allowing thus comparison of the widths of the lines. **Inset:** PLE spectra of the exciton at 3.8 and 20 mW .

The resonances of all the PL lines exhibit pedestal enhancement with increasing excitation intensity. For lines ‘e’ (biexciton) and ‘f’ (Figure 6-26) this enhancement is much more important as the pedestal at high excitation intensities has a strength which is more than half of the main absorption line of the corresponding resonance. This kind of proportion of the strengths of the main absorption line and the pedestal is not expected for the biexciton in the case that the absorption occurs to an excited state. On the contrary it would have been expected that the absorption for the biexciton is super-linear (possibly quadratic) with excitation energy leading to a sharp absorption line with very high relative strength with respect to its pedestal.

6.10 Conclusions

Optical measurements were carried out on a single quantum dot by means of confocal microscopy and spectral filtering. Photoluminescence lines that were observed were identified by their dependence upon excitation density. The main lines observed were identified as the ground state exciton at 1327 meV and the biexciton at -0.7 meV shift relative to exciton (sre) . A third major line was also observed at higher energy (35.4 meV sre) and its power dependence indicates that is an excited excitonic state. Its energy shift relative to ground state exciton suggests that it is the p-state.

In order to confirm the connection of the excited state with the dot under investigation photoluminescence excitation spectroscopy measurements were performed. A strong resonance at energy (30.16 meV sre) close to that of the above line was observed. The difference in energy of the PL and PLE spectral features can be attributed to few body effects which are present in the luminescence experiments when the dot is multiply excited.

Furthermore under resonance excitation a line at energy (1 meV sre) higher than that of the excitonic ground state was also observed. This line is present only under resonant excitation and simultaneous non – resonant excitation causes it to disappear. Therefore this line was identified as coming from a charged exciton state. The existence of such a state was attributed to backround dopping of the sample (charge traps) whose effect is eliminated when excitation above the quantum dot barriers takes place leading to generation of free carriers which can neutralize the charge traps.

Having identified the possible p–state a time resolve two colour pump photoluminescence experiment was carried out. The aim of this experiment was to probe the ground state occupation indirectly, which would enable the realization of coherent measurements on the ground state without probing at the excitation energy. The latter is an inherent problem of the conventional pump and probe technique when probing the ground state as it leads to a big background resulting in poor signal to noise ratio. The time resolve two colour pump photoluminescence experiment does not suffer from background as it indirectly probes the ground state. In brief the main idea of this experiment is to use a non resonant pulse of strength which will lead to on average two excitons captured into the quantum dot. If these excitons arrive when the ground state is

empty this will lead to no, or little p-state luminescence. However if at the time of the arrival of the non resonant pulse the s-state is occupied due to some resonant excitation, then the p-state will become occupied and p-state luminescence will increase noticeably. This idea was implemented by using an infrared resonant excitation pulse and doubling the frequency of the infrared to produce the non resonant excitation pulse i.e. red – blue pump – probe.

A change in the photoluminescence intensity of the p–state was observed depending upon the intensity of the infrared pump, accompanied with a red shift in its emission energy. However both of the effects were found to be independent of the time delay between the infrared and blue pulses as well as the exact energy of the infrared pulse. This suggested that these effects were not simply related to the occupancy of the ground state.

In order to identify the origin of those two effects further measurements were undertaken. The temperature dependence in the range of 5 to 30 K of the photoluminescence under non resonant excitation was studied. The photoluminescence intensity of all of the observed spectral lines appeared to increase with temperature and shift its energy towards longer wavelengths showing that heating might contribute to effects observed at the two colour pump experiment. Furthermore the exciton emission wavelength was found to have an over-quadratic dependence on temperature which deviates from the quadratic dependence predicted by Varshni's formula possibly due to many body effects in the quantum dot. The photoluminescence intensity increase was attributed to more efficient relaxation processes due to the increase of phonon population with temperature.

The wavelength red shift due to increased excitation intensity under resonant or close to resonant excitation of the p-state was found not to depend upon excitation energy and was also observed for cw excitation. These measurements showed that this shift is not related with light absorption in the quantum dot or two photon absorption in the GaAs substrate. Furthermore all of the spectral lines shift equally as it would be expected if heating was the mechanism.

The photoluminescence intensity profiles of the exciton and the charged exciton exhibited oscillations with excitation intensity under the above resonant excitation

conditions. Oscillations of the excitonic photoluminescence intensity as a function of the excitation intensity under resonant exctition from sub-nanosecond pulses in quantum dots have been reported in the literature and their origin was attributed to Rabi oscillations. However in the current experiments similar oscillations were also observed under cw excitation which rules out the possibility of Rabi oscillations. The latter raised the suspicion that an excitation induced shift of the absorption might be fully responsible or contributing to the observed oscillations. A simple mathematical model was developed assuming that the absorption lines red shift with a fixed energy separation from the exciton and that the shape of the absorption line does not change with excitation intensity. Comparison of this model with the observed oscillations showed that it cannot be the sole explanation of the observed effect.

Photoluminescence excitation spectroscopy scans for different excitation intensities confirmed the suspected red shift of the absorption lines with excitation intensity. The resemblance of this effect with the red shift of the photoluminescence lines with temperature indicates that heating might contribute to the red shift induced by the excitation beam. Two more effects were observed. The first one is an increase of the absorption background with excitation intensity which was attributed to electronic transitions from electronic levels in the quantum dot to wetting layer holes[26,27]. The second one is a broadening of the red shifting absorption lines with excitation intensity. Comparison with the broadening of photoluminescence lines that were similarly red shifted due to temperature increase showed that the excitation induced broadening is considerably wider than the one caused by the temperature increase. Thus heating induced by excitation cannot be the sole explanation for the changes in the PLE spectrum. The overall mechanism that causes the red shift and the broadening of the absorption lines remains unknown. However the measurements indicate that the original concept for indirectly measuring the occupation of the ground state is not feasible.

6.11 Appendix I

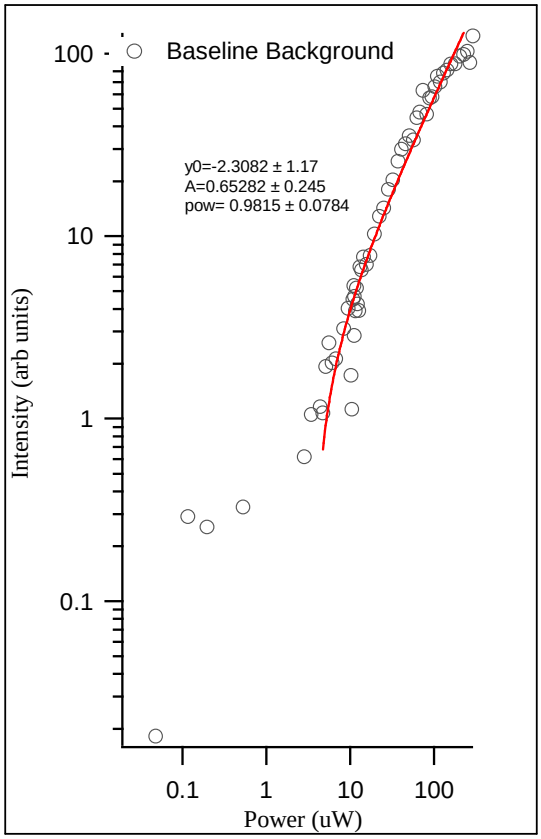

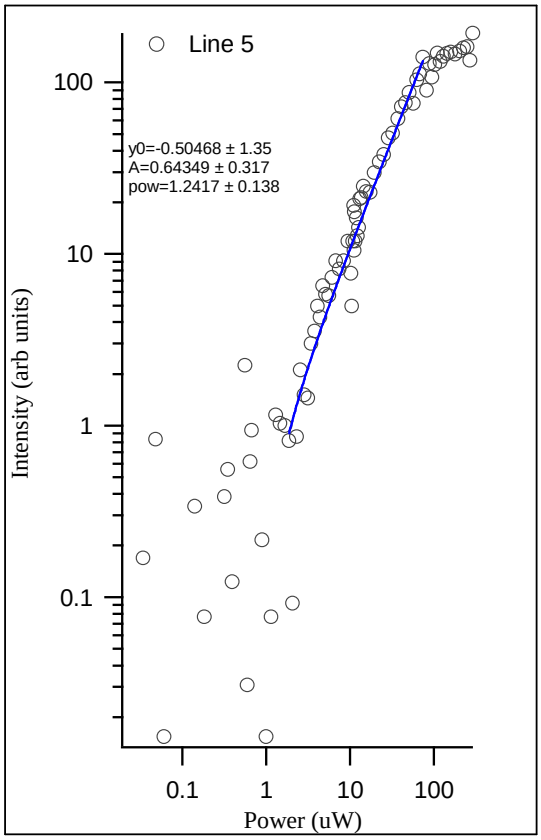

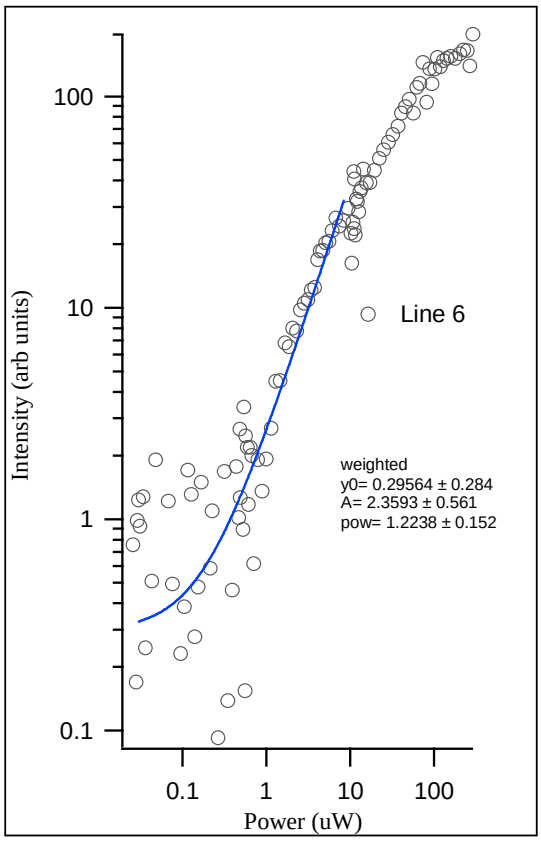

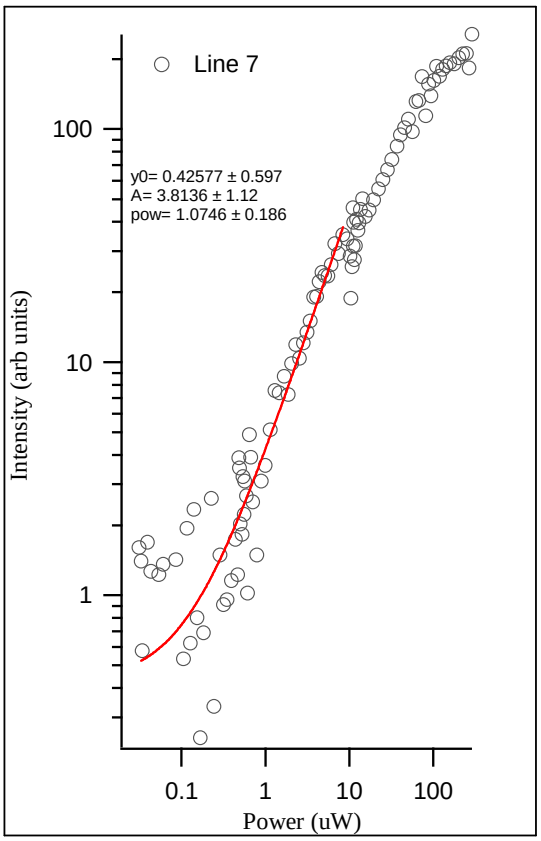

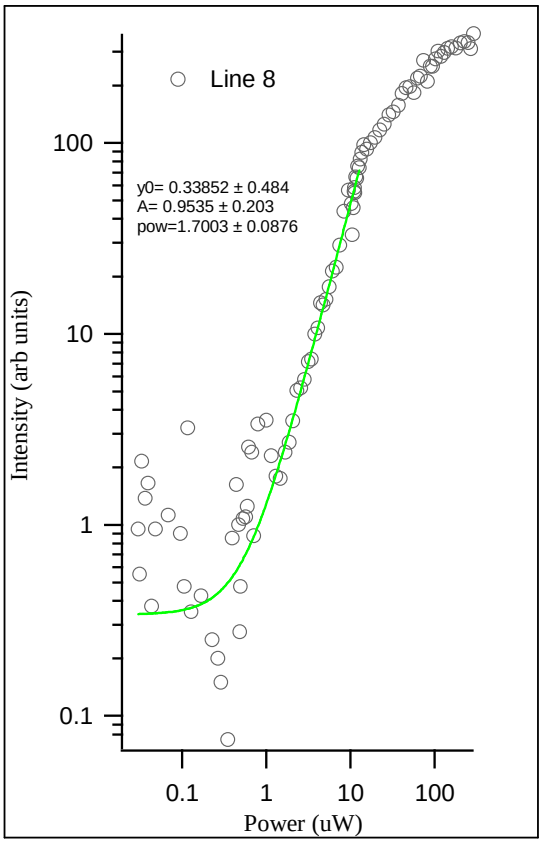
Line 8
y0= 0.33852 ± 0.484
A= 0.9535 ± 0.203
pow=1.7003 ± 0.0876
Intensity (arb units)
Power (uW)
0.1
1
10
100

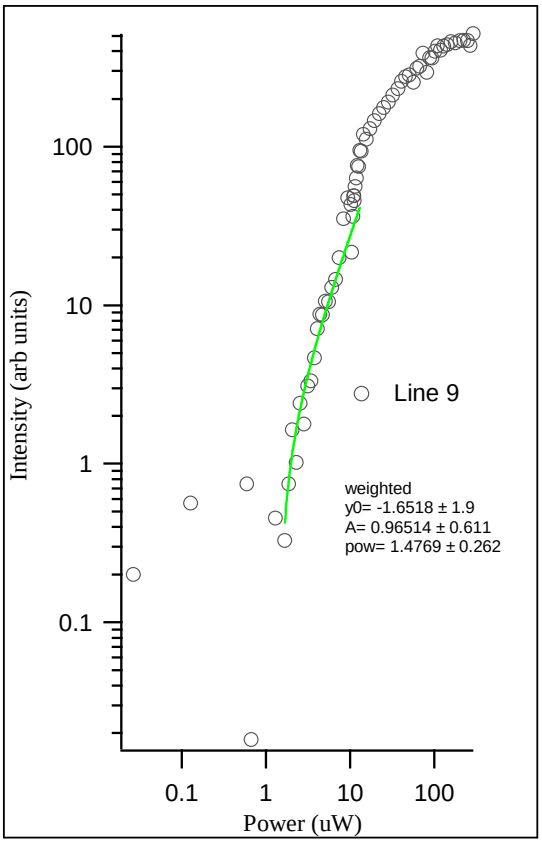
Line 9
weighted
y0= -1.6518 ± 1.9
A= 0.96514 ± 0.611
pow= 1.4769 ± 0.262
Intensity (arb units)
Power (uW)
0.1
1
10
100

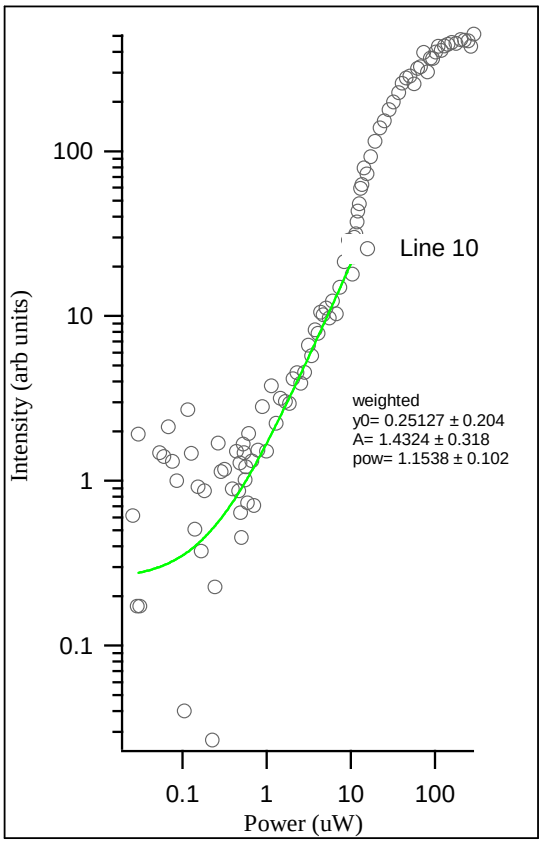
Line 10
weighted
y0= 0.25127 ± 0.204
A= 1.4324 ± 0.318
pow= 1.1538 ± 0.102
Intensity (arb units)
Power (uW)
0.1
1
10
100

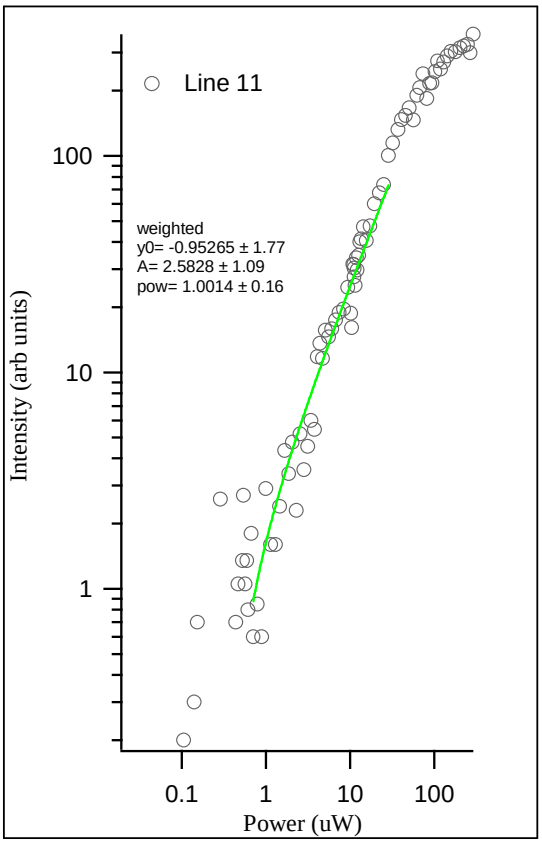
Line 11
weighted
y0= -0.95265 ± 1.77
A= 2.5828 ± 1.09
pow= 1.0014 ± 0.16
Intensity (arb units)
Power (uW)
1
10
100

6.12 Appendix II

Appendix II - Table 1 Fitting parameters for the power law fitting curves of the wavelength shifts of spectral line a-e for all sets of measurements

line	**λo**	**A**	**p**
a1	929.65±0.020709	0.016897±0.0021242	1.1289±0.02838
b1	932.7±0.039112	0.021317±0.0053426	1.0779±0.057771
c1	933.06±0.063553	0.010051±0.004895	1.2633±0.11357
d1	933.68±0.0099781	0.017142±0.0011388	1.1262±0.015272
e1	934.34±0.028734	0.020639±0.0040189	1.0828±0.045378
a2	929.68±0.023382	0.017475±0.0028124	1.1196±0.037276
b2	932.7±0.021408	0.0278±0.0036644	1.013±0.030514
c2	933.08±0.031584	0.01527±0.0036389	1.1485±0.055862
d2	933.71±0.0080766	0.017108±0.0010423	1.1221±0.014349
e2	934.4±0.027701	0.018159±0.0032648	1.1132±0.041258
a3	929.65±0.05518	0.01666±0.0053593	1.1268±0.071831
b3	932.79±0.18044	0.015365±0.015249	1.1345±0.21746
c3	933.03±0.040048	0.019975±0.0058763	1.0632±0.068094
d3	933.69±0.011632	0.016204±0.0013556	1.1293±0.019344
e3	934.35±0.070696	0.02723±0.011997	1.003±0.10071
a4	929.58±0.019532	0.021699±0.0018971	1.1535±0.020015
b4			
c4	933.02±0.023466	0.013108±0.0020503	1.2782±0.037914
d4	933.6±0.0080232	0.023905±0.0010484	1.13±0.010459
e4	934.27±0.016886	0.02534±0.0023532	1.1204±0.022425

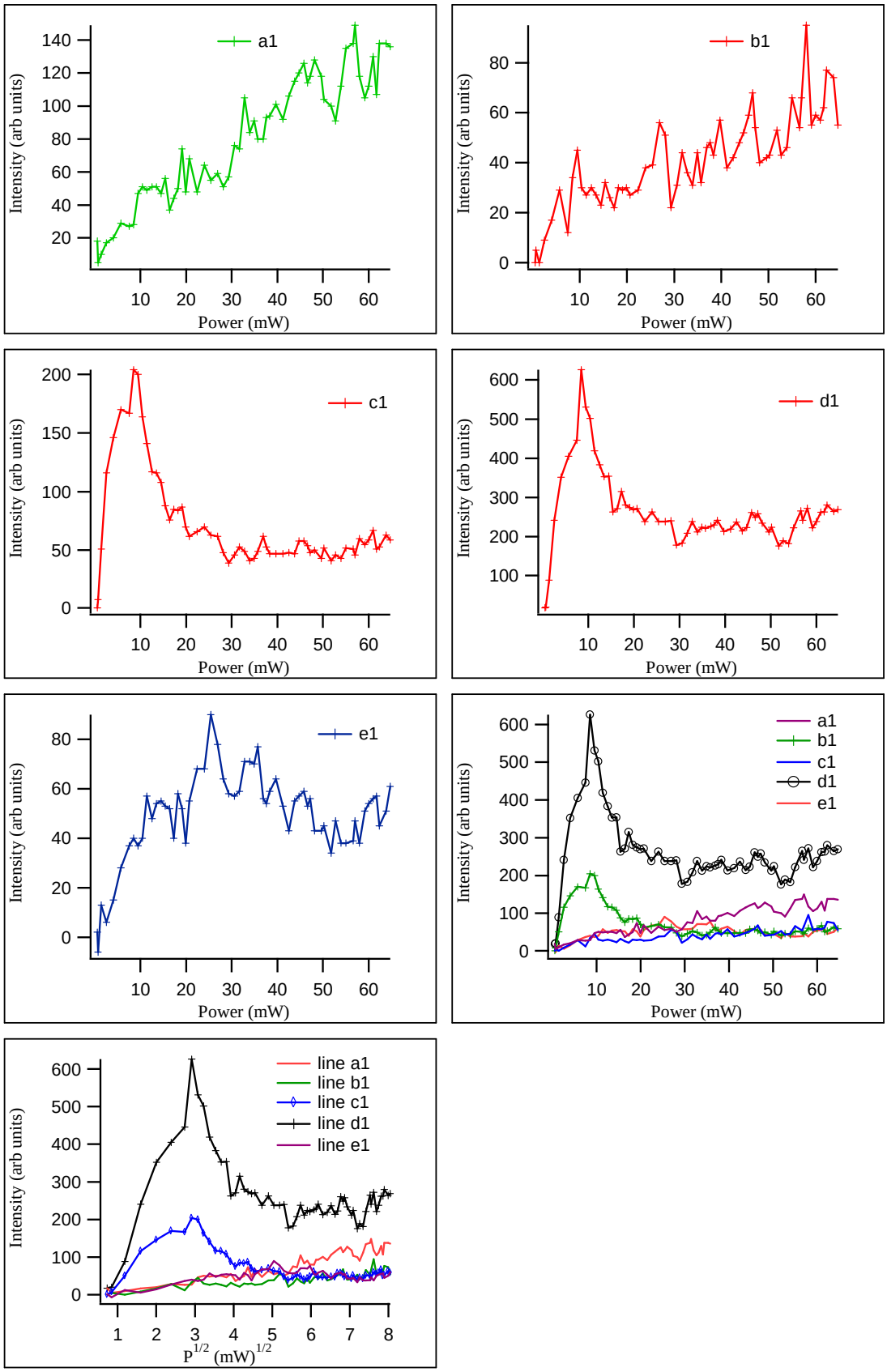

Appendix II - Figure 1 Intensity profiles of spectral lines a1- e1 as a function of the excitation density. At the bottom – right graph all the lines have been plotted together versus the excitation density. At bottom left the PL intensity of the lines have been plotted versus the square root of the excitation density.

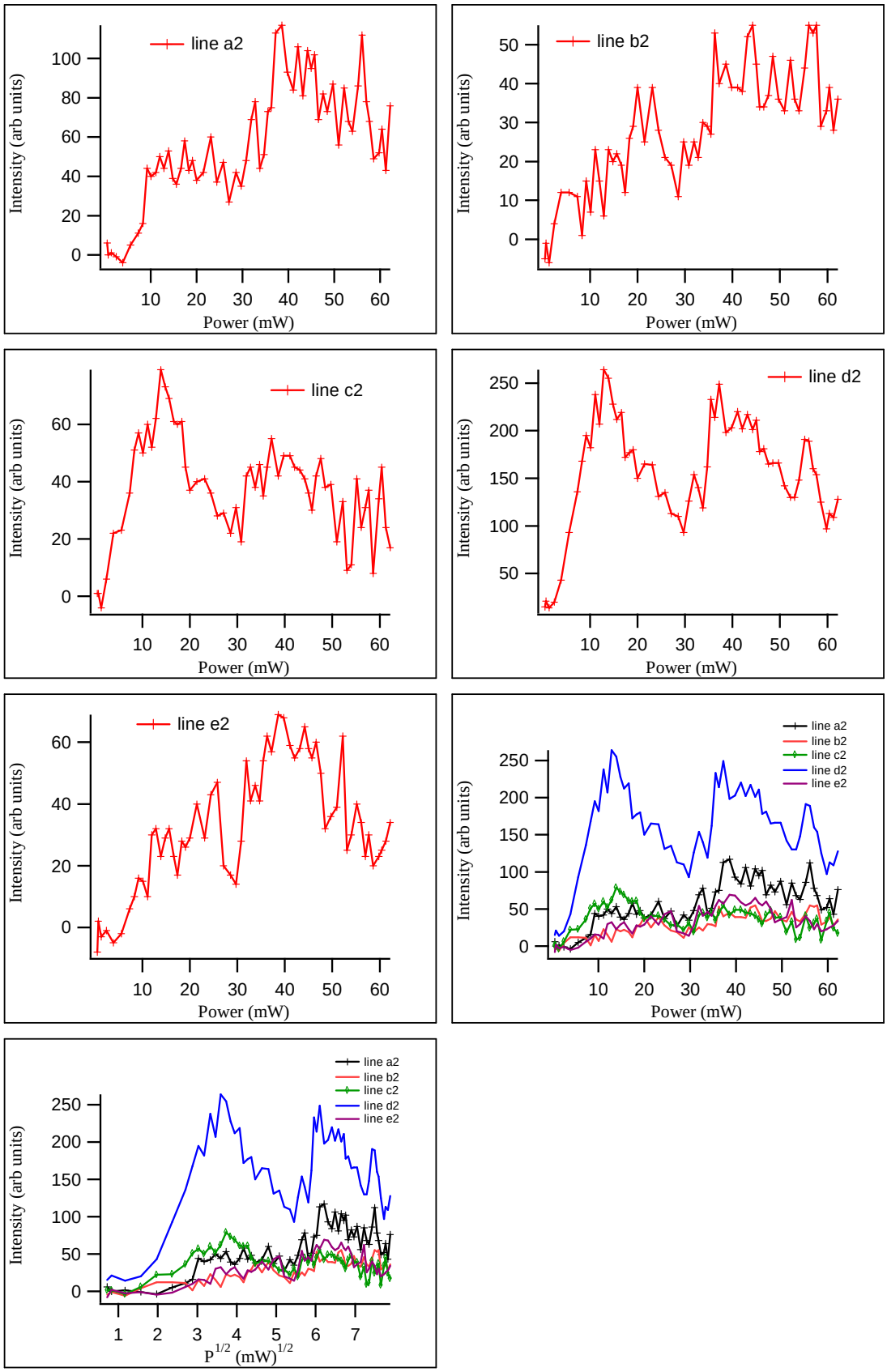

Appendix II - Figure 2 Intensity profiles of spectral lines a2- e2 as a function of the excitation density. At the bottom – right graph all the lines have been plotted together versus the excitation density. At bottom left the PL intensity of the lines have been plotted versus the square root of the excitation density.

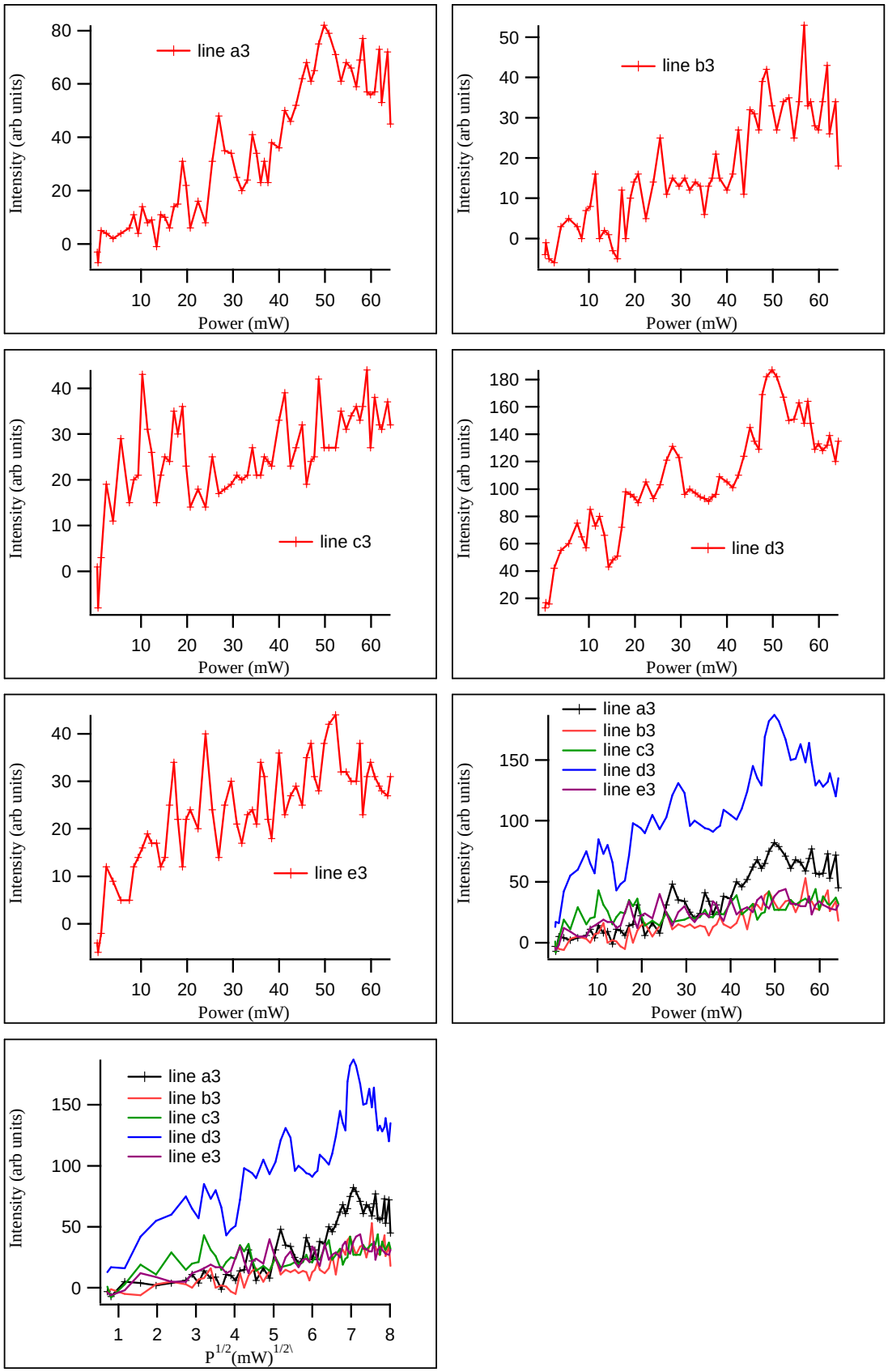

Appendix II - Figure 3 Intensity profiles of spectral lines a3- e3 as a function of the excitation density. At the bottom – right graph all the lines have been plotted together versus the excitation density. At bottom left the PL intensity of the lines have been plotted versus the square root of the excitation density.

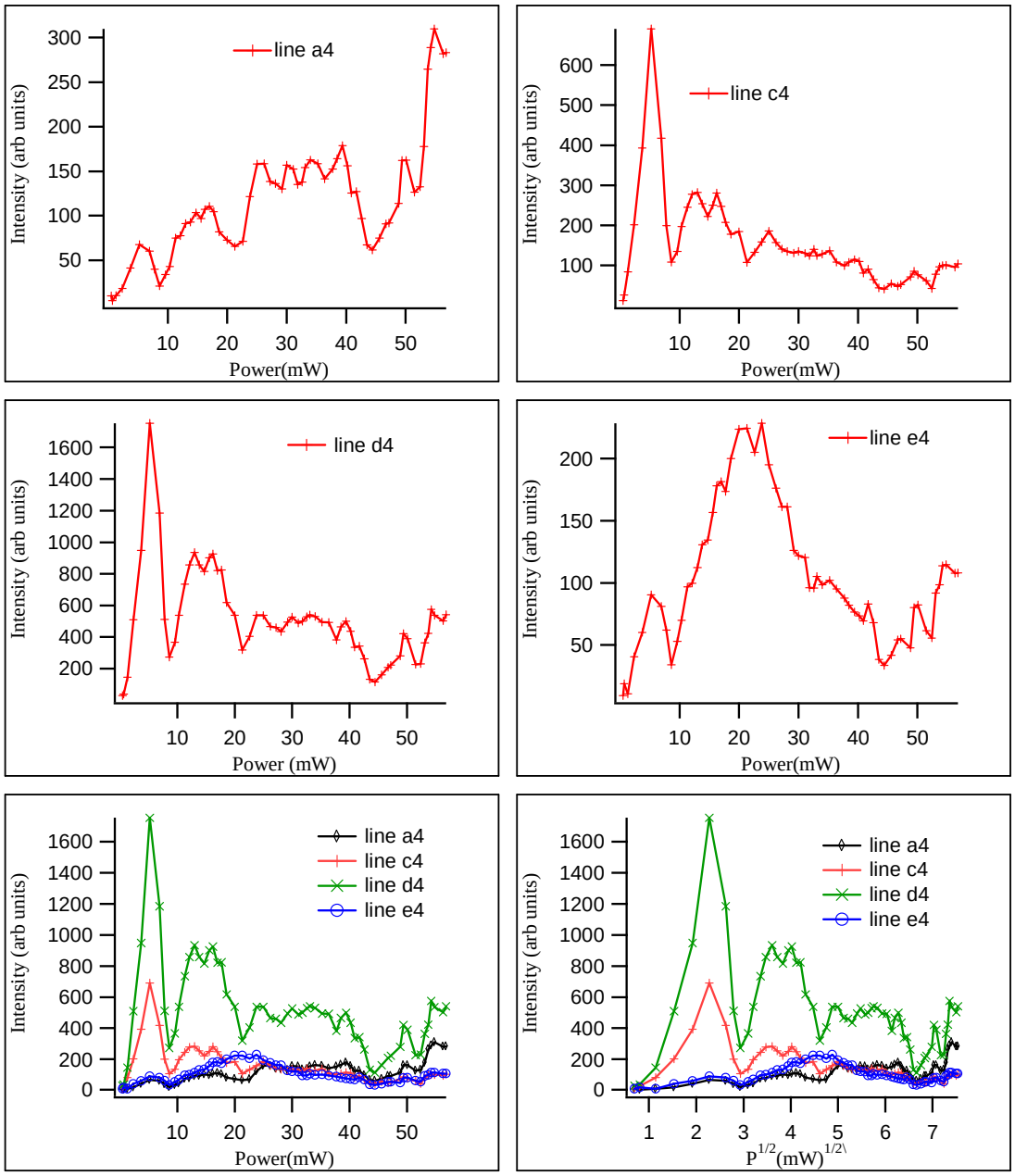

Appendix II - Figure 4 PL intensities of spectral line a4-e4 versus excitation density. Line b4 has been omitted as due to its very low intensity it was not possibly to be extracted form the data of fig. 18a. All of the PL lines versus excitation density and versus the square root of excitation density have been plotted in the bottom left and bottom right graphs respectively.

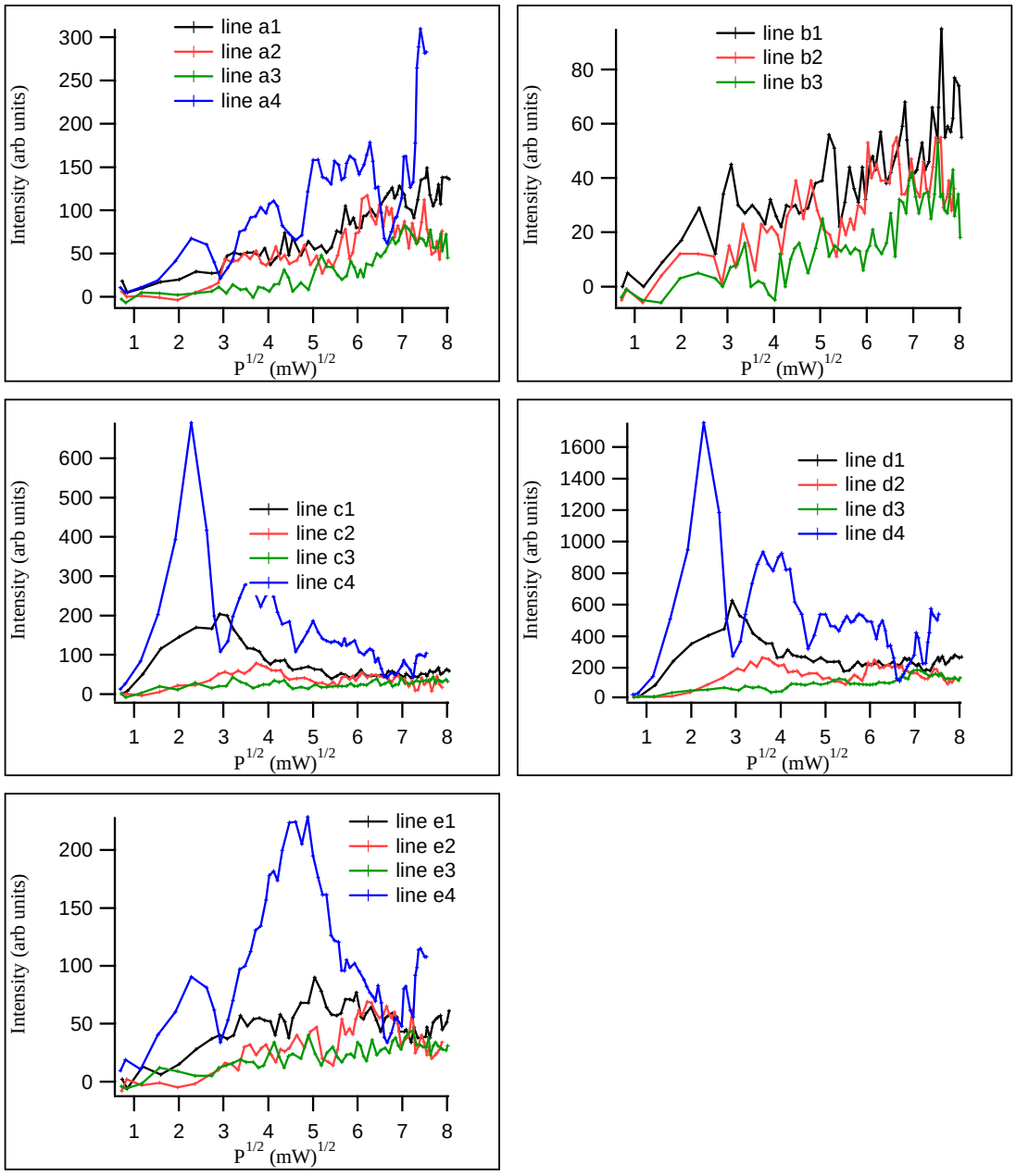

Appendix II - Figure 5 PL intensities of each of the a – e spectral lines versus the square root of the excitation density for all of the measurement sets (1-4) in each of the graphs.

6.13 *Appendix III*

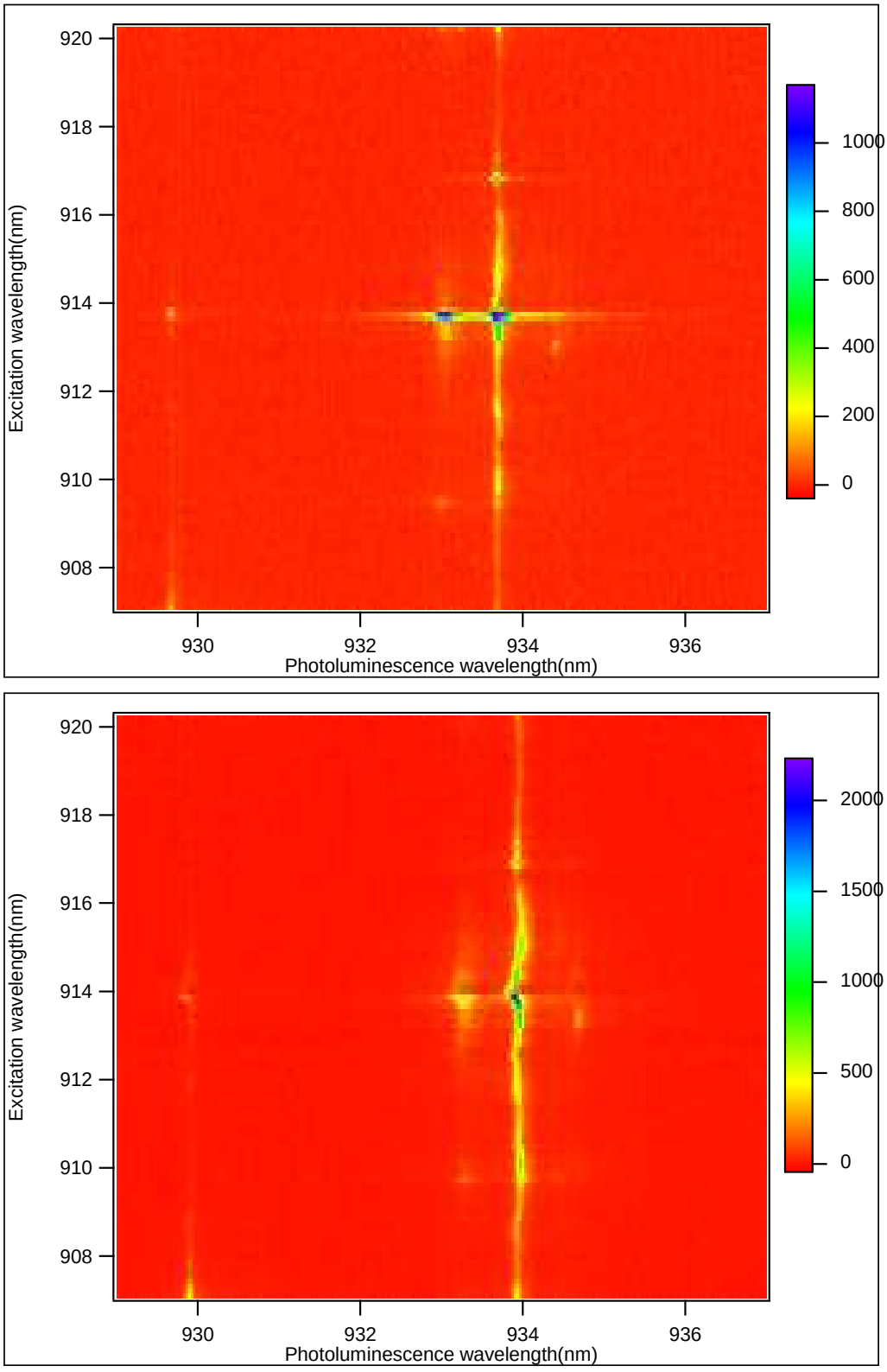

Appendix III - Figure 1 PLE scans for laser power 3.8mW (upper) and 10mW (lower)

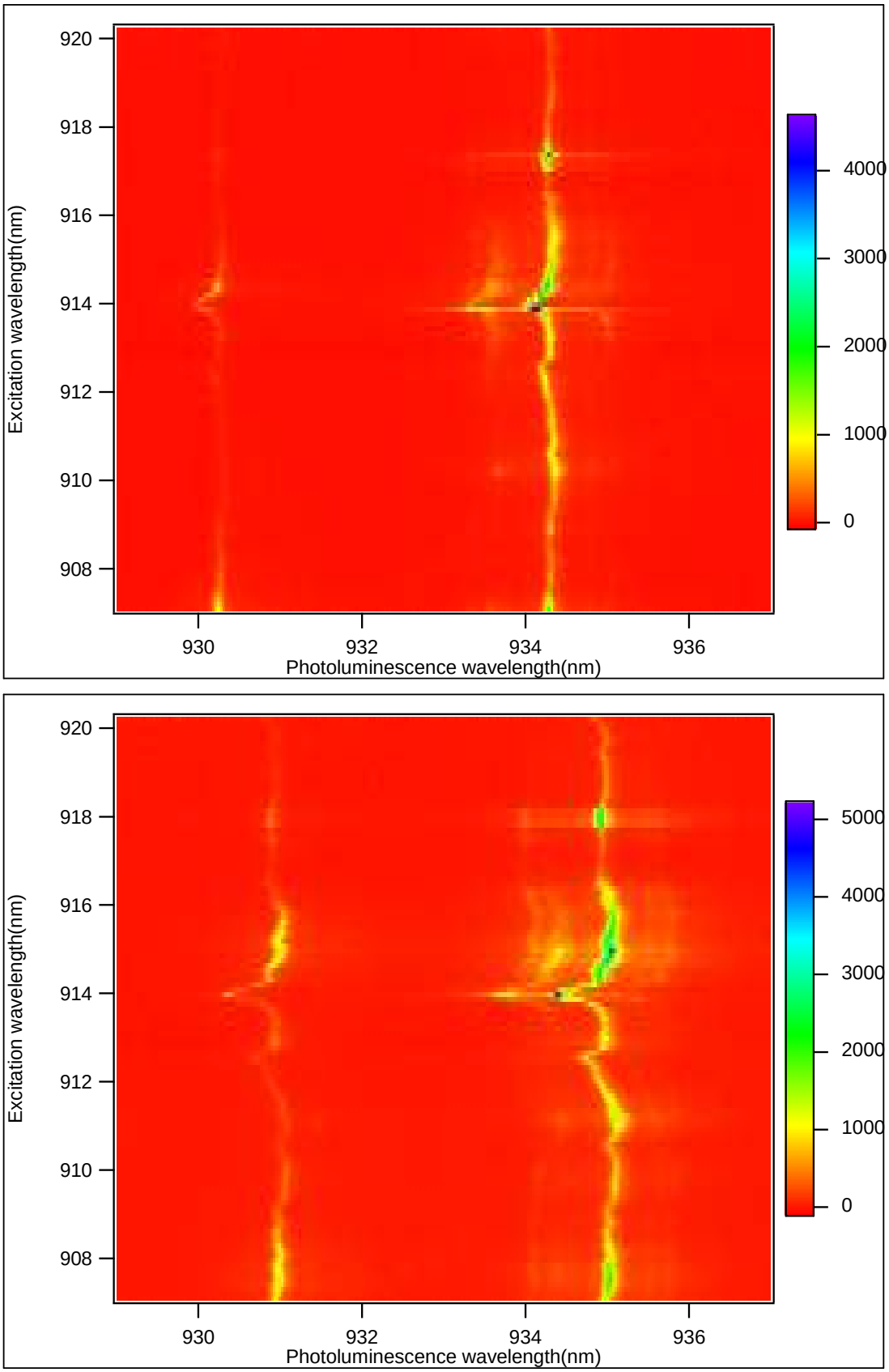

Appendix III - Figure 2 PLE scans for laser power 20mW (upper) and 40mW (lower)

Algorithm for extraction of PLE profiles: It was considered that the spectral distances between the lines remained as when exciting non – resonantly and also that in the PLE scans the exciton exhibits always greater intensity than all of the other lines. The routine finds the exciton wavelength by finding where the maximum in each spectrum is and then scans for a local maximum in a range of 6 points with a specified spectral distance from the main maximum (exciton)

References:

[1] L. Besombes, J. J. Baumberg, J. Motohisa, "Coherent Spectroscopy of Optically Gated Charged Single InGaAs Quantum Dots", Phys. Rev. Lett. 90, 25 (2003).

[2] I. N . Stranski., L. Krastanow, Akad. Wiss. Let. Mainz Math. Natur K1 IIb 146, 797 (1939).

[3] P. M. Petroff, S. P. Denbaars, "MBE and MOCVD growth and properties of self-assembling quantum-dot arrays in III-V semiconductor structures", Superlattices and Microstructures, 15 (1): 15-21 (1994).

[4] P. Bhattacharya, S. Ghosh, A.D. Stiff-Roberts "Quantum Dot optoelectronic devices", Annu. Rev. Mater. Res. 34, 1–40, (2004.)

[5] A weak background doping in the GaAs barriers is unavoidable. Typical values are $10^{15}/cm^3$. This doping will give rise to charging of the quantum dots which will reduce considerably their excitonic ground state emission. Low temperature growth of GaAs and subsequent annealing introduces charge traps that capture the carriers from the dopant thus minimising the charging of the quantum dots. (however the traps usually catch e^-) J. Allam private communications.

[6] N. H. Bonadeo, J. Erland, D. Gammon, D. Park, D. S. Katzer, D. G. Steel, "Coherent Optical Control of the Quantum State of a Single Quantum Dot", Science, 282 (1998).

[7] A. P. Heberle, J. J. Baummberg, K. Köhler, "Ultrafast Coherent Control and Destruction of Excitons in Quantum Wells", Phys. Rev. Lett. 75, 13 (1995)

[8] T. H. Stievater, Xiaoqin Li, D. G. Steel, D. Gammon, D. S. Katzer, D. Park, C. Piermarocchi, L. J. Sham3, "Rabi Oscillations of Excitons in Single Quantum Dots", Phys. Rev. Lett. 87, 13 (2001).

[9] H. Kamada, H. Gotoh, J. Temmyo, T. Takagahara, H. Ando, "Exciton Rabi Oscillation in a Single Quantum Dot", Phys. Rev. Lett. 87, 24 (2001).

[10] C. Dalsavio, K. Pierz, G. Ade, H. U. Danzebrink, E. O. Goebel, A. Hangleiter, "Optical study of single InAs on $In_{0.12}Ga_{0.88}As$ self assembled quantum dots: biexciton binding energy dependence on the dot size", Appl. Phys. B 84, 317 – 322 (2006).

[11] D. Sarkar, H. P. van der Meulen, J. M. Calleja, J. M. Becker, R. J. Haug, K. Pierz, "Phonons in InAs/AlAs single quantum dots observed by optical emission", Phys. Rev. B 71, 081302, (2005).

[12] K. Hinzer, P. Hawrylak, M. Korkusinski, S. Fafard, M. Bayer, O. Stern, A. Gorbunov, A. Forchel, "Optical spectroscopy of a single $Al_{0.36}In_{0.64}As/Al_{0.33}Ga_{0.67}As$ quantum dot", Phys. Rev. B, 63, 075314, (2001).

[13] D. J. Mowbray, M. S. Skolnick, "New physics and devices based on self-assembled semiconductor quantum dots", J. Phys. D: Appl. Phys. 38, 2059-2076, (2005).

[14] M. S. Skolnick, D. J. Mowbray, "Self – Assembled Semiconductor Quantum Dots: Fundamental Physics and Device Applications" Annu. Rev. Mater. Res. 34, 181-218, (2004).

[15] S. Sanguinetti, E. Poliani, M. Bonfanti, M. Guzzi, E. Grilli, M. Gurioli, N. Koguchi, "Electron-phonon interaction in individual strain-free GaAs/Al0.3Ga0.7As quantum dots", Phys. Rev. B 73, 125342 (2006).

[16] L. Besombes, J. J. Baumberg, J. Motohisa, "Excited States in optically – gated charged single InAs quantum dots", Phys. Stat. Sol. (c) , 5, 1501 – 1505, (2003).

[17] U. Bockelmann, W. Heller, A. Filoramo, Ph. Roussignol, "Microphotoluminescence studies of single quantum dots. I. Time – resolved experiments", Phys. Rev. B, 55, 4456, (1997)

[18] E. Dekel, D. Gershoni, E. Ehrenfreund, D. Spector, J. M. Garcia, P. M. Petroff, "Multiexciton Spectroscopy of a Single Self-Assembled Quantum Dot", Phys. Rev. Lett. 80, 4991, (1998)

[19] L. Landin, M. S. Miller, M. – E. Pistol, C. E. Pryor, L. Samuelson, "Optical Studies of Individual InAs Quantum Dots in GaAs: Few-Particle Effects", Science, 280, 262-264, (1998).

[20] F. Findeis, A. Zrenner, G. Böhm, G. Abstreiter, "Phonon – assisted biexciton generation in a single quantum dot", Phys. Rev. B, 61, 10579, (2000).

[21] A. Lemaître, A. D. Ashmore, J. J. Finley, D. J. Mowbray, M. S. Skolnick, "Enhanced phonon assisted absorption in single InAs/GaAs quantum dots", Phys. Rev. B, 63, 161309, (2001).

[22] Y. Toda, O. Moriwaki, M. Nishioka, Y. Arakawa, "Efficient Carrier Relaxation Mechanism in InGaAs/GaAs Self-Assembled Quantum Dots Based on the Existence of Continuum States", Phys. Rev. Lett. 82, 4114, (1999).

[23] M. Bayer, A. Forchel, P. Hawrylak, S. Fafard, G. Narvaez, "Excitonic States in In(Ga)As Self-Assembled Quantum Dots", phys. stat. sol. (b) 224, No. 2, 331–336 (2001).

[24] D. V. Regelman, E. Dekel, D. Gershoni, W. V. Schoenfeld and P. M. Petroff, "Dynamics of Excitons in Single Semiconductor Quantum Dots Probed by Time-Resolved Optical Spectroscopy", phys.stat. sol. (b) 224, No. 2, 343–348 (2001).

[25] G. Ortner, M. Schwab, M. Bayer, R. Pässler, S. Fafard, Z. Wasilewski, P. Hawrylak, A. Forchel, "Temperature dependence of the excitonic band gap in In*x*Ga1−*x*As/GaAs self-assembled quantum dots", Phys. Rev. B, **72**, 085328 (2005).

[26] R. Oulton, J. J. Finley,A. I. Tartakovskii,D. J. Mowbray, M. S. Skolnick, M. Hopkinson, A. Vasanelli,R. Ferreira, G. Bastard, "Continuum transitions and phonon coupling in single self-assembled Stranski-Krastanow quantum dots", Phys. Rev. B, 68, 235301, (2003).

[27] A. Vasanelli, R. Ferreira, G. Bastard, "Continuous Absorption Background and Decoherence in Quantum Dots", Phys. Rev. Lett. 89, 216804, (2002).

Conclusions of Part II

The focus of the second part of the thesis was on quantum dots and more specifically on their optical and coherent properties. In chapter 5 a brief literature review of their electronic and optical properties was presented. The effect of the three dimensional quantum confinement, and its various regimes, as function of the quantum dot size, the effect of various excitonic complexes as well as the coherent properties of a two level system were described.

In chapter 6 the experimental work on the optical spectroscopy of a single quantum dot was presented. By means of micro – Photoluminescence measurements extensive characterisation of a single quantum dot was carried out. The ground state of the quantum dot was identified from the linear dependence of its photoluminescence intensity upon the non resonant excitation intensity. By the same means as well as by photoluminescence excitation spectroscopy (PLE) the emission line at approximately 36 meV higher energy was identified as possibly originating from the first excited state of this quantum dot. A small discrepancy between the non resonant photoluminescence measurements and the resonance observed by means of PLE was attributed to many body effects.

During the PLE experiments an emission line having the same resonance as that of the excitonic ground state was also observed at 1 meV higher energy than the ground state. By carrying out simultaneous resonant and non resonant optical pumping this line was identified as the charged exciton. Its occurrence only when pumping at resonance (or close to it) was attributed to the existence of background doping resulting charge traps which are neutralised by the free carriers when the quantum dot barriers are pumped.

In order to study the coherence properties of the quantum dot ground state a time resolved two colour pump photoluminescence experiment was performed. The key idea of this method is to use an optical probe for the coherence of the ground excitonic state whose energy is different than the laser excitation and thus allows detection at zero laser background therefore improving significantly the signal to noise ratio. In brief the experiment consists of two pulses; a low energy one that pumps the ground state of the dot and high energy one that pumps the barriers at a delayed time and whose intensity is such that would lead to an average of two

excitons in the dot. The optical probe is the photoluminescence of the first excited state whose intensity would depend upon the occupation probability of the ground state. The latter is controlled by the intensity of the low energy pulse. This technique would enable the indirect observation and measurement of coherent effects such as Rabi oscillations.

When performed the time resolved two colour pump photoluminescence experiment, a change of the intensity as well as a red shift of the first excited state were observed. Both of them appeared to depend upon the intensity of the low energy pulse but were found to be independent of the time delay suggesting that the origin of those effects was not simply related with the occupancy of the ground state.

Further experiments were undertaken in order to identify the origin of these effects and also to find out if the study of the coherence of the ground state with the time resolved two colour pump photoluminescence method was feasible. Temperature dependence photoluminescence measurements showed all of the emission lines to red shift and increase their intensity with temperature in the range of 5 to 30 K. The red shift was found to have over-quadratic dependence on temperature thus deviating from the Varshni's formula. This deviation could be possibly attributed to many body effects. The intensity rise of the emission is probably the effect of the increase of the phonon population with temperature which results in more efficient relaxation mechanisms

Photoluminescence measurements under resonant excitation of the first excited state showed that the red shift caused by the excitation intensity increase does not depend upon the exact energy of the excitation or upon the excitation being pulsed or cw. Therefore the observed red shift is independent of light absorption in the quantum dot or two-photon absorption in the GaAs substrate. Furthermore all of the observed emission lines the same amount of red shift which resembles their shift due to heating.

The intensity of the emission of the exciton and charged exciton exhibited oscillations as the excitation intensity was increased under resonant or close to resonance excitation. These oscillation were observed for pulsed as well as for cw excitation thus excluding the possibility of being a manifestation of Rabi oscillations. The possibility the observed oscillations might be a convolution of a red shifting absorption with an increasing excitation was explored through the means of a mathematical model. The latter showed that the red shift of the absorption although

might contribute to the effect cannot be the only mechanism that causes the observed oscillations.

The red shift of the absorption was confirmed by photoluminescence excitation spectroscopy measurements for various excitation intensities. The observation that all of the absorption lines exhibited a red shift with excitation intensity resembling that of the emission lines indicated further towards the thermal origin of this effect. In the same experiments, an increase of the absorption background with excitation intensity was also observed and attributed to electronic transitions from electronic levels in the quantum dot to wetting layer holes. Additionally, a broadening of the absorption lines with excitation intensity occurred. This broadening was found to be considerably wider than the one exhibited by emission lines which have similarly been shifted due to temperature increase. The latter shows that the changes of the photoluminescence excitation spectra cannot be explained only by heating induced by the excitation. The overall mechanism of the red shift and broadening of the absorption lines remains unknown. Finally the above experiments indicate that the original concept for indirectly measuring the occupation of the ground state is not feasible.